# ABSTRACT

| | |
|---|---|
| Title of Document: | FOOD PROTEIN-BASED NANOPARTICLES AS BIOAVAILABILITY ENHANCING ENCAPSULANTS |
| | Zi Teng, Doctor of Philosophy, 2015 |
| Directed By: | Associate Professor Qin Wang Department of Nutrition and Food Science |

Proteins are attractive bioavailability enhancers for poorly absorbed nutraceuticals or drugs, owing to their natural abundance, amphiphilic nature, and desirable biocompatibility. This study systematically investigated the preparation, characterization, and application of protein-based nanoparticles as effective nutraceutical/drug carriers. Soy protein, one of the most widely utilized proteins, was firstly employed for preparing nanoparticles. The particle formation involved partial unfolding of protein molecules, limited aggregation in the presence of the antisolvent, crosslinking via chemical bonds, and refolding of the constituent monomers. Satisfactory encapsulation efficiency (EE) and time-dependent release of curcumin, a chemopreventive compound, were observed. The nanoparticles were further subjected to conjugation with folic acid, a cancer cell-targeting ligand. A pronounced increase in the accumulation in tumor cells such as Caco-2 was achieved upon folic acid conjugation, which demonstrated the potential of this technique for

the targeted delivery of anti-cancer drugs. To overcome the rapid digestion of soy protein nanoparticles in the gastrointestinal tract, carboxymethyl chitosan was employed as a second coating layer by a simple ionic gelation method. The formed particles exhibited satisfactory EE for vitamin $D_3$ and controlled releasing profile *in vitro*.

Beta lactoglobulin (BLG) as another protein of interest is a major component of whey protein, serving as a natural carrier for lipophilic nutrients. Our study suggested that the interaction between BLG and curcumin could be promoted by tuning the antisolvent content. A loading capacity (LC) and EE of up to 11% and 98% respectively could be achieved under the optimal conditions. Moreover, nanoparticles prepared with cationic beta lactoglobulin (CBLG) were able to transport most of the encapsulated drug intact through the gastrointestinal (GI) tract owing to its desirable particle integrity. Other advantages of CBLG-based systems included superior mucoadhesion, permeation across the small intestine epithelia, and cellular uptake. Finally, as CBLG molecules/nanoparticles absorbed the negatively charged serum proteins in the cell culturing medium, their surface properties, cytotoxicity, and cellular uptake were significantly altered. This series of studies not only demonstrated the efficiency and versatility of protein-based nanoparticles as bioavailability enhancers but also shed some light on the mechanisms for the encapsulation, transport, and delivery of nutraceuticals or drugs.

FOOD PROTEIN-BASED NANOPARTICLES AS BIOAVAILABILITY
ENHANCING ENCAPSULANTS


By


Zi Teng


Dissertation submitted to the Faculty of the Graduate School of the
University of Maryland, College Park, in partial fulfillment
of the requirements for the degree of
Doctor of Philosophy
2015

Advisory Committee:
Dr. Qin Wang, Chair
Dr. Thomas W. Castonguay
Dr. Jiuzhou Song
Dr. Joonil Seog
Dr. Thomas TY Wang

# Dedication

This dissertation is dedicated to my wife, Ying Li, who devoted most of her time and energy to our family and my career development. No achievement could have been made without her unconditional love and support. I would also like to congratulate her on the exciting progress in her own research and will support it with my maximal enthusiasm.

I also dedicate this work to my beloved daughter, Gloria Chumeng Teng. The birth of the little one in August 2014 was the most joyful event in my life. It has been such a sweet experience to watch her grow and learn, and her heart-melting smile simply cures me from any fatigue and frustration. Ying and I are making every effort to make every moment in her life enjoyable, just as we enjoy every minute with her!

Finally, I would like to dedicate this work to my parents who brought me up and supported me selflessly. They did not only offer countless guidance and immense help in my study but also taught me about the imperative traits of a man: prudence, confidence, modesty, and integrity. I am very proud for having such great parents and will endeavor in my life to make them proud.

# Acknowledgements

It was so fortunate to me that I received countless assistance and support from so many professors, colleagues, friends, and family members. Their help has made my PhD study a fruitful and unforgettable experience in my life. First of all, I would like to express my greatest gratitude to my advisor, Dr. Qin Wang, for her generous support during my PhD study. Dr. Wang not only shared her precious experience in my research with me but also endeavored to help me succeed by every means. She provided me with the best research conditions possible, as well as the best opportunity to present my studies in multiple academic conferences.

My sincere thanks also go to the members of my dissertation committee: Dr. Thomas W. Castonguay, Dr. Jiuzhou Song, Dr. Joonil Seog, and Dr. Thomas TY Wang. It has been a great time working with these respectable professors. They are always ready to lend me a hand whenever I need guidance in designing the framework of my dissertation or conducting a specific experiment. Their effort throughout my study is highly appreciated.

I would also like to acknowledge my lab mates, Dr. Boce Zhang, Dr. Yangchao Luo, Dr. Zhenlei Xiao, and Mr. Yunpeng Wu, as well as Dr. Haiqiu Huang and Mr. Boyan Gao from Dr. Liangli (Lucy) Yu's lab. These people offered me numerous advices and extensive assistance, not only in my research, but also

in every aspect of my life in the United States. Without their help, I could not have finished my PhD study smoothly and enjoyably.

I owe my deepest thanks to my family members for their everlasting dedication to my life and study. I am particularly thankful to my wife, Dr. Ying Li, for her unconditional love and belief in me. Since our college years, we have experienced all the happiness and bitterness in our lives. In order to accompany and support me, she resigned from her well-paid position in China without any hesitation. Also, I am forever in awe of the dedication by my parents, who raised, guided, and supported me selflessly for decades. I could have achieved nothing in my career without their care.

Last but not least, I also appreciate the University of Maryland for providing such a good academic environment. I would like to thank the Graduate School for the generous tuition remission and fellowships, and the faculty and staffs in the Department of Nutrition and Food Science for their kind help in my academic affairs.

# Table of Contents

# List of Figures

# List of Tables

# Chapter 1 Introduction

## 1.1   Background of nano-encapsulation

Nano-encapsulation has been extensively studied as an effective approach for enhancing the bioavailability of poorly absorbed nutraceuticals or drugs [1, 2]. This technique takes advantage of the ability of a polymer or multiple layers of polymers that assemble spontaneously into nano-scale matrices in the presence of certain stimuli (e.g., pH, organic solvent, temperature, electrolytes). The target compounds being encapsulated are either insoluble or unstable in the freestanding from. They associate with the polymeric matrix through various interactions, such as electrostatic attraction, hydrophobic interaction, hydrogen bonding, and van der Waals force. A broad range of food and pharmaceutical compounds, from natural colorant to anti-cancer drugs, from vitamins to antimicrobial agents, have been encapsulated into polymeric nanoparticles. By carefully selecting the matrix composition and fine-tuning the environmental parameters, one could prepare bioactive compound-loaded particles with an average size of 50-500 nm, together with narrow size distribution and desirable dispersion stability. These nano-scaled systems provided the compounds with numerous benefits, such as improved water solubility, increased resistance against chemical degradation, better absorption in human body, prolonged circulation, controlled release, elevated cellular uptake and target-specific delivery.

## 1.2    Key factors for successful encapsulation and delivery

### 1.2.1    Loading capacity (LC)

LC is the mass ratio between the encapsulated compound and the polymeric matrix, and it indicates the efficiency of the delivery system. LC is dependent on the type and strength of association between the compound and the matrix [3]. In general, charged compounds interact strongly with oppositely charged polymers via electrostatic attraction [1], and hydrophobic chemicals tend to associate with the core region of the encapsulant through hydrophobic interaction [2]. It is also important to note that these interactions are significantly influenced by environmental factors, such as pH, ionic strength, and temperature [4]. Therefore, for each compound of interest, it is essential to choose an (or a combination of) appropriate encapsulant(s) and suitable particle forming conditions that provide sufficient core-shell association. These considerations are crucial for achieving desirable loading capacity for a specific compound in a physiologically relevant environment.

### 1.2.2    Dispersion stability

The stability of a colloidal system (e.g., an aqueous dispersion of nanoparticles) is governed by the attraction and repulsion between colloidal particles, and it is vital for the bioabsorption of the target compounds. Attractive forces include hydrogen bonding, van der Waals interaction, hydrophobic association, and electrostatic attraction, while the repulsive interaction arises from the electrostatic repulsion

and steric hindrance between particles. Zeta potential gauges the electric charge at the boundary of a colloidal particle, and it is an important index for its surface charge. Zeta potential determines the electrostatic repulsion among them and is accountable for their stability against precipitation, and it is usually obtained by measuring and converting from the electrophoretic mobility of the particles. As recommended by American Society for Testing and Materials (ASTM), zeta potentials with an absolute value of higher than 30 mV are indicative for "moderate to good" stability of colloidal systems [5].The higher the zeta potential, the better the stability of a dispersion. A desirable zeta potential could be obtained by choosing highly charged polymers (e.g., soy protein or chitosan) as an encapsulant. On the other hand, when poorly charged materials (e.g., zein) are employed for encapsulation, a second layer of highly charged polymers may be introduced to improve the dispersion stability [6-8].

### 1.2.3 Controlled release

When the encapsulated compound is consumed via the oral route, it enters the digestive system and needs to be delivered in a controllable manner. The term "controlled release" indicates (1) timed release of entrapped compounds or (2) delivery of the compound at designated regions in the gastrointestinal (GI) tract. The former goal could be achieved in virtually all encapsulation systems because the core-shell association could delay the release of entrapped compounds. The latter feature is vital for elevating the bioavailability of orally administrated

compounds while lowering their side effects. For common nutraceuticals such as vitamins and polyphenols, they should be well protected against acidic degradation in the stomach and completely released in small intestine where absorption takes place [6]. This could be realized by choosing proper polymers that is indigestible by strong acids and pepsin in the stomach while being degradable in the intestinal environment. In some other applications, the encapsulated compounds should arrive intact at the wanted regions (such as colon) without significant loss in other tissues. This requires an encapsulant that resists both gastric and intestinal digestion and degrades only upon the exposure to a specific stimulus, such as pH and enzyme, at the target site.

### 1.2.4 Mucoadhesion

Upon arrival to the small intestine, the bioactive compounds traverse the intestinal lining before entering the systemic circulation. Mucin is a negatively charged glycoprotein secreted by the small intestine epithelia. It covers the intestinal wall densely as a gel-like layer and serves as the first barrier for incoming molecules or microorganisms [9]. Adhesion to mucin, known as mucoadhesion, is therefore essential for the bioavailability of nutraceuticals or drugs [10]. Mucoadhesion improvement could be achieved by encapsulating bioactive molecules in cationic polymer matrices, among which chitosan is the most popular choice [11, 12]. Anionic or neutral polymers such as sodium alginate and dextran derivatives,

4

respectively, also exhibit remarkable mucoadhesive properties, probably due to the extensive hydrogen bonding with the mucin layer [13].

### 1.2.5 Circulation

After entering the circulative system, it becomes important for the delivering vehicle to reside for sufficient time before the bioactive compounds are released and absorbed. However, as many types of vehicles are recognized by the immune system as invading substances, they are rapidly opsonized and cleared by the macrophages [14]. One of the common approaches to prolonged circulation is the surface modification by PEG, whose long polymeric chain prevents the binding of serum components by steric hindrance. Several other strategies have been developed, including modification with CD47 (a protein recruited by the human body to identify cells as "self"), modulation of mechanical properties, engineering particle morphology and hitchhiking on red blood cells [15].

### 1.2.6 Cellular uptake

The last step for the delivery is the uptake by target cells. For bioactives that do not require site-specific delivery, their cellular uptake could be improved by carefully tuning the surface properties of the delivery vehicles. For example, cationic vehicles exhibit higher affinity to most types of cells because of the abundance of negatively charged glycoprotein on cell membrane [16]. Delivery vehicles with higher surface hydrophobicity have also been revealed to permeate the cell membrane better, thus promoting cellular uptake [17, 18]. For compounds

that have effect on specific sites (e.g., tumors), they could be incorporated to a polymeric vehicle that is conjugated with target-specific ligands such as folic acid [19].

## 1.3    Protein-based nanoparticles as a delivery system

Nanoparticles are nano-scale assemblies of inorganic or organic molecules. Their sub-micron size provides several advantages such as prolonged gastrointestinal residence, better tissue penetration and superior cellular uptake [20]. Proteins are amphiphilic polymers that possess well defined charged, hydrophilic (polar but non-charged) and hydrophobic domains [20, 21]. This character allows protein-based nanoparticles to associate strongly with various types of bioactive compounds, providing satisfactory encapsulating capacity. In addition, since proteins are natural biopolymers, protein nanoparticles exhibit satisfactory biodegradability and biocompatibility [22]. Depending on the nature of different proteins, various strategies have been developed to synthesize nanoparticles, including organic solvent desolvation, liquid-liquid dispersion, and ionic gelation.

### 1.3.1    Protein nanoparticles prepared by organic solvent desolvation

This method is applicable to proteins that are highly soluble in water whereas virtually insoluble in certain water-miscible organic solvents [23]. A wide variety of albumins (including bovine and human serum albumins) [3, 23] and globulins (such as soy proteins and BLG) [24, 25] have been employed to encapsulate hydrophobic compounds using this method. A typical protocol using this method

includes the following procedures. Protein is firstly dispersed in an aqueous buffer at a relatively high concentration (e.g., 50 mg/mL), while the compound of interest is dissolved in an organic solvent (e.g., ethanol or acetone). Then, the organic phase is introduced dropwise into the aqueous phase under vigorous stirring. This initiates the aggregation of protein molecules and allows the interaction between the protein and the target compound. When a desirable concentration of organic solvent (usually higher than 80%) is achieved, the mixture turns from a clear solution into an opaque colloidal dispersion, indicating the extensive formation of nanoparticles. Trace amount of crosslinker (e.g., glutaraldehyde or genipin) is introduced at this point to harden the structure of particles via chemical bonds. After several hours of reaction, the dispersion is subjected to evaporation under reduced pressure to remove the organic solvents. During this process, the nanoparticles are able to maintain their structure owing to the crosslinking procedure. In the meantime, the interaction between the hydrophobic compound and the hydrophobic sites on protein molecules is enhanced because of the increase in both solvent polarity and protein (and bioactive compound) concentration. Lastly, water is supplemented to the mixture to replace the evaporated solvents (optional). Further purification steps including gel filtration, dialysis, and ultracentrifugation could be taken, but they are not necessary. Optimal particle size (100-200 nm) and LC (5-10%, weight ratio) could be obtained by tuning the concentrations of protein, compound of interest, organic

solvent, and crosslinkers [23]. Other parameters such as pH and ionic strength also play an important role in the encapsulation process [26]. Nanoparticles prepared through this approach exhibit desirable dispersion stability due to the high solubility of the protein chosen, and they are also stable against dissociation upon dilution or in the presence of salts. The major challenge for this method lies in the relatively low loading capacity, because the content of hydrophobic sites of globulins and albumins are significantly lower than that of more hydrophobic proteins, such as prolamines [27, 28]. In addition, the application of toxic crosslinker (glutaraldehyde) leads to the concern on the safety of these nanoparticles.

### 1.3.2   Protein nanoparticles prepared by liquid-liquid dispersion

Liquid-liquid dispersion is a simple yet effective way to synthesize nanoparticles with water insoluble prolamines [29, 30], such as zein (the major protein from maize). These proteins show unique solubility that they could only dissolve in a water-alcohol system with a limited range of mixing ratio. Due to the hydrophobic nature of these proteins, this approach is suitable for encapsulating hydrophobic compounds. In a typical liquid-liquid dispersion process, the protein and target compound are co-suspended in a binary system containing more than 70% alcohol (e.g., ethanol). After a short period (about 30 min) of equilibrium, the organic phase is poured into a large amount of aqueous buffer under vigorous stirring to achieve an alcohol: water ratio of approximately 15:85. The burst in solvent

polarity drives extensive protein-protein and protein-compound association through hydrophobic interaction, in order to compensate the sudden decrease in systemic entropy. Such interaction results in the entrapment of bioactive compounds into of a considerable number of nanoparticles. Satisfactory particle size of 100-200 nm and loading capacity of typically 10-20% could be achieved by adjusting the composition of the organic phase, i.e., alcohol content, protein concentration, protein/compound ratio, etc. An additional evaporation step can be taken to remove residual alcohol. The greatest advantages of this method are the simplicity of operation and the absence of toxic crosslinking reagents. The formed particles maintain the original morphology upon dilution, but they are susceptible to precipitation in the presence of salt. In addition, the dispersion stability of these nanoparticles is not as ideal as that of albumin or globulin nanoparticles because of the lack of hydrophilic and charged amino acid residues [31]. To overcome this weakness, a bilayer nanoparticle system containing a protein emulsifier (e.g., sodium caseinate) and a water-insoluble protein (e.g., zein) has been developed [32, 33]. The idea was to disperse the organic phase in an aqueous solution of the emulsifier. The mixing of the two dispersions induces the encapsulation of zein, together with the hydrophobic compound, in a more hydrophilic layer comprising mainly sodium caseinate. The resultant nanoparticle suspension exhibits desirable dispersion stability owing to the high zeta potential, and it is resistant against precipitation at a salt concentration of 1.5M [34]. The introduction of a second

layer, however, has a negative effect on the LC, considering that the total weight of encapsulant is significantly increased [32, 33].

### 1.3.3 Protein nanoparticles prepared by ionic gelation

Ionic gelation, also known as cold gelation, is especially effective in incorporating charged nutraceuticals or drugs into a polymeric matrix. It is applicable to not only charged proteins (albumins or globulins) [25] but also polysaccharides such as chitosan and its derivatives [35, 36]. In this procedure, the protein is firstly solubilized in an aqueous buffer at pre-determined pH to ensure sufficient surface charge on the protein molecules. Another aqueous solution of a similarly (or oppositely) charged target compound is then introduced into the protein dispersion under mild stirring. After a brief period of equilibrium (around 30 min), a chemical reagent bearing multiple opposite electric charges is dripped slowly into the abovementioned dispersion. The added chemicals contain multivalent ions such as calcium ($Ca^{2+}$) and tripolyphosphate (TPP, $P_3O_{10}^{5-}$), which could act as an ionic bridge between the proteins through strong electrostatic attraction. An opaque aqueous dispersion of nanoparticles is formed in less than 30 min, which could be then separated from excessive salts and non-incorporated compound via centrifugation, dialysis or gel filtration. Particles with satisfactory size (around 200 nm) and LC (typically 20-50%) could be formed by carefully tuning the pH and salt concentration, both of which have a significant impact on the surface charge of the polymer [37]. This method is highlighted for its simplicity and the

exemption from chemical crosslinking procedure. While it is more suitable for encapsulating charged molecules (e.g., water-soluble vitamins and peptides), it has also been widely applied to incorporate hydrophobic compounds The major shortcoming of this method is the dissociation of nanoparticles upon pH fluctuation, dilution or high salt concentrations, since all of these factors could disrupt the electrostatic interaction. In addition, since two oppositely charged molecules are mixed in this method, the prepared nanoparticles usually exhibit relatively low surface charge, which is unfavorable for their dispersion stability in the long term [38]. This problem could be overcome by adding stabilizers (such as Tween 20 or Pluronic® F-68) or using diluted product [39-41]. Lastly, in spite of the claimed high loading capacity, it was found that a considerable part of the "encapsulated" compound might be loosely bound at the perimeter of the polymeric matrix, rather than being embedded inside the nanoparticles. This hypothesis has been supported by FT-IR and X-ray diffraction study in many articles [35, 37, 40, 41]. Therefore, the protection to the incorporated compound by the nanoparticles may be limited.

### 1.3.4    Advantages and disadvantages of protein-based nanoparticles

As is discussed above, protein-based nanoparticles exhibit several significant advantages over polysaccharide- or synthetic polymer-based systems. Protein nanoparticles are capable to encapsulate different types of compounds-charged, polar or hydrophobic, owing to the variety of amino acid residues in the protein

molecules. Compared to polysaccharide nanoparticles that are mostly formed via ionic gelation, protein nanoparticles can be formed via several types of techniques, each of which endows them with desirable stability under different conditions. In comparison with nanoparticles formed with synthetic polymers (such as poly-lactic-co-glycolic-acid), protein-based systems exhibit superior biodegradability and lower toxicity. Lastly, the abundance of function groups on proteins (amino group, thiol group, etc.) allows further surface modification [42, 43], which could confer protein nanoparticles with more attractive attributes, such as target-specific delivery, prolonged circulation, and enhanced mucoadhesive properties.

Despite the abovementioned merits, several drawbacks limit the application of protein-based nanoparticles in food and pharmaceutical industry. One of the major problems is the susceptibility to degradation by the digestive system [44, 45]. Like the constituent molecules, most protein-based nanoparticles are digested rapidly in the stomach by pepsin [46]. As a result, the embedded compounds are left unprotected before they reach small intestine, where the majority of absorption process takes place. Therefore, most protein-based nanoparticle formulas are only suitable for injection and cannot work for oral administration. Another shortcoming lies in the complexity of protein molecules [47]. Synthetic polymers consist of only one or two repeating units, and they can aggregate into nanoparticles with preset diameters and narrow size distribution in a quite

controllable manner [14, 41, 48]. In contrast, proteins are rather delicate macromolecules comprising well-defined secondary structures that are assembled with twenty different amino acids. Therefore, protein-based nanoparticle systems tend to exhibit a relatively wide size distribution, and the sizes are more easily changed upon environmental fluctuation. The subtle structure of protein also indicates the potential instability of protein nanoparticles against heat or other harsh treatments [49]. To avoid protein denaturation during food processing, non-thermal treatment may be required to replace traditional sterilization methods, which may add to the cost of industrial production. Finally, a number of proteins (e.g., soy protein and whey protein) exhibit significant allergenicity, which should also be taken into account when preparing protein-based delivery systems.

## 1.4  Protein-polysaccharide complex nanoparticles for controlled release

To take advantage of the merits of protein-based nanoparticles while overcoming their drawbacks, a series of complex nanoparticles containing both proteins and polysaccharides have been developed in the past decades [6, 34, 46, 50, 51]. Two methods, liquid-liquid dispersion and ionic gelation, are employed to prepare these nanoparticles. The first method [32, 51] starts with the dissolution of protein (usually zein) and the target compound in aqueous alcohol, which is similar to the procedure introduced in **Section 1.4.2**. Thereafter, the organic phase is poured into an aqueous solution of a charged polysaccharide (e.g., chitosan) instead of pure water. In order to obtain stable complex nanoparticles, an ionic crosslinker (TPP

and CaCl$_2$ for cationic and anionic polymers, respectively) is added dropwise to the mixture. After a brief equilibrium phase, nanoparticles consisting presumably of a polysaccharide shell and a hydrophobic protein core are formed spontaneously. Nanoparticles prepared through this approach are highlighted for the following merits: (1) desirable dispersion stability due to high surface charge; (2) increased loading capacity because of the involvement of both polysaccharides and proteins in the encapsulation; and (3) protection against peptic digestion in the stomach, leading to satisfactory controlled release properties. The chief shortcoming of this method may be the poor solubility in salt solutions, probably due to the deprivation of surface charge together with the salting-out effect on zein.

The second method utilizes a protein and a polysaccharide that are oppositely charged at a certain pH and ionic strength [46, 52]. Since most water-soluble proteins are negatively charged at neutral pH, cationic polysaccharides such as chitosan are frequently selected to provide desirable electrostatic attraction. In a procedure for preparing chitosan-β-lactoglobulin (CS-BLG) complex nanoparticles, CS was firstly solubilized in acetic acid and added dropwise to an aqueous solution of BLG. Nanoparticles with an average size of 100-200 nm were formed spontaneous under mild stirring. Ionic crosslinkers such as TPP was then added to harden the particulate structure. The sign and magnitude of the surface charge on the formed nanoparticles could be engineered by varying the mixing ratio of CS and BLG, as well as the pH of the solution. The formed nanoparticles

might possess significant resistance to peptic digestion and achieve controlled release due to the low digestibility of both ingredients, although this was not tested by the authors. The major downside of this formula may be the poor solubility of CS at neutral or basic pH [39]. This causes the low dispersion stability of CS-BLG nanoparticles in physiologically relevant systems and limits their application severely.

## 1.5    Protein modification for enhanced encapsulation capacity

As stated before, protein molecules possess ample functional groups such as hydroxyl groups (-OH), amino groups (-NH$_2$) and thiol groups (-SH). These groups are frequently exploited for chemical modification that provides the protein with desirable properties, such as site-specific delivery, enhanced mucoadhesion, and prolonged clearance time, all of which contribute to increased bioavailability. When it comes to nano-encapsulation, the merits of the modified proteins can be conveyed to the nanoparticles. In this section, two protein modification methods, folic acid conjugation and cationization, are discussed in context with their potential in bioavailability enhancement.

### 1.5.1    Folic acid conjugation

Folic acid (FA, structure shown in **Figure 1.1**) is an essential micronutrient that plays a key role in DNA synthesis and cell differentiation [53]. The cell accumulation of FA is achieved mainly through two types or proteins, namely,

reduced folate carrier (RFC) and folic acid receptor proteins (FRps). RFC mediates the transmembrane transport of FA. It exhibits an FA dissociation constant ($K_d$) in the range of μM, and it is expressed ubiquitously in human body [54]. FRps, on the other hand, bind to FA with much higher affinity ($K_d$ in the range of 0.1-1 nM), but their expression is highly restricted in normal cells [19]. At least four forms of FRps, namely, FR-α (FOLR1) and FR-β (FOLR2), FR-γ (FOLR3) and FR-δ (FOLR4), have been identified by now [55]. FR-α and FR-β are glycosyl-phosphatidylinositol anchored glycoproteins, and they are the most abundant forms of FRps in human body. Elevated expression of FR-α was reported in a variety of carcinomas, including ovarian, prostate, breast, colon and lung cancer cells, resulting in a significantly increased affinity to FA in comparison with normal cells. For example, the FA binding capacity of fibroblast and CHO (human ovary) cells were less than 0.1 pmol per $10^6$ cells, while it was found to be 20 and 50-200 pmol/$10^6$ cells in Caco-2 and KB cells, respectively [39]. Likewise, FR-β is amplified in 70% of acute myelogenous leukemias (AML) as well as activated macrophages associated with rheumatoid arthritis and other chronic inflammatory diseases [56]. The overexpression of FRps by cancer cells, together with the fact that FRps exhibit $>10^3$ fold higher affinity to FA than RFC, enables cancer cells or macrophages to accumulate FA at a remarkably higher rate than normal cells.

γ-carboxylic group
pKa=4.7

α-carboxylic group
pKa=6.8

Pteridine ring (pKa=9.0 for hydroxyl group)
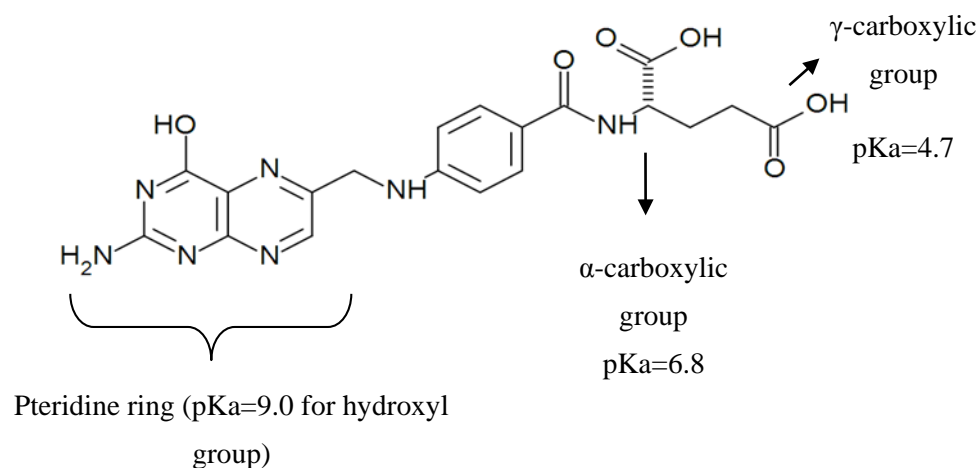
**Figure 1.1** Chemical structure of folic acid (FA)

To take advantage of specificity toward FA, various polymers including chitosan [57], human serum albumin [58], bovine serum albumin [56] and polylysine [59] have been conjugated with FA and used as carriers for anti-cancer drugs. The conjugation utilizes the primary amino group present in these molecules, which act as a nucleophile and attack the carbon atom on the α-carboxyl group of FA. To aid the coupling reaction, a co-reactant such as EDC (1-Ethyl-3-(3-dimethylaminopropyl) carbodiimide) is premixed with FA to activate its carboxyl group. The reaction is typically finished within 2 hours at room temperature for proteins and peptides. Excessive reactants can be easily removed by dialysis or gel filtration. It has been shown that conjugation of one FA molecule to a protein molecule is sufficient to yield a considerable enhancement in protein uptake by Caco-2 and KB cells. Owing to the simplicity and efficacy of FA conjugation, it has found application in areas such as immunotherapy, chemotherapeutics and therapeutic imaging [19, 53].

### 1.5.2 Cationization

As mentioned in **Sections 1.3.4** and **1.3.6**, cationic polymers show high affinity to two important anionic molecules, the mucin on the small intestine wall and the glycoprotein on the cell membrane. Such affinity enhancement leads to significantly improved in bioavailability. However, most natural proteins possess negative net charges at neutral or basic pH due to their amino acid composition. Cationic polysaccharides such as chitosan and its several derivatives are employed to develop mucoadhesive materials [60]. However, chitosan loses its positive charges and becomes insoluble in water at pH higher than 6.2, the pKa of its amino groups [21]. This character makes its claimed mucoadhesive capability questionable at neutral pH. Cationized proteins, on the other hand, retain their positive charge (pKa ~ 12.5 and 10.5 for arginine and lysine side chains, respectively) and thus exhibit desirable water solubility at a wide range of pH [16]. This feature makes them attractive candidates for the encapsulation of nutraceuticals or drugs.

The cationization process of protein is illustrated in **Figure 1.2**. Common cationizing reagents include diamines such as ethylenediamine (EDA) and polyamines such as polyethyleneimine (PEI). They usually possess two or more amine groups. One of the amine groups reacts with the carboxylic groups on the aspartic acid or glutamic acid residues, neutralizing their negative charge and forming an amide bond. The other amine groups remain intact and exhibit

different amount of positive charges depending on the type of cationizer. Ionic crosslinking is observed when more than one amine group of a same cationizer molecule react with one protein molecule, but such reaction can be prevented by providing a large excess of cationizing reagent [61]. The product can be further purified with dialysis, gel filtration or ion exchange chromatography. Several proteins, including bovine serum albumin and BLG, have been studied for cationization. These cationic proteins exhibited a prominent shift in their isoelectric points from pH~5 to pH~9.0, together with a reversal in the sign of their surface charges at neutral pH. Significant changes in the physicochemical and functional properties as well as transmembrane delivery were observed on these proteins [62, 63], but no data have been reported with aspect to nano-encapsulation.
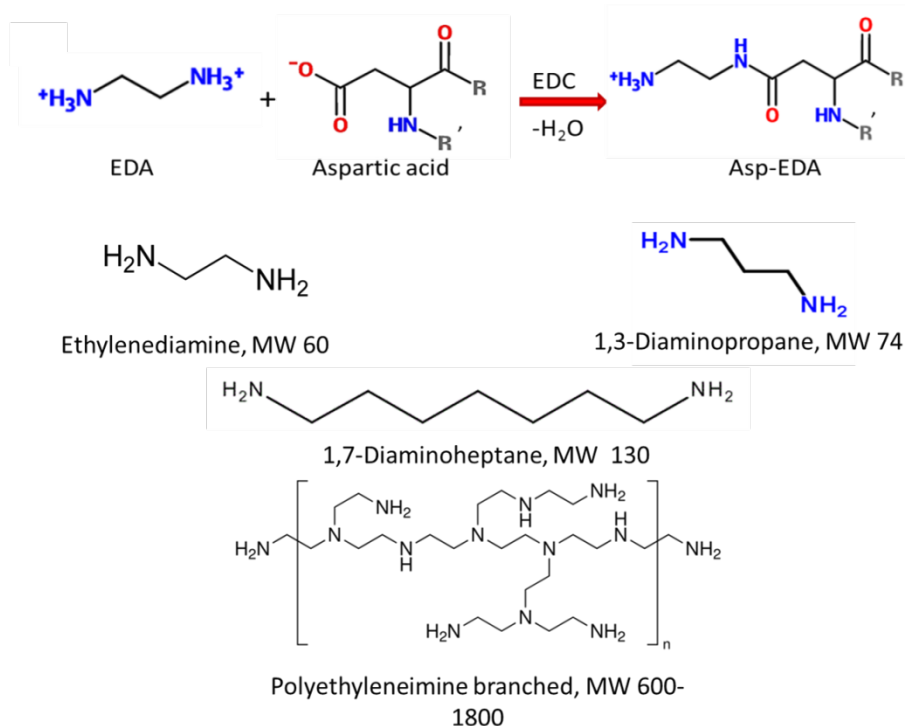
**Figure 1.2** Illustration for protein cationization process.
The upper panel shows a simplified chemical reaction for cationization with EDA. Both aspartic acid and glutamic acid residues were appropriate substrates. The net charge of each residue was altered by +2 (from -1 to +1) upon cationization. R or R' was adjacent peptide chains. The lower part displays the different molecules that could be employed for protein cationization.

## 1.6 Protein of choice as nanoparticle formers

### 1.6.1 Soy proteins

Soybean (*Glycine max* L.) is currently one of the most abundant sources of plant proteins [49]. The enriched form of soy protein, known as soy protein isolate (SPI), has been reported to exhibit high nutritional values and desirable functionalities, and its wide application as a food ingredient has been well documented [24, 25, 49, 64, 65]. The major components of SPI (shown in **Figure 1.3**) are glycinin (MW=360,000, approximately 60%) and β-conglycinin

20

(MW=180,000, approximately 40%) [66]. SPI is unique in its high content (>60%, molar ratio) of hydrophobic amino acids, together with a considerable percentage of charged residues [27]. The first property enables a strong hydrophobic interaction with encapsulated compounds. The latter feature does not only lead to desirable water solubility but also facilitates the protein-drug interaction through electrostatic attraction or hydrogen bonding. In aqueous environment, SPI exist majorly as globular molecules consisting of a hydrophilic shell and a hydrophobic kernel, together with a certain amount of small water-soluble aggregates. Upon the addition of anti-solvent or crosslinking agents, SPI molecules aggregate into various structures, such as microspheres, hydrogels and polymer blends [64, 67, 68].
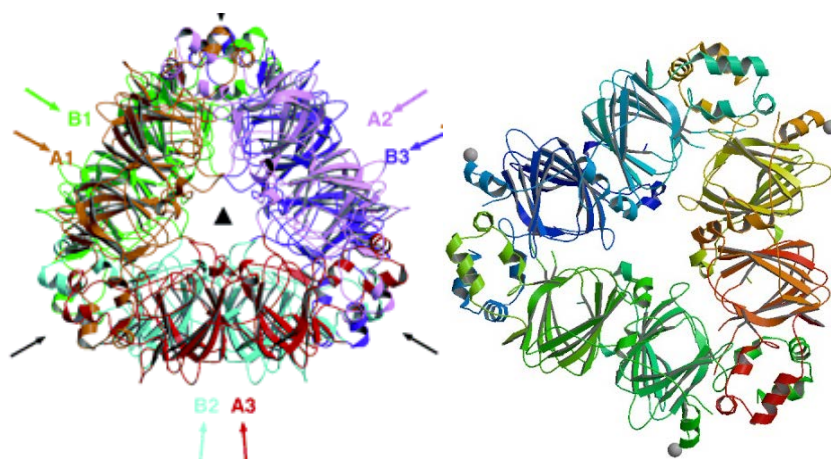


**Figure 1.3** Structure of soy 11S (left) and 7S (right) globulins

## 1.6.2 β-lactoglobulin (BLG)
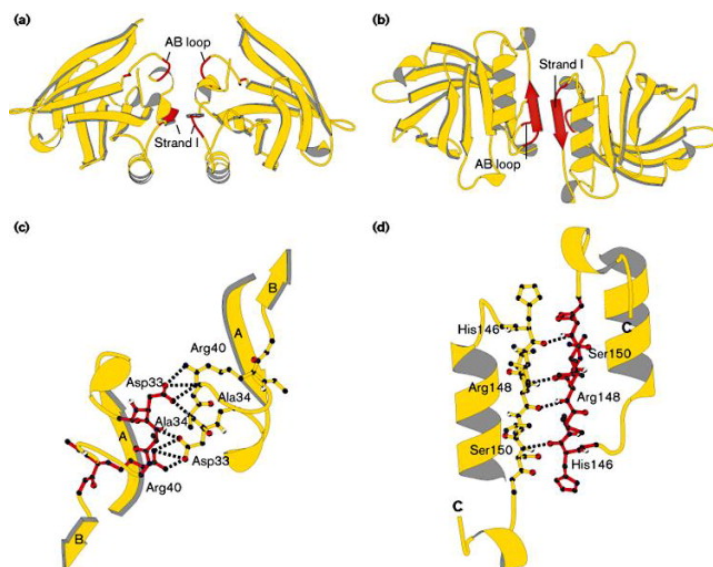


**Figure 1.4** Structure of BLG

Figures 4a and 4b depict the abundance of rigid β-sheet structures. Figures 4c and 4d illustrate the ligand-binding sites existing in a native BLG molecule.

BLG (**Figure 1.4**), a 162-residue globular protein, makes up approximately 60% of bovine whey protein *(72, 73)*. Commercially available BLG products contain two variants, namely, BLG variant A and B, which differ in only two amino acid residues *(74)*. BLG possesses high water solubility even near its isoelectric point, and it contains well-defined patches for binding lipophilic compounds. These unique properties make BLG a natural carrier for various nutrients, such as vitamins and fatty acids *(50)*. Furthermore, BLG demonstrated a significant resistance to peptic digestion due to its compactly folded conformation originated from the abundance of rigid β-sheet structures. On the other hand, it is much more readily degraded by trypsin in small intestine *(75)*. These characters provide BLG-based delivery systems with desirable controlled release property.

By far, various encapsulating systems have been developed with BLG, including microemulsions *(76)*, nanoparticles *(74)* and nanocomplexes *(77)*. These techniques demonstrated satisfactory protection to the entrapped compounds.

## 1.7 Compounds to be encapsulated

### 1.7.1 Curcumin

Curcumin or diferuloylmethane (**Figure 1.5**) is a yellow polyphenolic dye that is enriched in the extract from turmeric (*Curcuma longa*), a plant grown in tropical Southeast Asia [69]. It was firstly employed as a natural colorant in food and beverages [70]. Recently, curcumin has been reported to induce cell cycle arrest and/or apoptosis in a number of human cancer cell lines, including colorectal, lung, breast, pancreatic and prostate carcinoma, etc. [71]. These findings suggested the potential of curcumin in cancer therapy. In addition, several studies on experimental (chemical) carcinogenesis models have revealed that curcumin can also ameliorate the progression to cancer in a variety of organ sites, indicating the potential of this compound as a chemopreventive agent [72]. Furthermore, curcumin has been found to possess a wide range of other beneficial properties, including anti-inflammatory, antioxidant, and antimicrobial effects [70]. Despite these merits, the stability and solubility of curcumin remains a hurdle of its application. Curcumin has very low solubility (several micrograms per liter) in water, resulting in agglomeration and therefore a significant decrease in its bioavailability [35]. More importantly, it becomes less chemically stable as the

systematic pH increases to neutral or basic values. Study showed that more than

90% of curcumin degraded into ferulic acid, feruloylmethane and vanillin at 37 $^{\circ}$C

in PBS (phosphate buffered saline, 0.1 M, pH 7.2) within 30 min [73]. Besides,

light irradiation also causes the generation of curcumin-derived radicals, which

leads to the condensation of curcumin [74].
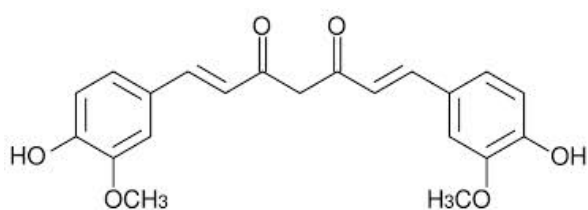


**Figure 1.5** Chemical structure of curcumin

To address these issues of curcumin, a broad variety of encapsulation

methods have been developed, employing proteins, synthetic polymers or

surfactants as a protectant [32, 35, 72, 75]. While these methods promoted the

solubility of curcumin and prevented its degradation, they suffered from several

drawbacks such as unsatisfactory LC and the utilization of non-biodegradable

materials. These shortcomings necessitate the development of innovative

encapsulating systems for curcumin. Another reason for choosing curcumin as a

target compound is the abundance of data on its encapsulation, together with the

convenience of its quantification. Based on these considerations, curcumin was

chosen as a model drug in our study that may provide reliable result for evaluating

the encapsulating performance of newly developed nanoparticle systems.

### 1.7.2 Vitamin D

Vitamin D (VD, **Figure 1.6**) is a fat soluble vitamin consisting of two major physiologically active forms, namely, vitamin $D_2$ (ergocalciferol) (VD2) and vitamin $D_3$ (cholecalciferol) (VD3). The latter one has been reported as a more effective form of VD [76]. The functions of VD include not only calcium absorption and homeostasis regulation, but also the prevention of a range of chronic diseases, such as type 2 diabetes, hypertension, cardiovascular disease, etc. [77]. Despite its importance, insufficient serum level of VD has been reported frequently in the US and Europe, where 30-60% populations have been diagnosed recently with VD deficiency [78]. As a result, the Food and Drug Administration has taken measures to encourage the fortification of VD to milk and cereals. In addition, the recommended daily allowance of VD in Dietary Guideline for Americans released by United States Department of Agriculture in 2010 has been raised to 600 IU per day for children and 800 IU per day for adults [79].

In addition to the amount of VD present in foods, the bioavailability of VD has also attracted extensive attention. VD as a hydrophobic vitamin exhibits very low solubility in water and is susceptible to degradation upon light or heat exposure [80]. These properties have a significantly negative effect on the absorption and utilization of fortified VD. As a result, various micro- and nano-encapsulation systems have been developed to protect and deliver VD. Several examples include β-cyclodextrin micelles [81], ethylcellulose/chitosan

microspheres [82], casein microparticles [83], and zein/carboxymethyl chitosan

nanoparticles [51]. However, the application of these methods in food industry is

impeded by several drawbacks, such as the involvement of harsh thermal

treatment, existence of toxic organic solvent, low loading capacity, and

precipitation in the presence of salts. A novel, industrially facile method of

encapsulation is hence needed to solve these problems and boost the VD level

among world population.
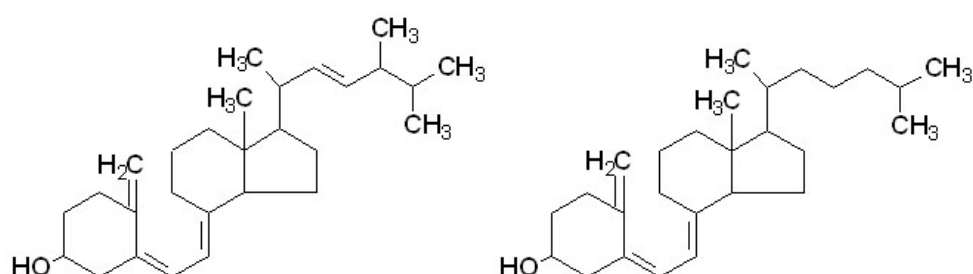


**Figure 1.6** Chemical structure of $VD_2$ (left) and $VD_3$ (right)

## 1.8    Research goals

This dissertation is focused on the fabrication, characterization, and application of

food protein-based nanoparticles as effective encapsulants. Two food-based

proteins, SPI and BLG, will be studied systematically for the first time for the

particle formation and surface modification process. The physicochemical

structure, encapsulating capacity, and release/delivery performance will be

investigated. The ultimate goal of this work is to prepare protein nanoparticles that

inherit the merits introduced in **Section 1.3.4**, while overcoming those disadvantages. Several objectives are proposed below.

**Preparation and characterization of protein-based nanoparticles.** SPI and BLG will be investigated for their particle forming behaviors by two methods, namely, ionic gelation and organic solvent desolvation. Particles with desirable sizes, stabilities, and encapsulation capacities were obtained by adjusting parameters such as pH, organic solvent content, protein concentration, and crosslinking time. The possible mechanism involved at each stage of nanoparticle formation was systematically investigated by a series of techniques including dynamic light scattering (DLS), $\zeta$-potential measurement, Fourier-transform infrared spectroscopy (FT-IR), X-ray diffraction (XRD), and scanning electron microscopy (SEM). Curcumin as a model compound was encapsulated into the as-prepared nanoparticles. The encapsulation efficiency and releasing profile of the nutraceutical-incorporated nanoparticles were systematically evaluated.

**Surface modified nanoparticles as advanced delivery vehicles.** Based on the synthesized nanoparticle platforms, different surface modification methods were employed to confer the nanoparticles with new properties. Folic acid was conjugated to soy protein nanoparticles to provide target-specific delivery in tumor cells. Cationization (the process of rendering a molecule positively charged) was performed to promote the bioavailability of encapsulated compounds by enhancing mucoadhesion and cellular uptake. The effect of chemical modification

on the structural properties, digestibility, dispersion stability, particle forming behaviors, mucoadhesive properties, and encapsulating efficiency was assessed using different techniques. Besides, the cytotoxicity and cellular uptake of the target compounds encapsulated in modified protein nanoparticles were assessed using cell culture assays.

**Protein-polysaccharide complex nanoparticles as nutraceutical/drug carriers with controlled release properties.** To overcome the rapid digestion of proteins in the stomach, polysaccharides such as carboxymethyl chitosan were utilized as a second coating layer via ionic gelation. The polysaccharide was expected to protect protein nanoparticles from peptic digestion, thus maximizing the protection to the entrapped compounds in the digestive system.

# Chapter 2 Preparation, Characterization, and Application of Nanoparticles Synthesized from Soy Protein

## 2.1 Abstract

Nanoparticles were synthesized from soy protein, one of the most abundant and widely utilized plant proteins, for the encapsulation of nutraceuticals and drugs. The preparation process consisted of dispersion, desolvation, drug incorporation, crosslinking and evaporation. The role of each procedure in the formation of nanoparticles was systematically investigated by means of particle size, size distribution, zeta potential, and as morphology observation. Curcumin as a model compound was encapsulated successfully into the nanoparticles, evidenced by Fourier transform infrared spectroscopy and X-ray diffraction. The average size of the curcumin-loaded nanoparticles was 220.1 to 286.7 nm, and their zeta potential was around -36 mV. The highest encapsulation efficiency and loading capacity achieved were 97.2% and 2.7%, respectively. The release of curcumin in phosphate buffer saline followed a biphasic pattern. Possible mechanisms of the formation of soy protein nanoparticles as well as the incorporation of curcumin were discussed based on the data obtained from this study.

## 2.2 Introduction

Biopolymer-based nanoparticles have gained increasing interest as delivering systems for drug and nutraceuticals in the past few decades [1, 22, 84]. Their

sub-cellular size provides several advantages such as prolonged gastrointestinal residence [2], better tissue penetration and superior cellular uptake [85]. Besides, they exhibit low toxicity owing to their biodegradability and non-antigenic property [23]. Proteins as amphiphilic biopolymers are deemed as ideal materials for preparing nanoparticles because they interact well with both the drug and solvent [84]. By far, drug-loaded nanoparticles have been synthesized successfully from various proteins [23, 30, 84, 86], including both water-soluble (bovine or human serum albumin) and insoluble proteins (zein, gliadin, etc.). These nano-scaled systems exhibited various advantages, such as improved solubility, controlled release property and enhanced bioavailability of encapsulated nutraceuticals. However, several limitations hindered their applications in pharmaceutical and food industry. For instance, albumins contain a relatively low content of hydrophobic amino acids, and they incorporate drugs majorly via electrostatic attraction or hydrogen bonds [58, 87]. Therefore, they are less capable in encapsulating highly hydrophobic drugs which are minimally charged and form few hydrogen bonds. On the other hand, nanoparticles prepared with zein or gliadin performed satisfyingly in incorporating hydrophobic chemicals [86, 88], but their low content in hydrophilic and charged amino acids resulted in a limited solubility in aqueous environment, unless a considerable amount of polysaccharides or surfactants was added [32, 88].

Soybean (*Glycine max L.*) is currently one of the most abundant sources of plant proteins. The enriched form of soy protein, known as soy protein isolate (SPI), has been reported to exhibit high nutritional values and desirable functionalities, and its wide application as a food ingredient has been well documented [27, 67, 89]. Besides, SPI possesses a balanced composition of non-polar, polar and charged amino acids [27], thus being able to incorporate drugs with its various functional groups. The major components of SPI were glycinin (MW=360,000, approximate 60%) and β-conglycinin (MW=180,000, approximate 40%) [66]. In aqueous environment, these components exist majorly as globular molecules consisting of a hydrophilic shell and a hydrophobic kernel, together with a certain amount of small water-soluble aggregates [26, 90]. Upon the addition of antisolvent or crosslinking agents, SPI molecules continue to aggregate and form various structures, such as microspheres [24], hydrogels [89] and polymer blends [64, 67]. However, to the best of our knowledge, there has been no systematic report by now on the fabrication of nanoparticles with SPI.

In this study, nanoparticles were synthesized with SPI using a desolvation technique followed by glutaraldehyde crosslinking [23]. The nanoparticles were characterized by the particle size, size distribution, count rate, zeta potential, and morphology. The effects of each step of preparation (i.e., desolvation, crosslinking and evaporation) on the abovementioned parameters were investigated systematically. Curcumin (diferuloylmethane) was selected as a model drug for

evaluating the encapsulating property of SPI nanoparticles. The Fourier transform infrared (FT-IR) spectrum, X-ray diffraction (XRD) pattern, encapsulation efficiency, and releasing profile of the curcumin-loaded particles were measured. Finally, a possible mechanism of the formation of blank and curcumin-loaded SPI nanoparticles was proposed based on the data obtained in this study.

## 2.3    Materials and Methods

### 2.3.1    Materials

Prolia$^{TM}$ 200/70 Defatted Soy Flour was a sample donated by Cargill Inc., Cedar Rapids, IA. The soy flour contained 54% protein (dry basis) and less than 1% oil. Curcumin (95% pure) was purchased from Sigma-Aldrich (St. Louis, MO, USA). All other chemicals (glutaraldehyde, Tween 20, phosphate buffer saline, etc.) were of analytical grade.

### 2.3.2    Preparation of SPI

SPI was prepared following an isoelectric precipitation method [91]. The defatted soy flour was suspended in 15-fold of deionized water with mild stirring, and the pH of the suspension was adjusted to 8.0 with 1 mol/L NaOH. After 1 h of extraction, the dispersion was centrifuged at 10,000 $g$ for 15 min. The supernatant was acidified with 1 mol/L HCl to pH 4.5 and centrifuged under the same condition. The precipitate was re-dispersed in water, adjusted to pH 7.5 with 1 mol/L NaOH, dialyzed against deionized water for 24 h and then lyophilized. The

moisture content of the final product was less than 5%, while the protein content was 90% as determined by Bradford assay using bovine serum albumin as the standard protein.

### 2.3.3 Preparation of blank nanoparticles with SPI

Nanoparticles were prepared with freshly prepared SPI following a desolvation method [23] with modifications. SPI was dissolved in deionized water at concentrations of 4 to 60 mg/mL and equilibrated for 1 h at room temperature. Desolvating agent (ethanol) was added dropwise into the dispersion. The concentrations of SPI and ethanol after mixing ranged from 4~12 mg/mL and 0~80%, respectively. After 15 min of equilibration, glutaraldehyde (25 mg/mL aqueous solution) was added as a crosslinker. The amount of glutaraldehyde was calculated as below. The average molecular weight of SPI (288,000) was estimated based on its composition which was described in the introduction, while the lysine content of SPI was obtained from previous literature [27]. These values, together with the fact that one glutaraldehyde molecule reacted with two lysine residuals, gave the amount of glutaraldehyde required for stoichiometric crosslinking, which was 28 μg/mg SPI or 77 mol/mol SPI. This ratio was defined as 100% glutaraldehyde equivalent, and the amount of added glutaraldehyde ranged from 0% to 150% calculated based on this value in our study. The purpose of adding more than 100% equivalent of glutaraldehyde was to achieve a higher reaction rate [3, 23]. After 16 h of crosslinking reaction at room temperature,

threefold of aqueous ethanol was added to dilute the dispersion without changing its ethanol/water ratio. Thereafter, rotary evaporation was applied using a Buchi Rotavapor RII at 30℃ (BUCHI Labortechnik AG, Flawil, Switzerland) to remove ethanol, which was then replaced with same volume of deionized water. The resultant dispersion, containing less than 10% ethanol, was centrifuged at 10,000 $g$ for 15 min to remove large aggregates. The percentage of protein in the supernatant was higher than 95%. The supernatant was either lyophilized or stored at 4 ℃ for subsequent assays.

### 2.3.4  Preparation of curcumin-loaded SPI nanoparticles

The encapsulation of curcumin into SPI nanoparticles was achieved as described below. Typically, SPI (60 mg/mL) was suspended in deionized water, while curcumin (3 mg/mL) was dissolved in ethanol as stock solution. After 1 h of equilibration, pure ethanol was added dropwise to the SPI dispersion to the concentration of approximately 60%. Curcumin stock solution was then added dropwise to attain a curcumin/SPI ratio of 1:20, 1:50 or 1:100 (w/w). Additional ethanol was introduced finally to achieve an ethanol/water ratio of 80:20 (v/v). The dispersion was then crosslinked, diluted, evaporated, re-diluted and centrifuged as described in the above section. The supernatant obtained after centrifugation was stored at 4 ℃ for subsequent analyses.

### 2.3.5 Determination of particle sizes and count rates

The dispersions of both empty and curcumin-loaded SPI nanoparticles were analyzed at different preparation stages. The particle size as well as the count rate was determined by dynamic laser scattering (DLS) using a BI-200 SM Goniometer Version 2 (Brookhaven Instrument Corp., Holtsville, New York, USA) equipped with a 35 mW He-Ne laser beam at a wavelength of 637 nm and a scattering angle of 90° [23]. The z-average size and size distribution were calculated by using the BIC Dynamic Scattering Software (Brookhaven Instrument Corp., Holtsville, New York, USA) based on the intensity of the scattered light. The refractive index and viscosity of water/ethanol mixtures with different volume ratios were applied for obtaining accurate results. In order to obtain comparable count rates, the samples were not diluted, and the power of laser was fixed at 10 mW. All of the analyses were conducted at 25ºC for 1 min.

### 2.3.6 Determination of zeta-potential of the nanoparticles

During the preparation process, the nanoparticle dispersions were measured for their electrophoretic mobility by laser Doppler velocimetry using a Nano ZS90 Zetasizer and compatible fold capillary cuvettes provided by Malvern Inc. (Malvern, UK). The electrophoretic mobility of each sample was measured three times, and at least twelve runs were performed in each measurement. The data were then converted to zeta potentials using the Smoluchowski model.

### 2.3.7  FT-IR study of the nanoparticles

The blank and curcumin-loaded nanoparticles were lyophilized before FT-IR analysis. Each sample (3 mg) was loaded on a Jasco FT/IR 4100 spectrometer (Jasco inc., Easton, MD, USA). The infrared spectra were collected from the wavenumber of 700 to 4000 $cm^{-1}$ at a resolution of 4 $cm^{-1}$. Each sample was subjected to at least 60 repeated scans. The spectra were averaged and smoothed, and their baselines were calibrated with the Spectra Manager software (Jasco inc., Easton, MD, USA).

### 2.3.8  X-ray diffraction (XRD) analysis

The X-Ray diffraction (XRD) patterns of SPI, curcumin, their physical mixture (curcumin: SPI=1:40, w/w) and SPI-encapsulated curcumin were recorded on a Bruker D8-Advance Diffractometer (Bruker AXS Inc., Madison, WI) with backgroundless sample holders. The working parameters were: voltage of 40 kV, current 40 of mA, and scanning rate of 3 $min^{-1}$.

### 2.3.9  Scanning electronic microscopy (SEM) analysis

SEM was performed to examine the morphological structure of empty and curcumin-loaded nanoparticles. Dispersions of particles were diluted with aqueous ethanol, so that the ethanol concentration was unchanged, while the protein concentration was approximately 0.5 mg/mL. Fifty microliters of the dispersion was cast-dried on an aluminum pan, which was cut into an appropriate size. The pan was adhered to a 1-inch specimen stub with conductive carbon tapes (Electron

Microscopy Sciences, Ft. Washington, PA). The stub was then coated with a thin layer (<20 nm) of conductive gold and platinum using a sputter coater (Hummer XP, Anatech, CA) before observation under SEM (Hitachi SU-70 Pleasanton, CA). Representative images were reported.

### 2.3.10 Determination of encapsulation efficiency and loadingcapacity

The encapsulation efficiency (EE), defined as the percentage of curcumin encapsulated in the suspended protein nanoparticles, was estimated as below. After the centrifugation mentioned in the nanoparticle preparation sections, both the precipitate and supernatant (defined as the 'primary' supernatant) were collected. The precipitate was extracted in 5 mL of ethanol with mild stirring for 5 min, after which the suspension was centrifuged at 9,000 $g$ and 20 °C for 5 min to remove protein aggregates. The resultant supernatant (defined as the 'secondary' supernatant') was subjected to spectrophotometric analysis at 426 nm with a DU-730 UV/VIS spectrophotometer (Beckman Coulter Inc., Fullerton, CA). The absorbance was converted to curcumin concentration based on the established standard curve ($R^2$=0.9991). Meanwhile, the primary supernatant was decanted into a Macrosep® centrifuge tube (Pall Corp., Ann Harbor, MI) with a built-in filtering membrane (MW cutoff = 10,000) with appropriate dilution [37]. After centrifugation at 5,000 $g$ and 20 °C for 30 min, the free (non-encapsulated) curcumin permeated the membrane and was quantified spectrophotometrically. The EE of the samples were calculated with the equation:

$$\text{EE (\%)} = 100 - \frac{\text{Precipitated curcumin} + \text{Free curcumin}}{\text{Total curcumin}} \times 100$$

On the other hand, the non-permeable part of the dispersion was collected and lyophilized. The mass of dry nanoparticles was measured, and the loading capacity (LC) was calculated as the mass ratio of entrapped curcumin to the nanoparticles.

## 2.3.11  Release of curcumin in phosphate buffer saline (PBS)

Five milligrams of lyophilized nanoparticles was weighed and dispersed in 10 mL of the release medium (PBS, pH 7.5 with 0.5% Tween 20). The dispersion was incubated at 37 $^{\circ}$C with mild shaking on a Multi-Purpose Rotator/Rocker (Scientific Industries Inc., NY, USA) for 0.5 to 8 h. The mixture was centrifuged at 51,500 $g$ and 20 $^{\circ}$C for 15 min, after which over 90% of the nanoparticles were precipitated (preliminary data not shown). The supernatant containing released curcumin was analyzed spectrophotometrically as mentioned before, using a calibration curve established in curcumin/Tween 20/PBS system ($R^2$=0.9993). The precipitate was disposed, and a fresh dispersion was then made for another measurement. The kinetic release profile of curcumin was plotted versus time.

## 2.3.12  Statistics

All measurements were performed in triplicates. The experimental results obtained were expressed as means $\pm$ standard error. Data were analyzed by analysis of variance ($p < 0.05$) using the Origin 7.5 software (OriginLab Corp., MA, USA).

## 2.4 Results and Discussion

### 2.4.1 Effect of the desolvation process

**Figures 2.1** showed the particle size and zeta potential of SPI dispersions, respectively, as influenced by ethanol and protein concentrations. Neither glutaraldehyde addition nor centrifugation was undertaken at this stage. The z-average size of SPI dispersion in pure water was around 320 nm, which was in accordance with previous literatures [68, 92]. As the concentration of ethanol increased to 30-40% (depending on the final protein concentration), the particle sizes increased gradually before reaching a peak. This was probably because that high ethanol content favored the exposure and interaction of the hydrophobic chains in protein molecules, which led to the formation of aggregates [26, 93]. Similar behavior was reported in the study on human serum albumin (HSA) nanoparticles [23]. Besides, the peak particle size averaged at 606 nm and 862 nm at SPI concentrations of 4 mg/mL and 12 mg/mL, respectively. This difference might be attributed to the fact that higher protein concentration favored the collision and aggregation of protein molecules [94]. As the percentage of ethanol increased to 80%, the particle sizes decreased significantly, and smaller average particle sizes were observed at higher protein concentrations (**Figure 2.1A**). The decrease in average size at high ethanol concentrations was unexpected and has not been reported in previous literatures. It could be attributed to either breakdown of larger aggregates or the extensive formation of smaller ones. To elucidate the

behavior of soy protein at high ethanol levels, the size distribution and count rate

of the dispersion were analyzed and presented as below.
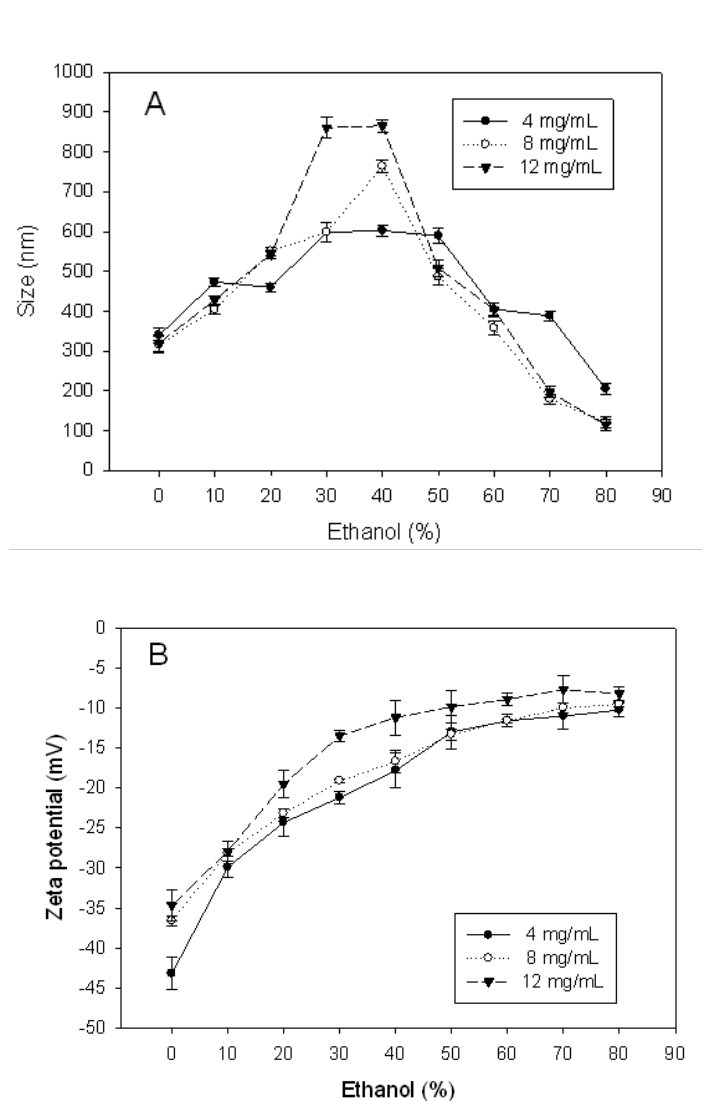


**Figure 2.1** Effect of ethanol and protein concentrations on the size (A) and zeta potential
(B) of SPI nanoparticles

Data were presented as mean ± standard error (n=3) in this and following figures.

**Figures 2.2** showed the size distributions of two SPI dispersions at the same

protein concentration (i.e., 8 mg/mL) but different ethanol percentages (i.e., 0%

for **Figure 2.2A** and 80% for **Figure 2.2B**). Two groups, one corresponding to

small particles (50-200 nm, similarly hereinafter) and the other representing for large aggregates (500-1000 nm, similarly hereinafter), were observed in both diagrams. Compared with the SPI dispersed in pure water, the one in 80% aqueous ethanol exhibited a significantly higher percentage of small particles, as suggested by the peak areas. Further study revealed that this percentage increased gradually from 20% in pure water to 60% in 80% ethanol (**Figure 2.2C**), and the trend was the same at all protein concentrations investigated. Besides, the total number of particles could be estimated indirectly from the count rate, the cumulative light pulses of the sample over the duration of the DLS experiment [23]. The count rate is proportional to the concentration of particles, but it also varies as the sixth power of their size, according to the Rayleigh scattering theory. Assuming the particle numbers were equal, because the particle size of the SPI dispersion in 80% ethanol was approximately 33% of that with 40% ethanol (**Figure 2.1A**), the count rate of the former one should have been less than 0.15% ($0.33^6$) of that with the latter one. However, the count rate actually increased nearly threefold as the ethanol concentration increased from 40% to 80% (**Table 1**), which implied an extensive increase in the number of particles. Moreover, the turbidity of the dispersion increased significantly as the ethanol concentration increased from 40% to 80% (data not shown), which also suggested the existence of aggregates in large quantity [95, 96]. These results, combined with the size distribution, indicated a rapid increase in both the number and the percentage of small particles. In addition,

because of the overwhelming increase in the total number, the count of the large aggregates might also have increased, although not as rapidly as the small ones. As inferred from the above discussion, the apparently smaller particle sizes observed in 80% ethanol was probably due to the extensive formation of new particles, especially the small ones, rather than the breakdown of large aggregates.

**Table 2.1** Effect of ethanol on the count rate of SPI nanoparticle dispersion*

| EtOH% | Count (kcps)** | EtOH% | Count (kcps) |
|-------|----------------|-------|--------------|
| 0 | 110±15[e] | 50 | 200±13 [cd] |
| 10 | 120±10[de] | 60 | 250±19 [c] |
| 20 | 140±20[d] | 70 | 320±18 [b] |
| 30 | 165±13[d] | 80 | 550±17 [a] |
| 40 | 140±16[d] | | |

* Data with different letters showed significant difference (n=3, P<0.05).
** Kilo counts per second, a unit describing the total number of scattered photons.

The zeta potential of SPI/ water dispersion ranged from -43.2 mV to -34.7 mV, depending on the protein concentrations (**Figure 2.1B**). The zeta potential decreased (in terms of magnitude, similarly hereinafter) with increasing ethanol concentration and reached a minimum value of -8.3 mV at 80% ethanol. This phenomenon was possibly due to the deprivation of water by ethanol that impaired the ionization of the charged groups in soy protein molecules [68]. It was noteworthy that the zeta potential continued decreasing as ethanol concentration increased from 40% to 80%. As a result, the electrostatic repulsion among protein molecules was weakened, thus promoting the formation of protein aggregates and

preventing their dissociation [26]. This was supportive for the above discussion on

the behavior of soy protein at high ethanol concentrations.
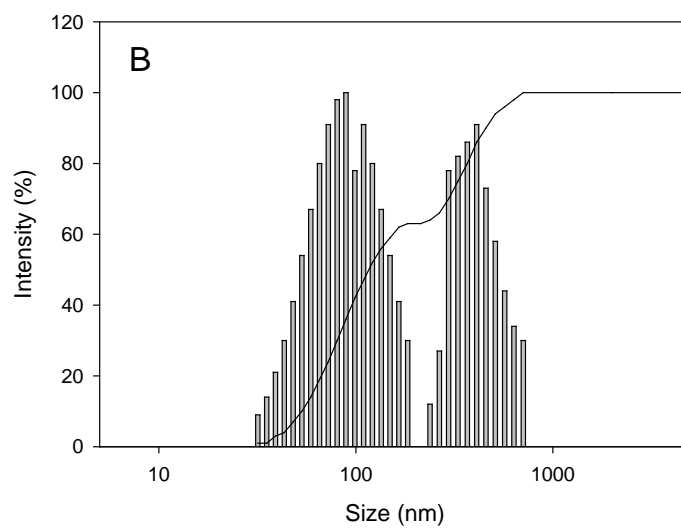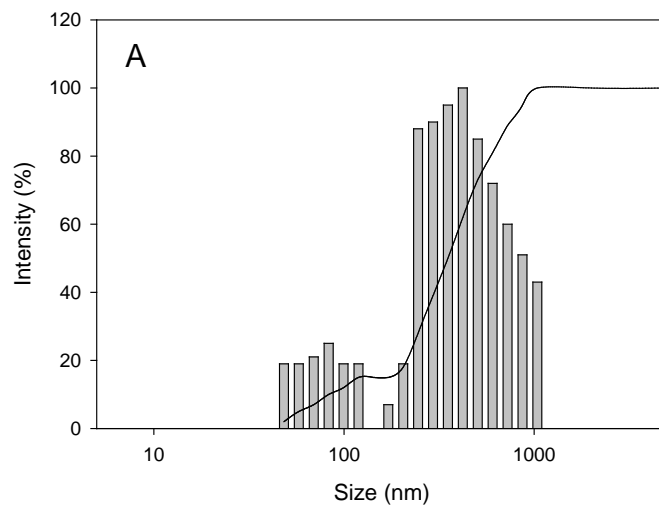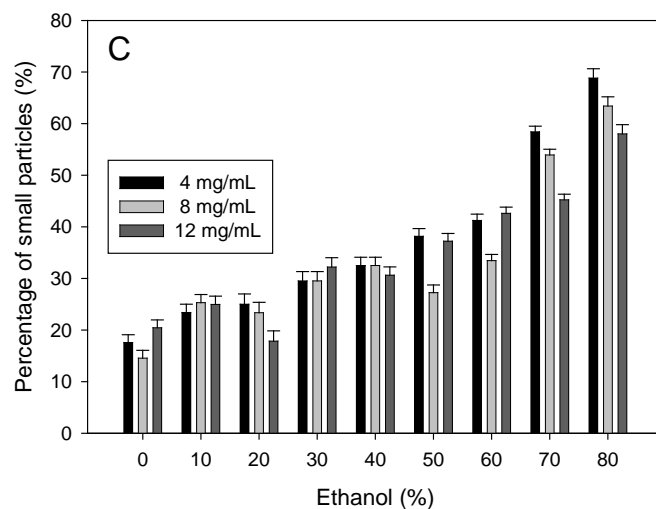
**Figure 2.2** Size distributions of SPI nanoparticles.
The protein concentration was 8 mg/mL. Particles were formed in (A) pure water or (B) 80% ethanol. Figure 2.2C showed the effect of ethanol concentration on the percentage of the small particles

## 2.4.2   Effect of crosslinking and evaporation procedures

Glutaraldehyde is used widely to harden protein nanoparticles or hydrogels as it crosslinks the ε-amino groups of lysine residues [1, 22]. One treatment (8 mg/mL SPI desolvated by 80% ethanol) was chosen to be further crosslinked by glutaraldehyde, and the effect of crosslinking and evaporation step on the particle size, count rate, and zeta potential was summarized in **Figures 2.3A**, **2.3B**, and **2.3C**, respectively. Similar results were observed at different protein and ethanol concentrations (data not shown). The sizes were measured after 16 h of crosslinking and were around 200-500 nm, generally higher than those observed immediately after the desolvation without crosslinking (**Figure 2.1A**). Before ethanol was evaporated, the particle size appeared independent on the

44

concentration of glutaraldehyde. Similar results were reported on HSA and legumin nanoparticles [23, 97]. Besides, the count rates did not change significantly at glutaraldehyde levels lower than 100% equivalent, but it increased by 50% at glutaraldehyde concentrations of 125% and 150% equivalent (**Figure 2.3B**). Since the particles sizes exhibited no statistical difference, the increase in count rate indicated that more particles with the same size were formed [23].
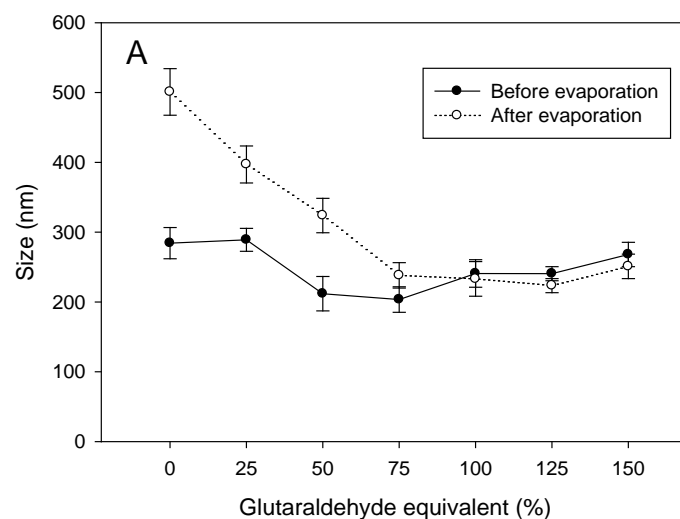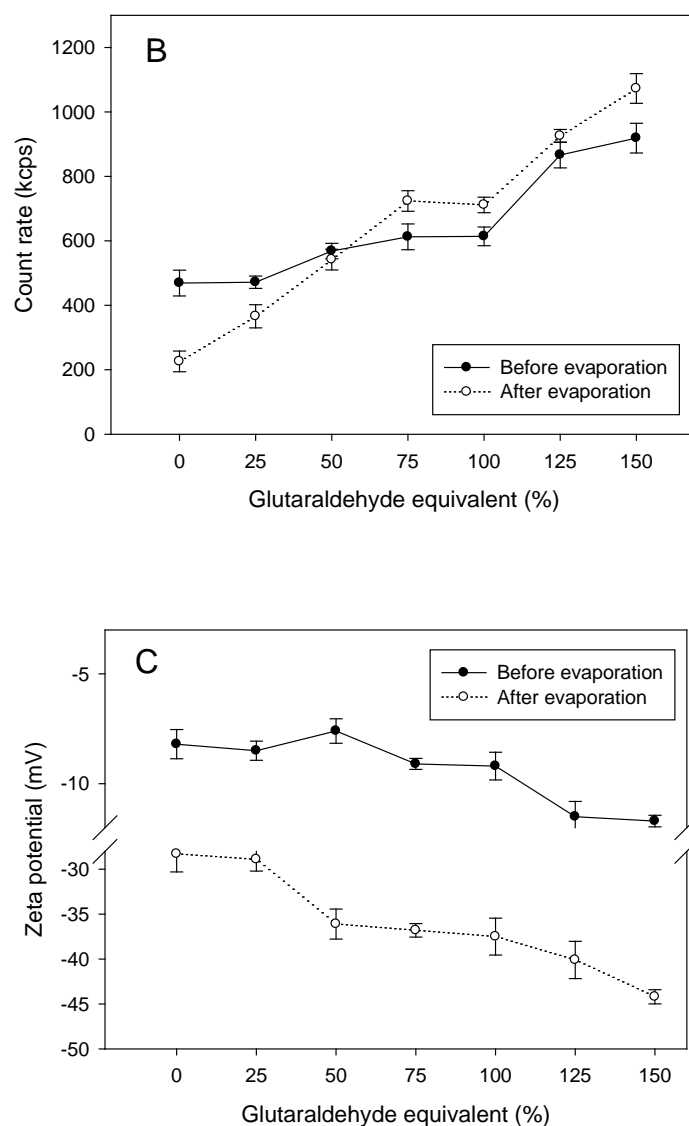
**Figure 2.3** Effect of glutaraldehyde on the size (A), count rate (B) and zeta potential (C) of soy protein nanoparticles after and before evaporation

After the removal of ethanol via rotary evaporation, the particle size and count rate increased and decreased respectively at the glutaraldehyde concentrations ranging from 0% to 50% equivalent (**Figures 2.3A** and **2.3B**). These values, as well as the size distribution (data not shown), were similar with those of the particles formed initially without ethanol. In **Section 2.4.1**, increased count rate and decreased

average size indicated the extensive formation of small nanoparticles upon the addition of ethanol. Similarly, the reversed change of these values after the removal of ethanol suggested that part of the particles might have dissociated. This might be related to the hydrophilic nature of soy proteins as explained in the introduction part. At glutaraldehyde levels higher than 75% equivalent, however, the particle sizes and count rates did not change significantly after evaporation. This indicated adequate hardening of the soy protein nanoparticles, which is vital for their stability and application in physiological systems [1]. When more than 100% equivalent of glutaraldehyde was added, both the size and count rate increased significantly ($P<0.05$). Based on the result above, it could be inferred that at low concentration glutaraldehyde played a role in maintaining the size and count of existing particles, while at high concentrations glutaraldehyde contributed to the formation of new particles.

**Figure 2.3C** displayed the effect of glutaraldehyde on the zeta potential of nanoparticles formed with 8 mg/mL SPI desolvated with 80% ethanol. Before evaporation, the zeta potentials ranged from -7.6 mV to -10.7 mV. According to the American Society for Testing and Materials, these values indicated "incipient instability" of the nanoparticle dispersions [5], which was in consistence with the emergence of minor flocculates. After ethanol was evaporated, the zeta potential increased to -28.3 mV or -44.2 mV in the presence of 0% or 150% equivalent of glutaraldehyde, respectively. These data were indicative for "moderate to good"

stability [5]. The removal of organic solvent increased the polarity of the dispersion, which might have facilitated the electrolysis of protein molecules and increased the zeta potential consequently. In addition, higher glutaraldehyde concentrations resulted in more negative zeta potentials, probably because of the consumption of positively charged ε-amino groups by glutaraldehyde [23].

### 2.4.3 Encapsulation of curcumin into SPI nanoparticles

**Table 2.2** presented the EE, LC, particle size and zeta potential of blank and curcumin-loaded SPI nanoparticles. The EE increased with decreasing curcumin/protein (C/P) mass ratios and reached 97.2% at the C/P ratio of 1/100. The maximum LC achieved in this study was 2.7%, which was approximately 40% lower than the one attained with zein nanoparticles [32]. In comparison with soy protein, zein exhibited a higher hydrophobicity, which might have contributed to the protein-curcumin interaction and yielded a higher LC [27, 28]. Furthermore, considerable amount of sodium caseinate was added with the zein nanoparticles (zein: caseinate= 1.25: 1, w/w) as a stabilizer [32], which might further facilitate the encapsulation of curcumin in zein nanoparticles.

**Table 2.2** Characteristics of blank and curcumin-loaded SPI nanoparticles*

| Curcumin/Protein Ratio | Encapsulation efficiency (%) | Loading capacity (%) | Particle size (nm) | Zeta potential (mV) |
|---|---|---|---|---|
| 0 (pure SPI) | - | - | 201.5±9.2[c] | -36.8±1.0[a] |
| 1.00% | 97.2±2.0[a] | 1.1±0.1[c] | 220.1±17.8[b] | -36.0±2.1[a] |
| 2.00% | 81.2±1.2[a] | 1.7±0.1[b] | 252.6±13.4[ab] | -35.2±0.8[a] |
| 5.00% | 52.8±3.0[b] | 2.7±0.2[a] | 286.7±10.1[a] | -34.5±1.4[a] |

* Data with different letters showed significant difference (n=3, P<0.05).

The sizes and zeta-potentials of empty and curcumin-loaded SPI nanoparticles were measured after the encapsulation procedures. As shown in **Table 2.2**, the size of empty nanoparticles averaged at 201.5 nm, and it increased with the C/P ratio to a maximum of 286.7 nm. The zeta potentials of blank and curcumin-loaded nanoparticles were around -35 mV with no significant difference. Similar results were reported by Ashok et al. on curcumin-loaded zein nanoparticles [32]. Curcumin possesses four ionizable protons and exhibited a zeta potential of around -6 mV in ethanol or Tween 20/water as measured in our study (data not shown). Therefore, curcumin was unlikely to interact electrostatically with the negatively charged soy proteins, and the zeta potential of the nanoparticle dispersion was thus not influenced by the presence of curcumin.

## 2.4.4 FT-IR study

The FT-IR spectra of SPI, curcumin, their physical mixture (S/C Mix, SPI: curcumin=40:1) and curcumin-loaded SPI nanoparticles (S/C Encap, SPI: encapsulated curcumin=39:1) were presented in **Figure 2.4A**. The characteristic peaks of SPI [98] were amide I (band a, C=O stretching, 1637 $cm^{-1}$), amide II (band b, N-H bending, 1536 $cm^{-1}$), C-N stretching (band c, 1450 $cm^{-1}$) and amide III (band d, C-O and C-O-C vibration, 1238 $cm^{-1}$). On the other hand, CUR exhibited several absorbance peaks [99], of which three were also observed in the S/C mixture: band e, C-O stretching, 1206 $cm^{-1}$, band f, trans CH=CH stretching, 1026 $cm^{-1}$, and band g, C-O-C asymmetric stretching, 856 $cm^{-1}$. The spectrum of

S/C Encap, however, nearly overlapped with that of SPI, and none of these three peaks was detected. This phenomenon indicated that no or little amount of curcumin existed in S/C Encap as free molecules [75, 100].
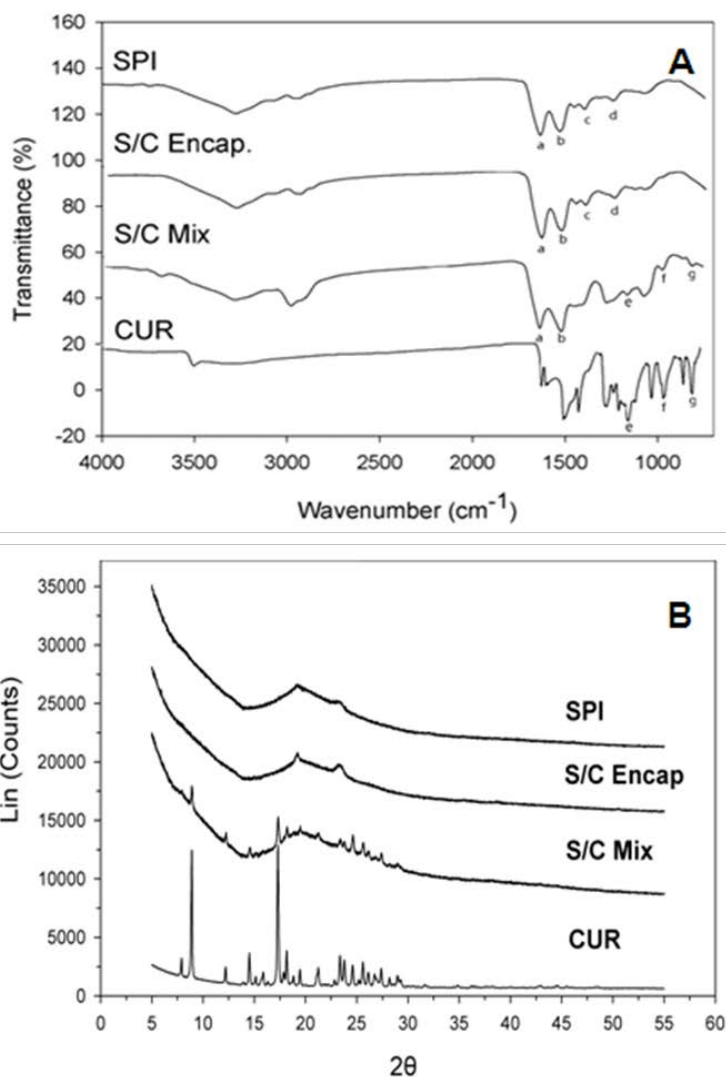


**Figure 2.4** FT-IR spectra (A) and XRD patterns (B) of soy protein isolate (SPI), curcumin (CUR), their physical mixture (S/C Mix) and curcumin-loaded SPI nanoparticles (S/C Encap.)

**Figure 2.4B** showed the XRD patterns of SPI, curcumin, their physical mixture (S/C Mix, SPI: curcumin=40:1) and curcumin-loaded SPI nanoparticles (S/C Encap, SPI: curcumin=39:1). The characteristic peaks of curcumin at 8.84, 12.10,

14.39, 17.20, 23.33, 24.50, 25.52 and 28.87 degree suggested its highly crystalline nature, which was in consistence with previous literatures [32]. These peaks were also observed in the S/C Mix, but with significantly lower intensities. On the contrary, these peaks disappeared in the XRD pattern of S/C Encap, which consisted mostly of amorphous humps. These results indicated the successful incorporation of curcumin in the nanoscale SPI matrix, which facilitated the conversion of crystalline curcumin into the amorphous state [32, 101].

### 2.4.5   SEM analysis of the blank and curcumin-loaded nanoparticles

The morphology of blank and curcumin-loaded SPI nanoparticles was investigated under SEM (**Figure 2.5**). When 12 mg/mL of SPI was dispersed in pure water), a film-like structure was observed under SEM. Similar images were obtained when the same concentration of SPI was desolvated with 80% ethanol without crosslinking (not shown). This structure was possibly formed by non-particulate soy proteins that attached each other during the drying process [30]. Intermolecular attraction and hydrophobic interaction might have played a role in the formation of the network structure [49]. After crosslinking was performed with 75% equivalent of glutaraldehyde, the proportion of particulate soy protein appeared to increase significantly. The particles exhibited an approximately spherical shape with a smooth surface. The particle size under SEM ranged from 50 to 200 nm, which was about 30% lower than the values obtained by DLS. This

difference was probably due to the shrinkage caused by the cast-drying process as well as the vacuum environment in SEM imaging [97].
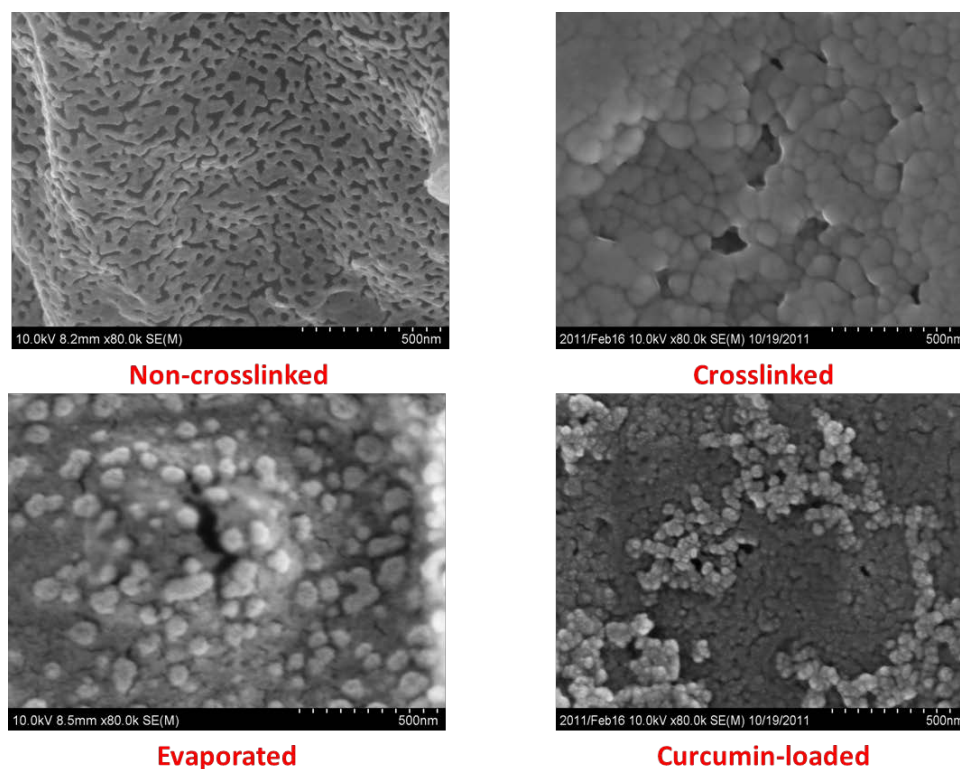


**Figure 2.5** SEM images of soy protein nanoparticle dispersions at different stages of synthesis

After the removal of ethanol by rotary evaporation, the particles tended to separate from each other. This result could be attributed to the increased polarity of the solvent, which induced the burial of hydrophobic chains of protein molecules [94]. In addition, the nanoparticles carried more negative charges on the surface after the evaporation as discussed before. These factors led to strengthened electrostatic repulsion and weakened hydrophobic interaction among protein nanoparticles, both of which inhibited the association of particles upon drying. After the

incorporation of curcumin, clusters of individual particle units were formed with particles, which was responsible for the aforementioned increase in particle sizes.

### 2.4.6 Release of curcumin from SPI nanoparticles

**Figure 2.6** showed the kinetic release profiles of curcumin from SPI nanoparticles in the PBS/Tween 20 system. A biphasic trend was observed for the samples with different C/P ratios, namely, 1/100, 2/100, and 5/100. In the first 1.5 h, over 50% of the encapsulated curcumin was released for all formulations. This phenomenon known as the burst effect was due to the swelling and breakage of the protein matrix [37]. In addition, the majority of curcumin that was initially bound to the peripheral domain of the protein matrix might have migrated to the releasing medium during the first 1.5 h [86]. Similar results have been reported on the nanoparticles prepared with different proteins, such as albumin [87] and zein [32]. Possible strategies for reducing the burst effect include chemical modification of proteins, optimization of encapsulation procedure as well as preparation of multilayer encapsulation systems with protein and polysaccharides, such as chitosan derivatives [51, 102]. Between hours 2 and 8, a sustained release phase was observed, in which the concentration of released curcumin increased slowly with time. At the end of 8 h, the total percentage of curcumin released ranged from 58% to 78%, and it continued to increase in the following 24 hours (data not shown). These results correspond to the migration of curcumin encapsulated within the hydrophobic core of protein molecules. In addition, nanoparticles with

lower C/P ratio exhibited higher releasing rates in the PBS/Tween 20 system. This was probably due to their smaller sizes and greater area-to-volume ratios, which facilitated the contact with the releasing medium [103].
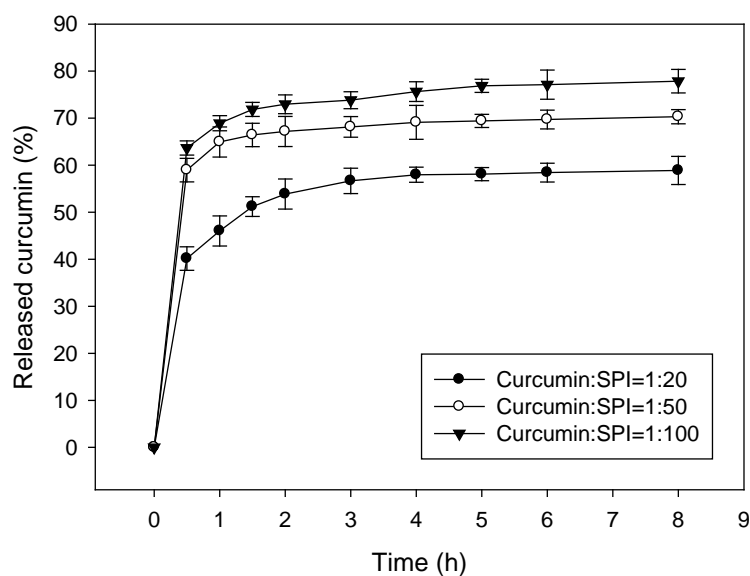


**Figure 2.6** Release of curcumin from the soy protein nanoparticles in phosphate buffer saline with Tween 20

### 2.4.7 Proposed mechanism of nanoparticle preparation and encapsulation

Based on the results obtained in previous sections, an illumination for the formation of blank and curcumin-loaded SPI nanoparticles was proposed in **Figure 2.7**. When dispersed in pure water (phase 1), soy protein existed mostly in its native state, i.e., globular molecules consisting of a shell of charged or polar groups together with a kernel formed by hydrophobic chains [26, 49]. There existed a small amount of aggregates, especially the large ones with diameters of 500-1000 nm. When ethanol was added to the concentration of 40%, the hydration

and ionization of protein were disrupted, leading to a decrease in the zeta potential (phase 2). Meanwhile, part of the hydrophobic chains were exposed to the surface of the molecule [26]. As a consequence, the attraction among protein molecules was enhanced, and a relatively small amount of protein aggregate began to form, resulting in an increase in the average particle size. As shown in our study, the desolvation process could be partly reversed if ethanol was evaporated at this point. Then, curcumin-ethanol solution was added to achieve an ethanol content of 50-60%, so that (a) curcumin could disperse well without agglomeration, (b) the hydrophobic chain of protein was further exposed, and (c) extensive aggregation of protein did not occur and the hydrophobic sites in soy protein molecules was not consumed completely for protein-protein interaction (phase 3). Thereafter, the concentration of ethanol was increased to 80% (with 8-12 mg/mL SPI), which led to extensive formation of nanoparticles, especially those with smaller sizes (50-200 nm). At this stage, part of curcumin was entrapped inside the protein particles, while some curcumin molecules were bound to their peripheral domains. A certain amount of the curcumin also existed as freely dissolved molecules.

After adequate hardening by glutaraldehyde, sufficient amide bond were formed to prevent the deformation of the particles (phase 4). Therefore, the size and number of the particles was not changeable upon the removal of ethanol. However, the constituent part of the nanoparticles, either protein monomers or oligomers, was prone to adopting their native core-shell conformation (phase 5). This was

speculated from the fact that the zeta potential of the nanoparticles after ethanol removal was close to that of the SPI dispersion before desolvation took place. In addition, as was discussed before, the SEM images of samples before and after evaporation also suggested the burial of hydrophobic chains and the exposure of polar and charged sites. In addition, the removal of ethanol resulted in an increased polarity of the dispersion, which favored thermodynamically the hydrophobic interaction (a) among curcumin molecules and (b) between curcumin and the non-polar groups of the protein. The former interaction might have caused the precipitation of the unbound curcumin [30], while the latter one facilitated the entrapment of curcumin into the protein matrix [86, 88]. As a result, little or no curcumin existed in the final product as freestanding molecules.
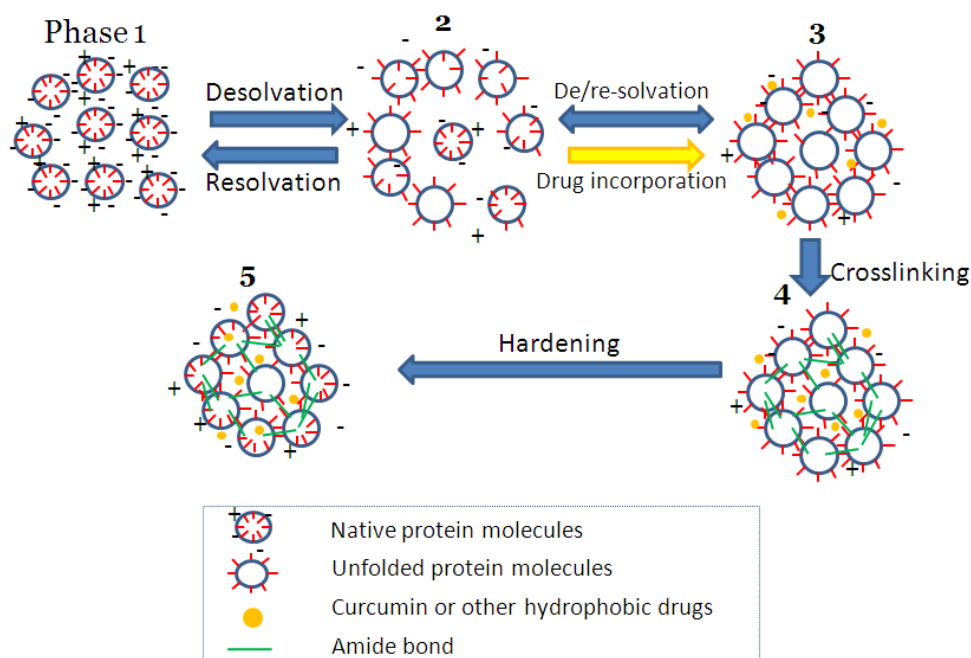


**Figure 2.7** Proposed mechanism of the formation of soy protein nanoparticles

## 2.5    Conclusions

Nanoparticles were successfully synthesized with SPI using the desolvation method. An ethanol concentration greater than 80% was required for extensive formation of particles, while more than 75% equivalent of glutaraldehyde was necessary for adequate hardening. The zeta potential of the nanoparticle dispersion was around -36 mV, which indicated moderate to good stability. The synthesized nanoparticles exhibited an approximate spherical structure with a smooth surface. These particles were then evaluated for their encapsulating capability, and a highest encapsulation efficiency of 97.2% was achieved. No or little curcumin existed as unbound molecules in the yielded particles, as was supported by FT-IR and XRD results. The release of curcumin in PBS/Tween 20 system followed a biphasic trend, and the releasing rate varied with the C/P ratio. Nanoparticles prepared from SPI exhibited satisfactory encapsulating properties and a desirable stability at high concentrations. These properties made SPI nanoparticles a promising delivery system for drugs or nutraceuticals.

# Chapter 3 Development and Application of Nanoparticles Synthesized with Folic Acid-Conjugated Soy Protein

## 3.1 Abstract

In this chapter, soy protein isolate (SPI) was conjugated with folic acid (FA) to prepare nanoparticles for target-specific drug delivery. Successful conjugation was evidenced by UV spectrophotometry and primary amino group analysis. An increase in count rate by at least 142% was observed in FA-SPI nanoparticles compared to the non-conjugated ones, whereas the particle size was decreased upon FA conjugation. This was probably attributed to the substitution of positively charged lysine residues by the FA backbone. The zeta potential ranged from -36 to -42 mV depending on the conjugation degree, indicating desirable dispersion stability. Curcumin as a model drug was encapsulated successfully into FA-SPI nanoparticles, evidenced by X-ray diffraction study. The highest encapsulation efficiency and loading capacity were around 92.7% and 5.4%, respectively, which were significantly higher ($P<0.05$) than those with non-conjugated SPI nanoparticles. In addition, a faster and more complete release of curcumin was observed for FA-SPI nanoparticles in PBS/Tween 20 buffer. Cell culture study showed that conjugation of FA resulted in an increase in cellular uptake by at most 93% in Caco-2 cells. These results suggested that FA-SPI is a potential wall material for encapsulation and enhanced delivery of anti-cancer drugs.

## 3.2    Introduction

Targeted delivery of nano-encapsulated drugs has attracted increasing interest in the past decades. By improving the cellular uptake at specific sites, this method could significantly increase the efficacy of bioactive compounds while minimizing the toxicity to healthy tissues [43]. Targeted delivery can be achieved in two approaches, namely, enhanced permeability and retention (EPR) and specific binding [54]. The first approach involves decreased systemic drug elimination through renal excretion, prolonged circulation, and low tumor lymphatic drainage when the drug forms a complex with a polymeric matrix, such as a protein nanoparticle [20]. The second approach requires the attachment of target-specific ligands to the drug carrier, which facilitates the acquisition and internalization of the encapsulated drugs or nutraceuticals into the target cells or tissues [53].

Protein-based nanoparticles have been studied extensively as a vehicle for delivering nutraceuticals and drugs [25, 30, 48, 51, 86]. The amphiphilic nature of protein molecules facilitates the interaction with both the solvent and the packaged drugs or nutraceuticals leading to improved solubility, better tissue penetration and enhanced cellular uptake of compounds [1, 2]. Compared with synthetic polymers, proteins exhibited lower toxicity and better degradability, which made them an attractive candidate in the food and pharmaceutical industry [1]. Soy protein isolate (SPI) is the most widely produced and utilized plant protein in the world. It is unique in its high content (over 60%, molar ratio) of hydrophobic amino acids

[104], together with a considerable percentage of polar and charged residues [27]. The first property enables a strong hydrophobic interaction with encapsulated compounds. The latter feature not only leads to desirable water solubility, but also facilitates the protein-drug interaction through electrostatic attraction and hydrogen bonding. In our previous study [105], nanoparticles were successfully prepared with SPI using an ethanol desolvation method. These nanoparticles exhibited desirable average size (150 nm), zeta potential (-36 mV), and encapsulation and releasing properties. In addition, the chemical crosslinking reaction during the preparation process helped preventing the nanoparticles from dissociation, thus providing additional protection to the embedded drugs. Furthermore, the abundance of functional groups, such as primary amino groups on the lysine residues, enables the conjugation of site-specific ligands to soy protein molecules, making it a potential candidate for drug delivery vehicles.

Folic acid (FA, structure shown in **Figure 1.1**), a diet-derived micronutrient, has been found to be an effective target-specific ligand for tumor cells [19]. The cell accumulation of FA is achieved mainly through a folic acid receptor protein (FRp) identified as GP38, which is an overexpressed, glycosyl-phosphatidylinositol anchored glycoprotein. Elevated expression of GP38 was reported in a variety of carcinomas, including ovarian, prostate, breast, colon and lung cancer cells [20], resulting in a significantly increased affinity of FA in comparison with normal cells. For example, the FA binding capacity of fibroblast and CHO (human ovary)

cells were less than 0.1 pmol per $10^6$ cells, while it was found to be 20 and 50-200 pmol/$10^6$ cells in Caco-2 and KB cells, respectively [106]. To take advantage of specificity toward FA, various polymers including chitosan [55], human serum albumin [107], bovine serum albumin [108] and polylysine [59] have been conjugated with FA and used as carriers for anti-cancer drugs. These conjugates formed nanoparticles with satisfactory encapsulation capabilities and enhanced target delivery properties. However, the major drug-matrix interaction involved in these systems was electrostatic attraction and hydrogen bonding, which could be significantly weakened changing temperature, pH and ionic strength [1]. Soy proteins, on the other hand, may provide a stronger interaction with the bioactive compound as described above. However, to our best knowledge, the synthesis and evaluation of FA-conjugated SPI nanoparticles (FA-SPI) have not been reported.

In this study, FA-SPI conjugates were synthesized by a carbodiimide aided method and then employed to prepare nanoparticles via ethanol desolvation. The sizes, zeta potentials, and morphologies of the FA-SPI particles were compared with the ones prepared with non-conjugated SPI. Curcumin (structure shown in **Figure 1.5**) was chosen as a model drug to be incorporated into SPI and FA-SPI nanoparticles, due to its known chemopreventive activity [109], need for improved solubility and stability [101], and ease of quantification [32]. The encapsulation and releasing profiles of curcumin-loaded SPI and FA-SPI nanoparticles were

compared. Finally, the nanoparticles were subjected to cell culture studies to verify the enhanced uptake of FA-SPI nanoparticles in cancer cells.

## 3.3    Materials and Methods

### 3.3.1    Materials

Prolia$^{TM}$ 200/70 Defatted Soy Flour was a sample donated by Cargill Inc., Cedar Rapids, IA. The soy flour contained 54% protein and less than 1% oil (dry basis). Folic acid (98% purity), N-(3-dimethylaminopropyl)-N-ethylcarbodiimide (EDC, 97% purity), curcumin (98% purity), and 2, 4, 6-trinitrobenzenesulfonic acid solution (TNBS, 5%, w/v in $H_2O$) were purchased from Sigma-Aldrich (St. Louis, MO, USA). Cell culture-related reagents were purchased from Invitrogen Inc. (Carlsbad, CA, USA). All other chemicals (dimethyl sulfoxide, valine, trichloroacetic acid, etc.) were of analytical grade.

### 3.3.2    Preparation of SPI

SPI was prepared following an isoelectric precipitation method [105]. In brief, defatted soy flour was firstly extracted with water at pH 8.0 and centrifuged to precipitate insoluble fibers. The supernatant was then acidified to pH 4.5 and centrifuged again, and the protein-rich curd was recovered, neutralized, dialyzed against deionized water and lyophilized. The moisture content of the final product was less than 5%, while the protein content was 90% as determined by Bradford assay with bovine serum albumin as the standard protein.

### 3.3.3 Preparation of FA-conjugated SPI (FA-SPI)

FA molecules were conjugated with SPI using a previously reported carbodiimide-catalyzed method [43], with several modifications. To avoid the degradation of FA, all of the following procedures were carried out in darkness. SPI powder was dissolved in deionized water at a concentration of 5 mg/mL, and the pH of the dispersion was adjusted to 8.5 using 1 mol/L NaOH. FA was dissolved in dimethyl sulfoxide (DMSO) at a concentration of 2.5 mg/mL, to which EDC was added as a coupling reagent at a molar ratio of FA: EDC=1:5. The resulting solution was stirred at room temperature for 1 h to allow the activation of the carboxylic group on FA molecules. Then, the activated FA solution was added to the SPI dispersion at an SPI: FA molar ratio from 1:5 to 1:75. Upon the addition of FA, the pH of the SPI solution was kept at 8.5 manually using 1 mol/L NaOH. This step was taken instead of using sodium bicarbonate as a buffering solvent, because precipitates of both FA and SPI were observed in this buffer. The conjugation was finished in 30 min, after which the mixture was dialyzed thoroughly against deionized water (adjusted to pH 8.0 using 1 mol/L NaOH) for 48 h. The retentate exhibiting a pH of 7.0-7.5 was then lyophilized. A control sample was prepared similarly with the abovementioned procedures, except that the FA solution was not activated by EDC.

### 3.3.4 Determination of conjugation degrees and primary amino group contents

FA-conjugated or control SPI was dissolved in phosphate buffered saline (PBS) at a concentration of 10 mg/mL and equilibrated for 15 min. The protein content was determined by Bradford Assay after appropriate dilution, while FA was quantified by measuring the optical density at 345 nm using a DU-730 UV/VIS spectrophotometer (Beckman Coulter Inc., Fullerton, CA). This wavelength was chosen based on the data from a preliminary wavelength scanning analysis. The conjugation degree was calculated as the molarity of FA divided by that of SPI.

The contents of primary amino groups in SPI and FA-SPI were determined using a TNBS assay that was reported previously [56]. In brief, SPI and FA-SPI powders were dissolved in water and reacted with TNBS in a $NaHCO_3$ buffer. Dialysis centrifugation (5,000 $g$, 1 h) was then performed using a Macrosep® centrifuge tube (Pall Corp., Ann Harbor, MI) with a built-in filtering membrane (MW cutoff = 10,000). The filtrate containing non-reacted TNBS was reacted with a water of valine for 1 h and subjected to spectrophotometric measurement at 410 nm. A blank solution was prepared following the same procedure, except that trichloroacetic acid solution was used instead of valine. The content of non-conjugated TNBS was calculated by a linear regression equation ($R^2$=0.9996). The number of primary amino groups that was theoretically equal to the content of reacted TNBS was reported.

### 3.3.5   Preparation of nanoparticles with SPI and FA-SPI conjugates

Nanoparticles were formed with freshly prepared SPI or FA-SPI conjugate using an ethanol desolvation method [105] with modifications. SPI or FA-SPI was dissolved in deionized water at a concentration of 15-30 mg/mL (pH 7.5-8.0), and the dispersion was equilibrated for 1 h at room temperature. For the preparation of empty nanoparticles, ethanol was added dropwise into the dispersion to achieve an ethanol/water ratio of 80/20 (v/v). To prepare curcumin-loaded nanoparticles, the ethanol/water ratio was firstly adjusted to 60/40 (v/v) using pure ethanol, and curcumin/ethanol solution (3 mg/mL) was added dropwise to a curcumin: protein mass ratio of 1:10 or 1:20. Additional ethanol was then added to achieve a final ethanol/water ratio of 80/20 (v/v). In both blank and curcumin-loaded nanoparticle dispersions, the concentration of FA-SPI or SPI in the binary solvent was 3-6 mg/mL. After 15 min of equilibration, glutaraldehyde (25 mg/mL aqueous solution) was added as a crosslinker. The requirement of glutaraldehyde was estimated as 28 μg/mg SPI or 77 mol/mol SPI (or FA-SPI), according to our previous study [105], and the crosslinking reaction was finished in 16 h. The ethanol was then removed using a Buchi Rotavapor RII at 30°C (BUCHI Labortechnik AG, Flawil, Switzerland) and replaced with same volume of deionized water. For some of the samples, it was necessary to remove the large aggregates in the dispersion by centrifugation at 10,000 $g$ for 15 min. The percentage of protein remaining in the supernatant was higher than 95%, as

determined by Bradford Assay. The supernatant was lyophilized or stored at 4ºC for subsequent assays.

### 3.3.6 Characterization of SPI and FA-SPI nanoparticles

Both SPI and FA-SPI nanoparticle dispersions were subjected to the following measurements. The particle size and count rate were determined separately by dynamic laser scattering [105] using a BI-200 SM Goniometer Version 2 (Brookhaven Instrument Corp., Holtsville, New York, USA). Particle dispersions in both 80% ethanol (before evaporation) and deionized water (after evaporation) were measured without dilution. The refractive index of soy protein solution (1.43) and the viscosity of different ethanol/water mixtures were applied to obtain accurate results. The laser power and aperture pinhole size were set consistently at 10 mW and 400 μm, respectively. All analyses were conducted at 25ºC for 1 min.

The electrophoretic mobility of nanoparticle dispersions in deionized water was determined by laser Doppler velocimetry using a Nano ZS90 Zetasizer. (Malvern, UK). Each sample was measured three times, and at least twelve runs were performed per measurement. The data were then converted to zeta potentials using the Smoluchowski model.

Morphology was observed under scanning electron microscopy (SEM). Fifty microliters of nanoparticle dispersion (4 mg/mL, in 80% ethanol or deionized water) was drawn, cast dried on an aluminum pan, mounted on a conductive

carbon tape, coated with gold/platinum and observed under SEM (Hitachi SU-70 Pleasanton, CA). Representative images were reported.

The X-ray diffraction (XRD) patterns of dry nanoparticles were recorded on a Bruker D8-Advance Diffractometer (Bruker AXS Inc., Madison, WI) with backgroundless sample holders. The working parameters were as follows: voltage 40 kV, current 40 mA, and a scanning rate of 3 $min^{-1}$.

### 3.3.7 Determination of EE and LC

The EE of curcumin-loaded nanoparticles was determined as previously reported [105]. The insoluble (suspending) curcumin was precipitated by centrifugation (9,000 $g$, 10 min). The resultant supernatant was subjected to dialysis centrifugation as was described for the TNBS assay, and free (non-encapsulated but soluble) curcumin was recovered in the filtrate. The two parts of curcumin were combined, diluted with ethanol and subjected to spectrophotometric analysis at 426 nm, using an established standard curve ($R^2$=0.9991). The EE of the samples were calculated with the equation:

$$EE\ (\%) = 100 - \frac{Insoluble\ curcumin + Free\ curcumin}{Total\ curcumin} \times 100$$

In addition, after the dialysis centrifugation mentioned above, the retentate consisting mainly of curcumin-encapsulated nanoparticles was collected and

lyophilized. The dry nanoparticles were weighed, and the LC was calculated as the mass ratio of encapsulated curcumin to the obtained nanoparticles.

### 3.3.8 Release of curcumin in phosphate buffer saline (PBS)

After lyophilization, five milligrams of the curcumin-loaded nanoparticles was dispersed in 10 mL of the release medium (PBS, pH 7.4, containing 0.5% Tween 20). The dispersion was incubated at 37°C with mild shaking on a Multi-Purpose Rotator/Rocker (Scientific Industries Inc., NY, USA). At designated intervals, the suspension was centrifuged at 51,500 $g$ and 20°C for 15 min. The supernatant was then subjected to dialysis centrifugation as mentioned above. The released curcumin recovered in the filtrate was quantified spectrophotometrically at 426 nm, using a calibration curve established in the curcumin/Tween 20/PBS system ($R^2$=0.9993). The precipitate was disposed, and a fresh dispersion was then prepared for another measurement. The kinetic release profile of curcumin was plotted as a function of time.

### 3.3.9 Cell culture

Human colon adenocarcinoma cell line (Caco-2) was purchased from the American Type Culture Collection (Manassas, VA, USA) and cultured in folic acid-free RPMI 1640 medium, which was supplemented with 10% (v/v, same in this section) fetal bovine serum, 1% nonessential amino acids and 1% penicillin-streptomycin. The cells were cultured in a humidified environment with 5% $CO_2$ at 37 °C. The medium was changed every other day, and the cells were

subcultured after reaching 80-90% confluence. Caco-2 cells between 10-15 passages were used in this study.

### 3.3.10  Cell uptake study

Both SPI and FA-SPI nanoparticle dispersions were labeled with an FITC Labeling Kit (Thermo Fisher Scientific Inc., Rockford, IL, USA). The cells were seeded in a black 96-well plate at $3\times10^4$ cells/well and incubated to achieve 80% confluence. The growth medium was then replaced with a transport buffer (HBSS, pH 7.4, containing 50 mmol/L HEPES) and incubated at 37°C for 30 min. After the removal of transport buffer, two hundred microliters of the labeled nanoparticle dispersion was added and incubated with the cells for 2 to 24 h. At designated time intervals, the cell monolayer was washed with PBS for three times to remove unabsorbed nanoparticles. The cells were then treated with lyse buffer containing 0.5% Triton X-100 and 0.2 mol/L NaOH to expose the internalized nanoparticles. The fluorescent intensity was measured using a PerkinElmer Victor X3 multilabel plate reader (PerkinElmer Inc., Waltham, MA, USA) with an excitation and emission wavelength at 485 nm and 535 nm, respectively.

### 3.3.11  Statistics

The cellular uptake study was conducted in at least six replicates. All other measurements were performed in triplicates. The results were expressed as means ± standard error. T test was performed for the *in vitro* release and cellular uptake studies. All other data were subjected to analysis of variance ($P < 0.05$) followed

by Tukey's test with an experimentwise confidence level of α=0.10 using SAS 9

software (SAS Institute Inc, Cary, NC).

## 3.4    Results and Discussion

### 3.4.1    Conjugation of FA on SPI
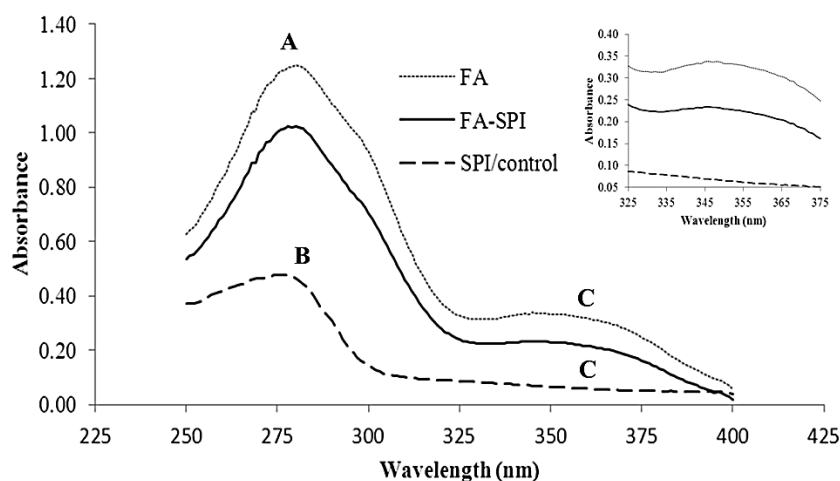


**Figure 3.1** UV spectra of FA (dotted line), SPI (dash line) and FA-SPI conjugates (solid line) in PBS.

FA has been reported to conjugate to different polymers via an amide linkage

through the γ-carboxylic group of FA [19]. In this study, the γ-carboxylic group of

FA was firstly activated by EDC and then reacted mainly with the primary (ε-)

amino group on the lysine residue of SPI [43]. **Figure 3.1** showed the UV spectra

of FA, SPI and FA-SPI conjugate. Within the range of wavelength tested, SPI

showed a single absorption peak at 280 nm (peak B). A control sample was

prepared through a similar process as for the FA-SPI conjugate, except that FA

was physically mixed with SPI without the activation by EDC. The spectrum of

the control sample was observed to overlap with that of SPI, suggesting that the majority of free (non-conjugated) FA molecules have been removed by dialysis during the preparation process.

On the other hand, FA exhibited two absorption peaks at 278 nm (peak A) and 345 nm (peak C) respectively. Unlike the overlapping peaks A and B, peak C was not found in that of the control sample but was observed in the spectrum of FA-SPI, in spite of its low intensity. This result confirmed successful conjugation of FA to soy protein molecules. Therefore, peak C was chosen for the determination of conjugation degree in this study.

**Table 3.1** The conjugation degrees and primary amino group contents of FA-SPI *

| Sample name | FA:SPI ratio mol/mol | Conjugation degree mol FA/mol SPI | Primary amino groups mol/mol SPI |
|---|---|---|---|
| Control | 0 | 0 | $69.82 \pm 0.25^a$ |
| F5 | 5 | $1.28 \pm 0.20^e$ | $69.09 \pm 0.35^a$ |
| F10 | 10 | $4.54 \pm 0.35^d$ | $68.15 \pm 0.43^b$ |
| F20 | 20 | $9.21 \pm 0.17^c$ | $65.11 \pm 0.60^c$ |
| F50 | 50 | $16.97 \pm 0.18^b$ | $55.11 \pm 0.98^d$ |
| F75 | 75 | $32.48 \pm 1.25^a$ | $48.17 \pm 1.17^e$ |

* Data with different letters showed significant difference (n=3, P<0.05).

**Table 3.1** showed the conjugation degree and the content of primary amino groups of FA-SPI as a function of mixing ratio. As the FA: SPI ratio increased from 0 to 75, the conjugation degree increased gradually and reached a maximum value of 32.48 (mol/mol) at a mixing ratio of FA: SPI = 75:1. Concomitantly, the content of primary group decreased from 69.82 to 48.17 mol/mol protein. The data from these two different assays matched approximately, which further indicated that FA

71

was conjugated to SPI via a chemical linkage to the primary amino groups. The minor discrepancy between these data could be explained by the following reasons. Firstly, a small amount of free FA molecules might have not been completely removed by dialysis and were counted as conjugated FA. Secondly, part of FA might have been conjugated with the secondary amino group on the arginine residues [108].

### 3.4.2 Particle sizes and count rates of FA-SPI nanoparticles

In this study, nanoparticles were prepared with FA-SPI by a desolvation method [110], and its physicochemical properties were compared with the counterparts prepared with control SPI. The polydispersity indices for all samples were between 0.100 and 0.180 without significant difference (P<0.05, same hereinafter; data not shown). As can be seen in **Table 3.2**, FA-SPI formed nanoparticles at a concentration between 3 and 6 mg/mL, and the maximum protein concentration for particle formation decreased as the conjugation degree increased. In addition, at a same protein concentration (4 mg/mL), FA-SPI nanoparticles exhibited a significantly lower size (up to 15% less) and higher count rate (up to eight-fold) than the ones formed with control SPI. Besides, in order to achieve a comparable particle count rate, the required concentration of control SPI was three to four times that of FA-conjugated SPI. It was also noteworthy that the particle size and count rate tended to decrease and increase respectively with increasing conjugation degree. Similar results have been reported on FA-conjugated human

serum albumin (HSA) and bovine serum albumin (BSA) nanoparticles [58, 107]. The count rate of a colloidal system indicates the intensity of the scattered laser, which is proportional to the number of the particles as well as the sixth power of their size [23]. As discussed in the last chapter [105], an increase in count rate and a simultaneous decrease in average particle size suggested that a greater number of smaller nanoparticles were formed by FA-SPI as compared to control SPI.

**Table 3.2** Characteristics of FA-SPI nanoparticles *

| Sample | Concentration (mg /mL) | Before evaporation | | After Evaporation | |
|---|---|---|---|---|---|
| | | Particle size (nm) | Count (kcps) | Particle size (nm) | Count (kcps) |
| Control | 12** | 162.5±3.5$^b$ | 98.0±7.5$^d$ | 171.2±8.5$^{ab}$ | 100.2±2.5$^c$ |
| F10 | 6** | 111.8±9.5$^d$ | 99.3±8.2$^d$ | 122.6±4.2$^c$ | 82.8±3.2$^d$ |
| F10 | 5 | 170.2±5.3$^a$ | 75.7±5.7$^e$ | 190.1±7.3$^a$ | 67.9±1.2$^f$ |
| F20 | 5** | 113.7±7.2$^d$ | 137.5±8.3$^b$ | 123.4±4.7$^c$ | 123.8±7.5$^b$ |
| Control | 4 | 150.3±2.7$^{bc}$ | 27.6±4.5$^f$ | 155.4±8.1$^b$ | 28.4±2.8$^g$ |
| F10 | 4 | 168.7±2.6$^a$ | 69.8±5.0$^e$ | 181.4±4.3$^a$ | 62.3±2.4$^f$ |
| F20 | 4 | 109.7±5.6$^d$ | 80.8±6.3$^e$ | 132.2±8.5$^c$ | 77.7±3.7$^e$ |
| F50 | 4** | 137.6±5.3$^c$ | 210.1±10.7$^a$ | 124.6±9.5$^c$ | 153.5±10.2$^a$ |
| F50 | 3 | 124.0±6.2$^{cd}$ | 114.4±5.3$^c$ | 156.5±5.6$^b$ | 98.5±3.4$^c$ |

* Data with different letters showed significant difference (n=3, P<0.05).

** Maximum protein concentration for nanoparticle formation in 80% ethanol. Precipitation was observed at protein concentrations higher than these values.

The formation of protein nanoparticles were considered as driven by attractive forces between protein molecules, such as hydrogen bonding, van der Waals interaction and hydrophobic interaction [2]. When SPI was grafted with FA molecules, part of its primary amino groups lost their positive charges after they formed covalent bonds with FA backbone, which consists of a relatively long non-polar chain and an alpha carboxylic group. The latter group exhibited a

73

negligible ionization at neutral pHs (pKa=6.8) and contributed little to the polarity of SPI [111]. Therefore, conjugation with FA might have resulted in a higher hydrophobicity of the soy protein molecules. In addition, the amino and hydroxyl groups on the pteridine ring could provide additional hydrogen-bonding, if appropriate orientation was allowed. Both of these changes facilitated the aggregation of SPI into nanoparticles.

In our previous study [105], a crosslinking agent (glutaraldehyde) was employed to harden the structure of SPI nanoparticles via amide bonds between the primary amino residues of soy protein. Insufficient crosslinking would result in the dissociation of nanoparticles into free polymers upon the removal antisolvent, which could be characterized by a significant change in either size or count rate [23, 105]. After conjugation with FA, the number of these amino groups was reduced as shown in **Table 3.1**. Therefore, it was important to determine whether the amount of glutaraldehyde applied on non-conjugated SPI (28 μg/mg or 77 mol/mol) was sufficient to fix the structure of FA-SPI nanoparticles. As presented in **Table 3.2**, the particle sizes and count rates of nanoparticles formed by FA-SPI were not significantly decreased after the removal of ethanol by rotary evaporation. These indicated sufficient crosslinking between the formed protein nanoparticles. Addition of excessive glutaraldehyde should be avoided, because it led to partial precipitation of the nanoparticles as we have observed and might increase the toxicity of the product [112].

### 3.4.3  Zeta potentials of FA-SPI nanoparticles
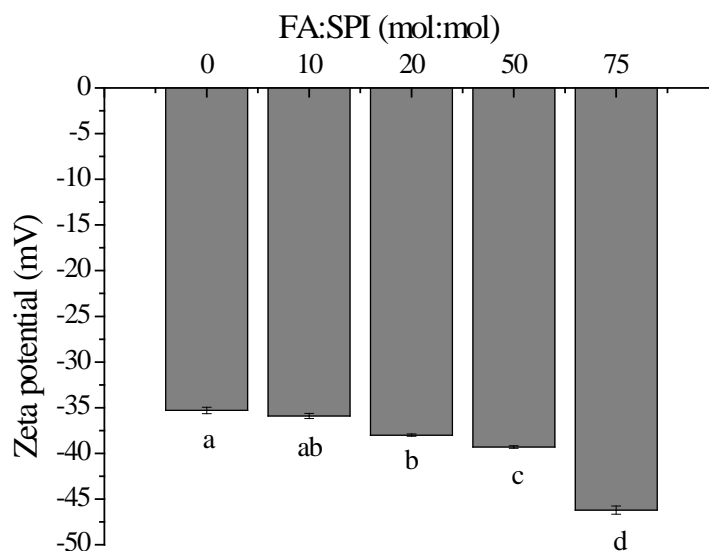


**Figure 3.2** Effect of FA conjugation on the zeta-potential of SPI nanoparticles

The effect of FA conjugation on the zeta potential of SPI nanoparticle dispersions was displayed in **Figure 3.2**. The dispersions were evaporated to remove ethanol prior to the measurements. The nanoparticles formed with control SPI showed a zeta potential of -35.3 mV. The value became more negative as the conjugation degree increased and achieved a minimum of -43.2 mV when the initial FA: SPI molar ratio was 75:1. The decrease in zeta potential was attributed to the substitution of the positively charged primary amino group by the non-charged (or partly negatively charged) residue of FA. According to the American Society for Testing and Materials [5], zeta potentials with an absolute value of higher than 30 mV were indicative for "moderate to good" stability of colloidal systems, owing to the strong electrostatic repulsion between the charged particles.

### 3.4.4 Encapsulation of curcumin into FA-SPI nanoparticles

The particle size, zeta potential, EE and LC of curcumin-loaded SPI or FA-SPI nanoparticles were summarized in **Table 3.3**. For comparison purpose, the control SPI was used to form curcumin-loaded particles at a same concentration (4 mg/mL). The sizes of FA conjugated SPI nanoparticles were significantly greater than that of non-conjugated ones, and they increased from 170.3 nm to 338.8 nm with increasing conjugation degree. This was possibly because the samples with higher conjugation degree possessed a larger amount of the hydrophobic FA backbone as discussed before, which promoted the hydrophobic interaction and allowed more protein molecules to aggregate into nanoparticles. In addition, the particle size increased expectedly when a higher curcumin: protein ratio was adopted. The zeta potential, on the other hand, was not significantly changed when curcumin was incorporated..

The LC and EE of the FA-SPI nanoparticles were observed to increase and decrease respectively with increasing curcumin: protein ratio, regardless of the conjugation degree (**Table 3.3**). The highest EE of approximately 90% was observed when the curcumin/protein mass ratio was 1:50 (w/w), which was comparable with other polymeric delivery systems [32, 99, 113]. In addition, there was a significant difference in the LC between the nanoparticles formed with control and FA-conjugated SPI. The maximal LC achieved with FA-SPI were within the range of 4.4-5.4%, which was approximately 57% higher than that for

control SPI nanoparticles. Compared to other curcumin-loaded delivery systems such as FA-PLGA particles [114], FA-SPI nanoparticles showed a lower LC (5.4% vs. 6.2%) but higher EE (89% vs. 62%). In addition, both LE and EE were higher than those for nanoparticles prepared with some non-conjugated polymers including zein-caseinate [32] and fibrinogen [115]. An important contributor to the improved LC by FA conjugation might have been the enhanced hydrophobic interaction and hydrogen bonding that was discussed above. Besides, similar to the case for empty nanoparticles, the count rate of curcumin-loaded FA-SPI nanoparticles was significantly higher than that for non-conjugated ones at 4 mg/mL (data not shown). This difference indicated that a larger number of FA-SPI molecules were involved in particle formation and curcumin encapsulation than non-conjugated SPI, which allowed a stronger protein-curcumin interaction and thus resulted in higher EE and LC.

**Table 3.3** Characteristics of curcumin-loaded FA-SPI nanoparticles *

| Sample | Curcumin: SPI (g/g) | Particle size (nm) | EE (%) | LC (%) | Zeta potential (mV) |
|---|---|---|---|---|---|
| F10 4 mg/mL | 1:10 | $198.3\pm9.2^d$ | $53.7\pm2.5^b$ | $5.37\pm0.25^a$ | $-35.6\pm0.78^c$ |
| F10 4mg/mL | 1:20 | $173.4\pm1.5^e$ | $89.0\pm1.2^a$ | $4.45\pm0.34^b$ | $-35.7\pm0.98^c$ |
| F20 4mg/mL | 1:10 | $276.1\pm7.3^b$ | $32.5\pm3.5^c$ | $3.25\pm0.27^d$ | $-37.4\pm0.63^b$ |
| F20 4mg/mL | 1:20 | $251.9\pm2.1^c$ | $88.4\pm4.2^a$ | $4.42\pm0.15^b$ | $-38.2\pm0.74^{ab}$ |
| F50 3mg/mL** | 1:10 | $338.8\pm7.5^a$ | $40.6\pm3.5^c$ | $4.06\pm0.08^c$ | $-39.0\pm0.92^a$ |
| F50 3mg/mL** | 1:20 | $313.0\pm10.2^{ab}$ | $87.9\pm5.0^a$ | $4.39\pm0.30^b$ | $-39.1\pm0.58^a$ |
| Control 4mg/mL | 1:20 | $160.7\pm7.3^e$ | $57.8\pm3.4^b$ | $2.89\pm0.17^e$ | $-35.7\pm0.88^c$ |

* Data with different letters showed significant difference (n=3, $P<0.05$).

** Precipitation was observed for curcumin-loaded nanoparticles formed with 4 mg/mL F50/curcumin sample.

It was suggested from the results above that hydrophobic interaction played an important role in the formation and drug incorporation of FA-SPI nanoparticles. However, there has been no standard method to quantify hydrophobic interaction directly to our knowledge. Instead, several methods are proposed for further studies to measure this interaction in an indirect way. Tryptophan fluorescence could be altered when the hydrophobicity of its micro-environment changed, thus reflecting the conformational change of FA-SPI upon curcumin loading. Titration calorimetry could be used to gauge the gross energy change when the protein-curcumin association takes place, giving data on the protein-curcumin affinity. Furthermore, if the hydrophobic interaction involves the burial of surface groups of the protein, its intensity could be estimated by surface properties such as surface charge and hydrophobicity.

### 3.4.5   SEM analysis of blank and curcumin-loaded FA-SPI nanoparticles

**Figure 3.3** showed the morphology of curcumin-loaded FA-SPI nanoparticles at different stages of preparation. When FA-SPI molecules were desolvated by ethanol, they aggregated into spherical particles with smooth surfaces (**Figure 3.3A**). The size varied from 150 to 250 nm, which was consistent with the data from DLS study. The conjugation degree did not show any significant influence on the size and shape of the particles under SEM; therefore, only one representative image for F20 (**Figure 3.3A**) and one for control SPI (**Figure 3.3D**) were shown.
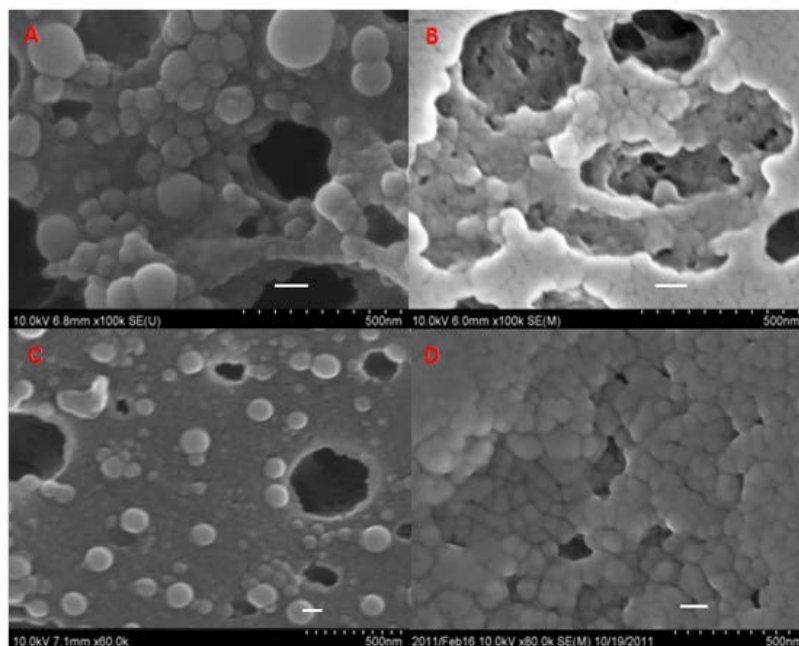
**Figure 3.3** SEM images of FA-SPI nanoparticles.
(A) FA-SPI (F20) nanoparticles desolvated by 80% (V/V) ethanol, (B) curcumin-loaded FA-SPI (F20) nanoparticles, (C) same as B, with ethanol evaporated, and (D) nanoparticles formed with control SPI. The white bars indicated 100 nm.

When curcumin was incorporated, the particles maintained their spherical structure, although some of them were observed to approach each other and form denser clusters (**Figure 3.3B**). Similar results were reported in our study on non-conjugated SPI nanoparticles as well as some other research articles [62, 108]. After the evaporation of ethanol, part of the particles tended to separate from each other (**Figure 3.3C**). Such separation behavior was also reported in our previous study [105], and it was considered as driven by the folding of hydrophobic sites that caused a decreased hydrophobic attractive interaction, together with an increase in electrostatic repulsion upon the removal of desolvating reagents. On

the other hand, the size and shape of the particles were maintained, indicating

successful crosslinking within these particles by glutaraldehyde.

### 3.4.6 XRD analysis of blank and curcumin-loaded FA-SPI nanoparticles
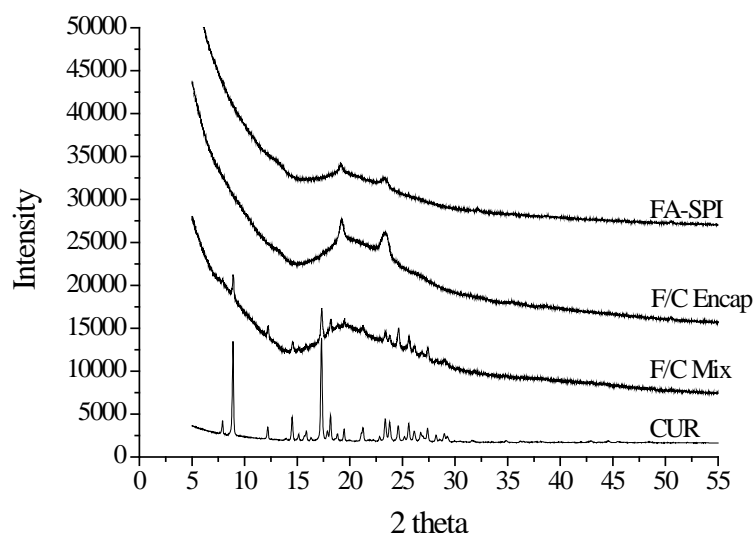


**Figure 3.4** XRD patterns of FA-SPI, curcumin (CUR), their physical mixture (F/C Mix, Curcumin: protein=1:20) and FA-SPI encapsulated curcumin (F/C Encap, Curcumin: protein= 1:20)

The encapsulation of curcumin in FA-SPI nanoparticles was further evidenced by

XRD analysis. As shown in **Figure 3.4**, curcumin exhibited several peaks at 8.84,

12.10, 14.39, 17.20, 23.33, 24.50, 25.52 and 28.87 degrees. These peaks suggested

the highly crystalline nature of curcumin, which was in consistence with previous

literatures [32]. On the contrary, FA-SPI nanoparticles showed only two humps

that suggested its amorphous structure. The characteristic peaks for curcumin was

also found on the XRD pattern of the physical mixture (F/C Mix) of curcumin and

FA-SPI (curcumin: protein = 1: 20, w/w), but they were not observed on the

diagram for the curcumin-loaded FA-SPI nanoparticles (F/C Encap). These results were indicative for the dispersion of curcumin in the polymeric matrix, which facilitated the conversion of curcumin to amorphous state.

### 3.4.7 Release profile of curcumin in PBS-Tween 20 buffer

**Figure 3.5** depicted the release of curcumin from control SPI and FA-SPI nanoparticles in PBS-Tween 20 buffer. For both samples, a burst effect was observed in the first 1 h, in which 24% (SPI) and 29% (FA-SPI) of the encapsulated curcumin was detected in the releasing medium. This phenomenon has been reported in a previous literature [37], and it was attributed to the swelling and decomposition of the protein matrix, as well as the migration of curcumin bound to the peripheral domains of the nanoparticles. In the following 7 h, a sustained release profile was observed, in which the curcumin content in the releasing medium increased at a lower rate as compared to the first hour. This phenomenon was possibly related to the release of curcumin entrapped inside the polymeric matrix. At the end of the eighth hour, 39% and 58% of the encapsulated curcumin was released from SPI and FA-SPI nanoparticles, respectively. The fact that less curcumin was released from SPI than the one reported in our previous study [105] was probably the application of dialysis centrifugation, which gave a higher efficiency of separating released (free) curcumin molecules from the bound ones. Compared with SPI, FA-SPI nanoparticles exhibited a faster and more complete releasing profile. This might be explained by the higher EE and LE of

FA-SPI nanoparticles, i.e., more curcumin molecules were encapsulated in the nanoparticle, resulting in a higher local concentration of curcumin. Therefore, the migration of curcumin molecules into the releasing buffer was facilitated.

In comparison with other FA-conjugated nanoparticles [53, 58, 108], the releasing rate observed for FA-SPI particles was significantly higher. This difference could be partly ascribed to the difference in methodology. In the literatures mentioned above, membrane dialysis was used to measure the releasing kinetics. In our preliminary study, however, it was found that the free drug permeated through the membrane at a relatively low rate (only 20% accumulative release after 4 h). Therefore, not all of the released drug can be collected timely in the filtrate, resulting in a lower releasing rate than observed in our study.
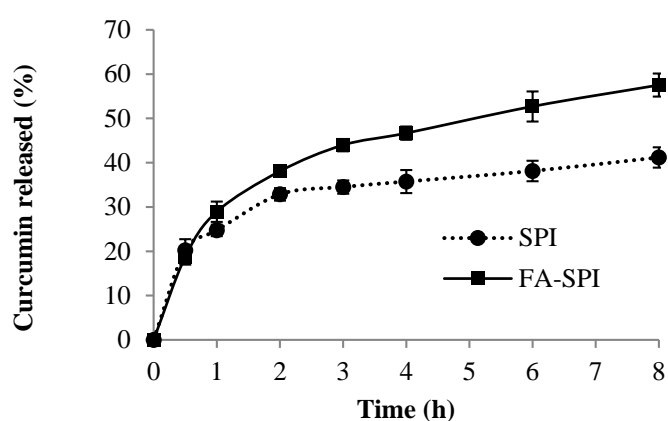


**Figure 3.5** Release of curcumin from SPI and FA-SPI nanoparticles in Tween 20/PBS

### 3.4.8 Cellular uptake of SPI and FA-SPI nanoparticles

**Figure 3.6** presented the time-dependent cellular uptake of FITC-labeled SPI and FA-SPI nanoparticles by Caco-2 cells. Compared with FITC, curcumin showed

weaker but detectable fluorescence. In addition, non-encapsulated curcumin could pass across the cell membrane in a certain amount, which complicates the interpretation of the results. To examine the 'pure' effect of FA on the uptake of SPI nanoparticles, empty particles were used instead of those loaded with curcumin. At all investigated concentrations, no significant cytotoxicity was detected by MTT assay (data not shown). At 200 μg/mL, the initial fluorescence intensities of the two nanoparticle dispersions were approximately 110,000 without significant difference. Compared with the control, FA-SPI nanoparticles exhibited consistently higher cellular uptake, and the advantage became more significant as the time or protein concentration increased. After 24 h, the uptake of FA-SPI nanoparticles was at most 93% higher than that for control SPI.
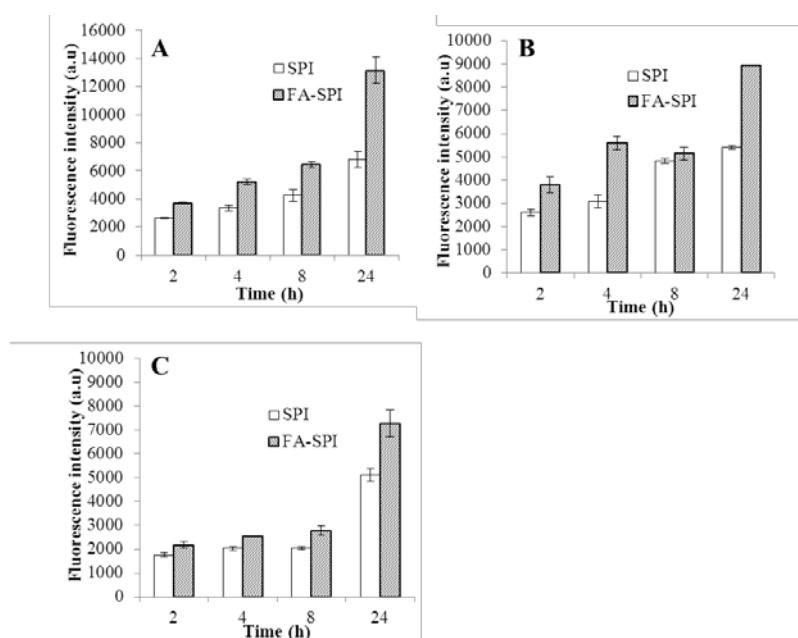


**Figure 3.6** Uptake of SPI and FA-SPI nanoparticles in Caco-2 cells.
The concentrations of protein nanoparticles were 200 (A), 100 (B) and 50 (C) μg/mL.
Bars with different letters (a and b) indicate significant (P<0.05) difference.

83

Enhanced cellular uptake by FA conjugation was also evidenced by the fluorescence micrographs of FITC-labeled nanoparticle loaded Caco-2 cells (**Figure 3.7**). Yang et al [55] reported the abundance of folate receptor protein in colorectal cancer cell lines such as HT29 and Caco-2. In their study, an improved uptake (50-75%) of positively charged chitosan nanoparticles by these two cell lines was achieved by FA conjugation, which was attributed to the receptor-mediated endocytosis. Our results were consistent with the aforementioned study, indicating that FA conjugation also improved the uptake of negatively charged SPI nanoparticles by Caco-2 cells. In addition, more significant improvement in the uptake of FA-conjugated nanoparticles has been reported on other cell lines [58, 108, 116], including prostate cancer (FA-HSA, accurate values not given), Y79 (FA-PLGA, 3-fold increase) and HeLa cells (FA-PEG-L-tyrosine polyphosphate, 5-fold increase). Therefore, we speculated that the improvement in uptake of FA-SPI nanoparticles by these cells would be more significant in those cells compared to Caco-2 cells.
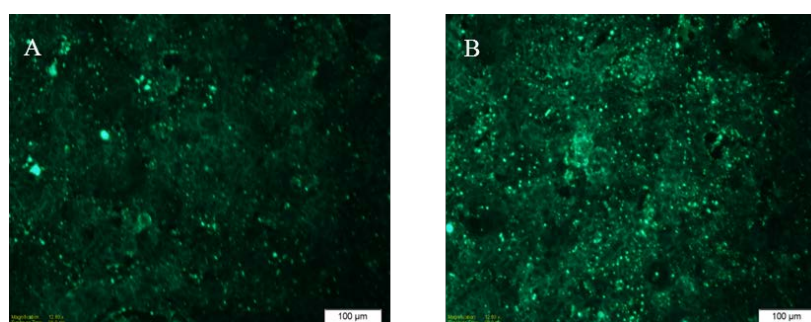


**Figure 3.7** Uptake of FITC-labeled SPI (A) and FA-SPI (B) nanoparticles by Caco-2 cells viewed by fluorescence microscopy.

## 3.5   Conclusion

FA-SPI conjugate was synthesized successfully by a carbodiimide aided method and employed as a nano-encapsulant. Particles with an average size of 150-170 nm and zeta potential of -35 to -42 mV were prepared. Compared with control SPI, FA-SPI conjugates formed a greater number of nanoparticles with a lower average size in 80% aqueous ethanol. In addition, they exhibited an LC that was 57% higher than SPI nanoparticles, and they demonstrated a faster and more complete release of curcumin in Tween 20-PBS buffer. These differences could be probably attributed to the introduction of folic acid backbone, which might have provided SPI with additional hydrophobicity and hydrogen bonding capacity. Cellular uptake of the SPI nanoparticles was improved by at most 93% upon the conjugation with folic acid, and no significant cytotoxicity was detected to Caco-2 cells. These merits made FA-SPI nanoparticles an attractive candidate for the encapsulation and target-specified delivery of nutraceuticals or drugs.

# Chapter 4 Carboxymethyl Chitosan-Soy Protein Complex Nanoparticles for the Encapsulation and Controlled Release of Vitamin D$_3$

## 4.1   Abstract

In this chapter, complex nanoparticles were developed from carboxymethyl chitosan (CMCS) and soy protein isolate (SPI) via a simple ionic gelation approach. The effect of $Ca^{2+}$ concentration, pH, and mass ratio on the formation of nanoparticles was systematically investigated. Vitamin D$_3$ (VD), a hydrophobic micronutrient, was successfully incorporated into the polymeric complex, forming particles with sizes between 162 and 243 nm and zeta potentials ranging from -10 to -20 mV. In comparison with CMCS, the CMCS/SPI complex formed a larger quantity of smaller nanoparticles at lower CaCl$_2$ concentrations, resulting in an increased loading capacity to 6.06%. Furthermore, the complex nanoparticles achieved significantly higher encapsulation efficiency (up to 96.8%), possibly due to their compact structure and high capability of hydrogen bonding as evidenced by Fourier transform infrared spectroscopy (FTIR). In contrast to the ones prepared with SPI, the complex nanoparticles exhibited a reduced (42.3% compared to 86.1%) release of VD in simulated gastric fluid and an increased (36.0% compared to 8.2%) release under simulated intestinal condition. These characteristics made CMCS/SPI complex nanoparticles an attractive candidate for the encapsulation and controlled release of hydrophobic nutraceuticals.

## 4.2 Introduction

Nutraceuticals and bioactives are frequently fortified in functional foods to provide desirable health benefits. However, the efficacy of these compounds is often compromised by their poor water solubility, rapid degradation and low absorption [117-119]. In the past decades, biopolymer-based nanoparticles have drawn increasing interest as a vehicle for the protection and delivery of bioactive compounds [1]. The nano-scaled size contributes to higher solubility, better tissue permeability, prolonged clearance time, and improved cellular uptake of the entrapped compounds [22]. In addition, the polymeric matrix provides remarkable protection to the incorporated compounds against thermo- or photo-degradation [32]. Compared with the synthetic polymer-based systems, these nanoparticles exhibit lower cytotoxicity and higher degradability [23]. All of these features make them an attractive candidate as an efficacy enhancer for the functional foods.

Proteins are amphiphilic biomacromolecules that can interact effectively with both the solvent and the encapsulated compounds. Among the proteins that have been utilized to develop nano-scaled delivery systems [23, 30, 86], soy protein has been highlighted for its natural abundance, desirable water solubility, and balanced amino acid profile that facilitates the protein-nutraceutical interaction [27]. Various soy protein-based delivery systems have been developed by far, including hydrogels, microspheres and microemulsions [24, 67, 89]. Recently, nanoparticles have been successfully prepared with soy protein isolate (SPI) by two methods,

ethanol desolvation from our lab [105] and $Ca^{2+}$-induced cold gelation from other labs [25], both of which resulted in a particles size of 150 to 200 nm with desirable stability. Our previous study showed that SPI nanoparticles exhibited satisfying encapsulation efficiency for hydrophobic compounds such as curcumin [105]. However, SPI exhibited a high digestibility under gastric conditions [120]. This makes SPI nanoparticles only capable for delivering bioactive compounds through injection, while their application in oral administration is limited.

Polysaccharides as another major category of biopolymers have found numerous applications in the food and pharmaceutical industry [121, 122]. Chitosan, the deacetylated form of chitin, has been reported extensively as an encapsulant for bioactive compounds, such as vitamins and minerals [39, 123], catechins [110] and proteins [41]. One of its derivatives, carboxymethyl chitosan (CMCS), exhibited desirable solubility at neutral pH because of its charged –$COO^-$ group [51]. Similar to SPI, CMCS was able to form nanoparticles through a simple ionic gelation process with $Ca^{2+}$. These nanoparticles were applied in the encapsulation of a number of therapeutic drugs [38, 124]. In addition, CMCS has been employed in complexation with proteins such as zein to prepare hybrid nanoparticles [51]. Probably due to a more compact structure, the complex nanoparticles were found to provide additional protection to the embedded compounds against heat or light-induced degradation. More importantly, CMCS becomes insoluble and forms a gel-like barrier in the polymeric matrix at gastric pH (1.4~2.0) due to the

protonation of the carboxylic group. Such feature allows CMCS to detain significantly the decomposition of the protein matrix, thus minimizing the release of the embedded compounds in the stomach and maximizing their availability for intestinal absorption.

In the present study, complex nanoparticles were prepared from CMCS and SPI by ionic co-gelation with $Ca^{2+}$. The particles were analyzed for their average size, count rate, and morphology, in comparison with those formed by single encapsulants (i.e., CMCS or SPI). The effects of $CaCl_2$ concentration, CMCS/SPI mass ratio and pH were systematically investigated. A typical micronutrient, vitamin $D_3$ (VD), was incorporated in the nanoparticles as a model compound. The encapsulation capability and releasing profile in simulated gastrointestinal tract were evaluated. Finally, Fourier transform infrared (FT-IR) spectrometry and zeta potential analysis were carried out to probe into the possible interactions involved in the encapsulation process.

## 4.3    Materials and methods

### 4.3.1    Materials

Prolia$^{TM}$ 200/70 Defatted Soy Flour was a sample generously provided by Cargill Inc., Cedar Rapids, IA. The soy flour contained 54% protein and less than 1% oil (dry basis). Chitosan with deacetylation degree of 77% and medium molecular weight was purchased from Sigma-Aldrich (St. Louis, MO, USA). Calcium chloride, vitamin $D_3$ (VD) and all other reagents were of analytical grade.

### 4.3.2 Preparation of SPI

SPI was prepared by an isoelectric precipitation approach. Defatted soy flour was extracted for 1 h with 15-fold (w/w) of deionized water, which was adjusted to pH 8.0 using 1 mol/L NaOH. The dispersion was centrifuged at 10,000 $g$ for 15 min, after which the precipitation was discarded, and the supernatant was then acidified to pH 4.5 with 1 mol/L HCl. A second centrifugation was undertaken, after which the protein-rich precipitate was re-suspended in water and adjusted to pH 7.5 with 1 mol/L NaOH. The suspension was dialyzed against deionized water for 24 h and lyophilized for 48 h. The moisture content of the final product was less than 5%, and the protein content was 90% as determined by Bradford assay with bovine serum albumin as a standard protein. The following composition of the product was estimated by SDS-PAGE densitometry [66]: 56% glycinin, 37% β-conglycinin, and 7% others (aggregates, α-conglycinin, lipoprotein, etc.).

### 4.3.3 Preparation of CMCS

CMCS was prepared using a previously reported method [125]. Sodium hydroxide (27.2 g) was dissolved in an isopropanol-water mixture (160: 40, v/v), in which 20 g chitosan was added and stirred gently at 50 °C for 1 h. Thereafter, 30 g of monochloroacetic acid dissolved in 40 mL isopropanol was added dropwise to the dispersion and incubated at 50 °C for 4 h. The resultant suspension was then filtered with a Whatman No. 1 filter paper and washed with 80% aqueous alcohol (v/v) until the filtrate was neutral. The remaining solid was oven dried at 60°C to obtain the CMCS powder. The degree of carboxymethylation of the product was

0.67 as was determined by a previously reported conductimetric titration method [126]. The average molecular weight of CMCS was 139 kDa estimated by viscosity measurement together with classic Mark–Houwink equation $[\eta] = 7.92 \times 10^{-5}$ M [127].

### 4.3.4 Preparation of empty and VD-loaded SPI/CMCS nanoparticles

Nanoparticles were synthesized with SPI, CMCS, and their mixtures, using an ionic gelation method [25]. To avoid the degradation of VD, all of the treatments and assays in the following paragraphs were conducted in darkness. The stock solutions of SPI and CMCS were prepared by dissolving them in deionized water at a concentration of 10 mg/mL, followed by the removal of large aggregates via centrifugation at 10,000 $g$ for 15 min. In order to prepare nanoparticles with single ingredient, appropriate dilution was carried out so that a concentration of SPI or CMCS of 0.9 mg/mL was achieved. For the preparation of CMCS/SPI complex nanoparticles, the stock solution of CMCS was added to that of SPI dropwise, after which proper dilution was performed. The mass ratio of CMCS and SPI in the mixed dispersion was set at 2:1, 1:1 and 1:2, while the total polymer concentration was fixed at 0.9 mg/mL. Mild stirring was applied throughout the mixing process to avoid precipitation. The pH of the aforementioned suspension varied from 7.5-9.8, and it was adjusted to 6.5, 7.5, 8.5 and 9.5 ,using 1 M HCl or NaOH. To prepare VD-encapsulated nanoparticles, VD solution (10 mg/mL in pure ethanol) was added dropwise to the resulting solution to achieve a polymer:

VD mass ratio of 10:1. For the preparation of empty nanoparticles, a same amount of pure ethanol without VD was mixed with the dispersion. To 2.5 mL of the mixture, 4 mL of $CaCl_2$ solution was added dropwise under vigorous stirring. The final concentration of SPI, CMCS, or their mixture in the resulting suspension was 0.36 mg/mL, while the content of $CaCl_2$ ranged from 0.1 to 1.8 mg/mL. The formed nanoparticles were purified by centrifugation at 30,000 *g* for 15 min, re-dispersed in deionized water at the same concentration and freeze dried.

### 4.3.5 Determination of particle sizes and count rates

At different stages of preparation, both empty and VD-loaded nanoparticles were measured for their particle sizes and count rates by dynamic laser scattering (DLS). A BI-200 SM Goniometer Version 2 (Brookhaven Instrument Corp., Holtsville, NY, USA) with a 35 mW He-Ne laser beam at a wavelength of 637 nm and a scattering angle of 90° was used. The obtained data were analyzed using cumulant algorithm, and the z-average size was reported. All samples were measured in two separate assays, and no dilution was performed before each measurement. To obtain an accurate particle size, appropriate apertures were selected so that the count rates were within the range of 100 to 300 kcps, and the refractive indices for CMCS (1.55) and SPI (1.43) were applied. The influence of CMCS, SPI and $Ca^{2+}$ on the viscosity of solvent was not detected at all investigated concentrations (data not shown). Therefore, the viscosity of solvent (water) at 25 °C was used throughout the study. In order to obtain comparable count rates, the power of laser

was fixed at 10 mW (except for the dispersions containing only CMCS and less than 0.2 mg/mL $CaCl_2$, for which 20 mW was used), and an aperture pinhole size of 400 μm was adopted consistently. All assays were conducted at 25ºC for 1 min, and the data were analyzed by the BIC Dynamic Scattering Software (Brookhaven Instrument Corp., Holtsville, NY, USA).

Based on the results obtained from this section, the range of $Ca^{2+}$ concentrations for nanoparticles formation and precipitation were determined as a function of pH [38]. Nanoparticles were deemed 'formed' in a solution when the following two criteria were met: (1) the average particle size exceeded 50 nm, and (2) the turbidity was at least than twice that of the polymer solution without $Ca^{2+}$.

### 4.3.6 Determination of the zeta potential

Both empty and VD-loaded nanoparticle dispersions were measured for their electrophoretic mobility by laser Doppler velocimetry, using a Nano ZS90 Zetasizer (Malvern Inc., Malvern, UK) with compatible fold capillary cuvettes. The samples were prepared and measured in triplicates, and at least twelve runs were carried out for each measurement. The data were then converted to zeta potentials using the Smoluchowski model.

### 4.3.7 Morphological and compositional analysis

The morphology of empty and VD-loaded nanoparticles was observed by scanning electron microscopy (SEM). Forty microliters of the nanoparticle

dispersions was dripped and cast-dried on an aluminum pan, which was cut into appropriate sizes and then adhered to a 1-inch specimen stub with conductive carbon tapes (Electron Microscopy Sciences, Ft. Washington, PA, USA). The samples were then coated with a thin layer (<20 nm) of gold and platinum using a sputter coater (Hummer XP, Anatech, CA, USA) and observed under SEM (Hitachi SU-70 Pleasanton, CA, USA). Representative images were reported.

Meanwhile, the dispersions of the empty nanoparticles were cast dried, coated and analyzed for their composition under SEM with an energy dispersive X-ray (EDX) detector [128]. In the SEM-EDX analysis, the elements in the nanoparticles were excited by the electron beam from the SEM anode and produced characteristic X-ray peaks, which were acquired by the a Bruker SOL-XE detector and analyzed by the integrated software (Bruker AXS Inc., Madison, WI). In this study, the contents of different elements (C, O, N, Ca and Cl) were estimated as the percentage of their corresponding peaks by normalized area in the EDX spectrum.

### 4.3.8 Determination of EE and LC

The EE of VD-loaded nanoparticles was calculated by a previously reported method [51]. Ten milligrams of the freeze-dried nanoparticles was washed with approximately 5 mL hexane, and the suspension was filtrated through a Whatman No. 1 filter paper. The filtrate was subjected to spectrophotometric measurement at 264 nm with a DU-730 UV/VIS spectrophotometer (Beckman Coulter Inc., Fullerton, CA, USA). This procedure was repeated for two to four times until the

last filtrate did not exhibit any absorbance. Then all the filtrates were combined and measured again for its absorbance at 264 nm, which was converted to the content of free (non-encapsulated) VD using an established calibration curve ($R^2$=0.9997). The powder (nanoparticles) remaining after the filtration was dried under reduced pressure and weighed. The EE and LC of the samples were calculated with the equations:

$$EE\ (\%) = 100 - \frac{Weight\ of\ free\ VD}{Weight\ of\ formulated\ VD} \times 100$$

$$LC\ (\%) = \frac{Weight\ of\ formulated\ VD - Weight\ of\ free\ VD}{Weight\ of\ nanoparticles} \times 100$$

### 4.3.9 Release of VD in simulated gastrointestinal tract

After lyophilization, the VD-loaded nanoparticles were washed with hexane as discussed above. Eight milligrams of the resulting powder was dispersed in 15 mL of simulated gastric fluid containing 1 mg/mL pepsin and 5 mg/mL Tween 20. The suspension was incubated at 37 °C with gently shaking on a Multi-Purpose Rotator/Rocker (Scientific Industries Inc., NY, USA) for 0.5 h, after which the mixture was adjusted to pH 7.5 to deactivate pepsin. After a centrifugation at 20,000 $g$ and 4 °C for 15 min, the supernatant containing the released VD was collected and freeze-dried, while the precipitate was re-dispersed in simulated intestinal fluid containing 10 mg/mL pancreatin and 5 mg/mL Tween 20. The dispersion was incubated and shaken as abovementioned for 4 h, and a second centrifugation under the same condition was carried out. The supernatant was

freeze-dried, while the precipitate was discarded. The powder yielded after lyophilization was suspended in cold hexane and extracted under vigorous stirring for 10 min. The suspension was then filtered again and measured for its absorbance at 264 nm, which was converted to the content of released VD.

### 4.3.10 FT-IR study of the nanoparticles

Both the empty and VD-incorporated nanoparticles were analyzed for their infrared spectra. After being freeze-dried and washed with hexane, approximately three milligrams of each sample was mounted onto a Jasco FT/IR 4100 spectrometer (Jasco Inc., Easton, MD, USA). The infrared transmittance was acquired from the wavenumber of 1000 to 4000 $cm^{-1}$ at a resolution of 4 $cm^{-1}$. At least 90 scans were performed for each sample. The spectra were averaged and smoothed, and their baselines were calibrated with the Spectra Manager software (Jasco Inc., Easton, MD, USA). Quantitative studies were performed using the OMNIC software (Thermo Scientific, West Palm Beach, FL, USA).

### 4.3.11 Statistics

All measurements were performed in triplicates. The results obtained were presented as means ± standard error. Data were analyzed by analysis of variance ($p < 0.05$) using the Origin 7.5 software (OriginLab Corp., MA, USA).

## 4.4 Results and Discussion

### 4.4.1 Effect of $Ca^{2+}$ on the formation of CMCS/SPI nanoparticles

The sizes and count rates of the nanoparticles formed with CMCS, SPI and their complexes in the presence of different concentrations of $CaCl_2$ at pH 7.5 were compared in **Figure 4.1**. At $CaCl_2$ concentrations of 0 and 0.2 mg/mL, the average sizes of CMCS were 7.4 and 20.5 nm, respectively (**Figure 4.1A**). The majority of CMCS molecules might have existed as free polymers or oligomers as indicated by low count rate (**Figure 4.1B**) and turbidity (not shown). As the concentration of $CaCl_2$ increased to 1.2 mg/mL, the particle size increased gradually to 206.7 nm, together with a continuous increase in the count rate. The count rate of a colloidal system was derived from the intensity of the scattered laser, which is proportional to the number of the particles as well as the sixth power of their sizes [23]. When the sizes are comparable, increasing count rates was indicative for an increase in the number of nanoparticles [105]. When more than 1.6 mg/mL of $CaCl_2$ was present in the dispersion, particles with sizes of greater than 1000 nm were formed, and they precipitated within 30 minutes after the formation.

The dispersion of SPI, on the contrary, exhibited an average particle size of 94.8 nm and a count rate of 15.4 kcps in the absence of $CaCl_2$, and these numbers increased rapidly to 427.7 nm and 490 kcps as the concentration of $CaCl_2$ increased to 0.2 mg/mL. Further addition of $CaCl_2$ induced the precipitation of the particles. These results implied that SPI tended to aggregate into nanoparticles at

97

relatively low CaCl$_2$ concentrations. In addition, a comparison was made between the nanoparticle dispersions formed with 0.35 mg/mL SPI, 0.1 mg/mL CaCl$_2$, and those with 0.35 mg/mL CMCS, 1.2 mg/mL CaCl$_2$. The former dispersion exhibited a lower particle size, but its count rate was 107% higher than that of the latter one. According to our previous study [105], such results suggested that smaller particles could be formed in greater amount by SPI than by CMCS.
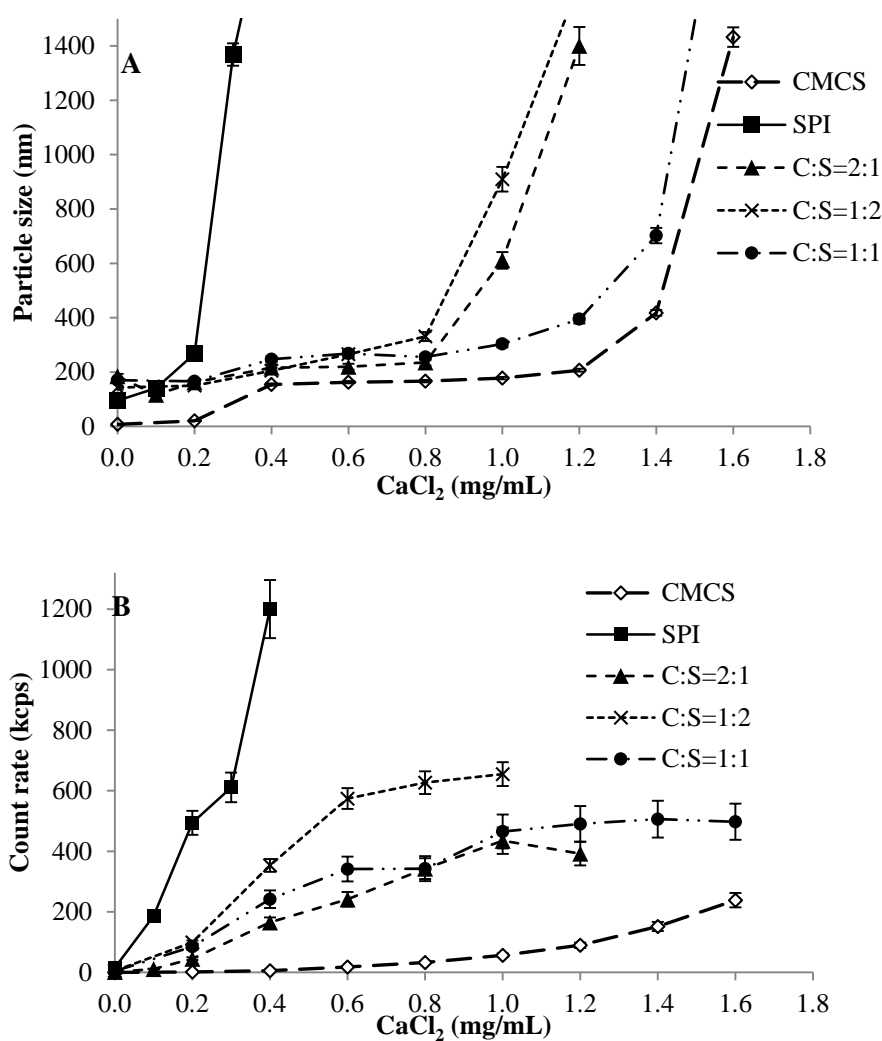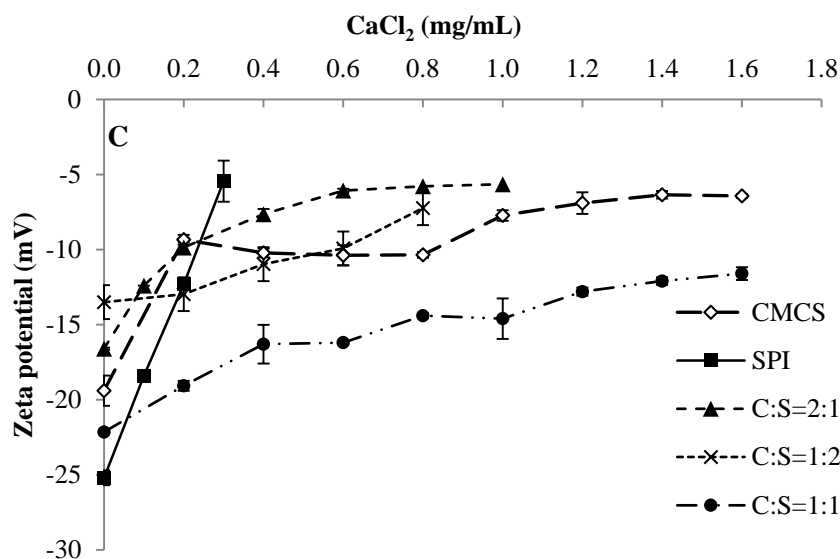
**Figure 4.1** Effect of CaCl2 concentrations on the size (A), count rate (B) and zeta potential (C) of CMCS/SPI nanoparticles at pH 7.5 and a total polymer concentration of 0.35 mg/mL.

Electrostatic interaction between oppositely charged molecules is the chief driving force of nanoparticles formation through cold gelation [2]. To elucidate whether the surface charge was the major reason for the different particle forming behaviors between CMCS and SPI, we measured the zeta potentials of the prepared nanoparticle dispersions. As can be seen in **Figure 4.1C**, at pH 7.5, CMCS and SPI exhibited a zeta potential of -19.4 and -23.2 mV, respectively, and all of the mixtures were negatively charged. When CaCl2 was introduced into the dispersion, the zeta potential decreased gradually (in terms of its absolute value, same hereinafter), indicating the adsorption of $Ca^{2+}$ to the surface of CMCS or SPI molecules, which helped crosslinking these molecules into nanoparticles. However, the minor difference in zeta potentials between CMCS and SPI was insufficient to explain for the remarkable discrepancy in the particle forming

phenomena of these two molecules. Instead, two other factors, surface hydrophobicity and chain rigidity, might have played a major role. Compared with polysaccharides, protein molecules are known to possess a greater amount of hydrophobic side chain on their surfaces [52, 129]. In addition, polysaccharides such as CMCS tend to adapt an extended linear conformation because of the existence of its bulky sugar ring [130], whereas globulins such as SPI generally exhibited a convoluted structure with higher chain flexibility [65]. Therefore, it could be speculated that CMCS molecules exhibited weaker hydrophobic associative interactions together with stronger steric repulsions in comparison with SPI. Therefore, more $Ca^{2+}$ was required to adsorb to CMCS in order to provide stronger electrostatic attraction, which brought the CMCS molecules into proximity and then cross-linked them to form spherical nanoparticles. This inference was supported by the fact that the $Ca^{2+}$-crosslinked CMCS nanoparticles exhibited a less negative zeta potential than the SPI counterparts.

For the CMCS/SPI complexes, they formed nanoparticles with similar sizes and count rates as SPI in the presence of 0 to 0.2 mg/mL $CaCl_2$ (**Figure 4.1A**, **4.1B**). These values continued to increase until precipitation occurred at a threshold $CaCl_2$ concentration, depending on the mixing ratio. Besides, the complex dispersion exhibited significantly ($P<0.05$, same hereinafter) higher count rates than the single ones. A maximal count rate of 626.8 kcps was achieved in the presence of 0.12 mg/mL CMCS, 0.23 mg/mL SPI and 0.8 mg/mL $CaCl_2$. This

value was 46% and 190% higher than the highest ones obtained with SPI and CMCS, respectively. Meanwhile, the average size of CMCS/SPI particles pairing with the greatest count rate was 265.6 nm, which was lower than the corresponding values for SPI (267.4 nm) and CMCS (417.6 nm). These results indicated that a larger quantity of nanoparticles with smaller size could be formed by the complexation of CMCS and SPI. At the $CaCl_2$ concentration of 0.2 to 1.6 mg/mL, the particles formed with a CMCS/SPI ratio of 1:1 exhibited a highest zeta potential (**Figure 4.1C**). This result suggested that a maximum number of charged groups were exposed to the surface of the particles at this mass ratio.

**4.4.2 Effect of pH on the formation of CMCS/SPI nanoparticles**

The boundary $CaCl_2$ concentrations for nanoparticle formation and precipitation were depicted in **Figure 4.2**. The natural pH of water solutions were 9.5 and 7.5 for CMCS and SPI, respectively. The minimal concentration required for CMCS nanoparticle formation was highly dependent on pH, increasing from 0.2 mg/mL at pH 6.5 to 3.0 mg/mL at pH 9.5. In contrast, the critical concentration for SPI nanoparticle formation only increased from 0.02 to 0.04 mg/mL as pH increased. At $CaCl_2$ concentrations higher than 0.225 mg/mL, rapid precipitation was observed in the SPI dispersion at all the pH studied. CMCS, however, did not precipitate until a $CaCl_2$ concentration varying from 0.8 mg/mL (pH 6.5) to 4.0 mg/mL (pH 9.5) was achieved. These results revealed the difference between CMCS and SPI in their particle forming properties.
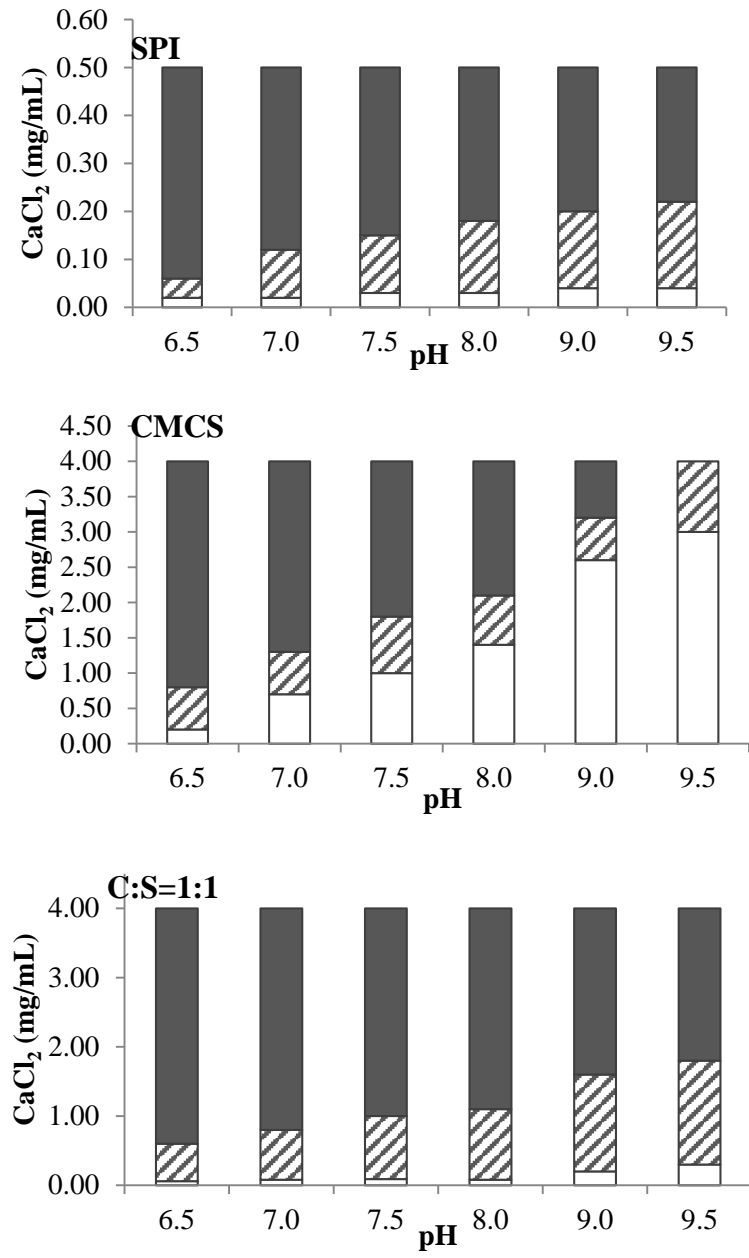
**Figure 4.2** Critical concentrations of CaCl2 for the formation of SPI, CMCS and CMCS/SPI mixture (1:1, w/w) as a function of pH. White open bars – clear solution, gray shaded – nanoparticles, gray solid – precipitate.

In addition to the critical concentrations, the optimal CaCl$_2$ concentrations for the formation of CMCS/SPI nanoparticles at different pH were determined and summarized in **Table 4.1**. At each pH, an optimized CaCl$_2$ concentration was chosen based on the following criteria. Firstly, the criteria for consideration of

particle formation listed in **Section 4.2.5** were met. When the first requirement was satisfied, a minimal particle size should be achieved at this pH. Lastly, when the size difference between two formulas was less than 20 nm, the $CaCl_2$ concentration that resulted in a maximal count rate was chosen. As the pH was decreased from 9.5 to 6.5, there was a significant decrease (from 6.0 to 0.4 mg/mL) in the optimal concentration of $CaCl_2$ for CMCS to form nanoparticles. In the meantime, the sizes of the formed particles decreased greatly from 1068 nm at pH 9.5 to 162.7 nm at pH 6.5, while the count rates increased from 7.5 to 190.0 kcps concomitantly. On the contrary, the mean size and count rate of SPI nanoparticles kept stable at around 150 nm and 190 kcps, respectively, at pH 6.5-9.5. In addition, the optimal $Ca^{2+}$ concentration was only one fourth (pH 6.5) to one thirtieth (pH 9.5) of that for CMCS nanoparticles.

From the results discussed above, it is clear that the particle forming behaviors of CMCS and SPI were significantly different, especially at neutral to basic pH. Theoretically, this difference could be attributed to two factors, i.e., surface charge and polymeric chain rigidity. The zeta potential of CMCS dispersion at pH 9.5 (-58.7 mV) was significantly higher than that at pH 6.5 (-16.3 mV), suggesting that more $Ca^{2+}$ was required to overcome the stronger electrostatic repulsion among CMCS molecules and crosslink them into nanoparticles at pH 9.5. In addition, the potent repulsion between the –COO⁻ groups on a single CMCS molecule might have further increased the chain rigidity, especially at higher pHs

[12]. This added to the difficulty for CMCS to fold, rotate, or approach each other, which might explain for the large particle size and low count rate at relatively high pH. On the other hand, SPI dispersion exhibited more similar zeta potentials (-36.8 and -24.2 mV, respectively) at pH 9.5 and 6.5. Besides, the globular conformation of SPI might have facilitated the formation of nanoparticles as discussed in the previous section. Therefore, there was no need for additional $Ca^{2+}$ to overcome the electrostatic or steric repulsion at pH 9.5 compared to pH 6.5.

From the perspective of application, the above results suggested that SPI was a more suitable particle former than CMCS in the presence of $Ca^{2+}$. Firstly, a larger quantity of nanoparticles (indicated by higher count rate) with smaller average size could be formed by SPI, giving a higher yield of particles. Secondly, the $CaCl_2$ content in SPI nanoparticles was less than one tenth that for CMCS, which helps lowering the risk of calcium overdose after oral administration. Lastly, since the particle formation of SPI was virtually not influenced by pH, it could be utilized over a broader range of pH or in the environment with fluctuating pH.

**Table 4.1** Effect of pH on the $CaCl_2$ dose, size and count rate of CMCS/SPI nanoparticles

| pH | $CaCl_2$ (mg/mL) | Particle size (nm) | Count rate (kcps) |
|----|------|------|------|
| CMCS | | | |
| 9.5 | 6.0 | 1068.0±25.4[a] | 12.5±0.8[i] |
| 8.0 | 3.6 | 637.5±10.5[b] | 25.8±2.5[h] |
| 7.5 | 1.2 | 417.6±7.8[c] | 87.9±4.5[g] |
| 7.0 | 1.0 | 255.1±6.5[d] | 181.1±12.7[e] |
| 6.5 | 0.6 | 162.7±10.2[f] | 190.0±10.6[e] |
| SPI | | | |

| | | | |
|---|---|---|---|
| 9.5 | 0.20 | $157.4\pm5.3^f$ | $180.4\pm10.2^e$ |
| 8.0 | 0.14 | $143.6\pm2.4^g$ | $190.7\pm9.5^e$ |
| 7.5 | 0.12 | $137.1\pm1.7^g$ | $186.1\pm10.0^e$ |
| 7.0 | 0.12 | $141.7\pm4.2^g$ | $200.5\pm7.7^e$ |
| 6.5 | 0.10 | $152.6\pm7.6^f$ | $201.7\pm2.5^e$ |
| | | | |
| C:S=1:1 | | | |
| 9.5 | 0.40 | $238.8\pm9.5^d$ | $96.5\pm4.6^g$ |
| 8.0 | 0.30 | $243.2\pm6.7^d$ | $125.3\pm10.5^f$ |
| 7.5 | 0.20 | $267.4\pm3.5^d$ | $314.3\pm23.5^d$ |
| 7.0 | 0.20 | $265.1\pm7.4^d$ | $360.9\pm13.2^c$ |
| 6.5 | 0.15 | $162.7\pm5.2^f$ | $425.7\pm15.7^b$ |

* Data with different letters showed significant difference (n=3, P<0.05).

When CMCS and SPI were co-dispersed in water, the abovementioned advantages of SPI were inherited. At pH 6.5-8.0, the CMCS/SPI complex formed nanoparticles at $CaCl_2$ concentrations lower than 0.1 mg/mL. The average size was 163 nm at pH 6.5 and kept stable at 240-260 nm as pH was increased from 7.0-9.5, and the count rate was more than two times that achieved by CMCS at any given pH. Similar to the case of SPI, these results indicated that CMCS/SPI complex could form a larger quantity of smaller particles than CMCS alone over a wide range of pH. Therefore, it could be postulated that stronger protection might be provided by CMCS/SPI complex than CMCS alone to the encapsulated compounds. In addition, this similarity suggested that SPI might have played a major role in the extensive formation nanoparticles.

### 4.4.3 Effect of centrifugation and lyophilization on the nanoparticles

Two preparation procedures, centrifugation and lyophilization, were investigated for their influence on the size and count rate of the nanoparticles. Results were presented in **Figure 4.3**. Centrifugation is frequently used for separating the

nanoparticles from non-encapsulated drugs/nutraceuticals. In our study, all of the samples tested could be reconstituted after centrifugation at 30,000 $g$ for 15 min. Increasing the centrifugal force or time, however, led to the inability of reconstitution. The particle size and count rate after reconstitution were decreased approximately by 10% and 40%, respectively. This was probably due to the partial separation of the nanoparticles as well as $Ca^{2+}$ into the supernatant. In addition, the zeta potential of the nanoparticles was virtually unchanged upon centrifugation. After lyophilization, the samples could be re-dispersed in water at a concentration of 5 mg/mL, and they were stable for at least 1 week. However, the particle size increased by approximately 80%. The removal of solvent might have allowed the nanoparticles to approach each other and then aggregate via hydrophobic and van der Waals interaction [108].
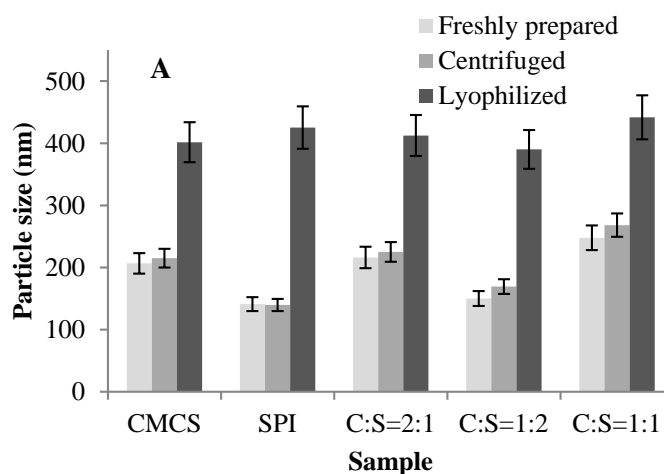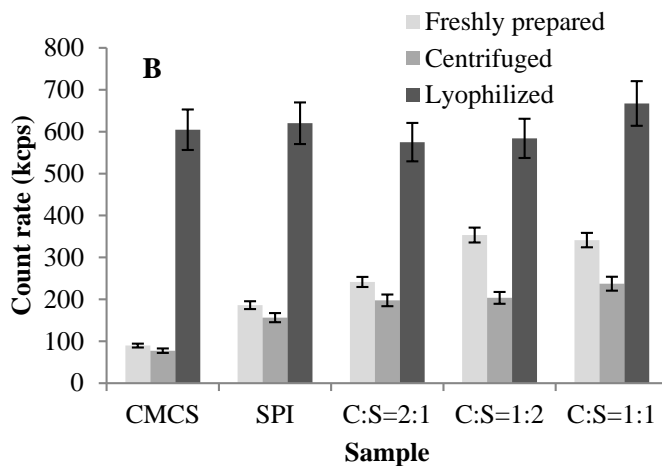
**Figure 4.3** Effect of centrifugation and lyophilization on the size (A) and count rate (B) of CMCS/SPI nanoparticles

### 4.4.4 Characteristics of VD-loaded nanoparticles

**Table 4.2** summarized the particle sizes, zeta potentials, EE, and LC of the VD-loaded nanoparticles. Compared with the SPI, the CMCS nanoparticles yielded a higher EE (80.5%). A possible explanation for this difference was that CMCS nanoparticles possessed a greater particle size, which allowed for a higher capacity of VD incorporation [105]. As for the CMCS/SPI complex nanoparticles, they exhibited higher EE than the ones prepared with a single ingredient. In addition, increased ratio of CMCS in the complex resulted in increased EE and LC. This result suggested that the complex nanoparticles possessed a more compact structure, with more functional groups involved in the polymer-vitamin interaction. A highest EE of 96.8% was achieved with the nanoparticles formed with a CMCS/SPI mass ratio of 2:1, a VD/polymer mass ratio of 1:10 and a $CaCl_2$ concentration of 0.8 mg/mL $CaCl_2$. However, the overall LC of the CMCS or CMCS/SPI nanoparticles was only 3% higher than that achieved by SPI. This was

probably because of the higher $CaCl_2$ concentration applied in these formulas, which added to the total weight of the nanoparticles. Our follow-up study showed that a higher LC could be achieved by increasing the polymer concentration while reducing the $CaCl_2$: polymer mass ratio (data not shown).

**Table 4.2** Characteristics of VD-loaded nanoparticles

| Sample | Particle size (nm) | Zeta potential (mV) | EE % | LC % | VD conc. (µg/mL) |
|--------|--------------------|---------------------|------|------|------------------|
| CMCS | $213.7\pm10.5^b$ | $-10.35\pm0.25^a$ | $80.52\pm2.54^b$ | $2.99\pm0.16^c$ | $10.76\pm0.52^c$ |
| SPI | $162.4\pm6.7^c$ | $-18.36\pm0.37^c$ | $50.19\pm1.97^c$ | $5.88\pm0.26^a$ | $21.16\pm0.77^a$ |
| C:S=2:1 | $225.2\pm10.3^{ab}$ | $-9.97\pm0.09^a$ | $94.83\pm2.54^a$ | $4.64\pm0.37^b$ | $16.71\pm1.01^b$ |
| C:S=1:2 | $178.4\pm9.6^c$ | $-13.97\pm0.19^b$ | $84.46\pm1.67^b$ | $6.06\pm0.15^a$ | $21.83\pm0.47^a$ |
| C:S=1:1 | $243.1\pm12.4^a$ | $-16.25\pm0.86b^c$ | $96.75\pm1.99^a$ | $5.48\pm0.25^{ab}$ | $19.74\pm0.74^{ab}$ |

\* Data with different letters showed significant difference (n=3, P<0.05).

The final concentration of loaded VD in the nanoparticle dispersion ranged from 10.8 to 21.8 µg/mL as indicated in **Table 4.2**. It is worth mentioning that these values were measured before centrifugation and lyophilization; therefore, they corresponded to a total polymer concentration of 0.36 mg/mL. After lyophilization, the particles could be reconstituted at 5 mg/mL, and the concentration of VD in the dispersion was increased accordingly to at most 303 µg/mL.

Regardless of the formula, there was no significant difference in the zeta potentials of the empty and VD-loaded nanoparticles. This could be attributed to the fact that VD was slightly negatively charged in water, with a zeta potential of -6 mV. Therefore, there was little likelihood that VD was encapsulated by the negatively charged SPI or CMCS via electrostatic interaction. Other factors including

hydrogen bonding, hydrophobic and van der Waals interaction might have played

a significant role in the incorporation process.

### 4.4.5   FT-IR study on the nanoparticles

The FT-IR spectra of blank and VD-loaded nanoparticles formed with CMCS, SPI

and their complex were presented in parallel with that of free VD, as shown in

**Figure 4.4**. A major band at 3366 and 3280 cm$^{-1}$ was observed in the spectra of

CMCS and SPI nanoparticles respectively. These peaks were denoted to the

stretching of hydrogen-bonded O-H groups [131]. The sharp peak at 1589 cm$^{-1}$ in

the spectrum of CMCS nanoparticles was assigned to the stretching of ionized

carboxylic group (-COO$^{-}$), which indicated successful carboxymethylation of the

chitosan molecules [125]. On the other hand, SPI nanoparticles exhibited two

characteristic bands [105] at 1635 (amide I, C=O stretching) and 1526 cm$^{-1}$ (amide

II, N-H bending).
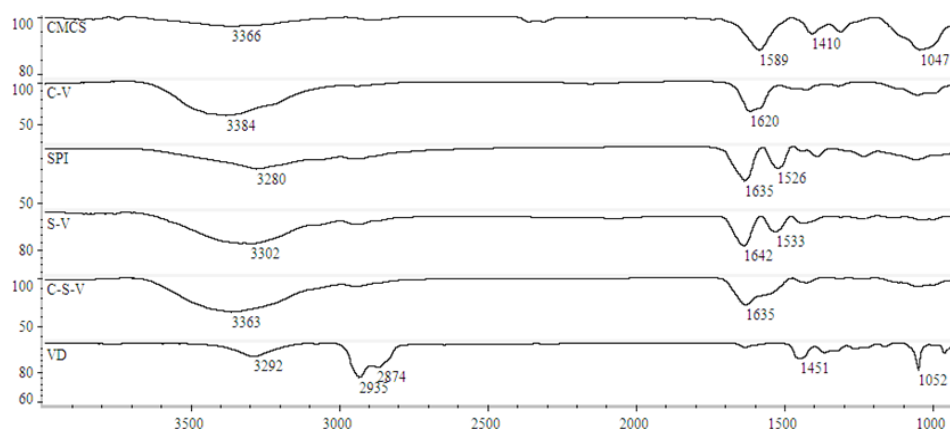


**Figure 4.4** FT-IR spectra for empty CMCS, SPI, VD-loaded CMCS (C-V), SPI (C-V) and
CMCS/SPI complex (C-S-V) nanoparticles (CMCS: SPI=1: 1, w:w),. and VD.

A series of bands were observed on the spectrogram of VD, one for hydrogen

bonded O-H stretch (3292 cm$^{-1}$), two for alkyl C-H stretch (2935 and 2874 cm$^{-1}$)

and several others in the wavenumber range of 1000-800 cm$^{-1}$ indicating C-H bend. These peaks, however, were not detected in the spectra of VD-loaded nanoparticles (the minor band at 2949 in the spectrum SPI-VD was derived from that of SPI instead of VD). The disappearance of these characteristic peaks indicated successful encapsulation of VD in the polymeric matrix [105]. On the other hand, as shown in **Table 4.3**, there was an increase by up to 246% in the intensity of the peaks corresponding to O-H stretch in the spectra of VD-loaded nanoparticles, compared to those for the empty nanoparticles. In the meantime, the position of these peaks shifted to higher wavenumbers (**Table 4.3**). These differences suggested increased involvement of hydrogen bonding, especially in the hydroxyl groups [8], probably with the incorporated VD. In addition, the area percentage of this peak was the highest in the spectrum of CMCS-SPI complex, followed by that of CMCS and SPI. This sequence was consistent with that of the EE as discussed above, which indicated that hydrogen bonding might have played a major role in the incorporation of VD into the polymeric matrix. Similar results have been reported in previous studies on protein-vitamin complexation [8, 51]. From these results, it is speculated that a maximal hydrogen bonding was achieved through the complexation between CMCS and SPI, which was favorable for the encapsulation of VD.

**Table 4.3** Peak assignment for the spectra of empty and VD-loaded nanoparticles*

| Band | | CMCS | C-V | SPI | S-V | C-S-V | VD |
|---|---|---|---|---|---|---|---|
| **O-H stretching** | Position (cm$^{-1}$) | 3366 | 3384 | 3280 | 3302 | 3363 | 3292 |

| | | | | | | | |
|---|---|---|---|---|---|---|---|
| | Normalized Area% | 18.08% | 59.75% | 21.02% | 44.59% | 62.67% | 17.03% |
| **Amide I** | Position (cm$^{-1}$) | ND | ND | 1635 | 1642 | 1635** | ND |
| **COO$^-$ stretching** | Position (cm$^{-1}$) | 1589 | 1620 | ND | ND | ND | ND |
| **C-H stretching** | Position (cm$^{-1}$) | ND | ND | ND | ND | ND | 2935 2874 |

* Refer to **Figure 4.4** for original spectra and denotation for samples. CMCS and SPI: empty nanoparticles formed with individual ingredients. CMCS-VD and SPI-VD: vitamin D$_3$-loaded nanoparticles formed with individual ingredients. CMCS-SPI-VD: vitamin D$_3$-loaded CMCS/SPI complex nanoparticles. VD free: non-encapsulated vitamin D$_3$ crystal.

** Mixed components of amide I and COO$^-$ stretching.

### 4.4.6 SEM-EDX study on the nanoparticles

The morphology of nanoparticles formed with different formulas was compared in **Figure 4.5**. All of the prepared nanoparticles exhibited an approximate spherical shape and a smooth surface (**Figures 4.5A, B and C**). The particle size varied from 150 to 250 nm, which was consistent with the data from DLS study. Figure **4.5D** showed the structure of VD-loaded CMCS/SPI complex nanoparticles (VD: polymer= 1:10, w/w) after centrifugation, lyophilization and reconstitution. The nanoparticles maintained their structure, but they varied in sizes more significantly than the freshly prepared samples. At lower magnifications, aggregates having size bigger than 1000 nm were observed in the micrograph of the freeze dried nanoparticles (data not shown), which could explain for the increased average particle size observed in the DLS study.
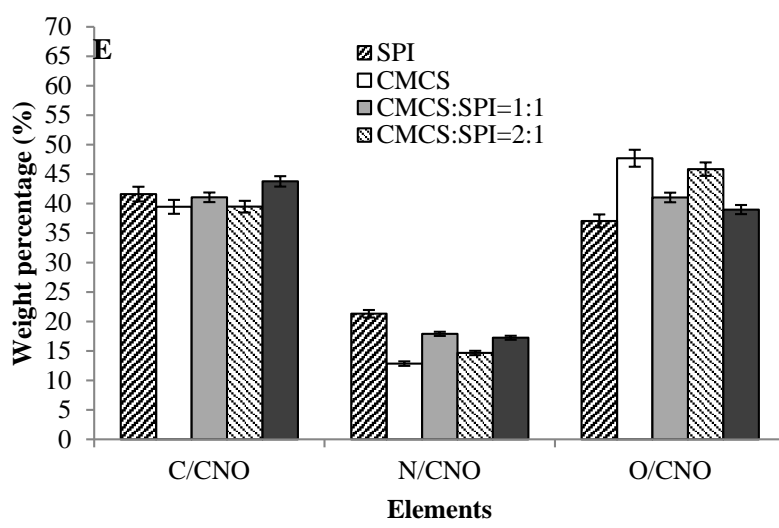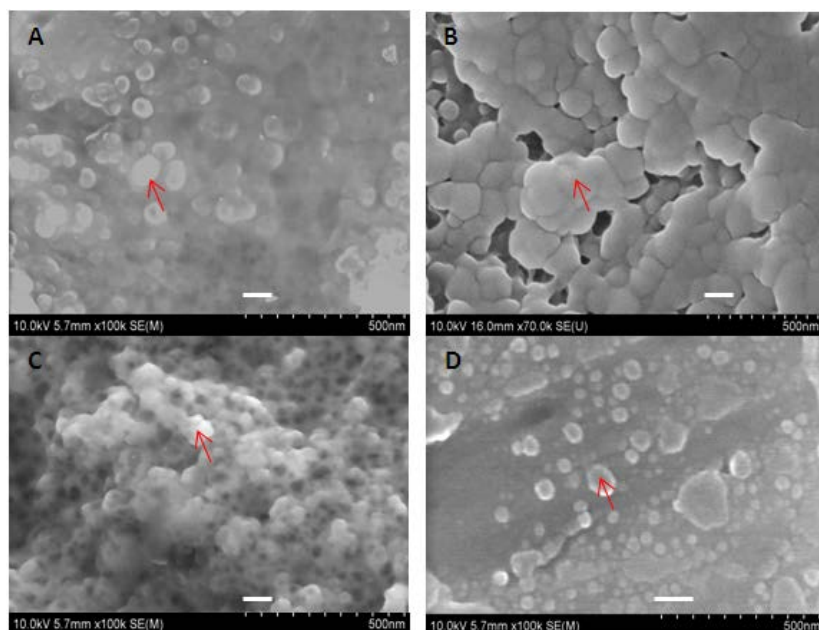
**Figure 4.5** SEM-analysis of CMCS (A), SPI (B) and CMCS/SPI (C) nanoparticles, and VD-loaded CMCS/SPI nanoparticles after lyophilization (D), as well as the elemental analysis of the abovementioned samples (E).

The elemental compositions of the prepared nanoparticles were presented in **Figure 4.5E**. The spectra were acquired at chosen locations on the SEM images that were marked by the red arrow in **Figures 4.5A, B and C**. Compared with

CMCS, SPI exhibited a higher content of nitrogen and lower content of oxygen. This was consistent with their chemical composition. In the spectra of the complex nanoparticles, the contents of oxygen and nitrogen were between those of the single ingredients, and they varied according to the mixing ratio. These results suggested that both CMCS and SPI participated in the formation of the complex nanoparticles.

### 4.4.7 Release of VD in simulated digestive fluids
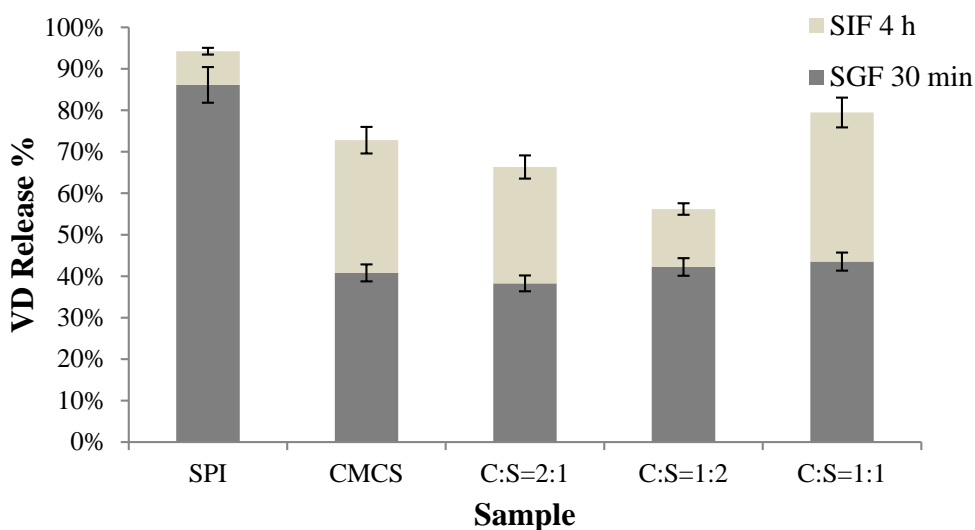


**Figure 4.6** Release of VD in simulated gastric and intestinal fluid from CMCS, SPI and CMCS/SPI nanoparticles

The releasing profiles of VD-loaded nanoparticles were depicted in **Figure 4.6**. After incubation at 37 °C in simulated gastric fluid for 30 minutes, over 80% of the VD was released from the SPI nanoparticles. In contrast, less than 35% of the VD was detected in the releasing medium containing CMCS nanoparticles. Such significant difference might be attributed to the following two factors. Firstly, simulated gastric fluid exhibited a pH of 1.4~2.0, at which SPI was highly

positively charged and soluble [132], whereas CMCS carried none electric charge and agglomerated into a gel layer [51]. Besides, the polymeric matrix formed with SPI was highly digestible by pepsin [27], while that consisting of CMCS was resistant to pepsin digestion and acted as a barrier for the diffusion of vitamins [51]. For the CMCS/SPI complex nanoparticles, the releasing rates were at most 56% lower than that for SPI, suggesting the protection effect provided by CMCS. When transferred to the simulated intestinal fluid (pH 7.4), the samples containing CMCS became negatively charged and therefore soluble. As a result, at most 83% of the remaining VD was released from the polymeric matrix in the following 4 h. In addition, among the three tested complex formulas, the one with a CMCS: SPI mass ratio of 1:2 resulted in a least amount of released VD. This was probably attributed to the greater number of particles achieved by this formula compared with the other two, which was evidenced by a higher count rate as discussed in **Section 4.3.1**. The involvement of large quantities of nanoparticles in the encapsulation of VD might have reduced its release from the polymeric matrix. Based on the above results, CMCS/SPI complex nanoparticles demonstrated prominent protection on VD against degradation in the gastric fluid, together with an increased amount of VD being delivered to the small intestine, in comparison with the nanoparticles formed with single ingredients.

## 4.5    Conclusion

CMCS/SPI complex nanoparticles were successfully synthesized and employed as a delivery system for VD. The particles exhibited an average size of 162 to 243 nm, and they maintained desirable solubility and stability after centrifugation and lyophilization. Compared with CMCS, the CMCS/SPI complex required lower concentration of $CaCl_2$ to form nanoparticles, and it formed a significantly greater number of particles (more than two times higher as indicated by count rate) with lower average size. These factors contributed to an increase in both EE (80.5% to 96.8%) and LC (2.99% to 6.08%). Besides, the complex nanoparticles inherited the desirable pH adaptability from SPI. Therefore, they could be applied flexibly over a wide range of pH as well as in an environment with fluctuating acidity. In comparison with the ones prepared with SPI, the complex nanoparticles provided improved EE (96.8% compared to 50.1%), reduced release of VD in simulated gastric fluid and enhanced release under simulated intestinal condition. FT-IR study showed that the complex nanoparticles provided stronger interaction with VD through hydrogen bonding in comparison with the ones formed with single ingredients, which might have facilitated the encapsulation and detained the release of VD. These results made the complex nanoparticles an attractive candidate for the encapsulation and controlled release of nutraceuticals and drugs.

# Chapter 5 Insight into Curcumin-loaded β-lactoglobulin Nanoparticles: Incorporation, Particle Disintegration and Releasing Profiles

## 5.1 Abstract

This chapter is aimed at developing protein nanoparticles with desirable loading capacity (LC) and low crosslinker concentration. Using β-lactoglobulin (BLG) and curcumin as a model system, we demonstrated that the LC could be improved by up to 157% by maintaining low antisolvent content before mild evaporation. Moreover, the optimal level of glutaraldehyde decreased by 50% as the curcumin/protein ratio increased, suggesting that toxic crosslinkers could be partly replaced with natural phenols such as curcumin. The BLG-curcumin nanoparticles showed average size of 164-214 nm, zeta potential of -42 mV, and LC of up to 11%. Interestingly, BLG nanoparticles showed rapid disintegration and nutraceutical release in simulated gastric fluid (SGF) at pH 2, in spite of the known resistance of BLG against pepsin. However, they maintained integrity in SGF at pH 5. This phenomenon, followed by the extensive tryptic digestion, suggested the controlled release property of BLG nanoparticles.

## 5.2 Introduction

In the past few decades, protein-based nanoparticles have been studied extensively as a promising bioavailability enhancer for poorly absorbed bioactive compounds

[1, 22]. Known as amphiphilic molecules, proteins were capable of incorporating target compounds via various approaches, including hydrophobic interaction, electrostatic attraction, hydrogen bonding, and van der Waals force [133]. This characteristic enables protein nanoparticles to encapsulate non-polar, polar or charged compounds. In addition, proteins exhibit superior biocompatibility and nutritional value in comparison with synthetic polymers [25]. A wide array of proteins, such as serum albumin [23, 134], zein [51, 135], soy protein [25, 105, 133], and sodium caseinate [33, 136], has been utilized by far to prepare nanoparticles. These nano-scaled assemblies of protein molecules provided encapsulated compounds with desirable solubility [32], stability [7], stimulus-responsive release [113, 137], and cellular uptake [20, 133], all of which resulted in considerable enhancement of their bioavailability.

In spite of these advantages, the application of protein-based nanoparticles has been impeded by several drawbacks. Firstly, the loading capacity (LC, weight ratio between the loaded compound and the matrix) of protein nanoparticles is generally low compared to synthetic polymeric nanoparticles [138] or other encapsulation systems (such as the nanoemulsion and hydrogel) [127, 139]. The typical LC for hydrophobic compound-loaded protein nanoparticles is around 5% [6, 32, 140-142]. It should be pointed out a number of literatures claimed LC values over 50%, but these results were arguably inaccurate because of improper measuring methods, e.g., counting precipitated nutraceutical molecules as

encapsulated ones [143, 144], or neglecting the weight of a secondary coating polymer when calculating LC [32]. The second disadvantage lies in the toxicity of chemical crosslinkers. Crosslinking is necessary procedure for the preparation of nanoparticles with a number of water-soluble proteins (e.g., serum albumin and soy globulin), which dissociate readily into their monomeric forms upon the removal of antisolvents [105]. Compared with physical crosslinking with couterions (e.g., $Ca^{2+}$), which is highly dependent on the pH and ionic strength of the environment [137], chemical (covalent) crosslinking with glutaraldehyde may provide protein nanoparticles with higher stability in various of physiologically relevant systems [105]. However, the involvement of chemical crosslinkers gives rise to safety concerns, because of their significant toxicity [112].

To overcome the abovementioned drawbacks of protein-based nanoparticles, two strategies were proposed in this study. The first strategy is the adjustment of antisolvent content before evaporation. **Figure 5.1** compares the progression of solvent composition during the preparation of nanoparticles by conventional and modified procedures. In both methods, the protein is dispersed in water (step 1) and desolvated at high concentration of antisolvent in order to achieve a high yield of nanoparticles (step 2). After crosslinking (step 3), a simple procedure (step 3') was added in the modified method to adjust the content of organic solvent to lower values, followed by a brief period of equilibration before evaporation (step 4). This added step was expected to improve the LC by enhancing the

protein-nutraceutical interaction and reducing nutraceutical precipitation. The principle and outcomes of this procedure will be covered in detail in **Section 5.4**.

Meanwhile, lower levels of glutaraldehyde were applied for preparing BLG nanoparticles with higher drug/BLG ratios. This was inspired by a series of recent studies on epigallocatechin gallate (EGCG)-loaded protein nanoparticles [145, 146]. As suggested by these studies, protein aggregated into nanoparticles in the presence of polyphenols such as EGCG, and these particles remained stable without additional crosslinkers. The strong interaction between protein and polyphenols, including hydrogen bonding and π-π interaction [147], made EGCG a possible crosslinker surrogate. Likewise, if the target compound e.g., (resveratrol or curcumin) shows certain similarity in the structure and protein affinity with EGCG, the dose of glutaraldehyde could be lowered accordingly. Excessive dose of glutaraldehyde may not only cause higher toxicity, but also lead to lower LC, considering that excessive crosslinking by both glutaraldehyde and the phenol might cause extensive formation of insoluble complexes.

It should be pointed out that great efforts have been made to seek alternative crosslinkers (e.g., genipin and transglutaminase) for the preparation of protein network structures, such as protein oligomers or hydrogels [148-150]. However, with regard to protein nanoparticles, glutaraldehyde remains the major crosslinking agent. This is probably because nanoparticles are compact assembly

of proteins which are very close to each other. Glutaraldehyde is a relatively small molecule which can easily approach the functional groups (primary amino groups which is likely to be exposed at the surface of proteins) on protein nanoparticles. Other crosslinkers, such as transglutaminase, are relatively bulky molecules whose reactivity is hindered by the steric hindrance. By replacing glutaraldehyde partially with phenolic compounds such as curcumin, one may achieve satisfactory crosslinking effect while reducing the toxicity of the final product.
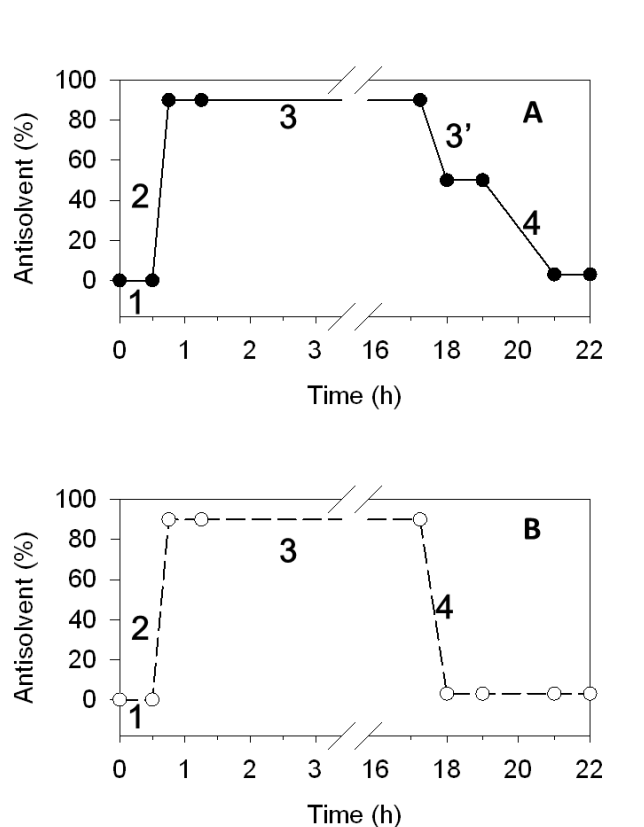


**Figure 5.1** Change in antisolvent content during the preparation for protein nanoparticles. Steps 1, 2, 3, and 4 represent dispersion, desolvation, crosslinking and evaporation, respectively. Compared to the conventional method (B), a new step (3') was added between steps 3 and 4 in the new method (A), in order to lower the antisolvent content to 40-60% before evaporation.

In this study, BLG was chosen as a model protein to implement these strategies. BLG is the major component of whey protein and a natural carrier for various lipophilic nutrients [47, 151]. Curcumin as an antioxidant [152] and chemopreventive [70] compound was selected as a model nutraceutical to be incorporated. According to previous literatures (excluding those that might have counted co-precipitated curcumin molecules as encapsulated ones), the LE of curcumin-loaded protein nanoparticles varied from 2 to 5% [32, 105, 133, 153, 154]. The binding between curcumin and BLG nanoparticles in different water-acetone binary systems was firstly assessed by investigating the distribution of curcumin in different phases. The optimal acetone content before evaporation was then determined based on the result. The effect of glutaraldehyde level and curcumin loading on the LC was also investigated. The formed nanoparticles were characterized for their size, surface charge and morphology. Finally, since BLG is known for its remarkable resistance against pepsin and moderate digestibility by trypsin [155], the nanoparticles were anticipated to show controlled release property, i.e., minimal and maximal release in the stomach and small intestine, respectively. Therefore, the nanoparticles were studied for their integrity as well as releasing profile in PBS and simulated gastric/intestinal fluids.

### 5.3 Materials and Methods

### 5.3.1 Materials

Bovine BLG (90% purity), pepsin (3,200-4,500 units/mg), trypsin (10,000 BAEE units/mg), and curcumin (98% purity) were purchased from Sigma-Aldrich (St. Louis, MO, USA). Simulated gastric and intestinal fluids (abbreviated as SGF and SIF, respectively) were obtained from Ricca Chemical (Arlington, TX, USA). All other chemicals (acetone, glutaraldehyde, buffers, etc.) were of analytical grade.

### 5.3.2 Preparation of curcumin-loaded BLG nanoparticles

BLG nanoparticles were prepared by desolvation method [23] with several modifications. The whole process was undertaken in darkness with constant stirring (800 rpm). BLG was dissolved in deionized water at 10 mg/mL, and curcumin was dispersed in acetone at 4 mg/mL. Both dispersions were equilibrated for 1 h. To 2 mL BLG dispersion, 3 mL pure acetone was added dropwise, after which appropriate amount of curcumin solution was introduced to achieve predetermined curcumin/protein ratio (5%, 10% and 15%, w/w, same hereinafter). Additional acetone was then added to a total volume of 20 mL. After 30 min of equilibration, glutaraldehyde (5 mg/mL aqueous solution) was introduced as a crosslinker. Theoretically, each milligram of BLG needs 40 μg glutaraldehyde for stoichiometric crosslinking [151]. This ratio is defined as 100% glutaraldehyde equivalent, and three levels of glutaraldehyde (25%, 50% and 100% equivalent) were applied in this study. After 16 h of crosslinking, aliquots of 2 mL

were withdrawn and mixed with 4 mL of aqueous acetone. The composition of the aqueous acetone was designed so that the final acetone content ranged from 30% to 90% (v/v, same hereinafter). After 1 h of equilibration, the acetone was evaporated mildly at room temperature under reduced pressure using a VWR Symphony vacuum oven (VWR International, Radnor, PA, USA). The pressure was firstly kept at $5\times10^4$ Pa for 20 min to remove dissolved air and then maintained at $4\times10^3$ Pa to remove the acetone. This procedure typically lasted for 2-3 h, and additional water was supplemented to achieve a final volume of 6 mL. The dispersion (defined as the "final dispersion") was stored at 4ºC for subsequent assays. The initial and final pH of the dispersions ranged from 7.2 to 7.6.

### 5.3.3    Quantitative analysis of free and bound curcumin

Following the procedures described above, BLG-curcumin nanoparticles were prepared in 90% acetone, crosslinked using 100% equivalent of glutaraldehyde, and mixed with aqueous acetone to achieve various acetone contents. After equilibration for 1 h, the dispersion was centrifuged (9,000 $g$, 15 min, room temperature). The insoluble curcumin was recovered in the precipitate and dissolved in pure acetone, while the supernatant was subjected to dialysis centrifugation (5,000 $g$, 30 min, room temperature) using a Macrosep® centrifuge tube (MW cutoff 10 kDa, Pall Corp., Ann Harbor, MI). A preliminary study was conducted with 90% aqueous acetone containing 1 mg/mL curcumin. More than 90% of the dissolved curcumin was able to pass the dialysis membrane and

recovered in the filtrate. The filtrate containing freely dissolved (non-bound) curcumin was recovered and diluted with acetone. Both dispersions mentioned above were further diluted with acetone to achieve a final water content of <1%. The resultant mixtures were then measured for their absorbance at 426 nm by a DU-730 UV/VIS spectrophotometer (Beckman Coulter Inc., Fullerton, CA, USA). The percentages of insoluble and dissolved curcumin were calculated using an established standard curve ($R^2$=0.9991), and the ratio of nanoparticle-bound curcumin was derived by subtracting 100% by these two proportions.

### 5.3.4 Characterization of curcumin-loaded BLG nanoparticles

Freshly prepared "final dispersions" of curcumin-loaded BLG nanoparticles were subjected to the following measurements [151]. The particle size and count rate were determined by dynamic laser scattering (DLS) using a BI-200 SM Goniometer Version 2 (Brookhaven Instrument Corp., Holtsville, New York, USA) equipped with a 35 mW He-Ne laser beam. No dilution was undertaken prior to the assays. Two separate measurements were carried out on each sample in order to obtain accurate results. For count rate determination, the aperture pinhole size was fixed at 400 μm. To measure the particle size, appropriate aperture sizes were chosen to achieve a count rate between 100 and 300 kcps. The obtained data were analyzed using the Cumulant algorithm, and the quadratic mean particle size (z-average size) was reported.

The electrophoretic mobility of nanoparticle dispersions was determined by laser Doppler velocimetry using a Nano ZS90 Zetasizer (Malvern, UK). Each sample was measured for three times, and at least twelve runs were performed per measurement. The data were then converted to zeta potentials using the Smoluchowski model.

The structure of curcumin loaded BLG nanoparticles was investigated by Fourier-transform infrared (FT-IR) analysis. Samples (3 to 5 mg) were freeze dried and mounted onto a Jasco FT/IR 4100 spectrometer (Jasco Inc., Easton, MD, USA). The infrared transmittance was recorded at wavenumbers between 1000 and 4000 $cm^{-1}$ with resolution of 4 $cm^{-1}$. At least 100 scans were undertaken for each sample. The spectra were averaged, smoothed, and corrected for their baselines using the Spectra Manager software (Jasco Inc., Easton, MD, USA).

The morphology of nanoparticles was observed under scanning electron microscopy (SEM). Approximately 40 μL of the dispersion (after evaporation and water supplementation) was cast dried on an aluminum pan, mounted on a conductive carbon tape, coated with gold/platinum using a sputter coater (Hummer XP, Anatech, CA, USA) and observed under SEM (Hitachi SU-70 Pleasanton, CA). Representative images were reported.

### 5.3.5 Determination of EE and loading capacity LC

The EE of curcumin-loaded nanoparticles was determined as follows [105]. After evaporation and water supplementation as described in the section for nanoparticle preparation, the final dispersions were let stand at room temperature for 1 h and then centrifuged at 9,000 $g$ for 30 min. The insoluble curcumin was recovered from the precipitate and dissolved in pure acetone. The supernatant was subjected to dialysis centrifugation as was discussed in the **Section 5.3.3**, and the free curcumin was collected in the filtrate. The two parts of curcumin were diluted with acetone and measured for their absorbance at 426 nm, which was converted to the curcumin content using the same standard curve as described before. The EE was calculated as follows:

$$EE = 100 - \frac{Amount\ of\ precipitated\ curcumin}{Total\ amount\ of\ curcumin} \times 100 \quad (1)$$

In addition, after the dialysis centrifugation mentioned above, the retentate containing the curcumin-encapsulated nanoparticles was collected and lyophilized. The dry nanoparticles were weighed, and the LC was calculated as follows:

$$LC = \frac{Weight\ of\ encapsulated\ curcumin}{Total\ weight\ of\ nanoparticles} \times 100 \quad (2)$$

### 5.3.6 *In vitro* release of curcumin in different buffering systems

**Release in PBS.** Samples prepared with the following parameters were chosen for *in vitro* release study: curcumin loading of 5%, 10%, and 15% (w/w), initial acetone content of 90%, pre-evaporation acetone content of 50%, and

glutaraldehyde levels that resulted in optimal EE for each curcumin loading ratio. Samples were taken after evaporation but prior to supplementation of water. All buffers used in this section contained 5 mg/mL Tween 20. Unless specified, the PBS used in this section was at pH 7.2 and 0.1 mol/L.

Two milliliters of the abovementioned samples was mixed with two milliliters of PBS (pH 7.2, 0.2 mol/L). After incubation at 37 °C for 30 min, the mixture was injected into a sealed dialysis tube (MW cutoff 10 kDa), which was then placed in a flask containing 60 mL PBS (preheated at 37 °C). The flask was then incubated in a reciprocal shaking bath (Thermo Scientific, Odessa, TX, USA) at 37 °C under constant shaking at 120 rpm. At predetermined time intervals, aliquots of 2 mL were withdrawn from the flask and diluted with appropriate amount of PBS. The resultant dispersion was measured for its absorbance at 426 nm, which was converted to the mass of released curcumin using a linear standard curve ($R^2$=0.9993). After each measurement, 2 mL of fresh PBS was added to the flask to maintain sink condition. The kinetic release profile of curcumin was plotted as a function of time and curve fitted to the first order kinetic model:

$$C = C_0 + k \ln t \quad (3)$$

Where C indicates the cumulative percentage of released curcumin, $C_0$ represents the initial percentage of curcumin present in the buffer, and t stands for the time.

**Release in SGF and SIF.** The nanoparticle dispersion with curcumin loading of 10% was chosen. Two milliliters of the sample was incubated at 37 °C and then diluted with 8 mL of two preheated buffers: SGF-2 (commercial SGF, adjusted to pH 2.0, containing Tween 20, 0.5 g/mL, and pepsin at a BLG/pepsin ratio of 100:1, w/w) or SGF-5 (same as SGF-2, except that the pH was adjusted to 5.0). These buffers mimicked the gastric environment at the fast and fed state, respectively [156]. After mixing, 0.5 mL of the dispersion was withdrawn immediately, diluted with 2.0 mL PBS, and then subjected to dialysis centrifugation (5,000 *g*, 30 min) using a Macrosep® centrifuge tube (MW cutoff 100 kDa, Pall Corp., Ann Harbor, MI). The filtrate containing the released curcumin was diluted appropriately with PBS before spectrophotometric measurement at 426 nm. The absorbance was converted to the amount of released curcumin as described before. Meanwhile, the abovementioned mixture was incubated at 37 °C in the reciprocal shaking bath (120 rpm), and aliquots of 0.5 mL were withdrawn and measured as mentioned above at predetermined time intervals. Fresh SGF was supplemented after each measurement to maintain sink condition.

On the other hand, another batch of the nanoparticle dispersions were mixed with SGF and digested for 60 min at 37 °C in the reciprocal shaking bath. The digesta was diluted with SIF (commercial SIF containing Tween at 0.5 g/mL and trypsin at a BLG/trypsin ratio of 100:1, w/w) and centrifuged as mentioned above, and the retentate containing intact nanoparticles was supplemented with PBS to 2 mL. The

dispersion was incubated at 37 °C for 15 min and then mixed with 8 mL preheated SIF. Immediately after mixing, 0.5 mL of the dispersion was withdrawn and subjected to dialysis centrifugation (5,000 $g$, 45 min, 4 °C), after which the filtrate was diluted with PBS and measured as discussed before. Similar procedures were followed to determine the percentage of released curcumin at desired time intervals, and fresh SIF was supplemented to maintain sink condition. The combined kinetic release profile of curcumin in SGF and SIF was plotted.

### 5.3.7 *In vitro* disintegration of BLG nanoparticles

The nanoparticle dispersion with curcumin loading of 10% was chosen for this study. Digestion in SGF was carried out following the same procedure as described in the previous section. Digestion in SIF was initiated by diluting the nanoparticle dispersion directly with SIF, without prior treatment with SGF. This was because the nanoparticles were either largely degraded (at pH 2.0) or intact (at pH 5.0), as indicated by the particle sizes, count rates and size distribution profiles observed at these two pH values. At desired time intervals, samples were drawn and measured for their particle sizes and count rates.

### 5.3.8 Statistics

All measurements were performed in triplicates. The results were expressed as means ± standard error. The data were subjected to analysis of variance followed by Tukey's test with an experimentwise confidence level of α=0.10 using SAS 9 software (SAS Institute Inc, Cary, NC).

## 5.4 Result and Discussion

### 5.4.1 Binding of curcumin to BLG nanoparticles as a function of acetone content
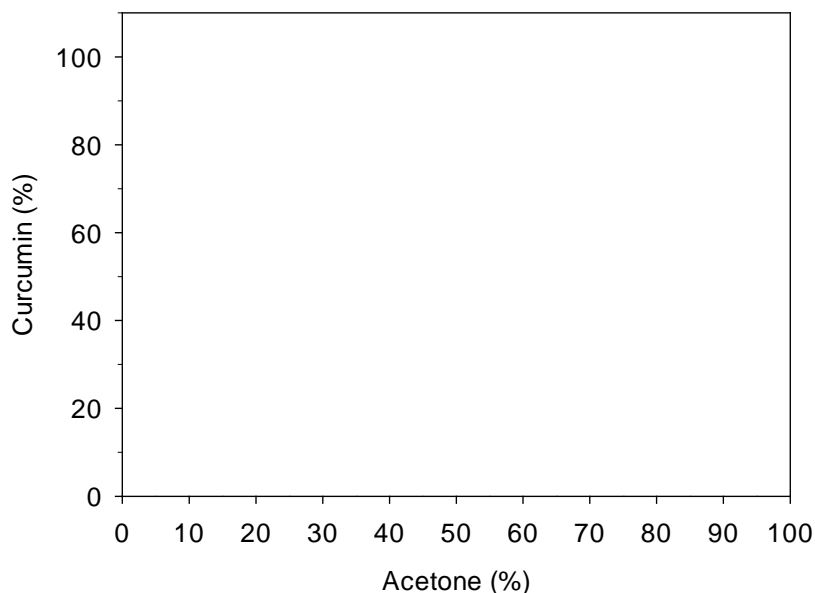


**Figure 5.2** Effect of acetone content on the distribution of curcumin in BLG nanoparticle dispersion crosslinked with 100% equivalent of glutaraldehyde.

In a water/acetone binary system containing BLG nanoparticles, curcumin molecules may exist in three forms: insoluble curcumin that was found in the precipitate, dissolved curcumin that permeated the dialysis membrane, and BLG-bound curcumin molecules. **Figure 5.2** shows the distribution of curcumin in the nanoparticle dispersion as a function of acetone content. The data were obtained after diluting the crosslinked dispersion (90% acetone) rapidly with appropriate water/acetone mixtures to achieve predetermined acetone contents. As can be seen, the percentage of free curcumin increased significantly at acetone

content higher than 30% (v/v, same hereinafter) acetone. Similar results were obtained from a relevant study on BLG monomers [157], which reported that the secondary structure and the capability of binding retinol was deprived in 30% or higher concentration of ethanol. The results from previous and current studies suggested weak interaction between curcumin and BLG nanoparticles. On the other hand, more than 80% curcumin molecules were detected in the precipitate in the presence of 10-20% acetone. This was probably because (1) curcumin as a hydrophobic compound exhibits low solubility in 10-20% acetone, and (2) most protein molecules were partly or fully folded, so that there were not sufficient hydrophobic sites that associated with curcumin [105]. It was noteworthy that previous studies on BLG monomers [157, 158] showed considerable binding to ligands (such as retinol) at low organic solvent concentrations (such as 10-20% ethanol). However, the native binding sites on BLG were limited, and the ligand/BLG ratio in our study was much higher than that of the previous study (equimolar, which was translated to a weight ratio of 1.4%). In addition, most of these binding sites lost their activity in the presence of organic solvents [159]. Therefore, the curcumin-BLG association involved in our study might have taken place majorly on the hydrophobic sites exposed by desolvation [105], rather than the native binding sites. As acetone content decreased rapidly from 90% to 20%, these sites were possibly buried inside the protein molecules. In addition, the solubility of curcumin was greatly reduced as acetone content decreased to 20%.

As a result, the originally dissolved curcumin molecules might not be able to establish strong association with BLG before extensive precipitation occurred.

In 30% acetone, a considerable percentage (71.5%) of curcumin molecules was found to associate with BLG. This phenomenon was possibly ascribed to two factors. Firstly, the high polarity of 30% acetone compared to 90% acetone drove more curcumin molecules to associate with other hydrophobic molecules, in order to minimize their contact with water. Secondly, a greater number of hydrophobic sites in BLG molecules were exposed in 30% acetone than in 20% acetone [105], which enabled the association and stabilization of more curcumin molecules. Such association might have been relatively strong, so that the majority of originally dissolved curcumin molecules were converted into the bound form without significant precipitation.

Based on dependence of curcumin distribution on acetone content, it can be inferred that the evaporation process during which the acetone content decreases continuously may be critical for the encapsulation of curcumin. We hypothesized that the LC of BLG nanoparticles might be improved by the lowering the acetone content from 90% to 30-50% after crosslinking and equilibrating the dispersion for a period of time to allow sufficient curcumin-BLG binding. Thereafter, the dispersion should be evaporated mildly, so that the acetone content could be

maintained slightly above 30% for maximal time before declining gradually to lower levels. This hypothesis will be tested in the next section.

### 5.4.2 Effect of acetone content and glutaraldehyde level on EE

**Figure 5.3** depicts the EE of curcumin-loaded BLG nanoparticles as a function of acetone content (before evaporation, same in this section) and glutaraldehyde level. In general, lower EE was observed as the curcumin content increased. In addition, regardless of the curcumin/BLG weight ratio and the glutaraldehyde concentration, a V-shape dependence of EE on acetone content was observed, with the highest EE achieved in the presence of 40-50% acetone. At 90% acetone, the LC was only 3.6% and 2.3% for the nanoparticles mixed with 10% and 15% curcumin, respectively. These values increased to 5.3% and 3.4% in the presence of 30% acetone, and they increased more significantly to 9.1% and 10.9% when the acetone content was adjusted to 50%. The low LC at 90% acetone could be ascribed to two factors. Firstly, as discussed in the previous section, the majority of curcumin molecules existed in the freely dissolved form in 90% acetone. Due to the high acetone concentration in the bulk dispersion, the evaporation might have proceeded rapidly, leading to a sudden decrease in the local acetone concentration on the surface of the dispersion. Such phenomenon resulted in a marked increase in local solvent polarity, which drove free curcumin molecules to precipitate rapidly without establishing a strong association with BLG nanoparticles. Secondly, higher acetone percentage suggested lower content of water and

consequently lower volume in the final dispersion. For instance, the final volume of a 6 mL water/acetone mixture was 3 or 0.6 mL if its initial acetone content was 50% or 90%, respectively. As a result, dispersion with 90% acetone content underwent more significant increase in the concentration of curcumin and BLG. This might have led to more extensive aggregation and precipitation as a result of intermolecular attraction.
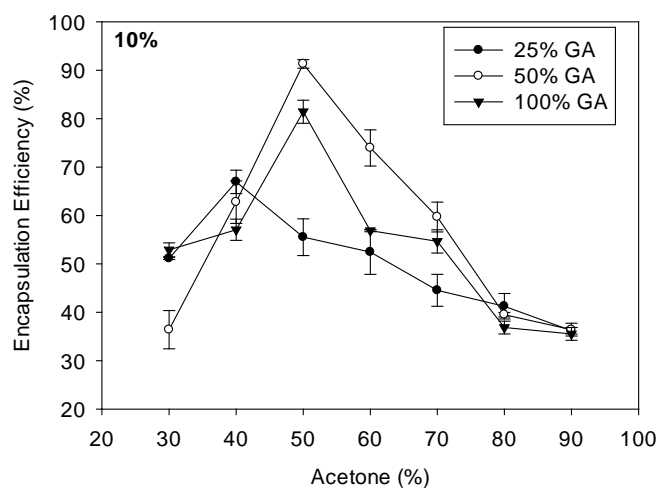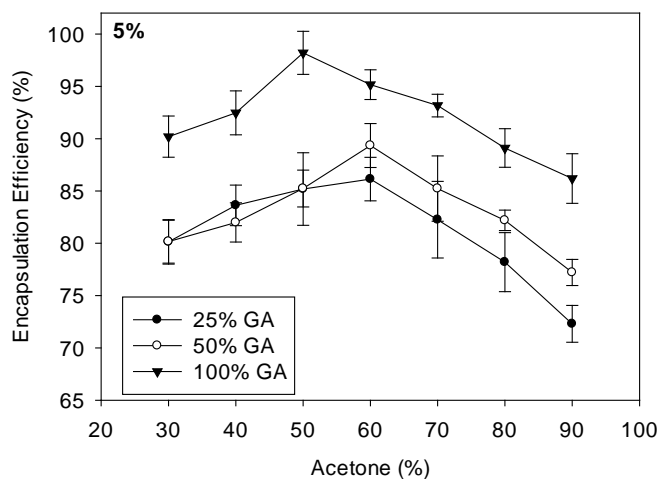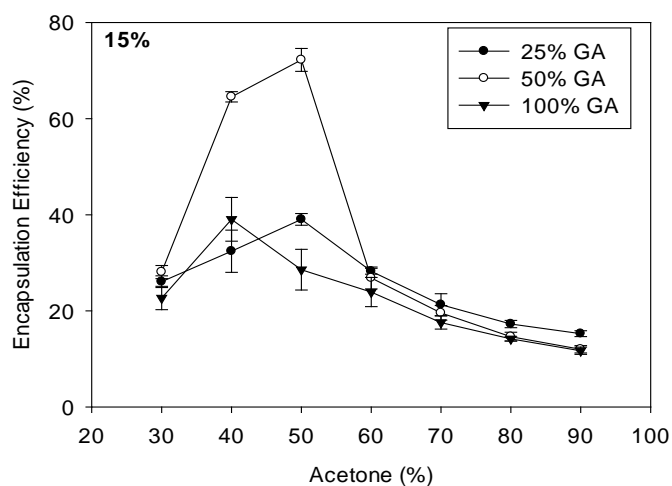
**Figure 5.3** Effect of acetone and glutaraldehyde content on the EE of BLG-curcumin nanoparticles at three curcumin-BLG mixing ratios: 5%, 10%, and 15%.

For the samples containing 30% acetone, the curcumin-BLG interaction was maximal as shown in the previous section. However, after evaporation began, the acetone content was lowered immediately to critical values (20% or below) that favored the precipitation of curcumin, and such condition was maintained virtually during the whole process of evaporation. As a result, the EE obtained from these samples were also not satisfactory, although they were generally higher than those achieved by samples with 80-90% acetone.

When the acetone content of the nanoparticle dispersion was adjusted to 50%, a relatively large number of curcumin molecules were bound to BLG nanoparticles, as was shown in **Figure 5.2**. During the slow evaporation process, the acetone content of the dispersion was maintained for a considerable period of time in an optimal range (30%-50%) where maximal curcumin-BLG association was observed. In addition, the mild evaporation led to a gradual increase in solvent

135

polarity, which served as a driving force for dissolved curcumin to associate with BLG nanoparticles [51, 105]. These factors resulted in minimal precipitation and maximum protein binding of curcumin, both of which contributed to higher EE.

Besides acetone content, the glutaraldehyde level also played a critical role in the EE of BLG nanoparticles (**Figure 5.3**). At 5% curcumin loading, the EE increased gradually as the glutaraldehyde level increased from 25% to 100% equivalent. Glutaraldehyde acts as a crosslinker that hardens the structure of nanoparticles via inter-molecular amide bonds [3]. Higher glutaraldehyde concentration was beneficial for maintaining the compact structure of curcumin-loaded BLG nanoparticles, thus preventing the release and precipitation of curcumin molecules [105]. As the content of curcumin increased to 10% and 15%, however, the highest EE was observed when 50% equivalent of glutaraldehyde was applied. In fact, flocculation occurred probably as a result of excessive crosslinking at glutaraldehyde level 100% and curcumin/BLG ratio of 15% of above, which resulting in low EE under these conditions (data not shown).

Based on these results, adjustment of acetone content was critical for achieving optimal LC and EE. In addition, lower glutaraldehyde dose could be applied to BLG nanoparticles with higher curcumin loading. This result further suggested that toxic crosslinkers such as glutaraldehyde could be partly replaced by natural phenolic compounds. Further studies need to be carried out to test this hypothesis.

### 5.4.3 Evidence on the crosslinking effect of curcumin

To confirm the role of curcumin as a partial crosslinking agent, we measured the particle sizes and count rates of a series of samples containing different amounts of curcumin as well as glutaraldehyde. The rationale of this experiment was that well crosslinked nanoparticles are able to maintain their shape and size. Therefore, the average size and count rate of their dispersion after the evaporation of acetone should be similar to those before evaporation [105, 133]. As shown in **Table 5.1**, the dispersions with higher glutaraldehyde levels (e.g. 100%) showed less significant change in the particle sizes after evaporation. In addition, the ratio of count rate after evaporation to that before evaporation was significantly higher for the samples with higher glutaraldehyde contents. These phenomena provided indirect evidence on the crosslinking effect of glutaraldehyde. On the other hand, at any given glutaraldehyde level, the dispersions with higher curcumin-to-BLG weight ratios exhibited less significant change in the particle size and count rate after evaporation. This was especially remarkable at 25% glutaraldehyde level, where the sample with 15% curcumin exhibited much higher retention in count rate (65%) compared to that without curcumin (21%). These results shed some light on the possible crosslinking effect of phenolic compounds such as curcumin.

**Table 5.1** Particle sizes and count rates of curcumin loaded BLG nanoparticles [*]

| GA% | CUR% | Before evaporation | | After evaporation | | |
|---|---|---|---|---|---|---|
| | | PS (nm) | CR (kcps) | PS' (nm) | CR' (kcps) | CR'/CR (%) |
| 25 | 0 | $61.3\pm2.5^b$ | $135.7\pm7.9^{cd}$ | $251.2\pm12.5^a$ | $28.3\pm3.9^f$ | $20.8\pm1.7^e$ |
| 25 | 5 | $62.4\pm1.7^b$ | $171.6\pm9.2^b$ | $262.9\pm10.4^a$ | $48.7\pm2.8^e$ | $28.4\pm1.2^e$ |

| | | | | | | |
|---|---|---|---|---|---|---|
| 25 | 15 | $64.2\pm3.4^{ab}$ | $164.3\pm10.1^{b}$ | $104.0\pm9.8^{d}$ | $106.9\pm2.7^{c}$ | $65.1\pm3.4^{c}$ |
| 50 | 0 | $77.5\pm3.1^{a}$ | $144.8\pm3.5^{cd}$ | $269.0\pm11.7^{a}$ | $73.5\pm4.5^{d}$ | $50.8\pm2.2^{d}$ |
| 50 | 5 | $66.5\pm2.6^{ab}$ | $133.4\pm4.7^{cd}$ | $271.5\pm15.6^{a}$ | $92.6\pm3.2^{c}$ | $69.4\pm2.5^{c}$ |
| 50 | 15 | $76.9\pm1.9^{a}$ | $214.4\pm7.2^{a}$ | $123.7\pm9.4^{d}$ | $153.1\pm7.1^{a}$ | $71.4\pm2.7^{c}$ |
| 75 | 0 | $74.3\pm4.6^{a}$ | $176.6\pm6.4^{b}$ | $226.3\pm3.6^{b}$ | $127.3\pm4.1^{b}$ | $72.1\pm3.1^{c}$ |
| 75 | 5 | $77.2\pm3.1^{a}$ | $126.0\pm5.8^{d}$ | $158.1\pm11.5^{c}$ | $100.2\pm3.2^{c}$ | $79.5\pm2.0^{bc}$ |
| 75 | 15 | $63.9\pm2.6^{ab}$ | $144.8\pm8.2^{c}$ | $119.1\pm2.4^{d}$ | $144.7\pm4.5^{a}$ | $100.0\pm1.2^{a}$ |
| 100 | 0 | $74.6\pm3.5^{a}$ | $133.8\pm9.1^{cd}$ | $104.6\pm7.4^{d}$ | $97.9\pm2.1^{c}$ | $73.5\pm0.3^{c}$ |
| 100 | 5 | $76.0\pm4.2^{a}$ | $154.5\pm4.4^{c}$ | $68.0\pm3.9^{e}$ | $150.7\pm6.8^{a}$ | $97.5\pm1.2^{a}$ |
| 100 | 15 | $70.1\pm1.9^{a}$ | $145.8\pm3.2^{cd}$ | $63.1\pm2.2^{e}$ | $122.0\pm2.4^{b}$ | $83.7\pm1.4^{b}$ |

* GA: glutaraldehyde dose (in % equivalent). CUR: curcumin/BLG weight ratio. PS: particle size. CR: count rate. Data with different letters showed significant difference (n=3, $P<0.05$).
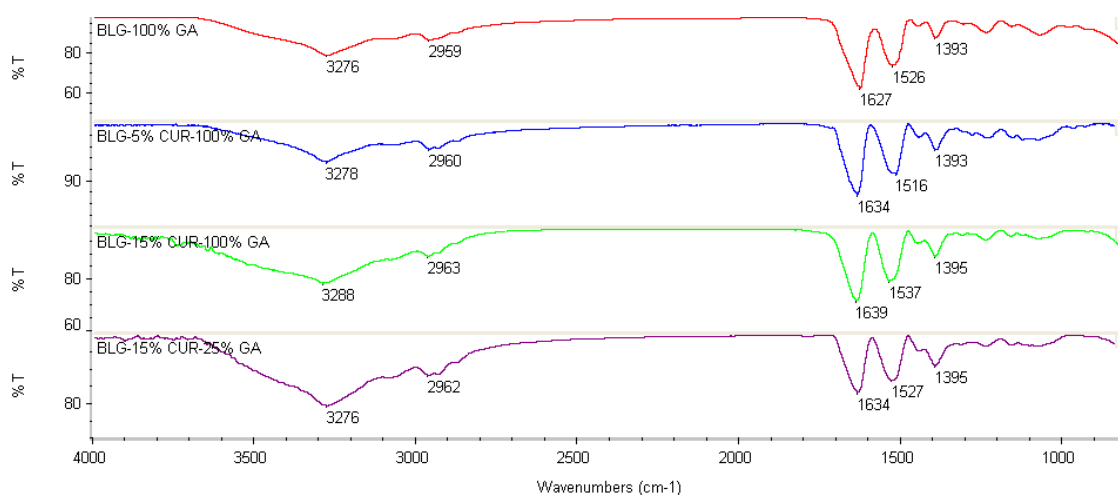


**Figure 5.4** FT-IR spectra of empty BLG nanoparticles and BLG/CUR nanoparticles with different CUR/BLG weight ratios and glutaraldehyde (GA) doses.

The interaction between phenols and proteins has been extensively studied in the past decades. Although the exact mechanism has not been fully established, it is generally recognized that hydrogen bonding, hydrophobic interaction, and π-π stacking were involved in the complexation between these two types of compounds [147, 160]. In this study, FT-IR was applied to investigate the possible mechanisms involved in the crosslinking role of curcumin. **Figure 5.4** showed the

FT-IR spectra of BLG nanoparticles containing different contents of curcumin and glutaraldehyde. The amide I (1627 cm$^{-1}$, C=O stretching) and amide II bands (1526 cm$^{-1}$, N-H bending and C-N stretching) in empty BLG nanoparticles shifted significantly in the presence of 5% or 15% curcumin, suggesting the possible involvement in the backbone carbonyl and/or amino groups in the BLG-curcumin interaction [105]. Furthermore, the wide band occurring at 3276 cm$^{-1}$ (O-H stretching) exhibited a marked increase in its intensity in the presence of curcumin. This phenomenon suggested the extensive involvement of hydrogen bonding in the curcumin-loaded nanoparticles [137]. Interestingly, at 15% curcumin/BLG ratio, the sample with 25% glutaraldehyde exhibited significantly higher absorbance at 3276 cm$^{-1}$ than that with 75% glutaraldehyde. This was confirmed by analyzing the relative percentage of areas of these two peaks (data not shown). This difference implied that more hydrogen bonds were formed between BLG and curcumin in order to stabilize the complex nanoparticles at low glutaraldehyde levels. Further studies need to be conducted to test this hypothesis.

### 5.4.4 Characterization of curcumin-loaded BLG nanoparticles
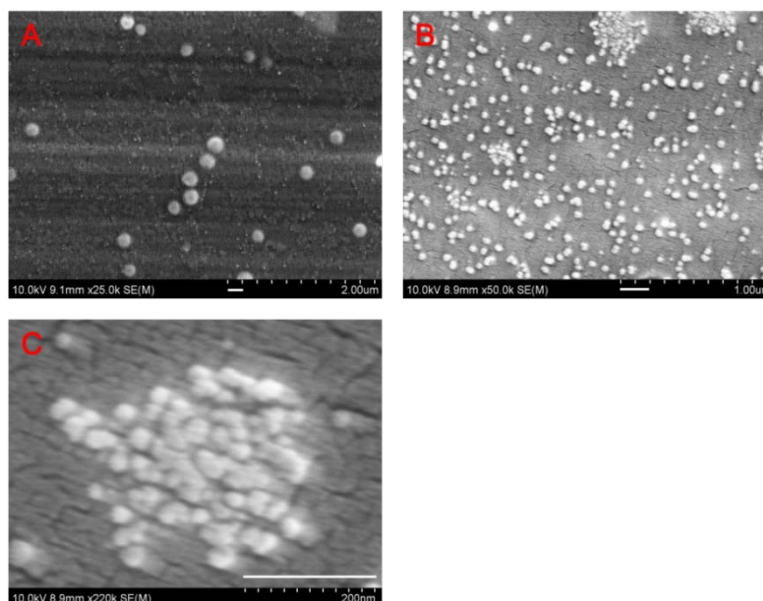
**Figure 5.5** SEM image of curcumin-loaded BLG nanoparticles.
All images were acquired from a same sample. Figure 5A shows the coexistence of larger and smaller particles. Figures 5B and 5C indicate that the larger particles might be the assembly of smaller ones. The white bars represent 200 nm.

**Table 5.2** summarizes the properties of curcumin-loaded BLG nanoparticles. For each curcumin loading ratio, the formula (shown in **Table 5.2**) yielding the highest EE was chosen for subsequent evaluation. The nanoparticles exhibited average size of 164-184 nm, with highly negative zeta potential. These properties were favorable for the dispersion stability of the formed particles. The polydispersity of the samples fell in the range of 0.100-0.250, indicating relatively narrow size distribution. The difference in the zeta potentials for BLG nanoparticles with 5% and 10% curcumin loading was statistically significant, and it was probably due to the consumption of the cationic amine groups in BLG molecules by different amount of glutaraldehyde [105]. The EE decreased with increasing curcumin/BLG ratio, but the LC kept increasing and reached 10.9% at

the curcumin/BLG ratio of 15%. This value was considerably higher than a number of protein-based nanoparticles and comparable to some synthetic polymeric encapsulation systems, which were summarized in the introduction.

**Table 5.2** Characteristics of curcumin-loaded BLG nanoparticles *

| CUR (%) | Acetone** (%) | GA (% eq.) | Particle size (nm) | Polydispersity (dimensionless) | ZP (mV) | EE % | LC % |
|---|---|---|---|---|---|---|---|
| 0 | 50 | 100 | 85.4±6.7[d] | 0.127±0.025[b] | -44.7±1.4[ab] | - | - |
| 5 | 50 | 100 | 164.4±8.5[c] | 0.187±0.034[ab] | -46.6±2.8[a] | 98.2±1.4[a] | 4.9±0.1[b] |
| 10 | 50 | 50 | 186.1±13.7[b] | 0.201±0.023[a] | -42.1±1.6[b] | 91.3±5.2[b] | 9.1±0.5[a] |
| 15 | 50 | 50 | 213.9±8.2[a] | 0.202±0.017[a] | -42.4±1.9[b] | 72.2±4.6[c] | 10.9±0.7[a] |

* CUR: curcumin/BLG weight ratio. GA: glutaraldehyde. ZP: zeta potential. Data with different letters showed significant difference (n=3, $P<0.05$).
** The percentages represented the acetone content before evaporation.

**Figure 5.5** shows the morphology of curcumin-loaded BLG nanoparticles observed under SEM. Since no significant difference was observed among the BLG nanoparticles with different curcumin/BLG weight ratios, only the images corresponding to 10% curcumin loading were presented. The particle appeared approximately spherical and exhibited smooth surface. Two major groups of particles were identified from the image: larger particles with an average size of around 200 nm (**Figure 5.5A**) and smaller ones showing diameters of 40~50 nm (**Figure 5.5B**). **Figure 5.5C** demonstrated that the former type of particles was possibly assembled from the latter ones. Such aggregates might have existed in the nanoparticle dispersion before drying, since their size was comparable to the average size obtained by DLS.

### 5.4.5  *In vitro* release of curcumin from BLG nanoparticles

**Figure 5.6A** shows the release of curcumin from BLG nanoparticles in PBS/Tween 20 system. The three formulas (one for each curcumin loading ratio) shown in the previous section were chosen for this study. It is noteworthy that curcumin degrades rapidly in PBS, but its stability could be greatly improved in the presence of non-ionic surfactants such as Tween 20 [161]. Regardless of the curcumin loading ratio, the releasing profile showed satisfactory fit with the first order kinetic model (**Table 5.3**). This result suggested that the release of curcumin was controlled by its dissociation from the porous polymer matrix [162]. The possible reasons why the release rate for nanoparticles with low curcumin loading was higher than that with high curcumin loading were: (1) the particles with higher curcumin loading exhibited greater sizes, and their specific surface area was hence lower, (2) the solubility of curcumin in the PBS/Tween 20 system is a constant in a given environment, and the dissolution of curcumin was slowed down as its concentration approached the equilibrium value, and (3) higher loading indicated higher concentration of curcumin accumulated in the outer buffer, which slowed down the diffusion of curcumin through the dialysis membrane. Further study needs to be conducted to validate these hypotheses.
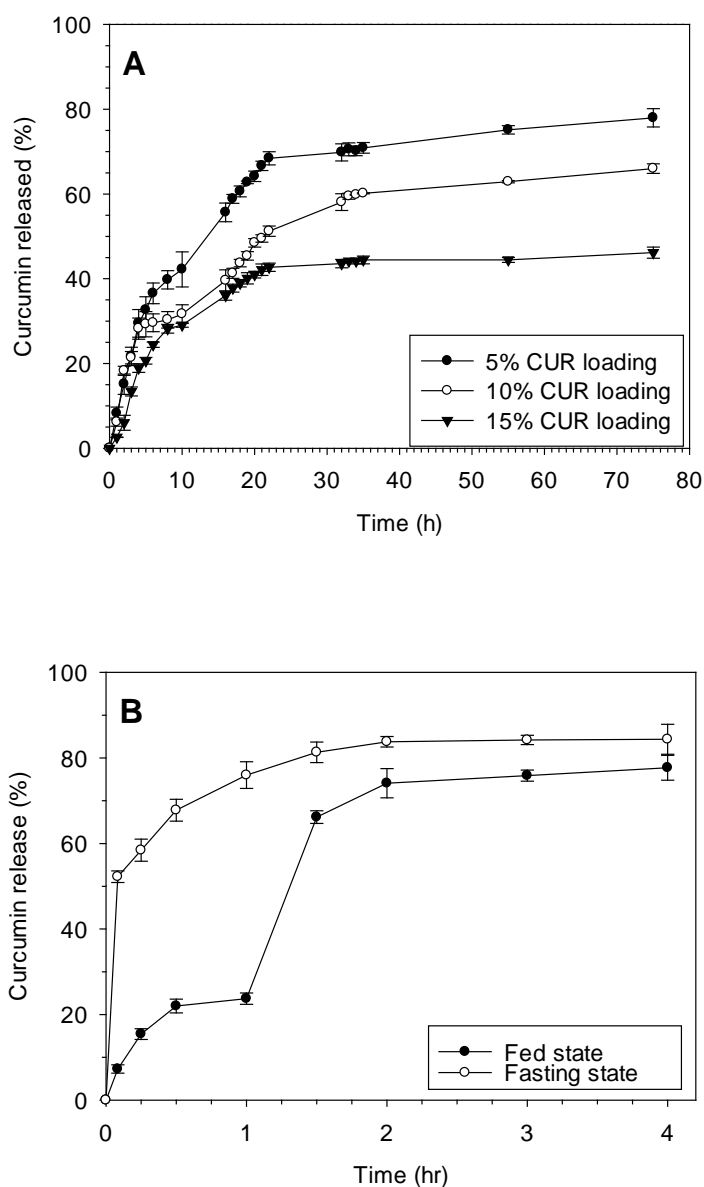
**Figure 5.6** Time-dependent release of curcumin from BLG nanoparticles in (A) PBS/Tween 20 and (B) simulated gastrointestinal environment

The release of curcumin in SGF and SIF was shown in **Figure 5.6B**. Our preliminary results indicated overlapping releasing patterns for nanoparticles with 5%, 10%, and 15% curcumin loadings (data not shown). Hence, only the releasing profile for nanoparticles with 10% curcumin loading is presented. The release in SGF was investigated at two different pHs: pH=2 that represents the gastric

143

condition in the fasting state and pH=5 that corresponds to the fed state [156]. After 1 h of digestion, the mixture was transferred to SIF to determine the release profile under simulated intestinal conditions. It was noteworthy that more than 70% of encapsulated curcumin was released in SGF at pH 2 (**Figure 5.6B**). This result is unexpected because BLG is known for its remarkable resistance against peptic digestion [155], and it was anticipated to prevent curcumin from being released in the stomach. We hypothesized from this result that the BLG nanoparticles were actually decomposed in SGF at pH 2, although the individual BLG molecules remained intact. This hypothesis will be tested and discussed in the next section.

**Table 5.3** Curve fitting of curcumin release profile from BLG nanoparticles

| CUR (%) * | $C_0$ (in percentage) | k | $R^2$ |
|---|---|---|---|
| 5 | 4.43 | 18.63 | 0.979 |
| 10 | 4.95 | 14.41 | 0.970 |
| 15 | 2.62 | 11.76 | 0.965 |

* CUR: curcumin/BLG weight ratio.

When dispersed in SGF at pH 5 (**Figure 5.6B**), the BLG nanoparticles exhibited significantly lower rate of release than at pH 2, with only 24% of encapsulated curcumin being released in 1 h. This phenomenon could be explained by two reasons. Firstly, pepsin tends to be much less active at pH 5 than at pH 2. Secondly, BLG exhibits an isoelectric point at around pH 5; therefore, the nanoparticles formed with BLG tended to form large agglomerates that were more resistant to peptic digestion. As a result, the curcumin molecules were more compactly encapsulated at pH 5 than at pH 2, leading to a lower release rate.

After being transferred to SIF (**Figure 5.6B**), the remaining curcumin molecules continued to be released from the nanoparticles. This was probably due to the degradation of residual BLG nanoparticles as well as the molecules, because of the known capability of trypsin to digest BLG [155]. The significant difference in the releasing pattern of dispersions previously treated at pH 2 and pH 5 was probably due to the different residual concentration of curcumin after the first digestion step. At the end of the two-step digestion, 70-80% of curcumin was recovered from the two buffers (SGF and SIF). Based on these results, BLG nanoparticles might not be suitable for the controlled release of curcumin in the fasting state, but they could release curcumin in a controlled and sustained manner if administrated during the fed state.

### 5.4.6 Disintegration of BLG nanoparticles in different buffers

We further investigated the disintegration of BLG nanoparticles in different buffers. The formula with 10% curcumin loading was chosen for this section. When incubated in SGF at pH 2 (**Figure 5.7A**), BLG nanoparticles exhibited a two-stage pattern of degradation. In the first 30 min, they showed a constant average size, while the count rate decreased continuously. These data suggested that, in spite of the decrease in number, there still existed a considerable number of BLG nanoparticles that maintained their size and probably morphology [105]. Thereafter, a rapid increase in the average size was observed, together with a slow decrease in the count rate. A possible explanation for this trend was that the

majority of smaller particles (around 160 nm) were decomposed by pepsin after 30 min, but some larger aggregates still remained intact. As a result, the average size shifted markedly to higher values, whereas the count rate declined only mildly, since larger particles contributed much more significantly to the count rate than did smaller ones [23, 105]. This was supported by the fact that the polydispersity index increased gradually from 0.177 (uniform distribution, **Figure 5.8A**) to 0.855 (broad distribution, **Figure 5.8B**), because of the increase in the relative content of larger particles. The data on size distribution obtained by DLS (**Figure 5.8**) also supported the disintegration of BLG nanoparticles.
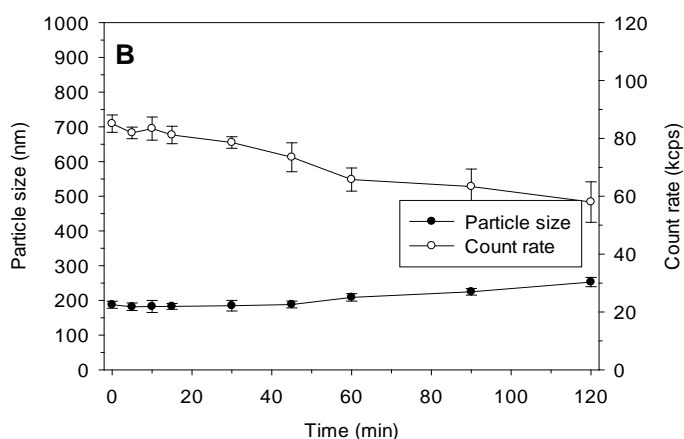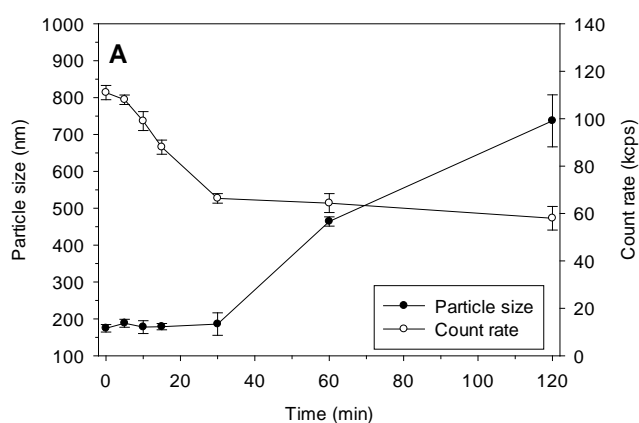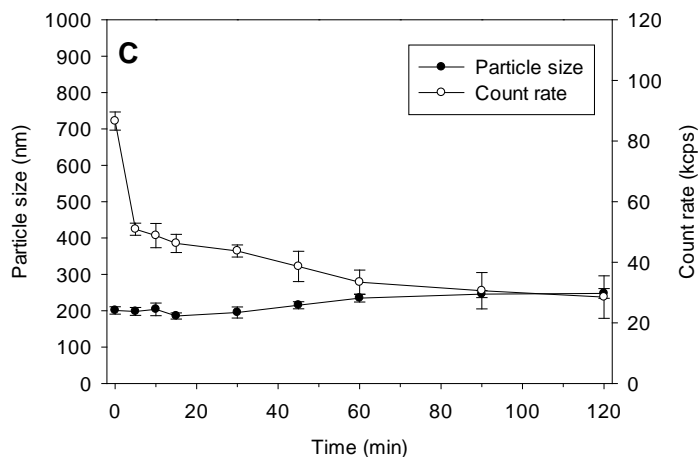
**Figure 5.7** Time-dependent disintegration of curcumin-loaded BLG nanoparticles in (A) SGF at pH 2, (B) SGF at pH 5, and (C) SIF

It was intriguing that BLG nanoparticles were susceptible to peptic digestion, considering that BLG itself is resistant against pepsin. A previous literature on BLG-EGCG nanoparticles [146] showed that BLG molecules remained intact after 120 min of peptic digestion (as evidenced by SDS-PAGE). Same results were obtained in our preliminary study. However, that study did not indicate whether BLG still maintained the morphology as spherical aggregates. Based on the findings from previous and current studies, we deduced that the intermolecular amide bonds produced by glutaraldehyde, instead of the original peptide bonds within BLG molecules, might be more prone to peptic digestion, and the breakage of these bonds might be responsible for particle disintegration. Our follow-up study (unpublished data) showed that nanoparticles prepared with cationized BLG (CBLG) exhibited remarkable resistance to pepsin, although this protein showed virtually the same resistance against pepsin as native BLG. Since CBLG contains abundant modified amine groups that could also be crosslinked by glutaraldehyde

147

[151, 163], it is likely that the different conformations of glutaraldehyde-induced amide bonds in native and cationized BLG resulted in the difference in particle digestibility. Another relevant study using turbidity also pointed out crosslinked BLG nanoparticles could be digested by pepsin, but the time needed for complete degradation was as long as 7 h [164]. The discrepancy between that and our study may be ascribed to the use of different enzyme activities and different measuring techniques (turbidity versus DLS measurement). However, that study was in consistence with the present one in that proteins with poor digestibility can assemble into digestible nanoparticles.
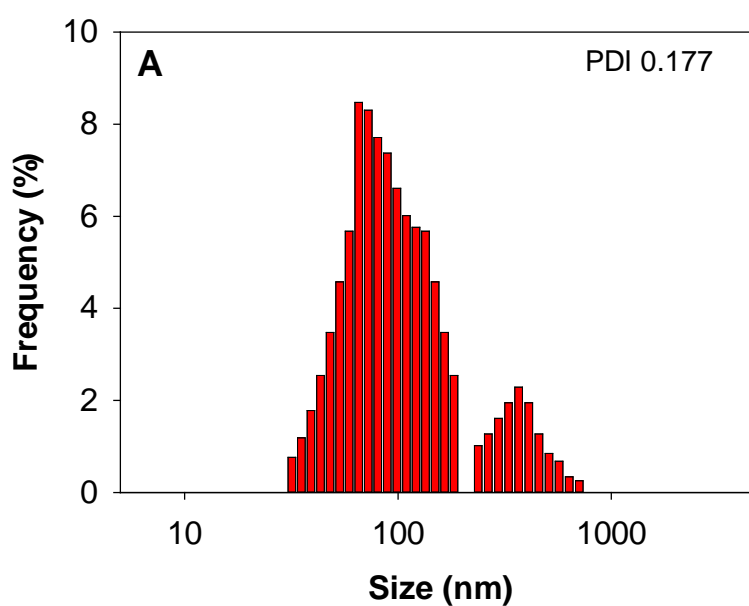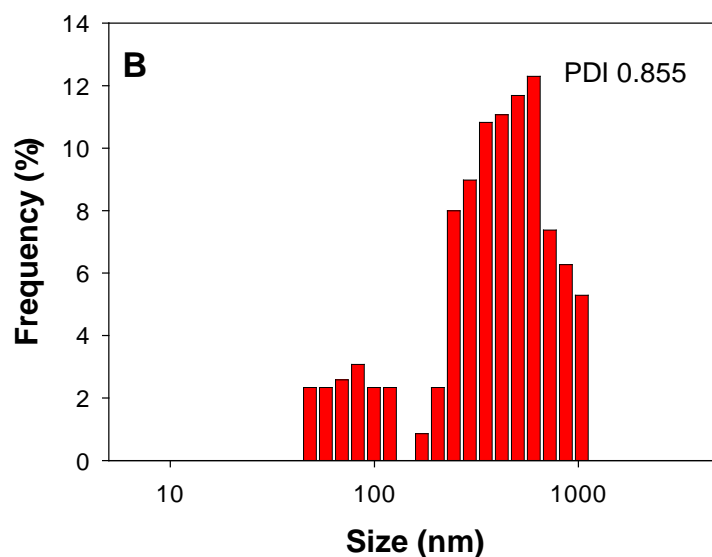
**Figure 5.8** Intensity based size distribution of CUR-BLG nanoparticle dispersions before (A) and after (B) digestion in SGF (pH = 2, containing pepsin)

On the contrary, the degradation of BLG nanoparticles proceeded at a much lower rate in SGF at pH 5 than at pH 2 (**Figure 5.7B**). During the experiment that lasted for 2 h, the average particle size did not show any significant change, while the count rate decreased by only 24%. The polydispersity maintained stable at 0.127-0.159 during the digestion (**Table 5.4**), which also suggested the stability of the nanoparticles. These results were in consistence with the slow release of curcumin as was indicated in the previous section. Lower activity of pepsin and the agglomeration of BLG at this pH were possible reasons for this difference, as was discussed before.

**Table 5.4** Progression of polydispersity index of curcumin-loaded BLG nanoparticles in SGF (pH 2 and 5) and SIF *

| Time (min) | PDI in SGF at pH 2 | PDI in SGF at pH 5 | PDI in SIF |
|---|---|---|---|
| 0 | $0.177\pm0.005^{e}$ | $0.127\pm0.004^{c}$ | $0.135\pm0.004^{b}$ |

| | | | |
|---|---|---|---|
| 15 | 0.189±0.004$^{e}$ | 0.145±0.002$^{a}$ | 0.149±0.003$^{b}$ |
| 30 | 0.204±0.002$^{d}$ | 0.129±0.003$^{c}$ | 0.158±0.005$^{a}$ |
| 45 | 0.211±0.007$^{cd}$ | 0.145±0.006$^{a}$ | 0.144±0.002$^{b}$ |
| 60 | 0.237±0.006$^{c}$ | 0.159±0.008$^{a}$ | 0.142±0.006$^{b}$ |
| 90 | 0.576±0.005$^{b}$ | 0.146±0.007$^{a}$ | 0.164±0.007$^{a}$ |
| 120 | 0.855±0.011$^{a}$ | 0.139±0.003$^{b}$ | 0.153±0.005$^{ab}$ |

* Data with different letters showed significant difference (n=3, $P<0.05$).

When the particles were incubated with SIF, the particles were more rapidly digested, as was indicated by the sharp decrease in the count rate (**Figure 5.7C**). As discussed before, trypsin shows higher capacity to digest BLG [155], which was probably the main reason for the rapid digestion of BLG nanoparticles. Interestingly, the average size was kept steady at around 200 nm, a trend that was different from the situation in SGF at pH 2.0. The polydispersity index varied from 0.135 to 0.164 without any significant difference (**Table 5.4**). This result suggested that trypsin could not only break down smaller nanoparticles, but also disintegrate larger aggregates. In the follow-up study that lasted for 4 h, very low count rate (less than 10 kcps) was detected (data not shown) in SIF, suggesting that BLG nanoparticles were nearly completely decomposed.

## 5.5 Conclusion

The encapsulation and releasing process of curcumin-loaded BLG nanoparticles were systematically investigated. The association between BLG nanoparticles and curcumin was affected significantly by the content of antisolvents such as acetone. Therefore, adjustment of acetone to moderate values (40-50%) followed by mild

evaporation led to a remarkable improvement in EE and LC. In addition, the optimal dose of glutaraldehyde decreased at higher curcumin loadings, which suggested that curcumin could replace part of toxic crosslinkers and aid the maintenance of particle structure. The nanoparticles formed through the optimized procedure showed average size between 164-214 nm, high zeta potential of -42 mV, and LC of at most 11%. Moreover, this study suggested that proteins that are resistant to peptic digestion could form nanoparticles that were digestible by pepsin at pH 2, probably because of the breakage of amide bonds formed with glutaraldehyde. As a result, no controlled release of curcumin was observed under simulated fast condition. However, satisfactory controlled release was achieved under simulated fed condition, i.e., digestion in SGF at pH 5 and then in SIF. The conclusions from this study may apply not only to the curcumin-BLG system, but also to a wide array of encapsulation systems consisting of a water-soluble protein encapsulant and a hydrophobic target compound. Therefore, this study provides insight into the assembly and disassembly of protein nanoparticles, and it may shed some light to the development of encapsulating systems with satisfying LC and reduced toxicity.

# Chapter 6 Cationic beta-lactoglobulin Nanoparticles as a Bioavailability Enhancer: Protein Characterization and Particle Formation

## 6.1 Abstract

Cationic beta-lactoglobulin (CBLG) was developed as a bioavailability enhancer for poorly absorbed bioactives. At most 11 anionic amino acid residues of beta-lactoglobulin (BLG) were substituted by ethylenediamine (EDA), resulting in a highly positive surface charge (zeta potential up to 39 mV at pH 7.0) and significantly increased surface hydrophobicity. These changes conferred CBLG with desirable water solubility and improved mucoadhesion by at most 252%, according to quartz crystal microbalance (QCM) study. Furthermore, CBLG inherited the unique resistance to gastric digestion from BLG, while the digestion under simulated intestinal condition was significantly improved. The latter was possibly due to the formation of aspartic acid-EDA conjugates, together with the randomization of protein conformation related with decreased percentage of β-sheet. Compared to BLG, CBLG formed smaller (75-94 nm), more uniform nanoparticles by acetone-desolvation method. These merits made CBLG a useful material that provides desirable solubility, controlled release and enhanced absorption to nutraceuticals or drugs.

## 6.2 Introduction

In the past few decades, nano-encapsulation has been recognized as an effective approach to enhanced bioavailability of poorly absorbed nutraceuticals and drugs [2]. For oral-administered compounds, successful absorption requires an appropriate encapsulant with a number of features. These include sufficient loading capacity, high dispersion stability [2], resistance to gastric digestion [6], satisfactory mucoadhesion [165], increased cellular uptake [133], and prolonged circulation time [14]. The last property could be obtained through the fabrication of nano-scaled vehicles [166], while the rest of them could be conferred to the encapsulants by carefully tuning their surface properties, among which charge and hydrophobicity play critical roles [61].

Cationic polymers, such as chitosan [10, 167], lactoferrin [21, 50] and polylysine [168], showed satisfactory mucoadhesive properties as well as cellular internalization efficacy. Such improvement was attributed to the enhanced electrostatic interaction with the anionic glycoproteins and glycolipids, which were abundant on the small intestinal wall or cell membrane [169, 170]. In addition, peptides that possess both positive net charge and a hydrophobic exterior (known as cell penetrating peptides or CPPs) were synthesized [18, 171, 172]. The conjugation of CPPs to drug-loaded nanoribbions [17], nanoparticles [173] or nanocomplexes [174] resulted in elevated cellular uptake. In spite of the abovementioned merits, there exist several drawbacks in these cationic

encapsulants that impeded the effective delivery of orally ingested bioactives. For example, chitosan-based nanoparticles were insoluble at neutral to basic pH, which might compromise their claimed mucoadhesion and cellular uptake enhancement *in vivo*. Such insolubility may also confine their application to acidic food systems. Cationic peptide- or protein-based delivery systems are soluble in water, but their susceptibility to peptic digestion in stomach may result in the loss of protection before absorption occurs [175]. These disadvantages necessitate the development of a water soluble, pepsin-resistant, cationic delivery system.

Beta-lactoglobulin (BLG), a 162-residue globular protein, makes up approximately 60% of bovine whey protein [176]. Owing to its high water solubility and unique structure, BLG serves as a natural carrier for various nutrients, such as vitamins and fatty acids [47, 177]. Furthermore, BLG demonstrated a significant resistance to peptic digestion [178] due to its compactly folded conformation originated from the abundance of rigid β-sheet structures [179], while it was much more readily degraded by trypsin in small intestine. These characters provide BLG-based delivery systems with desirable controlled release property. By far, various encapsulating systems have been developed with BLG, including emulsions [180, 181], nanoparticles [44, 46] and nanocomplexes [182]. These techniques demonstrated satisfactory protection to the entrapped compounds.

154

In this chapter, we are proposing a nanoparticle system prepared with cationic beta-lactoglobulin (CBLG). We hypothesized that CBLG and CBLG-based delivery systems could inherit the merits of both conventional cationic polymer and BLG, leading to a significant improvement in the encapsulation and absorption of bioactive compounds. It should be mentioned that a series of CBLGs were synthesized by Mattarella et al. [183] by amidation and esterification methods. However, their study was focused on functionality instead of encapsulation properties, and CBLGs prepared in that study might not be ideal for encapsulation due to their reduced solubility and increased digestibility [183]. To our knowledge, no study has been published by far on CBLG nanoparticles with the emphasis on encapsulation and delivery properties.

This paper was the first part of our study on CBLG nanoparticles. Ethylenediamine (EDA) was employed to synthesize CBLGs with sufficient positive charge and increased hydrophobicity, without compromising its original water solubility. The CBLGs were investigated for their physicochemical and conformational characteristics, which were then employed to explain for their digestion-resistive and mucoadhesive properties. Finally, CBLG nanoparticles were prepared using a desolvation method, and its particle forming behavior was compared in parallel with BLG.

## 6.3    Materials and Methods

### 6.3.1    Materials

The following chemicals were purchased from Sigma-Aldrich (St. Louis, MO, USA): N-(3-dimethylaminopropyl)-N-ethylcarbodiimide (EDC, 97% purity), bovine beta-lactoglobulin (BLG, 90% purity), ethylenediamine dihydrochloride (EDA, 98% purity), 2, 4, 6-trinitrobenzenesulfonic acid (TNBS, 0.5 mg/mL water solution), 8-anilino-1-naphthalenesulfonic acid (ANS, 97% purity), pepsin (3,200-4,500 units/mg), trypsin (10,000 BAEE units/mg), papain (10 units/mg), trichloroacetic acid (TCA) and bovine serum albumin (BSA, 98% purity). Porcine stomach mucin (PSM, type III, contains 0.5-1.5% sialic acid) was obtained from Himedia Co., India. Hanks' balanced salt solution (HBSS, pH 7.4) and phosphate buffer saline (PBS, 100 mM, pH 7.4) were purchased from Invitrogen Inc. (Carlsbad, CA, USA). All other reagents (sodium bicarbonate, acetone, acids and bases, etc.) were of analytical grade.

### 6.3.2    Preparation of cationic beta-lactoglobulin (CBLG)

CBLG was prepared by grafting positively charged EDA moieties to the negatively charged carboxyl groups on the aspartic and glutamic acid residues (**Figure 6.1**). This was achieved via a carbodiimide-aided approach that was previously reported [184]. In brief, 400 mg of BLG was dissolved in 5 mL deionized water, to which 50 mL of EDA solution at different concentrations (0.6, 0.9, 1.2 and 1.5 mol/L) was added under mild stirring. The mixture was adjusted

to pH 4.75 with 1 mol/L HCl and equilibrated for 30 min. Cationization was initiated by the addition of 150 mg EDC and terminated by 540 μL acetate buffer (4 mol/L, pH 4.75) after 2 h. The dispersion was dialyzed against deionized water at 4 °C for 48 h and freeze dried. The moisture content of the final product was less than 5%, and the protein content was at least 90% according to Bradford assay calibrated with BSA.

### 6.3.3   Determination of primary amino group contents and net charge

The contents of primary amino groups were determined by TNBS assay [185]. BLG and CBLG were dissolved in 0.1 mol/L $NaHCO_3$ buffer (pH 8.5) at a concentration of 100 μg/mL, and 0.5 mL of 0.2 mg/mL TNBS solution was added to 1 mL of each sample. After incubation at 37 °C for 2 h, the dispersion was mixed with 0.5 mL 10% sodium dodecyl sulfate (SDS) solution and 0.25 mL of 1 mol/L HCl to terminate the reaction. The resultant mixture was cooled to room temperature and measured for its absorbance at 420 nm using a DU-730 UV/VIS spectrophotometer (Beckman Coulter Inc., Fullerton, CA, USA). A calibration curve ($R^2$=0.9997) was established following a similar procedure, except that a series of concentrations of BSA (59 primary amino groups per molecule from its lysine residues) was employed instead of BLG/CBLG. The number of primary amino groups content was derived from the curve and then adopted to estimate the net charge of CBLG, considering that the introduction of each amino group altered

the net charge of BLG by +2 (**Figure 6.1**). The change in molecular weight upon

cationization was assumed negligible.
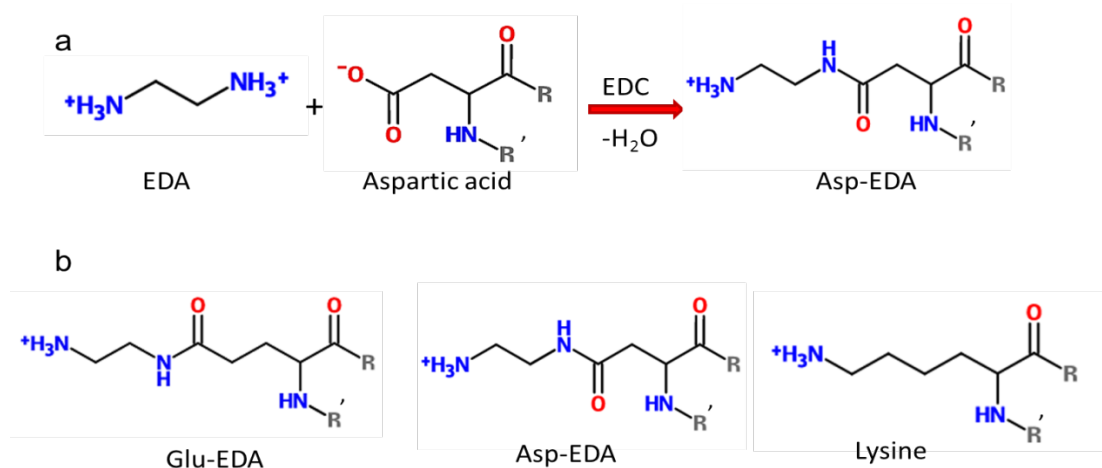


**Figure 6.1** Illustration of the cationization procedure.
Figure 6.1a presented the theoretical equation for EDA-induced cationization. Both Asp
and Glu residiues were appropriate substrates. The net charge of each residue was altered
by +2 (from -1 to +1) upon cationization. R and R' were adjacent peptide chains. Figure
6.1b compared the EDA-Asp/EDA-Glu conjugate with lysine to display their geometric
similarity.

## 6.3.4  Determination of zeta potential

The dispersion of BLG or CBLG in PBS (10 mmol/L, pH 7.0, same hereinafter)

and HBSS (140 mmol/L, no calcium or magnesium, pH 7.4, same hereinafter) was

measured for its electrophoretic mobility by laser Doppler velocimetry using a

Nano ZS90 Zetasizer (Malvern Inc., Malvern, UK). Each sample (1 mg/mL) was

measured for three times, and at least twelve runs were performed per

measurement. The data were then converted to zeta potentials using the

Smoluchowski model.

### 6.3.5 Determination of surface hydrophobicity

ANS fluorescence assay was carried out to determine the surface hydrophobicity of BLG and CBLG dispersions [186] in two buffers, i.e., PBS and HBSS. Stock solutions of proteins (BLG or CBLG, both at 1 mg/mL) and ANS (100 μg/mL) were prepared in a same buffer and filtered through a 0.22 μm Acrodisc® syringe filter membrane (Pall Co., Newquay, UK). The filtrates were mixed and diluted to achieve a fixed ANS concentration of 50 μg/mL and a protein concentration ranging from 5 to 50 μg/mL. After 1 h of incubation at 25 °C, the mixture was observed for its fluorescence intensity (FI) on a PerkinElmer Victor X3 multilabel plate reader (PerkinElmer Inc., Waltham, MA, USA). The excitation and emission wavelengths were 355 and 460 nm, respectively. For each protein sample, a linear regression equation was established for FI versus protein concentration ($R^2 > 0.995$), and the slope ($S_o$) was used as an index for surface hydrophobicity.

### 6.3.6 Secondary structure determination

Fourier-transform infrared (FT-IR) study was conducted to monitor the structural change of BLG upon cationization. The lyophilized samples (3 to 5 mg) were mounted onto a Jasco FT/IR 4100 spectrometer (Jasco Inc., Easton, MD, USA). The infrared transmittance was acquired at the wavenumbers from 1000 to 4000 $cm^{-1}$ at a resolution of 2 $cm^{-1}$. At least 100 repeated scans were undertaken for each sample. The spectra were averaged, smoothed, corrected for their baselines and converted to absorbance with the Spectra Manager software (Jasco Inc., Easton, MD, USA).

For quantitative study, the IR spectra were subjected to Fourier self-deconvolution (FSD) using the OMNIC software (Thermo Scientific, West Palm Beach, FL, USA). A band width at half-height of 23 cm$^{-1}$ and an enhance factor (K value) of 2.7 was adopted over the wavenumbers ranging from 2000 to 1300 cm$^{-1}$, according to previous literatures [179, 187]. The FSD spectra were then curve fitted assuming a Gaussian band profile. The resolved peaks were validated only when they were also found on the inverted secondary derivative (ISD) spectra obtained over the same wavenumber range [179]. Peak assignment was carried out following literatures on native BLG [179, 187], and the content of each secondary structure was expressed as its percentage of peak area in the FSD spectra.

### 6.3.7   Determination of *in vitro* digestibility

Two enzymes, pepsin and trypsin, were employed to investigate the degradation of BLG and CBLG. For peptic digestion [178], the samples and pepsin were dissolved separately at 1 mg/mL in 0.1 mol/L HCl, which was adjusted to pH 2.0 with 0.1 mol/L NaOH. For tryptic digestion, both the samples and trypsin were dispersed separately at the same concentrations in a NaHCO$_3$ buffer (0.1 mol/L, pH 8.0, same hereinafter). The dispersions were then preheated at 37 $^{\circ}$C for 15 min. To 15 mL of protein solution, 75 μL of the enzyme solution was added, thus achieving a substrate-to-enzyme ratio of 200:1 (w/w). The resultant suspensions were incubated at 37 $^{\circ}$C for preset times (10 min to 4 h), after which aliquots of 1.5 mL were drawn from the dispersions and mixed with 1.5 mL TCA solution (10%

in water, w/v). The mixtures were allowed to stand at room temperature for 15 min and then centrifuged (9,000 $g$, 20 ℃, 20 min). The precipitate was discarded, and the absorbance of the supernatant at 280 nm was recorded. For comparison purpose, a series of mixtures were prepared with BLG/CBLG and papain at a substrate-to-enzyme ratio of 20:1 (w/w) in NaHCO₃ buffer. After 4 h of incubation at 37 ℃, the hydrolysates were subjected to TCA precipitation, centrifugation and spectrophotometric measurement as mentioned above. According to previous literature [155], almost 100% of the BLG was degraded by papain within 2 h. Therefore, the absorbance at 280 nm of the supernatant after papain digestion was indicative for complete proteolysis, and the data obtained from all other treatments were divided by this value to provide an apparent digestibility.

### 6.3.8    Determination of mucoadhesive properties

**Turbidity analysis** [10]. Samples (BLG or CBLG) and mucin (PSM) were dispersed at 10 and 1 mg/mL in PBS, respectively, and they were both passed through a 1.2 μm Acrodisc® syringe filter. Thereafter, 4 mL of PSM dispersion was mixed with 0.1, 0.2 and 0.4 mL protein solution in order to achieve a protein concentration of 0.25, 0.5 and 1 mg/mL, respectively. The mixture was then incubated at 37 ℃ for 1 h and cooled to room temperature. The absorbance of 400 nm was recorded, using pure PSM dispersion as blank.

**Quartz crystal microbalance (QCM) analysis** [11]. In the QCM study, two thin layers of PSM and protein were deposited sequentially onto a gold-coated AT-cut

quartz crystal with a fundamental frequency of 4.95 MHz (QSX-301, Q-Sense Co., Linthicum, MD, USA), and the mass of deposited polymers was reflected by the change in frequency ($\Delta f$). Prior to the deposition, the crystal was soaked in Piranha solution ($NH_3 \cdot H_2O$: $H_2O_2$: $H_2O$=1:1:5, v/v/v) for 15 min at 70 $^{\circ}$C and dried with nitrogen. The crystal was then mounted on the Q-Sense E1 microbalance (Q-Sense Co., Linthicum, MD, USA), after which PBS was injected at a flow rate of 0.224 mL/min using a peristaltic pump (Ismatec Reglo, Glattbrugg, Switzerland). After the acquisition of a constant $\Delta f$, PSM solution (400 $\mu$g/mL in PBS, filtered through a 220 nm membrane) was introduced to the crystal chamber. This triggered a significant increase in $\Delta f$, which reached another plateau after approximately 10 min. A second rinse of PBS was applied to remove loosely bound PSM, after which the BLG/CBLG solution (1 mg/mL in PBS, passed through a 220 nm membrane) was injected to the chamber at a same flow rate. After 15 min of protein adsorption, the chamber was subjected to a final rinse of PBS, until the attainment of the third plateau of $\Delta f$. Changes in $\Delta f$, up to the 13th overtone, were collected by QTools 3 (Q-Sense Co., Linthicum, MD, USA). The fifth overtone was converted to deposited mass (in ng/cm$^2$ crystal surface) using the Sauerbrey model. Mucoadhesion was expressed as the mass ratio of BLG/CBLG to PSM deposited on the crystal surface.

### 6.3.9　Preparation of BLG/CBLG nanoparticles

Nanoparticles were prepared with BLG/CBLG via a desolvation process [44, 105]. Constant stirring (600 rpm) was applied throughout the mixing and crosslinking process. The protein was dissolved in deionized water at a preset concentration of 10 to 20 mg/mL (pH 7.5-8.0), and the dispersion was equilibrated for 1 h at room temperature. Thereafter, pure acetone was added dropwise to achieve an acetone/water ratio of 80/20 or 90/10 (v/v). The contents of protein and acetone were adjusted, so that the final protein concentration in the binary solvent was kept at 2 mg/mL. After 30 min of equilibration, glutaraldehyde was added as a crosslinker. The glutaraldehyde/protein mass ratio was set at 40 μg/mg in this study based on the lysine content of BLG (16 mol/mol), and it was adopted for all protein samples regardless of the extent of cationization. After 6 h of crosslinking, the acetone was evaporated under a constant nitrogen flow and replaced with same volume of deionized water. The resultant suspension containing the protein nanoparticles was stored at 4 °C for subsequent assays.

### 6.3.10　Determination of particle size and count rate

The particle size and count rate were determined [133] by dynamic laser scattering (DLS) using a BI-200 SM Goniometer Version 2 (Brookhaven Instrument Corp., Holtsville, New York, USA) equipped with a 35 mW He-Ne laser beam. All dispersions were measured without dilution. The following parameters were adopted: laser power of 10 mW, detection wavelength of 637 nm, scattering angle of 90°, temperature of 25 °C, and measurement time of 1 min. The refractive

indices and viscosities of different acetone/water systems were applied for all assays, since they were not significantly altered by protein or glutaraldehyde in our study (data not shown). Two separate measurements were carried out to obtain accurate results. For count rate determination, the aperture pinhole size was fixed at 400 μm; to measure the particle size, appropriate aperture pinhole sizes were chosen to achieve a count rate of 100-300 kcps. The obtained data were analyzed using cumulant algorithm, and the quadratic mean particle size was reported.

### 6.3.11 Scanning electron microscopy (SEM)

The morphology of BLG/CBLG nanoparticles was observed using a Hitachi SU-70 SEM (Hitachi, Pleasanton, CA, USA). Approximately forty microliters of the nanoparticle dispersions was dripped and cast-dried on an aluminum pan, which was cut into appropriate sizes and adhered to a 1-inch specimen stub with conductive carbon tapes (Electron Microscopy Sciences, Ft. Washington, PA, USA). To avoid the charging effect, a thin layer (<20 nm) of gold and platinum was deposited to the samples using a sputter coater (Hummer XP, Anatech, CA, USA) prior to the observation. Representative images were reported.

### 6.3.12 Statistics

All measurements were performed in triplicates. The results were expressed as means $\pm$ standard error. The data were subjected to analysis of variance ($P < 0.05$) followed by Tukey's test with an experimentwise confidence level of $\alpha=0.10$, using SAS 9 software (SAS Institute Inc., Cary, NC, USA).

## 6.4    Results and Discussion

### 6.4.1    Change in protein net charge upon cationization

The numbers of amino and carboxyl groups of BLG and CBLG were compared in

**Table 6.1**. The numbers in the sample names (0.6, 0.9, 1.2 and 1.5) indicated the

molarity of EDA applied in the cationization process. A native BLG molecule

possesses 16 lysine (TNBS-reactive), 3 arginine, 10 aspartic acid, and 16 glutamic

acid residues [188], all of which results in an overall charge of -7 per molecule.

Our TNBS assay showed 16.3 reactive primary amino groups on BLG, which was

in consistence with the theoretical value.

Table 6.1 Amino group content and net charge of BLG and CBLG*

| Sample name | EDA mol/L | TBNS reactive –NH₂ per molecule** | Total –NH₂ per molecule** | Total –COOH per molecule** | Net charge per molecule |
|---|---|---|---|---|---|
| BLG | 0 | $16.3\pm0.2^{d}$ | 19.3 | 25.7 | -7 |
| C-0.6M | 0.6 | $21.4\pm0.4^{c}$ | 24.4 | 20.6 | +3 |
| C-0.9M | 0.9 | $24.4\pm0.3^{b}$ | 27.4 | 17.6 | +9 |
| C-1.2M | 1.2 | $26.6\pm0.2^{a}$ | 31.6 | 13.4 | +17 |
| C-1.5M | 1.5 | $27.3\pm0.5^{a}$ | 31.3 | 13.7 | +17 |

*    Data with different letters showed significant difference (n=3, $P<0.05$).

** Reactive amino groups included the ones in the lysine residues and those introduced by cationization. Total amino groups were reactive amino groups plus the ones in the arginine residues. Total carboxyl groups represented the ones in the aspartic acid and glutamic acid residue. This number was deducted by one upon the addition of each amino group. The net charge (rounded up) was calculated by summing up the electric charges of all residues on BLG or CBLG.

When increasing amount of EDA was added during the cationization process, the

number of primary amino groups increased progressively to a maximum of 27.3

per molecule. Meanwhile, the deduced number of total carboxyl groups was

decreased from 25.7 to 13.7. These changes gave rise to a dramatic change in the net charge to +17 for C-1.2M and C-1.5M. The relatively high density of positive charges possessed by CBLG may benefit their mucoadhesive properties greatly as well as the cellular uptake, thus promoting the bioavailability of the bound nutraceuticals or drugs. It should be pointed out that cationic polymers may exhibit considerable cytotoxicity [189, 190]. However, the toxicity of cationic protein was found to be the lowest amongst all cationic polymers [191], probably owing to the biocompatibility of the original protein. The cytotoxicity of CBLG will be investigated in our next study.

### 6.4.2   Surface charge and hydrophobicity

The impact of cationization on the surface charge and hydrophobicity of BLG was summarized in **Table 6.2**. The zeta potential of BLG in PBS was -37.0 mV, which was comparable with previously reported results [192]. As the degree of cationization increases, the zeta potential shifted significantly toward a more positive value. This phenomenon confirmed the shift in molecular net charges, and it was indicative for adequate exposure of the conjugated EDA moieties on the surface of the molecule. It was noteworthy that the zeta potentials of C-1.2M (36.8 mV) and C-1.5M (38.9 mV) were comparable in magnitude to that of native BLG (-37.0 mV). According to the American Society for Testing and Materials [5], a zeta potential with an absolute value of higher than 30 mV were indicative for "moderate to good" stability of colloidal systems, due to the strong electrostatic

166

repulsion between the charged molecules or particles. The dispersion stability of CBLG was confirmed by our preliminary study (data not shown), in which CBLG was soluble in pure water or PBS at concentrations higher than 80 mg/mL.

Table 6.2 Zeta potential and surface hydrophobicity of BLG and CBLG *

| Sample | In PBS Zeta potential (mV) | Hydrophobicity (dimensionless) | In HBSS Zeta potential (mV) | Hydrophobicity (dimensionless) |
|---|---|---|---|---|
| BLG | -37.0±0.1[e] | 108.5±9.6[e] | -18.3±0.2[d] | 68.0±7.2[e] |
| C-0.6M | 18.1±0.3[d] | 740.1±10.2[d] | 6.7±0.1[c] | 305.8±11.4[d] |
| C-0.9M | 27.2±0.5[c] | 850.2±11.4[c] | 11.4±0.2[b] | 421.5±15.4[c] |
| C-1.2M | 36.8±0.4[b] | 1022.3±17.6[b] | 16.1±0.3[ab] | 571.0±14.2[b] |
| C-1.5M | 38.9±0.4[a] | 1269.8±15.4[a] | 17.5±0.3[a] | 628.9±16.3[a] |

* Data with different letters showed significant difference (n=3, $P<0.05$).

BLG was reported to exhibit a relatively low surface hydrophobicity ($S_o$) in PBS of approximately 100 [192]. This result was also confirmed by our study. The $S_o$ of CBLG, on the other hand, was at most 1070% higher than that of BLG. In addition, the highest $S_o$ achieved by CBLG (1270) was comparable with that of BSA (1000-2000) [193], a protein known for its high surface hydrophobicity. The remarkable increase in $S_o$ by cationization was also observed on cationic BLG prepared by esterification and amidation [183], and it was probably attributed to the following three reasons. Firstly, the introduction and exposure of the hydrophobic backbones of EDA played a major role in increased protein-ANS hydrophobic binding, which yielded a higher $S_o$ [183]. The positive charge on EDA, on the other hand, did not contribute to the hydrophilicity or hydrophobicity of BLG, because it did not alter the magnitude of net charge on the Asp or Glu

167

residue (-1 for unmodified Asp or Glu residues; +1 for the cationized ones). Secondly, CBLG might have formed a certain amount of electrostatic complexes with the anionic ANS, which exhibited minor fluorescence [194]. Thirdly, the randomization of BLG chain might have increased the quantum yield of ANS and led to an elevated apparent $S_o$ [195]. This will be demonstrated in the next section. In addition to these three factors, enhanced protein aggregation upon cationization was also taken into consideration. However, no significant difference in turbidity was observed between BLG and CBLG solutions (data not shown). Therefore, this phenomenon was excluded from the possible reasons.

HBSS was selected as a second buffer for evaluating zeta potential and $S_o$, because of its resemblance to intracellular fluids. This buffer exhibited a similar pH (7.4) with the PBS used in our study (7.0), but it contained thirteen-fold higher concentration of salt. As shown in **Table 6.2**, both BLG and CBLG exhibited decreased zeta potential (in terms of their magnitude) and $S_o$, which was consistent with previous studies [183, 196]. The reduced zeta potential was possibly attributed to the charge screening effect caused by increased ionic strength. Such change may result in weakened intra- and inter-molecule electrostatic repulsions and, therefore, the adoption of more compact conformations by BLG/CBLG. Consequently, the exposure of the grafted hydrophobic EDA moieties might have been diminished in the presence of HBSS, and the surface hydrophobicity was hence decreased. In addition, the partial electrostatic complexation between

168

protein and ANS might also have been compromised by charge screening, leading to a decrease in fluorescence intensity. In spite of these observations, the improvements in zeta potential and $S_o$ by cationization were as remarkable in HBSS as were in PBS. These results suggested that CBLG might adhere to cell membrane more effectively through both electrostatic and hydrophobic interaction, thus enhancing the cellular uptake of the bound compounds of interest.

### 6.4.3 Secondary structure

The conformation of protein is a key factor that governs its physicochemical and functional properties. Conformational changes of protein have a significant influence on the hydrogen bonding intensity at the proximity of peptide bonds, altering their stretching patterns and consequentially changing the IR absorbance of the corresponding peaks, among which amide I (C=O stretching) exhibited the highest sensitivity [197]. As can be seen in **Figure 6.2A**, three characteristic peaks of native BLG were observed at 1631 (amide I, C=O stretching), 1521 (amide II, C-N stretching and N-H bending), and 1450 (amide III, CN stretching, NH bending) cm$^{-1}$. These observations were in consistence with previous literature [179], indicating the predominance of β-sheet of BLG. After cationization, there was a significant shift of amide I to higher wavenumbers (1640 cm$^{-1}$ for C-1.5M), while the shifts of amide II and III were not observed. This change suggested a decrease in the β-sheet component, together with an increase in α-helix or random coils [198].
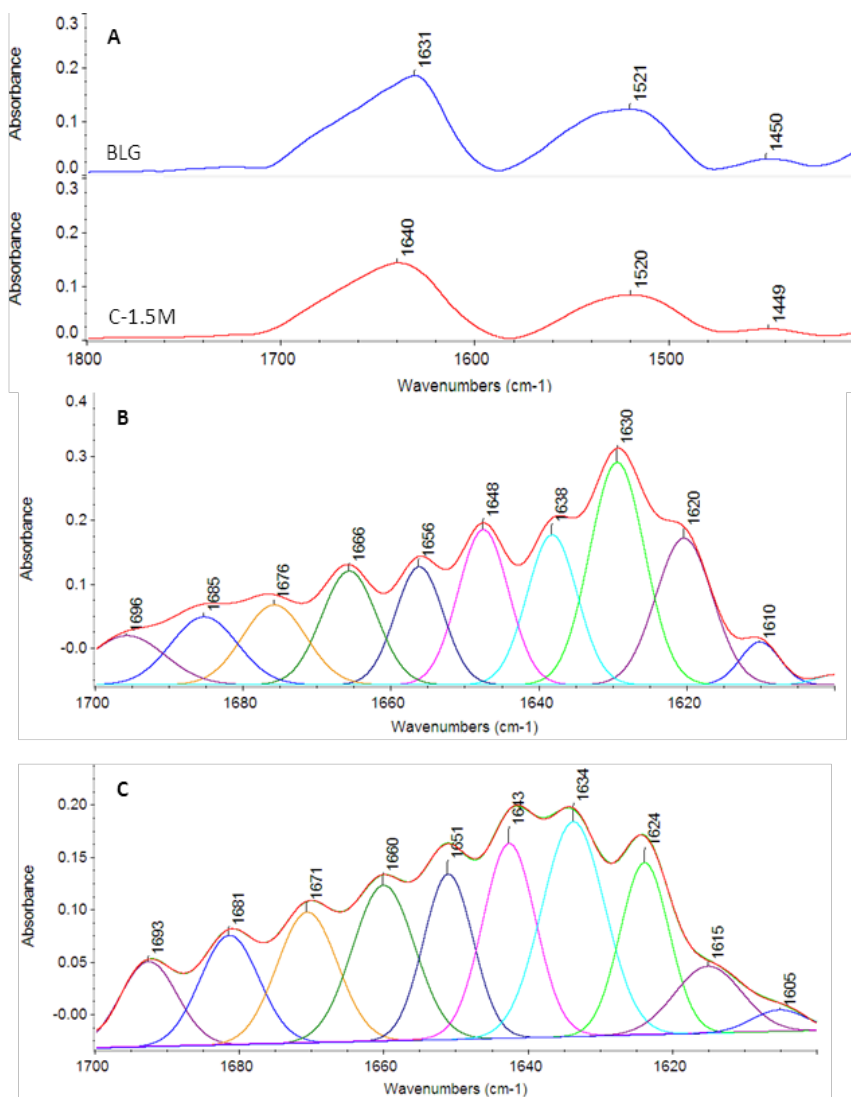
**Figure 6.2** FT-IR spectra of BLG and C-1.5M.
Figure 6.2A: original spectra showing amide I, II and III bands. Figures 6.2B and 6.2C: Fourier self-deconvolved (FSD) and curve-fitted spectra depicting detailed secondary structure profiles of BLG (2B) and C-1.5M (2C).

For quantitative assessment, the spectra were further subjected to FSD and Gaussian curve fitting procedure. Ten peaks were resolved and confirmed for both BLG and CBLG (**Figures 6.2B** and **6.2C**), which were assigned to different secondary structure components according to previous studies [179, 187]. As shown in **Table 6.3**, there was a significant increase in the percentages of α-helix

170

(by 34%) [199], turns (by 33%) [25] and random coil (by 26%) [200], at the expense of β-sheet (decreased by 29%) [201]. Such structural change was closely related to the consumption of glutamic acid and aspartic acid, both of which were found majorly in the β-sheet segments of BLG [202]. The conjugation of EDA moieties onto these amino acids might have weakened their ability to stabilize the relatively rigid β-sheet and produced flexible structures, such as helices, turns and coils. Such conformational transformation suggested a less rigid and more randomized structure of CBLG compared to BLG, which was expected to have a positive impact on the encapsulation, transportation and delivery of nutraceuticals or drugs. These hypotheses will be tested in the follow-up study focused on the incorporation, stabilization and controlled release of nutrients and drugs.

**Table 6.3** Assignment and relative band areas of infrared Fourier self-deconvolved spectra for BLG and CBLG *

| Band assignment | Native BLG Wavenumber (cm$^{-1}$) | Area% | C-1.5M Wavenumber (cm$^{-1}$) | Area% |
|---|---|---|---|---|
| Side chain | 1610 | ** | 1604 | ** |
| β-sheet | 1620 | 14.15 | 1614 | 6.28 |
| β-sheet | 1630 | 20.71 | 1624 | 15.39 |
| β-sheet | 1638 | 12.72 | 1634 | 15.53 |
| Random coil | 1648 | 12.54 | 1642 | 17.14 |
| α-helix | 1656 | 9.96 | 1651 | 13.33 |
| Turns | 1666 | 10.26 | 1660 | 12.82 |
| Turns | 1676 | 7.59 | 1671 | 11.48 |
| Turns | 1685 | 6.94 | 1681 | 9.58 |
| β-sheet | 1695 | 5.13 | 1693 | 6.78 |
| | | | | |
| Total α-helix | | 9.36 | | 13.06 |
| Total β-sheet | | 52.12 | | 36.94 |
| Total random | | 25.80 | | 33.20 |

| | | |
|---|---|---|
| coil | | |
| Total turns | 12.72 | 16.80 |

\* The sample C-1.5M was employed for the FSD process.

\*\* The IR intensity due to side chain vibration was excluded in the calculation for secondary structures.

### 6.4.4 Proteolysis profiles

BLG is known for its resistance to peptic digestion [178], a major advantage over other proteins with respect to the transportation and delivery of nutraceuticals and drugs. This character was confirmed by our study (**Figure 6.3A**), in which only 9% of BLG was degraded after 4 h of incubation with pepsin. As for CBLG, a similar resistance was observed, although the percentage of digested protein increased slightly to 13%. This indigestibility of BLG by pepsin is attributed to the stability of the β-sheet-predominated structure [178]. In addition, pepsin cleaves preferably the peptide bonds formed between hydrophobic amino acids [203], which are not sufficiently exposed as evidenced by a low surface hydrophobicity. As discussed in the previous section, a lower content of β-sheet in CBLG might have resulted in decreased chain rigidity and increased flexibility compared to native BLG. However, the results from peptic digestion suggested that such change had only limited influence on the exposure of hydrophobic amino acid residues. In light of this result, it was speculated that the significant increase in $S_o$ discussed before was more likely due to the exposure of EDA moieties than that of the original hydrophobic residues in BLG.

It was also noted that the Glu-/Asp-EDA conjugates produced upon cationization might be poor substrates for pepsin, in spite of the hydrophobicity caused by EDA. This was probably because that these conjugates exhibited little geometric similarity to any naturally occurring hydrophobic amino acids. In addition, the positive charge on EDA might have inhibited the catalytic triad on pepsin from approaching its substrate. As a result, CBLG inherited the high resistance to peptic digestion from BLG, which may enable it to minimize the loss of the encapsulated nutraceuticals and drugs in the stomach.

Compared to pepsin, trypsin exhibited a higher capacity in digesting BLG, yielding an apparent digestibility of 25% (**Figure 6.3**) in the first 20 min. The abundance of positively charged amino acids (lysine and arginine) in BLG may account for this phenomenon, considering that they were typical substrates of trypsin [183]. As for CBLG, the EDA-aspartic acid conjugate carried as much positive charge as lysine, it showed to a certain extent of geometric similarity to lysine as illustrated in **Figure 6.1**. These two characteristics, together with its sufficient exposure as discussed before, made EDA-aspartic acid conjugates a possible substrate for tryptic digestion. Consequentially, the apparent digestibility of CBLG was increased to at most 43% as expected. Similar results were reported previously for amidated and esterified BLG [183].

173
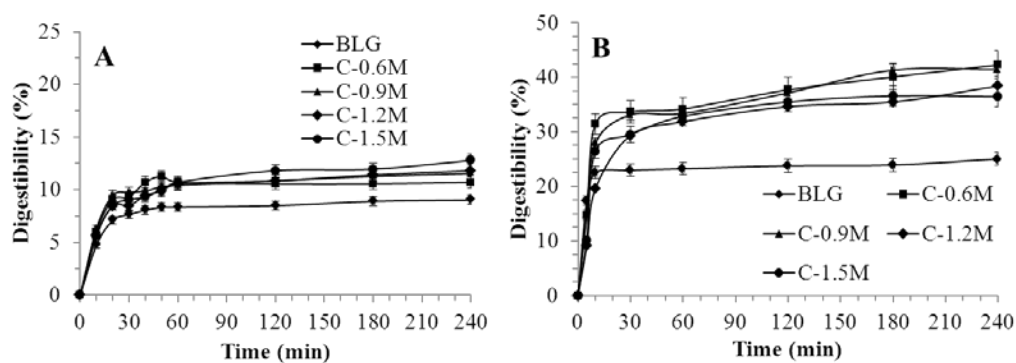
**Figure 6.3** In vitro digestions of BLG and CBLG in the presence of (A) pepsin and (B) trypsin

Improved digestibility by trypsin may have two different impacts on the transportation and delivery of nutraceuticals or drugs. On one hand, it suggested a more complete degradation of the protein matrix, leading to a more efficient release of the bound compound in small intestine. This property, together with the resistance to gastric digestion, is expected to confer CBLG nanoparticles with satisfactory controlled release feature. This hypothesis will be tested in our follow-up study. On the other hand, accelerated decomposition of the protein matrix in digestive system implied weaker protection to the entrapped compounds in the circulation process. This disadvantage, however, could be overcome by choosing proper cationizing reagents. For example, polyethylenimine (PEI) carries an equally high density of positive charges as EDA, and it provides considerable steric hindrance to the protein due to its branched structure [61]. Cationization of BLG by PEI, therefore, might detain both peptic and tryptic digestions, providing maximal protection to the incorporated compounds after intestinal absorption.

174

### 6.4.5  Mucoadhesive properties

The gel-like layer of mucin on the wall of small intestine serves as the first barrier for nutrient absorption [9]. The adhesion to this negative charged, highly glycosylated protein is vital for the diffusion and transportation of enteric nutraceuticals or drugs, and it is one of the key components of the rationale of protein cationization. Two methods, turbidity and QCM assay, were employed in this study to validate the improved mucoadhesion of CBLG. In the turbidity analysis (**Figure 6.4A**), BLG-PSM mixture exhibited a negative absorbance at both 400 nm and 500 nm (the latter not shown), regardless of the BLG. This result was probably due to the negative net charges on both BLG and PSM, which inhibited the association between these two molecules through a strong electrostatic repulsion. On the contrary, the dispersions containing CBLG and PSM exhibited a highly positive absorbance. The relatively low absorbance of C-0.6M compared to other CBLGs was probably attributed to its lower surface charge as discussed before. These phenomena suggested the extensive formation of CBLG-PSM aggregates, which might have been driven by electrostatic attraction and, less importantly, hydrophobic interaction.

The enhanced mucoadhesion property of CBLG was also evidenced by QCM analysis. **Figures 6.4B** and **6.4C** were typical QCM diagrams obtained with PSM-BLG and PSM-CBLG, respectively. The two stepwise increases in the adsorbed mass corresponded sequentially to the deposition of PSM onto the gold

crystal and the adsorption of BLG/CBLG onto the PSM layer. Compared with BLG, CBLG adsorbed to PSM at a significantly higher level. Furthermore, the adsorption of CBLG reached equilibrium within a shorter time, as suggested by a steeper slope of the second step. A quantitative comparison in the mucoadhesive properties was displayed in **Table 6.4** based on QCM analysis. The mass ratio of adsorbed protein to that of PSM increased in parallel with the cationization degrees, reaching a maximum of 1.259 (C-1.5M) that was 252% higher than that corresponding to BLG (0.357). It was worth noting that a certain amount BLG adsorbed to PSM in the QCM study, which was not observed in turbidity analysis. A possible explanation for this discrepancy was that part of the hydrophilic oligosaccharide chains that covered originally on the protein segment of PSM [9] might have been re-orientated to facilitate its deposition on the gold crystal. Such process facilitated the exposure of the more hydrophobic protein moieties [9], enabling them to associate with BLG through hydrophobic interaction.
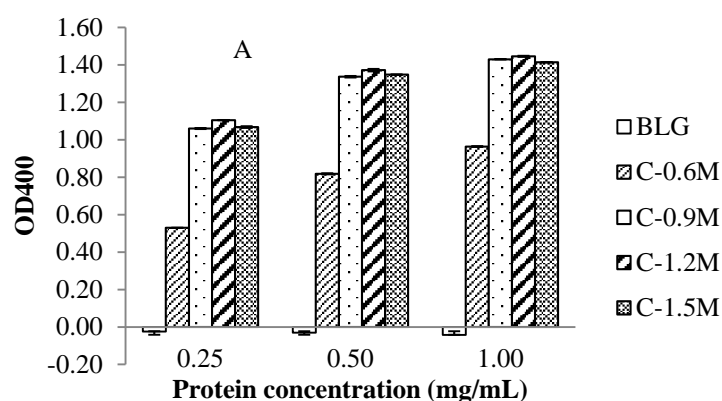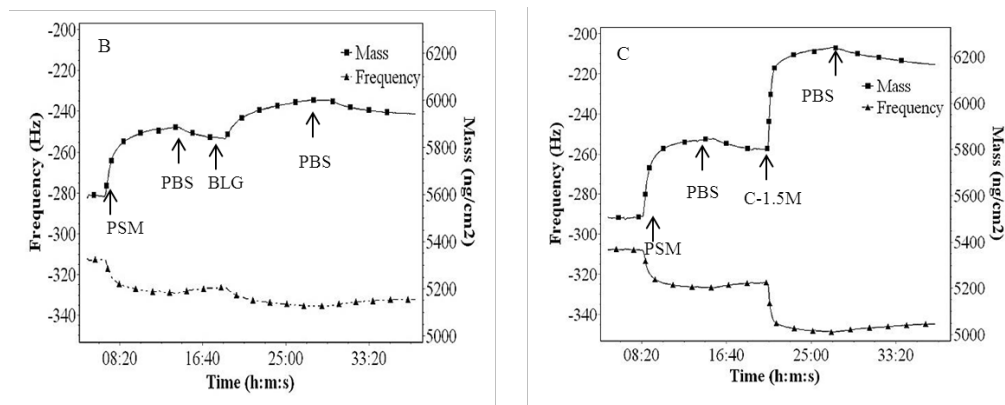
**Figure 6.4** Mucoadhesive properties of BLG and CBLG.
Figure 6.4A: turbidity measurement at a PSM concentration of 1 mg/mL and different BLG/CBLG concentrations. Figures 6.4B and 6.4C: QCM analysis showing the mucoadhesion of BLG (4B) and C-1.5M (4C), obtained at a PSM and BLG/CBLG concentration of 0.4 and 1 mg/mL, respectively. The 5th overtone was used for graph plotting and mass calculation.

Elevated mucoadhesive property of CBLG is one of its major merits. It resulted in shorter dwelling time in the small intestine, which suggested reduced opportunity for protein digestion and nutrient degradation. Both of these factors facilitated the absorption of CBLG and CBLG-bound molecules in their intact form. Although a number of studies have showed comparable mucoadhesion of other cationic polymers [10, 11, 60], most of them were conducted under acidic conditions (pH 2-6). This was possibly due to the low solubility at neutral or basic pH of these polymers. Such disadvantage would have a negative impact on the mucoadhesive capability in small intestine, whose average pH is around 7. CBLG, on the other hand, exhibited high solubility at neutral pH due to its amphiphilic nature. Such advantage made CBLG a suitable candidate for the transportation of nutraceuticals and drugs across the small intestine.

**Table 6.4** Mucoadhesion properties of BLG and CBLGs *

| Sample | PSM adsorption ng/cm$^2$ | Protein adsorption ng/cm$^2$ | Mass ratio (Pro: PSM) |
|--------|--------------------------|------------------------------|------------------------|
| BLG | 238±12$^c$ | 85±14$^c$ | 0.357±0.052$^e$ |
| C-0.6M | 359±17$^a$ | 231±15$^b$ | 0.643±0.013$^d$ |
| C-0.9M | 378±15$^a$ | 308±20$^{ab}$ | 0.815±0.020$^c$ |
| C-1.2M | 243±12$^c$ | 240±15$^b$ | 0.988±0.044$^b$ |
| C-1.5M | 294±10$^b$ | 370±14$^a$ | 1.259±0.071$^a$ |

\* Data with different letters showed significant difference (n=3, $P<0.05$).

### 6.4.6 Particle formation behaviors

The particle forming properties of BLG and CBLG investigated by DLS were compared in **Table 6.5**. In our preliminary study (data not shown), both BLG and C-0.6M aggregated spontaneously into nanoparticles in the presence of 80% aqueous ethanol. The other CBLGs (C-0.9M, C-1.2M and C-1.5M), however, did not show any observable aggregation even in 95% ethanol. Acetone, on the other hand, was able to initiate the particle formation of BLG and all CBLGs. It is generally believed that the formation of protein nanoparticles begins with the exposure of functional groups (hydrophobic site, thiol group, etc.), which induced intermolecular association and particle formation [44, 105]. Such process requires the contact between protein and antisolvent molecules, which triggers the unfolding of peptide chains [204]. When BLG was cationized, a considerable part of its exterior was covered by the grafted EDA moieties, as indicated by the highly positive zeta potential. Such coverage produced extra hindrance for relative polar organic solvents such as ethanol, due to the size of the cationizer (EDA) and the increase in surface hydrophobicity it induced [205]. This explained why ethanol

desolvated BLG and C-0.6M effectively but did not work for CBLGs with higher

cationization degrees. In addition, C-0.6M might have exhibited weaker

electrostatic repulsion due to a lower surface charge, which also facilitated the

aggregation. As for acetone, it possessed a stronger protein denaturation capacity

than ethanol [204]. In addition, its relatively low polarity suggested better contact

with the hydrophobic surface of CBLG [206], which further promoted the

desolvation and protein unfolding processes.

**Table 6.5** Characters of BLG and CBLG nanoparticles*

| Sample | Acetone % | Particle size nm | Count rate kcps | Polydispersity index |
|--------|-----------|------------------|-----------------|----------------------|
| BLG | 80 | $139.1\pm5.7^b$ | $47.4\pm5.2^d$ | $0.255\pm0.003^b$ |
| BLG | 90 | $136.3\pm11.2^b$ | $386.2\pm7.8^a$ | $0.142\pm0.002^d$ |
| C-0.6M | 80 | $172.3\pm6.2^a$ | $402.4\pm7.1^a$ | $0.086\pm0.002^e$ |
| C-0.6M** | 90 | - | - | - |
| C-0.9M | 80 | $170.4\pm10.7^a$ | $30.8\pm2.3^e$ | $0.293\pm0.004^a$ |
| C-0.9M | 90 | $93.5\pm3.4^c$ | $314.6\pm10.2^{bc}$ | $0.095\pm0.004^c$ |
| C-1.2M | 80 | $165.0\pm5.2^a$ | $26.1\pm1.4^f$ | $0.255\pm0.006^b$ |
| C-1.2M | 90 | $75.4\pm6.7^c$ | $259.4\pm12.5^c$ | $0.104\pm0.003^c$ |
| C-1.5M | 80 | $155.7\pm10.1^a$ | $15.8\pm1.6^g$ | $0.297\pm0.005^a$ |
| C-1.5M | 90 | $81.5\pm4.2^c$ | $280.4\pm13.1^c$ | $0.124\pm0.002^c$ |

* Data with different letters showed significant difference (n=3, P<0.05). A fixed protein concentration of 2 mg/mL was adopted.

** No data available due to protein precipitation.

As shown in **Table 6.5**, the particles formed with BLG or CBLG exhibited an

average size of 75-172 nm, which was ideal for the encapsulation and

transportation of nutraceuticals and drugs [20]. In addition, all samples except

C-0.6M exhibited lower particle size, higher count rate and lower polydispersity in

90% acetone as compared to 80% acetone. The count rate of a colloidal dispersion

is proportional to the quantity of particles and the sixth power of the average size;

therefore, these results suggested that a significantly greater number of

nanoparticles with lower, more uniformly distributed size were formed in 90%

acetone. The precipitation of C-0.6M in 90% acetone was probably due to the lack

of electrostatic stabilization as discussed before.
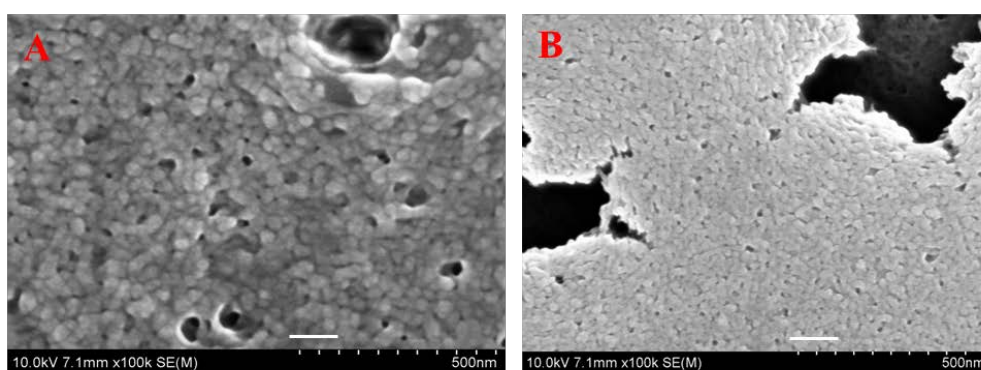


**Figure 6.5** SEM images for nanoparticles formed by BLG (6.5A) and C-1.5M (6.5B).
The white scale bars indicated for 100 nm. Images were taken after acetone was
evaporated and replaced with same volume of deionized water.

**Figure 6.5** displayed the morphology of BLG (A) and CBLG (B) nanoparticles

observed under SEM. The particles were approximately spherical, and they

exhibited a narrow size distribution between 50 and 80 nm. The maintenance of

particle structure after the evaporation of acetone evidenced successful

crosslinking of the particle structure by glutaraldehyde. The fact that the sizes

observed under SEM were lower than those obtained by DLS was probably due to

the shrinkage of nanoparticles under vacuum. Similar results were reported

previously [6, 7].

180

## 6.5    Conclusions

CBLG, a highly water-soluble cationic protein, was synthesized successfully with BLG and EDA. The attachment of EDA moieties induced a reversal in zeta potential (from -37 to +39 mV), together with a significant increase in surface hydrophobicity. FT-IR study showed the increase in helical and random secondary structure upon cationization at the expense of rigid β-sheets. Such conformational change led to an increase of apparent digestibility by trypsin, whereas the original resistance to peptic digestion of BLG was maximally retained. With regard to absorption, CBLG exhibited significantly enhanced association with PSM in turbidity assay compared with BLG, and its adsorption to PSM layer was improved by up to 252% in the QCM study. Nanoparticles with sub-100 nm size and narrow size distribution were prepared with CBLG using acetone as an antisolvent, evidenced by DLS and SEM. These features made CBLG and CBLG-based nanoparticles a suitable candidate for the encapsulation and delivery of poorly bioavailable nutraceuticals or drugs. Follow-up studies are being carried out on CBLG nanoparticles to evaluate their encapsulation capacity, controlled release in simulated GI tract, as well as the toxicological properties.

# Chapter 7 Cationic β-lactoglobulin Nanoparticles as a Bioavailability Enhancer: Comparison between Ethylenediamine and Polyethyleneimine as Cationizers

## 7.1 Abstract

In this chapter, cationic beta-lactoglobulin (CBLG) was synthesized by two strategies: extensive conjugation of ethylenediamine (EDA) and limited cationization with polyethyleneimine (PEI). Both methods provided CBLG with remarkable water solubility and resistance to peptic digestion. Compared with EDA-derived CBLG (C-EDA), PEI-derived CBLG (C-PEI) exhibited higher zeta potential (54.2 compared to 32.4 mV for C-EDA), which resulted in significantly elevated mucoadhesion (439% and 118% higher than BLG and C-EDA, respectively) in quartz crystal microbalance (QCM) study. In addition, PEI caused lesser extent of conformational disruption on BLG compared to EDA as evidenced by FTIR measurement. This character, together with the steric hindrance provided by PEI, caused a phenomenal reduction in tryptic digestibility by at least 75% compared to C-EDA. In the presence of aqueous acetone, C-PEI aggregated spontaneously into nanoparticles with average size of 140 nm and narrow size distribution. These merits made C-PEI a useful material that provides desirable solubility and protection for oral-administrated nutraceuticals or drugs.

## 7.2 Introduction

In the past decades, nano-scaled encapsulating and delivery systems have attracted increasing attention as transporters for nutraceuticals or drugs [1, 207]. Numerous nanoencapsulation strategies and systems have been developed by now, providing target compounds with desirable solubility [208], satisfactory stability [121], controlled release property [137] and elevated bioavailability [209]. It is generally believed that the success of delivery is highly dependent on the surface properties of the encapsulant, among which charge and hydrophobicity play a critical role [42]. For instance, cationic polymers such as chitosan [39], polylysine[59] and lactoferrin [50], have demonstrated significantly higher mucoadhesive capacity and cellular internalization compared with anionic macromolecules. This phenomenon was largely attributed to two factors. The first factor is the affinity of the polycations to the negatively charged glycoproteins, which are abundant on the epithelia cells or tissues (e.g., small intestine wall) [16]. The second advantage for cationic encapsulants is their ability to acquire a negative charged "corona" consisting majorly of serum proteins, which bind strongly to specific ligand on the cell membrane and thus promote the cellular internalization [210].

By far, a wide array of cationic polymers has been exploited as novel encapsulating systems [39, 50, 174]. However, these polymers are either insoluble at neutral pH (e.g., chitosan) or susceptible to digestion by either pepsin or trypsin (e.g., polylysine). Therefore, the protection provided by these materials would be

easily diminished when they enter the gastrointestinal tract, which is one of the major drawbacks of these polycations. Beta-lactoglobulin (BLG), a 162-residue globulin, makes up approximately 60% of bovine whey protein [47]. BLG is highlighted for two unique features, namely, high surface charges and abundance of rigid β-sheet secondary structure. The first characteristic ensures the dispersion stability of BLG-based encapsulating systems even near its isoelectric point (~pH 5.0). The second property endows BLG with remarkable resistance against peptic digestion [164], thus providing maximal stability and controlled release for oral-administrated bioactives.

To take advantage of both BLG and cationic polymers, our lab synthesized cationic BLG (CBLG) by grafting ethylenediamine (EDA) to the glutamic acid (Glu) or aspartic acid (Asp) residues of BLG [151]. The products exhibited highly positive surface charge, which resulted in significantly improved mucoadhesion. In addition, EDA-derived CBLG inherited the resistance to pepsin in simulated gastric environment, but the digestion by trypsin was significantly elevated. A possible explanation for this phenomenon lied in the formation of Glu-/Asp-EDA conjugates [151], which showed similar geometry and electric charge status to lysine. Since lysine is a known substrate for trypsin [205], generation of Glu-/Asp-EDA conjugates might result in a significant increase in tryptic digestibility. While increased tryptic digestibility provided EDA-derived CBLG with certain degree of controlled release property, such change was unfavorable

184

for delivering bioactive compounds that requires prolonged protection after leaving digestive tract and entering systemic circulation. Furthermore, the disintegration of EDA-derived CBLG implied the inability t`o gain the serum protein corona [210]. This could not only compromise the efficacy of cellular uptake, but also lead to considerable cytotoxicity, since the negatively charged corona played a crucial role in counterbalancing the toxicity induced by cationic polymers [211]. Increased digestibility of CBLG, therefore, might be detrimental for its function as a bioavailability enhancer for nutraceuticals or drugs.

Polyethyleneimine (PEI, structure shown in **Figure 1.2**) is a cationic polymer whose repeating units consist of an amine group and two methylene groups (-NH-CH$_2$-CH$_2$-). Owing to its low toxicity [212, 213], PEI has been permitted by FDA to be added as an enzyme immobilizing agent in the beer industry [214]. Amongst all commercially available PEI categories, branched PEI contains abundant primary amino groups that are reactive for cationization. Because of the high content of amino groups (one unit of positive charge in a mass unit of 43), conjugation of only a few PEI molecules is sufficient to introduce a significant amount of positive charge to the protein, without greatly altering its conformation [215]. By far, PEI has been used as a cationizer for various proteins [42], resulting in significantly improved cellular uptake and low cytotoxicity.
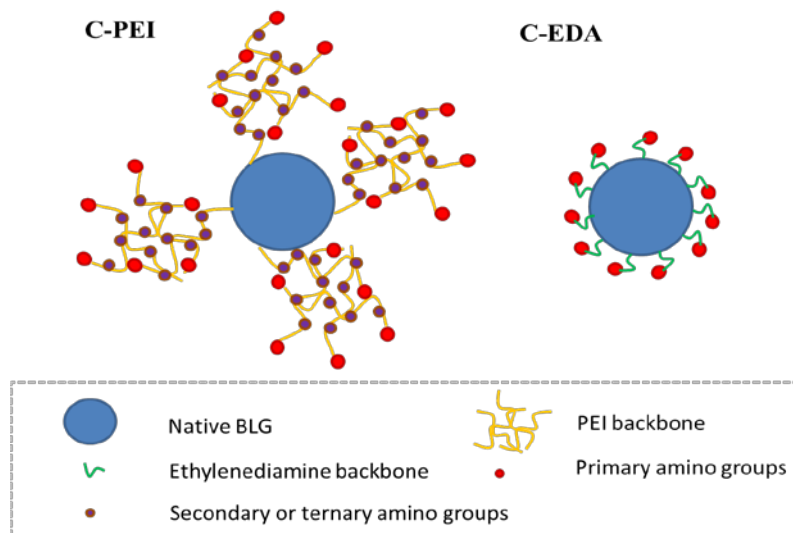
**Figure 7.1** Schematic illustration on the structure of PEI- and EDA-derived CBLG. The conjugates between EDA and Glu/Asp residues exhibit similar geometry and electric charge with lysine, a substrate for trypsin.

Hereby, we propose the synthesis of CBLG using branched PEI as a cationizer. The anticipated structures of EDA-derived CBLG (C-EDA) and PEI-derived CBLG (C-PEI) are illustrated in **Figure 7.1**. We expected that C-PEI exhibit similar resistance against pepsin and superior mucoadhesion, compared with BLG or C-EDA. In addition, we hypothesized that the product could maintain its integrity under simulated intestinal condition, because of the absence of Asp-/Glu-EDA conjugate, as well as steric hindrance provided by the highly branched PEI backbone. The product was compared in parallel with BLG and C-EDA, with respect to its conjugation degree, surface charge, secondary structure, *in vitro* digestibility and mucoadhesion. Finally, C-PEI-based nanoparticles were fabricated by organic solvent desolvation method, and the unique particle forming behaviors of this modified protein were reported.

186

### 7.3 Materials and Methods

### 7.3.1 Materials

The following chemicals were purchased from Sigma-Aldrich (St. Louis, MO, USA): bovine BLG (90% purity), ethylenediamine dihydrochloride (EDA, 98% purity), branched polyethyleneimine (PEI600 and PEI1200, with average MW of 600 and 1200 Dalton, respectively), sinapinic acid, pepsin (3,200-4,500 units/mg), N-(3-dimethylaminopropyl)-N-ethylcarbodiimide (EDC, 97% purity), trypsin (10,000 BAEE units/mg), and trichloroacetic acid (TCA). Porcine stomach mucin (PSM, type III, contains 0.5-1.5% sialic acid) was obtained from Himedia Co., India. All other reagents (trifluoroacetic acid, sodium bicarbonate, simulated gastric and intestinal fluids, etc.) were of analytical grade.

### 7.3.2 Preparation of cationic beta-lactoglobulin (CBLG)

CBLG was prepared by grafting cationic EDA or PEI moieties to the anionic carboxyl groups on the Asp and Glu residues on native BLG [151]. This was achieved via a previously reported EDC-aided reaction [62]. BLG and the cationizers (EDA or PEI) were dissolved in deionized water at 20 and 100 mg/mL, respectively. The pH was then adjusted to 4.75 using 1 mol/L HCl for BLG solution or concentrated HCl for cationizer dispersion. Thereafter, 5 mL of BLG solution was added slowly to 30 mL cationizer dispersion under mild stirring, and the mixture was incubated at room temperature for 15 min. Cationization was initiated by the addition of 30 mg EDC and terminated by adding 108 μL sodium

acetate buffer (4 mol/L, pH 4.75) after 4 h. The resultant dispersion was subjected

to dialysis centrifugation (5,000 *g*, 30 min), using a Macrosep® centrifuge tube

(Pall Corp., Ann Harbor, MI) with a built-in filtering membrane. Tubes with

different MW cutoff values (10,000 for EDA and PEI-600-derived CBLG and

100,000 for PEI-1200-derived CBLG) were chosen for different samples in order

to maximize the removal of unreacted chemicals, without compromising protein

yield significantly. The retentate obtained after centrifugation was further dialyzed

against deionized water at 4 °C for at least 48 h and freeze dried. The moisture

content of the final product was less than 5%, and the protein content was above

90% according to Bradford assay calibrated with BSA. The samples were

designated as C-EDA for EDA-derived CBLG and C-P600/C-P1200 for CBLG

synthesized with PEI-600/ PEI-1200.

### 7.3.3 Determination of molecular weight and net charge

The molecular weights (MW) of BLG and CBLG were measured by matrix

assisted laser desorption/ionization time-of-flight (MALDI-TOF) mass

spectrometry in linear mode [216]. The samples were dispersed at 25 mg/mL in

deionized water containing 1 μL /mL trifluoroacetic acid (TFA). The matrix

solution was prepared by dissolving 10 mg sinapinic acid in a mixture of 200 μL

pure acetonitrile and 200 μL water (containing 0.2 μL TFA). Prior to analysis, 1

μL matrix solution was spotted onto the target plate, and 1 μL of the sample

solution was doped above the matrix layer. A second matrix layer (0.5 μL) was

then dripped on top of the abovementioned two layers. Each layer was air dried at room temperature before doping the next one. The target plate was then loaded into a Shimadzu Axima-CFR MALDI-TOF spectrometer (Shimadzu North America, Columbia, MD, USA). Spectra were obtained by illuminating the samples with a $N_2$ laser beam (130 mJ per shot, 2 shots per second) and analyzed with the Kompact software. For each sample, at least 150 spot spectra were collected and averaged, and the peak values on the spectra were reported.

The amount of electric charge on CBLG was estimated based on the MW. The change in MW upon cationization ($\Delta M$) was firstly converted to the conjugation degree (CD, number of EDA or PEI molecules grafted to a single BLG molecule), using the equation $CD=\Delta M/m$, where m represented the theoretical mass change when one cationizer was attached. The value of m was 42 for EDA, which was calculated by subtracting its MW (60) by the MW of water (18). For PEI-600 and PEI-1200, the values of m were estimated as 582 and 1182, respectively. The net charge was then calculated as follows: Net charge $= z \times CD - 7$, where the number "-7" was the net charge of BLG molecules, CD was the conjugation degree, and z was the amount of positive charge on the cationizer. For EDA, the value of z was 2. For PEI, the z value was estimated as (molecular weight + 26) / 43 [215].

### 7.3.4 Determination of zeta potential

Samples were dispersed in PBS (10 mmol/L, pH 7.0, same hereinafter) and measured for their electrophoretic mobility by laser Doppler velocimetry, using a

Nano ZS90 Zetasizer (Malvern Inc., Malvern, UK). Each sample (1 mg/mL) was measured for three times, each time containing at least twelve runs. The data were then converted to zeta potentials using the Smoluchowski model.

### 7.3.5 Secondary structure determination

The structural change of BLG upon cationization was investigated by Fourier-transform infrared (FT-IR) analysis. Samples (3 to 5 mg) were freeze dried and mounted directly onto a Jasco FT/IR 4100 spectrometer (Jasco Inc., Easton, MD, USA). The infrared transmittance was recorded at wavenumbers between 1000 and 4000 $cm^{-1}$ at resolution of 2 $cm^{-1}$. At least 100 repeated scans were undertaken for each sample. The spectra were averaged, smoothed, corrected for their baselines and converted to absorbance using the Spectra Manager software (Jasco Inc., Easton, MD, USA). For quantitative study on protein conformation, Fourier self-deconvolution (FSD) was undertaken on the obtained IR spectra, using the OMNIC software (Thermo Scientific, West Palm Beach, FL, USA). Peak finding and assignment were performed according to our previous study [151].

### 7.3.6 Determination of *in vitro* digestibility

Samples were subjected to *in vitro* digestion test using two enzymes, i.e., pepsin and trypsin, following a procedure described in our previous study [151]. In brief, samples were dissolved in simulated gastric or intestinal fluid, incubated at 37 °C for 15 min, mixed with pepsin or trypsin solution at a substrate-to-enzyme ratio of

200:1 (w/w). At predetermined time intervals, aliquots of the sample were mixed with TCA solution to terminate digestion and then centrifuged. Digested protein was recovered in the supernatant and measured for its absorbance at 280 nm. For comparison purpose, another aliquot of the sample was digested by papain, which was known to digest BLG completely [151]. The absorbance observed for peptic or tryptic digestion was divided by the one obtained from papain digestion, thus giving the apparent digestibility for the samples.

### 7.3.7   Determination of mucoadhesion

**Quartz crystal microbalance (QCM) analysis** [11]. In the QCM study, two thin layers of PSM and protein (BLG or CBLG) were deposited sequentially on a gold-coated AT-cut quartz crystal with a fundamental frequency of 4.95 MHz (QSX-301, Q-Sense Co., Linthicum, MD, USA). The deposition of the two polymers induced the mass change of the crystal, which was reflected by the change in frequency ($\Delta f$). Prior to each treatment, the crystal was soaked in Piranha solution ($NH_3 \cdot H_2O$: $H_2O_2$: $H_2O$=1:1:5, v/v/v) for 15 min at 70 $^o$C, rinsed by deionized water and ethanol, and finally dried with nitrogen. The crystal was then mounted onto a Q-Sense E1 microbalance (Q-Sense Co., Linthicum, MD, USA), after which PBS was injected at a flow rate of 0.224 mL/min using a peristaltic pump (Ismatec Reglo, Glattbrugg, Switzerland). After obtaining a constant frequency, PSM solution (400 μg/mL in PBS, filtered through a 220 nm membrane) was pumped into the crystal chamber. The frequency was significantly

changed due to the deposition of PSM, and it reached another plateau after approximately 10 min. The chamber was rinsed with PBS for approximately 5 min to remove loosely deposited PSM molecules, after which protein solution (1 mg/mL in PBS, passed through a 220 nm membrane) was injected at a same flow rate. After 15 min of protein adsorption, the frequency became stable again, and the chamber was subjected to a final rinse of PBS, until the last plateau of frequency was observed. Changes in frequency, up to the 13th overtone, were collected by QTools 3 (Q-Sense Co., Linthicum, MD, USA) throughout the whole process. The $\Delta f$ of the fifth overtone was converted to deposited mass (in $ng/cm^2$ crystal surface) by QTools 3, using the Sauerbrey model. Mucoadhesion was expressed as the mass ratio between deposited BLG/CBLG and PSM. The temperature of the chamber was kept at 37 $^o$C during the measurement.

**Turbidity analysis** [10]. Samples (BLG or CBLG) and PSM were dispersed in PBS at 10 and 1 mg/mL, respectively, and they were both passed through a 1.2 $\mu$m Acrodisc® syringe filter. The two stock solutions were then diluted appropriately to achieve a fixed PSM concentration of 1 mg/mL and different protein concentrations (0.25, 0.5 and 1 mg/mL). The mixture was then incubated at 37 $^o$C for 1 h and cooled to room temperature. The absorbance at 400 nm of the mixture was recorded by a DU-730 UV/VIS spectrophotometer (Beckman Coulter Inc., Fullerton, CA, USA), using pure PSM dispersion (1 mg/mL, filtered as described above) as blank.

### 7.3.8 Preparation of BLG/CBLG nanoparticles

Nanoparticles were prepared with BLG/CBLG by desolvation [105] method. Constant stirring (600 rpm) was applied throughout the particle formation process. The protein was dissolved in deionized water at 10 mg/mL (pH 7.5-8.0), and the resultant dispersion was equilibrated for 1 h at room temperature. To initiate particle formation, pure acetone was added dropwise to achieve an acetone/water ratio of 90/10 (v/v). The suspension changed from a clear solution into an opaque dispersion, which was equilibrated for 30 min. A crosslinker (glutaraldehyde) was then added to harden the particle structure. Based on the lysine content of BLG (16 mol Lys per mol BLG), the amount of glutaraldehyde needed for sufficient crosslinking is 40 μg/mg. After cationization, the content of primary amino groups in the protein increased significantly, and greater amount of glutaraldehyde was therefore required. In this study, the mass ratio between glutaraldehyde and protein ranged from 40 to 160 μg/mg. Prior to the crosslinking process, the dispersion was diluted with 90% (v/v) aqueous acetone by fivefold. The reason for dilution will be discussed in the **Section 7.4.5**. After 8 h of crosslinking, the added acetone was evaporated under a constant nitrogen flow and replaced with same volume of deionized water. The resultant suspension containing the nanoparticles was evaporated under nitrogen flow to remove acetone, supplemented with deionized water to the original volume (before dilution), and stored at 4 °C for subsequent assays.

### 7.3.9 Determination of particle size and count rate

The particle size and count rate of BLG/CBLG nanoparticle dispersions were determined [133] by dynamic laser scattering (DLS) using a BI-200 SM Goniometer Version 2 (Brookhaven Instrument Corp., Holtsville, New York, USA) equipped with a 35 mW He-Ne laser beam. The measurements were undertaken at two stages during the nanoparticle formation process: before dilution and after water supplementation. No dilution was applied before the assays. The following parameters were adopted: laser power of 10 mW, detection wavelength of 637 nm, scattering angle of 90°, temperature of 25 °C, and measurement time of 1 min. The refractive indices and viscosities of different acetone/water systems were applied for all assays, since they were not significantly altered by low concentration of protein or glutaraldehyde in our study (data not shown). Two separate measurements were carried out on each sample in order to obtain accurate results. For count rate determination, the aperture pinhole size was fixed at 400 μm; to measure the particle size, appropriate aperture pinhole sizes were chosen to achieve a count rate between 100 and 300 kcps. The obtained data were analyzed using cumulant algorithm, and the quadratic mean particle size was reported.

### 7.3.10 Scanning electron microscopy (SEM)

The morphology of BLG/CBLG nanoparticles was observed using a Hitachi SU-70 SEM (Hitachi, Pleasanton, CA, USA) [105]. Approximately forty microliters of the nanoparticle dispersion was pipetted onto an aluminum pan and

air dried. The pan was then cut into appropriate sizes and adhered to a 1-inch specimen stub with conductive carbon tapes (Electron Microscopy Sciences, Ft. Washington, PA, USA). Prior to observation, a thin layer (<20 nm) of gold and platinum was deposited to the samples using a sputter coater (Hummer XP, Anatech, CA, USA). Representative images were reported.

### 7.3.11 Statistics

All measurements were carried out in triplicates. The results were expressed as means ± standard error. Analysis of variance ($P < 0.05$) was performed on the data using SAS 9 software (SAS Institute Inc., Cary, NC, USA). The results were then subjected to Tukey's test with an experimentwise confidence level of $\alpha=0.10$.

### 7.4    Results and Discussion

### 7.4.1    Effect of cationization on net charge and zeta potential

**Figure 7.2** showed the mass/charge ratio (m/z) distribution of native and cationized BLG. BLG exhibited a major peak at m/z=18215 with a shoulder at m/z=18314. These values corresponded to mono-charged bovine BLG variants A and B, respectively [216, 217]. Meanwhile, doubly charged BLG molecules were also observed at m/z=9116 (variant A) 9158 (variant B). Upon cationization, a significant shift towards higher values of m/z was observed. The peak for C-EDA centered at m/z=19188, indicating that approximately 21 EDA molecules were grafted to one BLG molecule. This result was in agreement with that obtained by

TNBS assay (data not shown), which indicated that approximately 19 EDA molecules were conjugated on one BLG molecule. The reason why this number was higher than that achieved in our previous study (11 EDA per BLG molecule) was probably prolonged reaction time [151]. For PEI-derived CBLG, they exhibited a wider distribution of m/z values, probably because of the polydispersity in MW of commercially available PEI products as indicated by the manufacturer. The central m/z values for C-P600 and C-1200 were 21305 and 23231, respectively. As estimated from these results, an average of five PEI-600 and four PEI-1200 molecules were attached respectively to one BLG molecule.
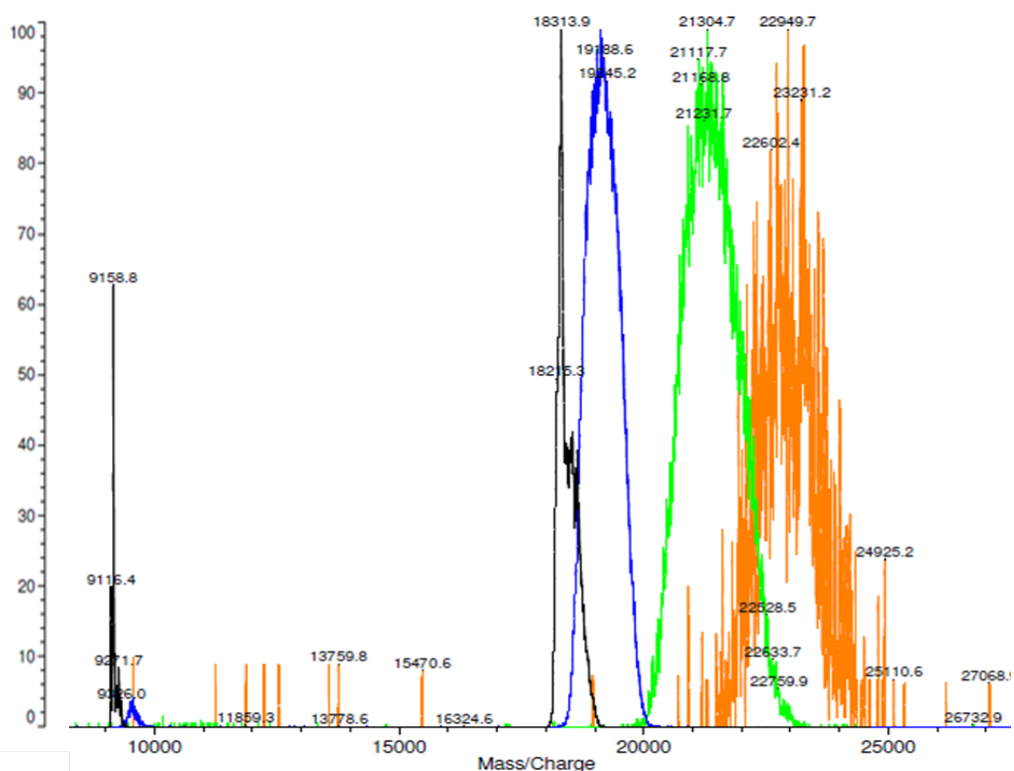


**Figure 7.2** MALDI-TOF spectra for BLG and CBLG.

**Table 7.1** summarized the net charges and zeta potentials of BLG and CBLG. Native BLG, taking average of its two variants, possesses 16 Lys, 3 Arg, 10 Asp and 16 Glu residues [217], all of which results in an overall net charge of -7 per molecule. Upon cationization with EDA, the net charge of BLG shifted to +25. When PEI-600 and PEI-1200 were used as cationizers, the net charge shifted more dramatically to +58 (C-P600) and +102 (C-P1200), in spite of relatively low conjugation degrees. It should be pointed out, however, that the estimated net charge for PEI-derived CBLG was the maximal theoretical value that could only be achieved when all of the amino groups on PEI were protonated. The actual charging status of PEI-derived CBLG was highly dependent on the structure of PEI (e.g., chain length, degree of branching, content of primary and secondary amino groups), as well as the environment (pH, ionic strength, etc.) [151].

**Table 7.1** Conjugation degree and charging status of BLG and CBLG.

| Sample name | Cationizer Type | Peak MW (Da) | Conjugation Degree* | Net charge per molecule* | Zeta potential in PBS (mV) |
|---|---|---|---|---|---|
| BLG | - | 18215 | - | -7 | -35.8±0.7[d] |
| C-EDA | EDA | 19188 | 20.8 | +35 | 32.4±1.0[c] |
| C-P600 | PEI-600 | 21305 | 5.2 | +58 | 46.8±1.5[b] |
| C-P1200 | PEI-1200 | 23231 | 4.2 | +102 | 53.4±1.3[a] |

* The conjugation degrees were estimated from the peak MW measured by MALDI-TOF.

Zeta potential reflects the surface charge and stability of colloidal particles. As shown in **Table 7.1**, native BLG exhibited a zeta potential of -35.8 mV, which was consistent with previous studies [151]. The zeta potential changed significantly to 32.4 mV upon conjugation with EDA, and it shifted towards more

197

positive values for C-P600 (46.8 mV) and C-P1200 (53.4 mV). The high zeta potentials of PEI-derived CBLG were probably due to the abundance of amino groups on PEI. Moreover, a considerable part of these amino groups was pushed towards the surface of CBLG (**Figure 7.1**), owing to the extended polymeric chains of PEI. This caused extensive exposure of protonated amino groups, which contributed to the highly positive zeta potential of C-PEI. As a result, all CBLG sample were soluble in water or PBS at concentrations higher than 100 mg/mL, without any observable precipitation in several weeks (data not shown).

### 7.4.2    Change in protein structure upon cationization

The FT-IR spectra of BLG and different CBLG samples were displayed in **Figure 7.3**. Native BLG exhibited three characteristic peaks: amide I (1631 cm$^{-1}$, C=O stretching), amide II (1520 cm$^{-1}$, C-N stretching and N-H bending), and amide III (1450 cm$^{-1}$, C-N stretching, N-H bending). The position of amide I (1631 cm$^{-1}$) was indicative for the predominance of β-sheet secondary structure in BLG, which was consistent with previous literatures [47]. After cationization with EDA, the amide I peak shifted to 1639 cm$^{-1}$, which suggested the formation of other secondary structures at the expense of β-sheet. No other peak was observed with significant shifting. These phenomena could be explained by the fact that C=O stretching is more sensitive to conformational change than other common stretching or bending patterns in proteins [179]. As protein molecules changed in their secondary structure, the intra-molecular hydrogen binding was either

198

strengthened or weakened, both of which altering the C=O pattern and leading to a shift in the amide I peak.

When PEI was used as a cationizer, the shift in amide I was not as significant as that for C-EDA. This phenomenon indicated a lower degree of conformational change induced by PEI compared with EDA. A possible explanation was that only four to five Glu or Asp residues of BLG were substituted by PEI, whereas more than 20 EDA molecules were attached to BLG. As Glu and Asp are found mainly in the β-sheet region of BLG [202], lower conjugation degree might be beneficial for the preservation of original protein structure. On the other hand, amide II and amide III exhibited a significant shift towards higher wavenumbers. Such results were more likely attributed to the IR absorption of PEI molecules rather than the change in protein conformation that they induced, considering the abundance of C-N and N-H bonding in PEI [218]. In addition, wide adsorption humps centered at 1075 and 1099 cm$^{-1}$ were observed for C-P600 and C-P1200, respectively. These peaks were assigned for C-N stretching of alkyl amines, which were typical for PEI [219].
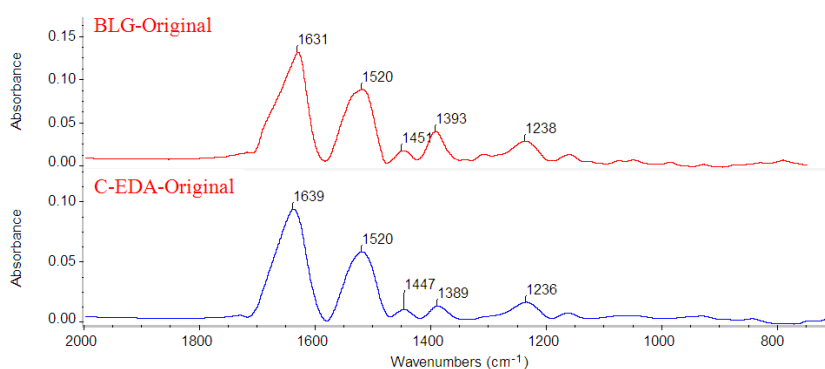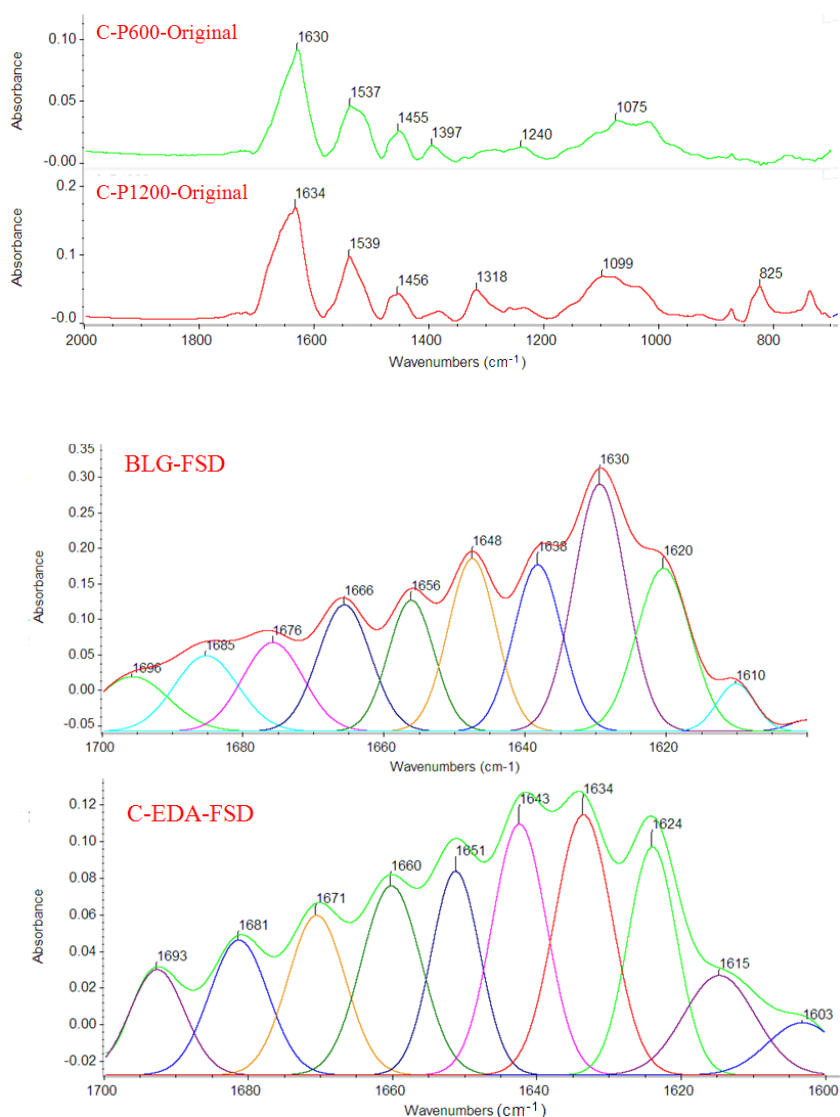
**Figure 7.3** Original and Fourier self-deconvoluted FT-IR spectra of BLG and CBLG.

**Table 7.2** Assignment and relative band areas of infrared Fourier self-deconvolved BLG and CBLG

| | **BLG** | | **C-EDA** | | **C-P600** | | **C-P1200** | |
|---|---|---|---|---|---|---|---|---|
| Band assignment | Wavenumber (cm$^{-1}$) | Area % | Wavenumber (cm$^{-1}$) | Area% | Wavenumber (cm$^{-1}$) | Area% | Wavenumber (cm$^{-1}$) | Area% |
| Side chain | 1610 | * | 1604 | * | 1603 | * | | * |
| β-sheet | 1620 | 14.15 | 1614 | 6.28 | 1614 | 11.20 | | 12.30 |
| β-sheet | 1630 | 20.71 | 1624 | 15.39 | 1624 | 13.14 | | 19.78 |
| β-sheet | 1638 | 12.72 | 1634 | 15.53 | 1631 | 18.89 | | 14.80 |
| Disordered | 1648 | 12.54 | 1642 | 17.14 | 1641 | 13.93 | | 12.98 |
| α-helix | 1656 | 9.96 | 1651 | 13.33 | 1649 | 12.22 | | 12.35 |

| | | | | | | | |
|---|---|---|---|---|---|---|---|
| Turns | 1666 | 10.26 | 1660 | 12.82 | 1659 | 13.58 | 12.60 |
| Turns | 1676 | 7.59 | 1671 | 11.48 | 1669 | 8.28 | 9.23 |
| Turns | 1685 | 6.94 | 1681 | 9.58 | 1681 | 5.12 | 4.25 |
| β-sheet | 1695 | 5.13 | 1693 | 6.78 | 1691 | 3.63 | 1.70 |
| | | | | | | | |
| **Total content** | | | | | | | |
| α-helix | | 9.36 | | 13.06 | | 13.20 | 12.28 |
| β-sheet | | 52.12 | | 36.94 | | 46.87 | 46.81 |
| Disordered | | 25.80 | | 33.20 | | 28.02 | 26.98 |
| Turns | | 12.72 | | 16.80 | | 11.91 | 13.93 |

\* The IR intensity due to side chain vibration was excluded in the calculation for secondary structures.

For further investigation on the secondary structure, the spectra were subjected to FSD and curve fitting. As shown in **Table 7.2**, native BLG contained 52.5% β-sheet. The predominance of β-sheet was in consistence with previous reports [187], in which it was considered responsible for the rigidity and indigestibility of BLG. When BLG was cationized with EDA, there was a significant conversion of β-sheet (decreased by 29%) into α-helix (increased by 34%), turns (increased by 33%) and random coil (increased by 26%) [179]. This change was attributed to the consumption of Asp and Glu, both of which are present in abundance in β-sheets [220, 221]. Similar results were also observed on PEI-derived CBLG; however, the conformational change induced by PEI was not as significant as that cause by EDA. The content of β-sheet was decreased by 7% and 10% for C-P600 and C-P1200 respectively. As suggested by these data, conjugation of a smaller number (4 or 5) of bulky cationic molecules might have led to a lesser extent of conformational change, compared with the grafting of a greater number (more than 20) of small cations, although the former approach introduced a significantly

greater amount of positive charge. In addition, the compositions of secondary structures for C-P600 and C-P1200 were not significantly different as shown in **Table 7.2**. This result suggested that, compared with the size of the cationizer, the structure (monomeric or polymeric) and number of cationic moieties might have played a more important role in determining the secondary structure of BLG. This postulation was further supported by a follow-up study (data not shown), in which cationization of BLG with PEI-1800 resulted in a similar extent of conformational change as PEI-600 and PEI-1200. Based on the discussions above, PEI might be a better reagent for cationizing BLG while preserving its unique structure. A similar hypothesis was also proposed in previous literatures [42].

### 7.4.3 *In vitro* digestibility of BLG and CBLG

The digestion profiles of BLG and CBLG are depicted in **Figure 7.4**. Native BLG is highlighted for its resistance against peptic digestion. This characteristic was confirmed by our study, in which only 9% of BLG was digested by pepsin in SGF after 4 h. When BLG was cationized by EDA or PEI, its digestibility increased to 17% and 15%, respectively. This phenomenon was probably due to the disruption of β-sheet structure as discussed in the previous section. This change might have led to higher flexibility of BLG molecules and increased exposure of their digestible sites, resulting in elevated accessibility of pepsin to BLG. Similar results were also reported and discussed in a previous literature [205]. In spite of the notable increase, the peptic digestibility of CBLG remained at a low level.

Therefore, CBLG was expected to provide significant protection to incorporated nutraceuticals or drugs against digestion in the stomach.

Under the simulated intestinal condition, approximately 25% of BLG was digested by. A higher tryptic digestibility (32%) was observed for C-EDA, probably due to the formation of Asp-EDA/Glu-EDA conjugates [151]. As discussed before, such amino acid derivatives exhibited similar geometric structure and electronic charging status with lysine, a major substrate of trypsin. Therefore, cationization by EDA might have produced suitable sites for tryptic cleavage, thus increasing the apparent digestibility. PEI, on the contrary, is a polymer with bulky branches and multiple positive charges, and the conjugate formed between Asp/Glu and PEI did not exhibit such similarity to lysine. In addition, the polymeric network of PEI might have acted as a barrier for trypsin (**Figure 7.1**). As a result, the tryptic digestibility of C-P600 (8%) or C-P1200 (6%) was significantly lower than that of BLG or C-EDA. In addition, C-P600 and C-P1200 exhibited similar tryptic digestibility. Such phenomenon indicated that the structure and number of conjugated cationic groups might be more important than their size in determining the apparent digestibility of CBLG. This was in agreement with the discussion in **Section 7.4.2**. Based on these results, PEI-derived CBLG may provide satisfactory protection against both peptic and tryptic digestion, and such protection might remain effective after the target compound enters the circulation system. This

feature is favorable for the encapsulation and delivery of nutraceuticals and drugs that are susceptible to degradation or clearance by the circulation system.
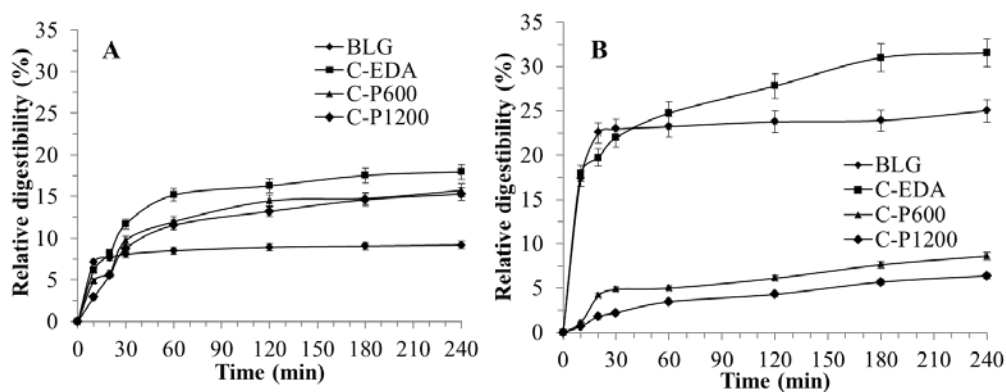


**Figure 7.4** *In vitro* peptic (A) and tryptic (B) digestion profiles of BLG and CBLG.

## 7.4.4 Mucoadhesive properties

Mucin is a highly glycosylated and negative charged protein [222]. Existing in abundance as a gel-like layer covering the small intestine wall, mucin serves as the first barrier for the entry of nutraceuticals or drugs into the circulation system [60]. Affinity to the mucin layer, known as mucoadhesion, is therefore a key factor that determines the bioavailability of oral-administrated bioactives. In this study, two assays (turbidity and QCM) were performed to evaluate the mucoadhesion of BLG and CBLG. In the turbidity analysis (**Figure 7.5A**), native BLG did not display any observable absorbance when mixed with mucin in PBS. On the other hand, CBLG exhibited significant absorbance at 400 nm, which was indicative for the extensive formation of mucin-CBLG aggregates. In addition, the absorbance of C-P600 or C-P1200 was more than twice that of C-EDA. The electrostatic

attraction between anionic mucin and cationic EDA/PEI moieties played a critical role in the aggregation process.
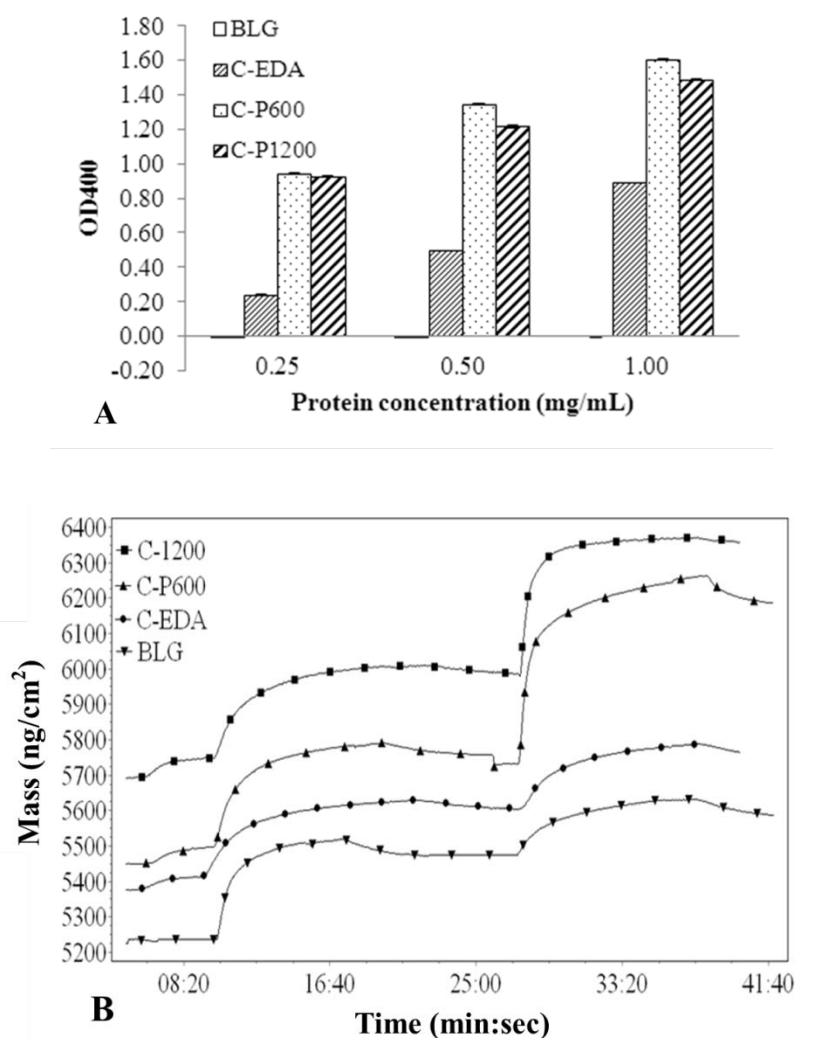


**Figure 7.5** Mucoadhesion of BLG and CBLG measured by (A) turbidity and (B) QCM-D

The improvement in mucoadhesion by cationization was also evidenced by the QCM study. As shown in **Figure 7.5B**, native BLG showed low affinity to the mucin layer that was pre-deposited onto the quartz crystal. After cationization, the mucoadhesion of BLG was increased significantly by 147%, 439%, and 366% for C-EDA, C-P600, and C-P1200, respectively (**Table 7.3**). Improved mucoadhesion

was likely contributed by the high density of positive charge introduced with EDA or PEI. In addition, PEI-derived samples demonstrated more significant improvement in mucoadhesive properties than EDA, probably owing to its highly positive surface charge. The similarity in the mucoadhesive properties of C-P600 and C-P1200 was probably due to the similarity in their conformation that was discussed before. In our preliminary study (data not shown), the surface hydrophobicity of C-P600 or C-P1200 was comparable to that of native BLG, and it was significantly lower than that of C-EDA. Combining these results, we postulated that the electrostatic attraction rather than hydrophobic interaction might have played a dominating role in the mucoadhesion process for cationic proteins. Based on the results on mucoadhesion and protein digestion, PEI-derived CBLGs might be a better solution for enhancing the bioavailability of nutraceuticals or drugs.

**Table 7.3** Mass accumulation of BLG and CBLG samples on mucin estimated from QCM assay *

| Sample | Mucin ng/cm$^2$ | Protein ng/cm$^2$ | Mass ratio (P:M)* |
|--------|-----------------|-------------------|-------------------|
| BLG | 238.3±15.4[a] | 85.4±9.7[c] | 0.357±0.005[c] |
| C-EDA | 195.4±10.7[b] | 172.2±12.5[b] | 0.881±0.100[b] |
| C-P600 | 239.1±20.8[a] | 460.1±40.1[a] | 1.924±0.215[a] |
| C-P1200 | 228.7±19.7[a] | 380.8±32.3[a] | 1.665±0.234[a] |

* Data with different letters indicate for significant difference (P<0.10, experimentwise)

** Weight ratio between deposited protein and mucin.

It was worth mentioning that all studies on mucoadhesion were undertaken at neutral pH. Although some common cationic polymers (e.g., chitosan and its

derivatives) were reported to show comparable mucoadhesive capability [36], these polymers were only positively charged at acidic pH, and they became insoluble at neutral or basic pH due to the deprotonation of their functional groups. The retention of positive charge over a wide range of physiologically relevant pH is a major advantage of CBLG over other polycations, and such property makes EDA- and PEI-derived CBLG an attractive vehicle for transporting bioactives through oral administration.

### 7.4.5 Nanoparticle forming behavior of BLG and CBLG

The particle formation capabilities of BLG and CBLG were summarized in **Table 7.4**. In 90% acetone, native BLG formed particles with an average size of 136.3 nm. After crosslinking with glutaraldehyde and evaporation of acetone, the particles exhibited slightly increased size with decreased count rate. These results suggested that the majority of the particles maintained their size and structure [105], and also indicated for successful crosslinking by glutaraldehyde. Similar results were observed for C-EDA, which aggregated into smaller particles that kept virtually consistent size and count rate.

When PEI-derived CBLGs were used as particle formers, the results on particle sizes and count rates were within a similar range as compared to BLG and C-EDA. However, two major differences were observed with respect to their particle forming behaviors. Firstly, the amount of glutaraldehyde needed for C-P600 and C-P1200 was at least 100% higher than that for BLG and C-EDA. Otherwise, the

nanoparticles were prone to dissociation as indicated by greatly decreased count rate of the dispersion (data not shown). This was probably because of the substantial increase in the number of primary amino groups upon conjugation with PEI. Since primary amino groups were the major substrate for glutaraldehyde-induced crosslinking [23], increased number of these groups suggested the requirement for higher dose of glutaraldehyde in order to achieve complete crosslinking. Furthermore, the large amount of positively charges introduced by PEI resulted in strong electrostatic repulsion between CBLG molecules. Such change necessitated more covalent bonds to overcome the repulsive force and maintain the compact structure of nanoparticles. Although excessive glutaraldehyde could be removed by dialysis, it is necessary to determine the level of residual glutaraldehyde as well as the toxicity of the final product. Substitution of glutaraldehyde by other reagents (genipin, citric acid, etc.) might also help lowering the toxicity of CBLG nanoparticles. Further studies are needed to address these issues.

**Table 7.4** Particle forming behaviors of BLG and CBLG *

| Sample | Glutaraldehyde ug/mg protein | Dilution factor | Particle size nm | | Count rate kcps | |
|---|---|---|---|---|---|---|
| | | | Before evaporation | After evaporation | Before evaporation | After evaporation |
| BLG | 40 | 100% | $136.3\pm7.6^a$ | $150.4\pm3.5^d$ | $386.2\pm20.5^a$ | $359.7\pm16.7^a$ |
| C-EDA | 40 | 100% | $93.5\pm5.2^c$ | $116.7\pm1.5^e$ | $314.6\pm11.4^b$ | $298.4\pm22.1^b$ |
| C-P600 | 80 | 100% | $145.6\pm2.4^a$ | $194.3\pm4.2^b$ | $259.1\pm30.1^a$ | $280.4\pm14.5^b$ |
| C-P600 | 80 | 200% | $144.1\pm3.1^a$ | $160.3\pm4.4^d$ | $187.3\pm16.5^c$ | $177.9\pm16.2^c$ |
| C-P1200 | 80 | 100% | $132.7\pm7.5^a$ | $400.2\pm8.9^a$ | $351.1\pm18.9^{ab}$ | $80.7\pm9.4^{de}$ |
| C-P1200 | 80 | 200% | $126.5\pm6.1^b$ | $170.6\pm6.7^c$ | $150.3\pm12.6^c$ | $100.4\pm7.5^d$ |
| C-P1200 | 80 | 400% | $115.4\pm4.2^b$ | $120.4\pm2.5^e$ | $80.6\pm9.4^d$ | $68.5\pm6.5^e$ |
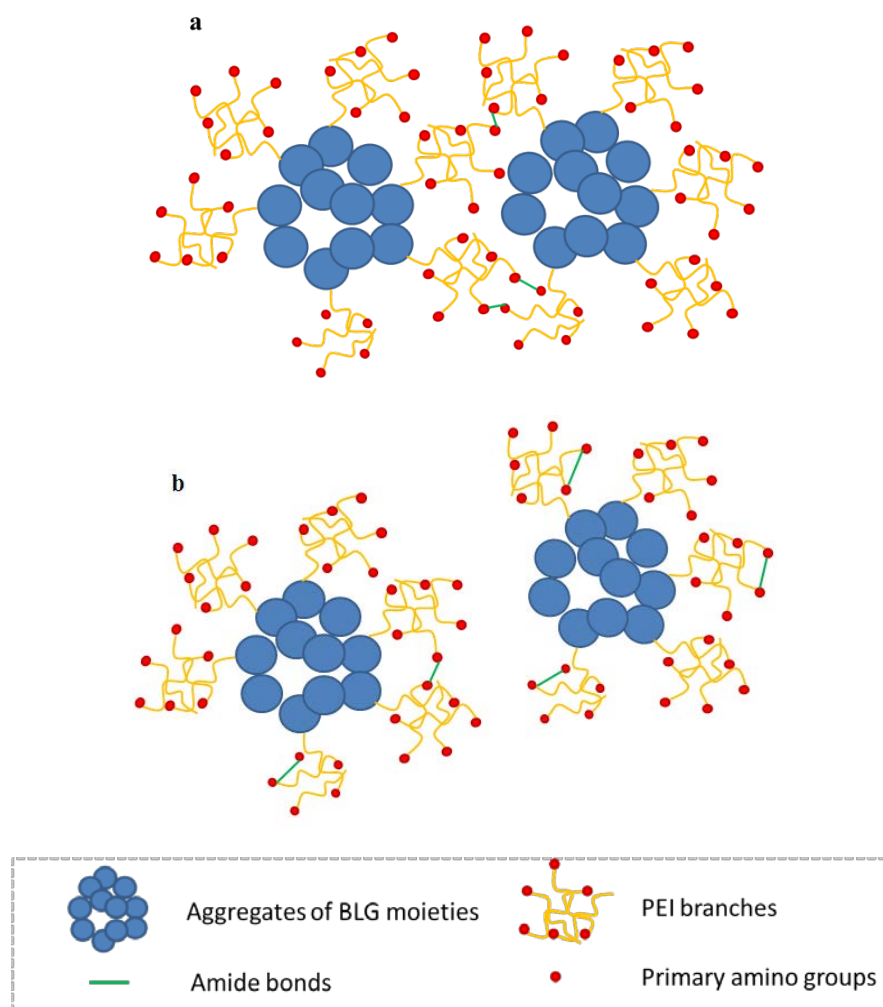
**Figure 7.6** Schematic illustration on the preferential crosslinking among C-PEI nanoparticles.

At higher concentrations (a), crosslinking across adjacent nanoparticles was favored, resulting in the formation of gel-like structure. Upon dilution (b), crosslinking was more likely to take place within a single particle. Such process contributed to the maintenance of nanoparticle morphology.

The second difference was that a dilution procedure was needed, especially for C-P1200. In our preliminary study, C-P1200 formed a significant number of nanoparticles in 90% acetone, but these particles were unable to maintain their morphology after evaporation. At lower glutaraldehyde doses (40-80 ug/mg

protein), the nanoparticle dispersion became a clear solution after evaporation. When higher doses of glutaraldehyde (120-160 ug/mg protein) were applied, the dispersion turned into a dark-colored gel. A possible explanation for these phenomena lied in the structure of branched PEI molecules. PEI possesses a highly branched structure with a large number of amino groups. However, only 30-40% of them are primary amino groups [61], which are reactive with glutaraldehyde. When PEI-derived CBLG formed nanoparticles, the surface of the particles was probably covered by PEI branches as indicated by the highly positive zeta potential. The distance between two reactive amino groups, together with internal steric hindrance caused by the PEI network, could therefore impede glutaraldehyde molecules from effectively crosslinking within a single particle. On the other hand, due to the large number of nanoparticles in the dispersion, there was an increased chance for two nanoparticles to approach each other, exposing their primary amino groups that could be connected by glutaraldehyde **Figure7.6a**). This could possibly explain the formation of gel instead of individual particles by C-P1200 after evaporation. When the dispersion was diluted, the odd for inter-particle crosslinking was greatly reduced, whereas the opportunity for crosslinking within a same particle was virtually unchanged (**Figure 7.6b**). Therefore, the average size and count rate of particles were better maintained. However, further studies need to be carried out to test such hypothesis and to establish new strategies to synthesize C-P1200-based nanoparticles.
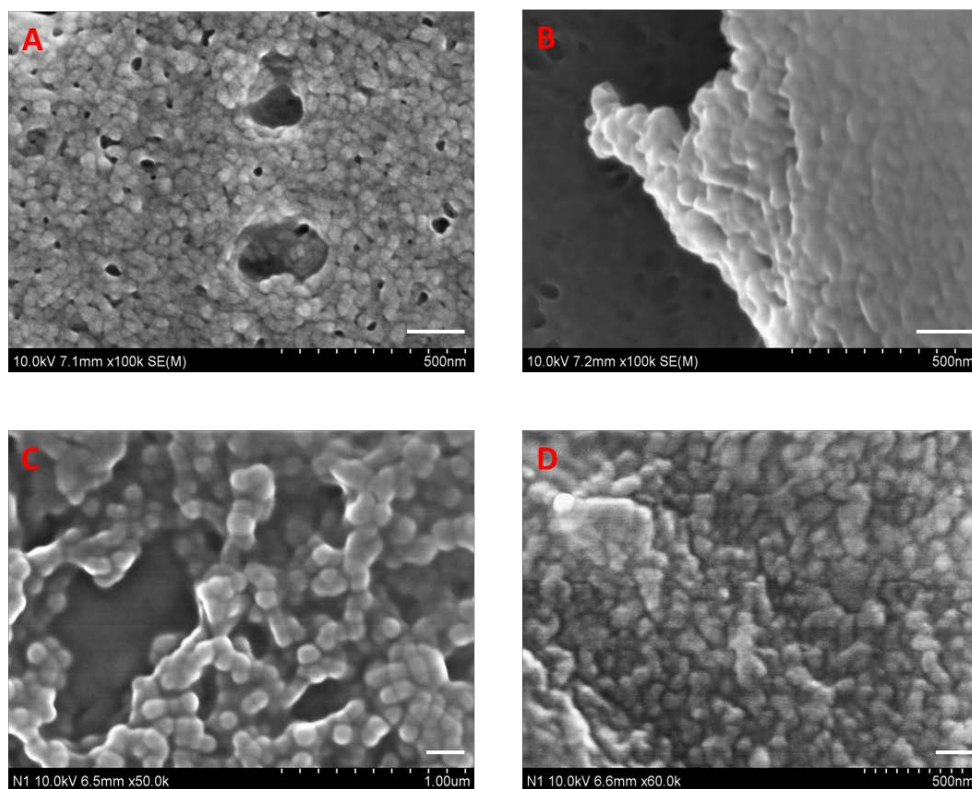
**Figure 7.7** SEM images of nanoparticles formed with (A) BLG, (B) EDA-derived CBLG, (C) PEI-derived CBLG, before evaporation, and (D) PEI-derived CBLG, after evaporation.

**Figure 7.7** showed the morphology of nanoparticles formed by BLG (A), C-EDA (B) and C-P600 (C). The particles were approximately spherical and smooth in surface. The sizes of BLG and C-EDA nanoparticles were slightly larger than that of C-P600 nanoparticles, which was consistent with the data from DLS study. This difference was possibly caused by the repulsion between the bulky, highly charged PEI moieties on C-P600. The reason why sizes observed under SEM were generally lower than those obtained by DLS was probably the shrinkage of particles under vacuum [51]. **Figure 7.7D** displayed the structure of C-P600 nanoparticles after crosslinking and evaporation. Most particles maintained their original shape and size, although some aggregates were observed under SEM.

## 7.5    Conclusions

CBLG was successfully synthesized from BLG using two strategies: coupling BLG with a larger quantity of cationic monomers (EDA) or with a smaller number of polycations (PEI-600 and PEI-1200). Both methods led to the reversal of net charge of BLG molecules, together with satisfactory dispersion stability at neutral pH. Compared with the EDA-involved approach, PEI-derived cationization resulted in lower conjugation degree, but the net charge and zeta potential obtained from the latter approach was significantly higher than that achieved through the former one. In the *in vitro* digestion study, cationization with PEI led to less significant conformational change of BLG, resulting in better inheritance of the resistance against peptic digestion from native BLG. In addition, PEI-derived CBLG was more resistant against tryptic digestion than BLG as well as C-EDA. Substantial improvement in mucoadhesion was observed for PEI-derived CBLG compared to BLG or C-EDA, probably owing to the steric hindrance provided by PEI. Lastly, in the presence of acetone and glutaraldehyde, PEI-derived CBLG could aggregate into nanoparticles with average size at 140 nm, and the formed particles maintained their morphology after evaporation. These characteristics made PEI-derived CBLG an attractive candidate as a bioavailability enhancer for poorly absorbed bioactives.

# Chapter 8 Cationic beta-lactoglobulin Nanoparticles as a Bioavailability Enhancer: Effect of Surface Properties and Size on the Transport and Delivery *in vitro*

## 8.1 Abstract

The chemical structure and environmental factors dictate the surface properties of nutraceutical or drug carriers, determining their stability and behavior in various physiological processes following oral administration. In this chapter, we firstly illustrated how these two factors influenced the surface charge, hydrophobicity, and size of cationized beta-lactoglobulin (CBLG) molecules and nanoparticles, a novel drug delivery system that we developed recently, followed by exploring the relationship between their surface properties and performances. The CBLG nanoparticles were able to transport most of the encapsulated drug intact through the gastrointestinal (GI) tract owing to its minimal particle digestion. Other advantageous properties of CBLG-based systems included superior mucoadhesion, permeation across the small intestine epithelia, and cellular uptake. Moreover, in a comparison between BLG/CBLG molecules and nanoparticles, the individual molecules exhibited better tight junction opening capacity and higher cytotoxicity, whereas the nanoparticles displayed superior mucoadhesion, permeation across the Caco-2 monolayer, and cellular uptake. Finally, as CBLG molecules or nanoparticles absorbed the negatively charged serum proteins in the cell culturing medium, their surface properties, cytotoxicity, and cellular uptake were

significantly altered. This research not only provided an attractive nutraceutical/drug delivering vehicle but also shed some light on the fate of nano-sized drug carriers upon oral administration.

## 8.2 Introduction

Nanoparticles as a promising bioavailability enhancer of poorly absorbed nutrients and drugs have been studied extensively in recent decades [223, 224]. Proteins as biopolymers are gaining increasing interest as encapsulants, owing to their natural abundance, biodegradability, and biocompatibility [225, 226]. In addition, proteins are amphiphilic polymers which could interact adequately with both the solvent and different types of drugs via electrostatic and hydrophobic interaction, as well as extensive hydrogen bonding [105]. Compared to polysaccharides that exhibit an extended linear or branched structure, proteins tend to adopt a more compact and flexible conformation that favors the formation of nanoparticles and inclusion of drugs [137]. Despite these merits, there exist several drawbacks that impede the application of protein-based nanoparticles. Firstly, oral administration is the most convenient route for the administration of drugs or nutraceuticals. However, many conventionally utilized proteins are rapidly digested in the GI tract, thus losing the protective effect on the entrapped compound [163]. In addition, most naturally abundant proteins are negatively charged [105, 227], which implies insufficient adsorption to biological surfaces such as the small intestinal epithelia and cell membranes, both of which carry negative net charges [170, 228]. Therefore, it is

meaningful to develop novel protein derivatives that overcome the shortcomings of native proteins while inheriting their advantages.

The transport and delivery of the encapsulated drugs in human body is a complex process that involves a number of biological interactions. Many of these procedures, ranging from the transport in the GI tract to the internalization by targeted cells or tissues, require the delicate design of drug-loaded vehicles that could interact appropriately with specific biological surfaces or compounds [228]. It is rational to deduce that these interactions are highly dependent on the surface properties of the drug carriers where the contact takes place, and that these properties are determined by both the chemical composition of the encapsulants and the environment they are situated in [229, 230]. *In vitro* studies provide a powerful tool reveal such dependency. Compared to *in vivo* studies which are focused on the overall effect of drug encapsulation, *in vitro* analyses enable us to illuminate the influence of structural and environmental factors on the fate of drug-loaded vehicles in individual processes, providing valuable guidance on the precise design of novel drug carriers.

Recently, we developed a novel protein derivative, cationic beta-lactoglobulin (CBLG) [151, 163]. Native BLG, a major component of the whey protein, is a highly water soluble globulin that possesses inherent patches for binding lipophilic nutrients. It also exhibits a unique resistance by pepsin together with moderate

digestibility by trypsin. The CBLG inherited these advantages from native BLG, and it exhibited marked mucoadhesion due to its positive charge. In this study, we synthesized nanoparticles from native BLG and two CBLGs with similar surface charge but distinct structures. The surface charge, surface hydrophobicity, and average size of BLG/CBLG molecules and nanoparticles were compared in different solvents to assess the combined effect of chemical structure and buffering solution. Furthermore, we evaluated the performances of BLG/CBLG molecules or nanoparticles in some key processes relevant to the delivery of oral-administrated nutraceutical/drug carriers: digestion, mucoadhesion, permeation across the small intestine, and cellular uptake. The role of surface properties and size on the behavior of BLG/CBLG molecules or nanoparticles will be discussed in details.

## 8.3 Materials and Methods

### 8.3.1 Materials

The following chemicals were purchased from Sigma-Aldrich (St. Louis, MO, USA): bovine BLG (90% purity), ethylenediamine dihydrochloride (EDA, 98% purity), branched polyethyleneimine (MW 600, abbreviated as P600), N-(3-dimethylaminopropyl)-N-ethylcarbodiimide (EDC, 97% purity), fluorescein isothiocyanate (FITC) curcumin (98% purity), pepsin (3,200-4,500 units/mg), and trypsin (10,000 BAEE units/mg). Porcine stomach mucin (PSM, type III, contains 0.5-1.5% sialic acid) was obtained from Himedia Co., India. All reagents involved

in cell study were purchased from Life Technologies (Grand Island, NY, USA). All other reagents were of analytical grade.

### 8.3.2 Synthesis and characterization of CBLG molecules and nanoparticles

CBLG was synthesized via an EDC-aided coupling reaction [151]. BLG and the cationizers (EDA or PEI) were dissolved in deionized water at 20 and 100 mg/mL, respectively. The pH was then adjusted to 4.75 using 1 mol/L HCl for BLG solution or concentrated HCl for cationizer dispersion. Thereafter, 5 mL of BLG solution was added slowly to 30 mL cationizer dispersion under mild stirring, and the mixture was incubated at room temperature for 15 min. Cationization was initiated by the addition of 30 mg EDC and terminated by adding 108 μL sodium acetate buffer (4 mol/L, pH 4.75) after 4 h. The resultant dispersion was subjected to dialysis centrifugation (5,000 $g$, 30 min), using a Macrosep® centrifuge tube (MW cutoff 10 kDa, Pall Corp., Ann Harbor, MI) with a built-in filtering membrane. The retentate obtained after centrifugation was further dialyzed against deionized water at 4 °C for at least 48 h and freeze dried. The moisture content of the final product was less than 5%, and the protein content was above 90% according to Bradford assay calibrated with BSA. The samples were designated as C-EDA and C-P600 for EDA- and P-600-derived CBLG, respectively.

Nanoparticles were prepared from BLG and CBLG by organic solvent desolvation as previously described [151]. The protein was dissolved in deionized water at pH 7.5 and a concentration of 1 (BLG), 0.75 (C-EDA), or 0.6 mg/mL (C-P600). After

217

one hour of equilibration, pure acetone was added dropwise to achieve an acetone/water ratio of 90/10 (v/v, same hereinafter), which triggered the formation of nanoparticles. Glutaraldehyde as a crosslinker was added thereafter to harden the particle structure. The mass ratios between glutaraldehyde and protein were 40, 80, and 120 μg/mg protein for BLG, C-EDA, and C-P600, respectively, as determined in our previous reports [163]. After 8 h of crosslinking, the added acetone was supplemented with water to achieve an acetone/water ratio of 50/50, and the acetone was evaporated under a constant nitrogen flow. The obtained dispersion was filtered through a 0.22 μm Acrodisc syringe filter membrane (Pall Co., Newquay, UK). The filtrate was then subjected to dialysis centrifugation (5,000 $g$, 30 min, molecular weight cutoff = 100 kDa) to remove free protein molecules and unreacted glutaraldehyde, as well as to enrich the nanoparticles to a concentration of 5 mg/mL, the latter of which was estimated by weight determination after lyophilization. To synthesize the curcumin-loaded nanoparticles, a curcumin/acetone stock solution (2 mg/mL) was applied in place of pure acetone in the desolvation process. All samples were stored at 4 °C until subsequent analyses. The nanoparticles prepared with BLG or CBLG were named as the terms of the constituent proteins followed by the abbreviation "NPs".

The molecular weights (MW) of BLG and CBLG were determined by matrix assisted laser desorption/ionization time-of-flight (MALDI-TOF) mass spectrometry as described **Section 7.3.3**. The difference in MW before and after

cationization ($\Delta M$) was adopted to calculate the conjugation degree and net charge of CBLG as discussed in **Section 7.3.3**. The dispersions of BLG, CBLG, and their nanoparticles were then diluted in three different buffers, namely, Hank's balanced salt solution (HBSS), Dulbecco's modified Eagle's medium (DMEM), and DMEM supplemented with FBS. The dispersions in DMEM with FBS were subjected to dialysis centrifugation as described above to remove unbound serum protein, while the other dispersions were measured without such treatment. All the dispersions were measured for their $\zeta$-potentials by laser Doppler velocimetry using a Nano ZS90 Zetasizer (Malvern Inc., Malvern, UK). The surface hydrophobicity ($S_o$) of the samples was measured using 8-anilino-1-naphthalenesulfonic acid (ANS) as a hydrophobic probe [151], as described in **Section 6.3.5**.

The particle sizes and count rates were measured by dynamic laser scattering (DLS) as described in **Section 7.3.9**. No dilution was carried out before the measurement. The data were analyzed using the cumulant algorithm, and the quadratic mean particle size was reported.

### 8.3.3 Determination of the releasing profile and particle disintegration

Curcumin as a model drug was incorporated into BLG or CBLG nanoparticles, which were analyzed for their releasing profiles by a previously reported method [227]. Release was initiated by mixing 2 mL of the sample with 8 mL SGF (commercial SGF containing 5 mg/mL Tween 20 and pepsin at a substrate/enzyme

ratio of 100:1, w/w), followed by incubation at 37 °C in a reciprocal shaking bath (120 rpm). At predetermined time intervals, 0.5 mL of the mixture was withdrawn, diluted with 2.0 mL PBS (pH 7.2, 100 mM, containing 5 mg/mL Tween 20) and analyzed for its particle size and count rate by DLS. Another aliquot of 0.5 mL was withdrawn and diluted using the same procedure, followed by dialysis centrifugation (5,000 $g$, 30 min) using a Macrosep® centrifuge tube (MW cutoff = 100 kDa, Pall Corp., Ann Harbor, MI). The curcumin-containing Tween-20 micelles were diluted appropriately with PBS and then measured for the content of released curcumin spectrophotometrically at the wavelength of 426 nm. When surfactant such as Tween 20 is added, the released curcumin maintained its stability, as was demonstrated in previous literatures [231]. Fresh mixture of SGF and Tween 20 was supplemented after each measurement to maintain sink condition.

On the other hand, another batch of the samples was mixed with SGF at a same ratio and digested for 60 min at 37 °C. The digesta was diluted with PBS and centrifuged as mentioned above, and the retentate containing intact nanoparticles was supplemented with PBS to 2 mL. The dispersion was incubated at 37 °C for 15 min and then mixed with 8 mL preheated SIF (commercial SIF added with 5 mg/mL Tween 20 and trypsin at a BLG/trypsin ratio of 100:1, w/w). The progressions in drug release, particle size, and count rate in SIF were tested following the similar procedure as that for SGF.

## 8.3.4 Determination of mucoadhesive properties

The mucoadhesion properties of BLG/CBLG molecules and nanoparticles were assessed by quartz crystal microbalance (QCM) analysis [151], using a gold-coated AT-cut quartz crystal with a fundamental frequency of 4.95 MHz (QSX-301, Q-Sense Co., Linthicum, MD, USA). PBS (pH 7.2, 10 mM) was used for dilution and rinsing in this section. Prior to the measurement, the crystal was soaked in Piranha solution (NH$_3$·H$_2$O: H$_2$O$_2$: H$_2$O=1:1:5, v/v/v) for 15 min at 70 °C, dried with nitrogen, and then mounted on the Q-Sense E1 microbalance (Q-Sense Co., Linthicum, MD, USA). Different dispersions were passed through the sample chamber using a peristaltic pump (Ismatec Reglo, Glattbrugg, Switzerland) in the following sequence: PBS, mucin dispersion (400 μg/mL in PBS, filtered through a 220 nm membrane), PBS, sample dispersion (diluted with PBS to 100μg/mL), and PBS. The deposition of mucin on the gold chip and that of BLG/CBLG on the mucin layer triggered a significant reduction in the oscillation frequency of the chip, which was recorded by the QTools 3 software (Q-Sense Co., Linthicum, MD, USA). The fifth overtone of the frequency was converted to deposited mass (in ng/cm$^2$ crystal surface) using the Sauerbrey model. Mucoadhesion was expressed as the mass ratio of BLG/CBLG to mucin deposited on the crystal surface.

### 8.3.5 Cell culture

Human colon adenocarcinoma cell line (Caco-2) was provided by the American Type Culture Collection (Manassas, VA, USA). The cells were cultured in Dulbecco's modified Eagle's medium (DMEM) supplemented with 10% (v/v, same in this section) fetal bovine serum (FBS) and 1% penicillin-streptomycin in a humidified incubator with 5% $CO_2$ at 37 °C. The growth medium was changed every other day, and the cells were subcultured after reaching 80-90% confluence.

### 8.3.6 Transport of nanoparticles via Caco-2 cell monolayer

Caco-2 cells were seeded at a density of $3 \times 10^5$ cells/cm$^2$ on a Costar Transwell 12-well plate (Corning Costar Corp., NY), which contained a tissue culture-treated microporous insert (diameter = 12 mm, growth area = 1.1 cm$^2$) in each well. The culturing medium was replaced every 48 h for the first 6 days and every 24 h thereafter. The transepithelial electrical resistance (TEER) values, measured with an EVOM$^2$ Epithelial Voltohmmeter (World Precision Instruments, Sarasota, FL, USA), reached 600-800 $\Omega$/cm$^2$ after 16-20 days. Prior to the assay, the culture media in both apical and basolateral compartments were carefully aspirated and replaced with pre-warmed HBSS, which was incubated at 37 °C for 30 min and displaced. Depending on the type of study, the apical (for apical-to-basolateral transport) or basolateral (for basolateral-to-apical transport) part of the plate was designated as the donor compartment and filled with proper volumes of samples (dispersed in HBSS). The other one defined as the receiving compartment was

added with HBSS only. At designated time intervals, appropriate amount of samples was withdrawn from the receiving compartment and analyzed for their FI, and an equal volume of fresh HBSS was then replenished to each receiving well. The apparent permeability coefficient (Papp) was calculated as follows:

$$P_{app} = \frac{\partial Q}{AC_0\, \partial t} \qquad (1)$$

Here $\partial Q/\partial t$ was the permeability rate, A stood for the surface area of the membrane filter, and $C_0$ represented the initial concentration in the donor compartment.

### 8.3.7 Cell uptake study

For quantitative study,, all samples were labeled with FITC using an FITC Labeling Kit (Thermo Fisher Scientific Inc., Rockford, IL). The cells were seeded in a black 96-well plate at $3\times10^4$ cells/well and incubated until a confluence of 80% was achieved. The growth medium was then replaced with a transport buffer (DMEM with or without FBS) and incubated at 37℃ for 30 min. Two hundred microliters of the labeled suspension was incubated with the cells for 4 h. At designated time intervals, the cell monolayer was washed with PBS three times to remove unabsorbed nanoparticles. The cells were then lysed with a solution containing 0.5% Triton X-100 and 0.2 mol/L NaOH to expose the internalized nanoparticles. The fluorescent intensity was then measured using a PerkinElmer Victor X3 multilabel plate reader (PerkinElmer Inc., Waltham, MA) with an excitation and emission wavelength at 485 nm and 535 nm, respectively.

### 8.3.8   Statistics

All measurements were performed in triplicates. The results were expressed as means ± standard error. To identify statistically significant difference, the data were subjected to analysis of variance followed by Tukey's test with an experimentwise confidence level of $\alpha=0.10$, using SAS 9 software (SAS Institute Inc., Cary, NC, USA).

### 8.4   Results and Discussion

### 8.4.1   Characterization of BLG and CBLG nanoparticles

**Figure 8.1** illustrates the surface structures of BLG/CBLG and compares several characteristics that are closely related to drug delivery. Upon cationization, the zeta potential was altered significantly to from -35.8 mV for BLG to 39.4 and 46.8 mV for C-EDA and C-P600, respectively, which was anticipated to favor the mucoadhesion and cellular uptake. On the other hand, the surface hydrophobicity ($S_o$) of C-EDA was 13-fold higher than that of BLG, whereas the $S_o$ of C-P600 was 60% lower than that of BLG. According to our previous study [151, 163], the disparity in $S_o$ was explained by the different extents of conformational change and the hydrophobic/hydrophilic nature of the EDA/P600 backbone [205]. Another important factor regarding the surface properties was that the positively charged amine groups are compactly distributed on the polymeric branches of P600, thus creating a multivalent environment which may benefit the mucoadhesion and cellular uptake of C-P600 [232, 233]. As for the nanoparticles,

they tended to exhibit a more negative (or less positive) zeta potential and higher

surface hydrophobicity, compared to their molecular form. The first change could

be explained by the consumption of cationic amine groups by crosslinking with

glutaraldehyde [105], while the latter one was probably due to the partial protein

unfolding by organic solvents [25].



BLG

MW: 18215
Net charge: -7
ZP: -35.8 mV (monomer);
    -42.6 mV (NPs)
$S_0$: 108.5 (monomer)
    198.4 (NPs)

C-EDA

MW: 19188
Conjugation degree: **21**
Net charge: +35
ZP: +39.4 mV (monomer);
    +33.7 mV (NPs)
$S_0$: 1419.4 (monomer);
    1782.3 (NPs)

C-P600

MW: 21305
Conjugation degree: **5**
Net charge: +58 (max)*
ZP: +46.8 mV (monomer);
    +39.9 mV (NPs)
$S_0$: 41.3 (monomer);
    78.3 (NPs)
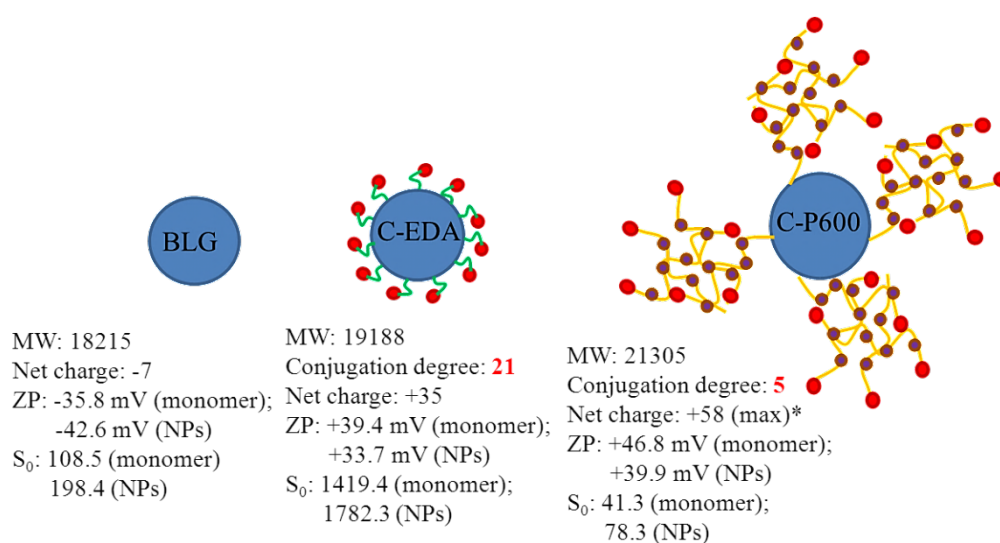
**Figure 8.1** Structure and physiochemical characteristics of BLG and CBLG.
\* Theoretical value when all of the amine groups on P600 are protonated.

When drug-encapsulating systems are consumed via oral administration, they are

exposed successively to various physiological buffers that may also alter their

surface properties [229, 230]. When conducting *in vitro* tests, one should use

appropriate buffers that are relevant to the intended application of the drug carriers,

and the effect of the buffering solutions on the outcome should not be overlooked.

Two of the most commonly used buffers for cell culture studies [151], HBSS and

DMEM, contained abundant ions that deprived the surface charge of the samples

and decreased their zeta potentials by up to 48% (in terms of their magnitude, same hereinafter, **Figure 8.2A**). This resulted in lower electrostatic repulsion among the charged groups, leading to extensive aggregation of BLG/CBLG molecules and nanoparticles as evidenced by greater average sizes (**Figure 8.2C**). Moreover, the reduction in electrostatic repulsion rendered the proteins and nanoparticles to adopt a more compact structure with less hydrophobic chains exposed [151], resulting in a decrease in $S_o$ (**Figure 8.2B**).
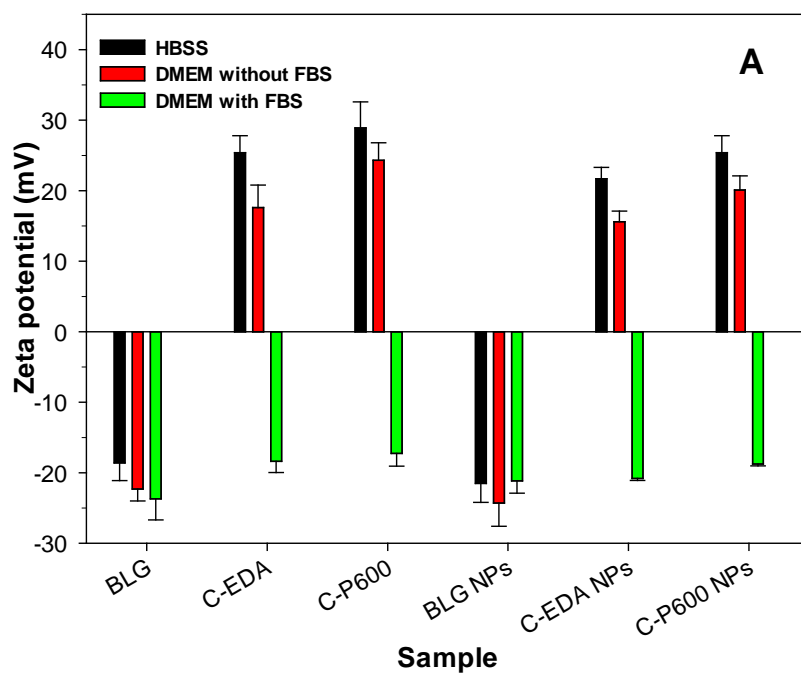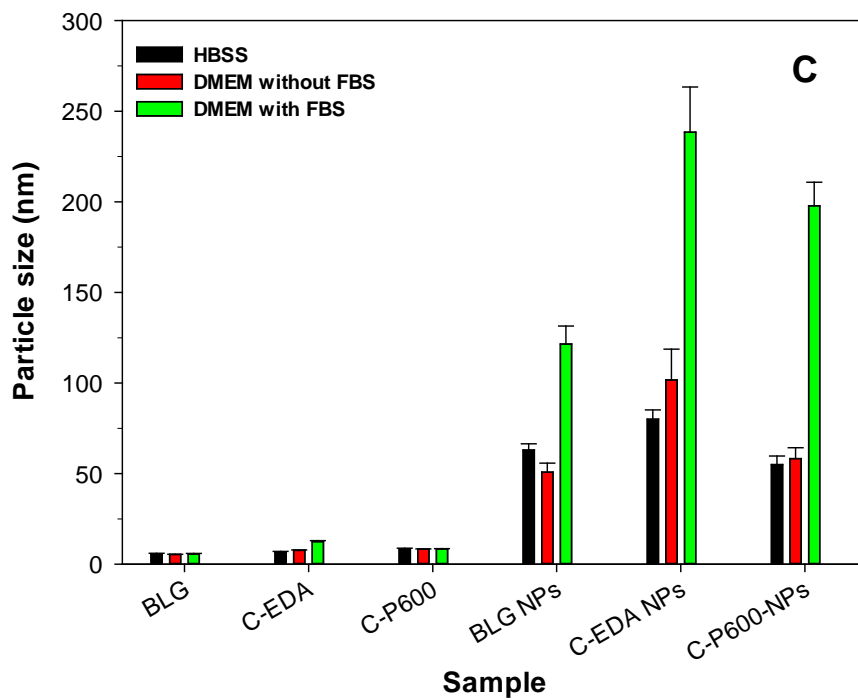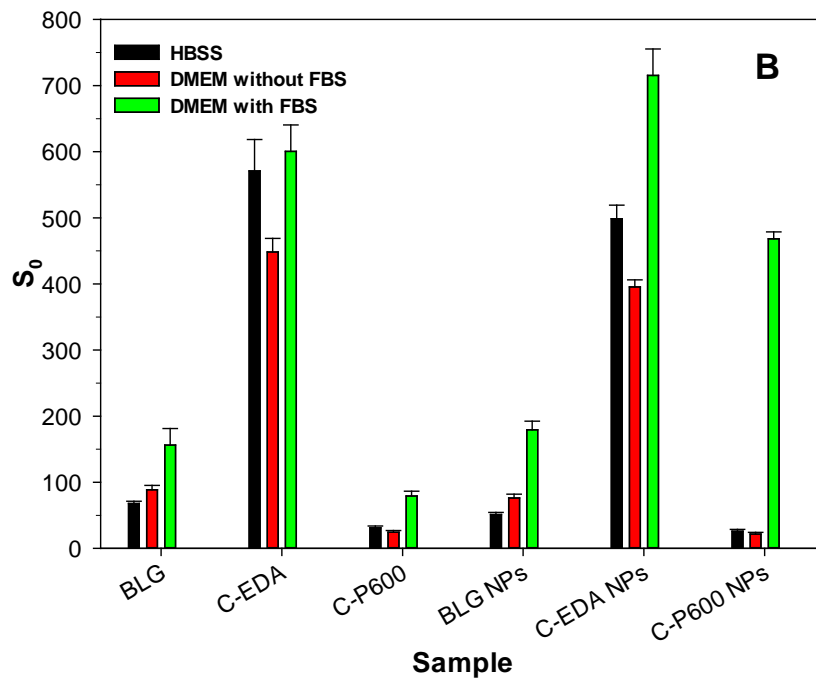
**Figure 8.2** Zeta potential (A), surface hydrophobicity (B) and particle size (C) of BLG/CBLG molecules and nanoparticles

227

FBS contains abundant negatively charged proteins such as bovine serum albumin (BSA) [234]. In FBS-containing DMEM, all the samples exhibited negative zeta potentials at around -20 mV and higher surface hydrophobicities, both of which are the characteristics of BSA [193]. These changes indicated the acquisition of a negatively charged serum protein corona [235], resulting in a significant increase in the particle size by up to 198% (**Figure 8.2C**). Amongst all samples, C-EDA nanoparticles exhibited the greatest increase in average size, possibly due to its high surface hydrophobicity that resulted in more significant aggregation via hydrophobic interaction.

In the following sections, the performance of BLG and CBLG molecules or nanoparticles in several biological procedures will be compared systematically, and their behaviors under these conditions will be correlated to the surface properties as discussed above.

### 8.4.2 Transport of BLG/CBLG nanoparticles through the GI tract

The first harsh environment that the drug encapsulants are exposed to is the GI tract, which contains strong acid and various enzymes [227]. Investigation on the particle disintegration and drug release is critical for biopolymer-based nanoparticles, since many biomacromolecules degrades readily in the digestive system. **Figure 8.3A** depicted the releasing profile of curcumin from the BLG/CBLG nanoparticles. The weight ratio between curcumin and BLG was 10%, and the encapsulation efficiency was over 95% (preliminary data not shown).

These numbers were higher than those achieved with many other polymers, such as zein [32] and soy protein [105]. As can be seen, more than 80% of the encapsulated curcumin was released from the BLG nanoparticles into SGF in the first 30 min, and the percentage continued to increase to 95% after the nanoparticles were placed in SIF. On the other hand, nanoparticles formed by CBLG exhibited significantly lower rate of release, with less than 25% of the curcumin being released after the treatments with SGF and SIF.

The rapid drug release from BLG nanoparticles was unexpected, because BLG molecules were resistant against pepsin and only moderately digested by trypsin [151]. This phenomenon prompted us to investigate the disintegration of BLG nanoparticles. As shown in **Figure 8.3B**, BLG nanoparticles showed an increase in their average size by 6-fold when treated in SGF, accompanied by a decrease by 39% in the count rate (**Figure 8.3C**). At the end of treatment, only 17% of the count rate was retained. Given the fact that the count rate changes proportionally to the number of the particles as well as the sixth power of the particle size [23], these results suggested that the number of smaller nanoparticles in the dispersion decreased significantly, whereas the larger particles were relatively stable [227]. When transferred into the SIF, both the size and count rate declined continuously, suggesting the decomposition of both smaller and larger particles. On the contrary, CBLG nanoparticles maintained remarkable stability against peptic and tryptic digestions, which could explain the low releasing rate of curcumin in these

samples. This character made CBLG nanoparticles an attractive candidate for delivering poorly absorbed nutrients or drugs via oral administration.

The difference in the particle integrity against digestive enzymes was speculated to arise from the covalent bonds maintaining the particle structure. Glutaraldehyde as a crosslinker reacts with the primary amine groups on the lysine residue of native BLG [23], forming amide bonds that might be susceptible to peptic and tryptic digestion. After cationization, the grafted EDA and P600 moieties might have reacted with glutaraldehyde and formed a significant number of amide bonds that were more difficultly digested, because their geometric and physicochemical properties were greatly different from the ones formed between glutaraldehyde and lysine. Alternatively, they might have shielded the glutaraldehyde-lysine bonds through steric hindrance, preventing them from being cleaved. A follow-up study using native BLG and a different crosslinker (such as an enzyme or polyphenol) to form nanoparticles is underway to validate these postulations.
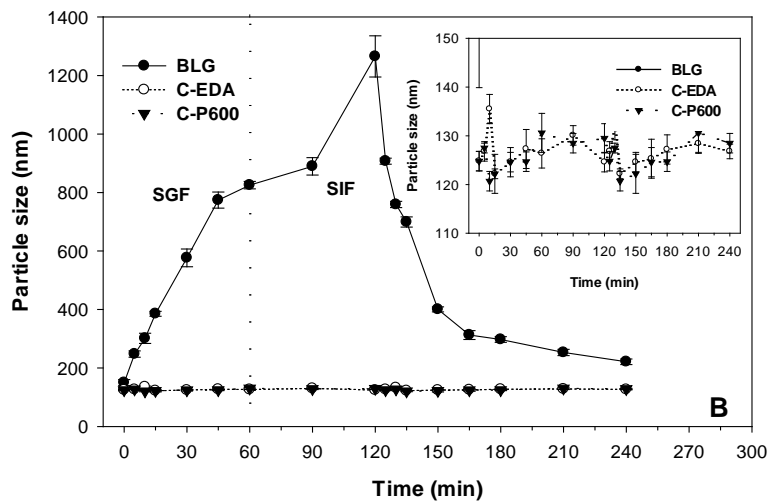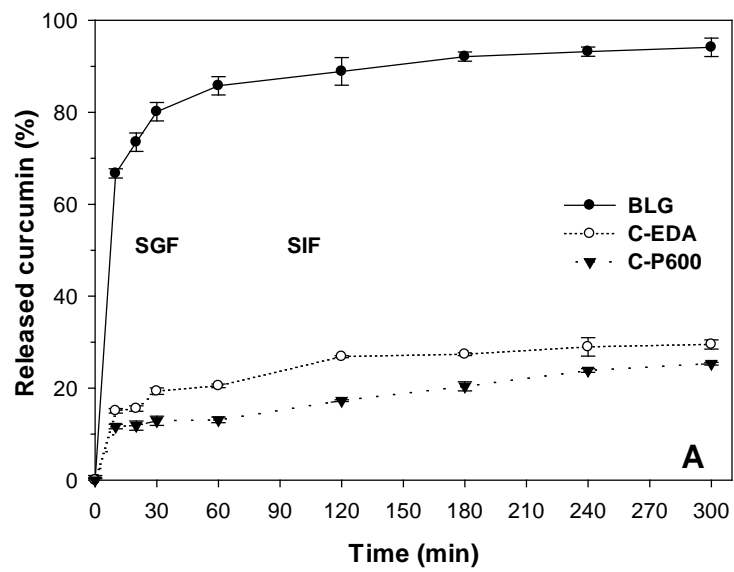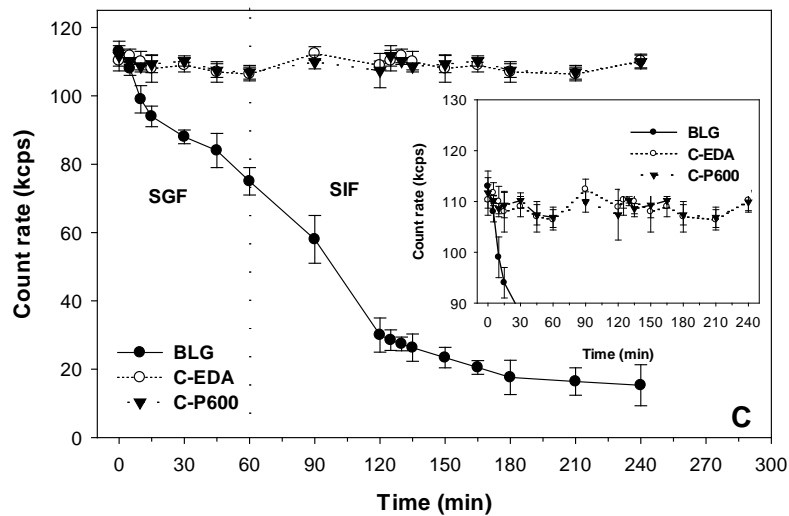
**Figure 8.3** Releasing profile (A) and particle disintegration (B and C) of curcumin-loaded BLG/CBLG nanoparticles.

## 8.4.3 Mucoadhesion

Once the drug carriers arrive intact at the small intestine, they adsorb to and pass through the small intestine epithelia. The transport across the small intestine depends on two procedures, namely, adhesion to the mucosa (mucoadhesion) and the permeation across the small intestine epithelia. Mucin as an anionic glycoprotein covers the small intestine mucosa, forming the first barrier for incoming nutrients or drugs [236]. Cationic polymers such as chitosan or poly (amido amine) (PANAM) dendrimers are highly mucoadhesive owing to their electrostatic attraction with mucin [237]. Some neutral (e.g., cellulose derivatives) or anionic (e.g., sodium alginate) macromolecules also demonstrate considerable mucoadhesion probably through extensive hydrogen bonding [238]. In our study, BLG showed a very low protein/mucin weight ratio of 0.171. On the contrary, C-EDA and C-P600 exhibited a protein/mucin ratio of 0.743 and 1.148,

respectively (**Figure 8.4A**), which were significantly higher than those for other biopolymers, including chitosan and hydrophobically modified polysaccharides [13]. The improvement in mucoadhesion could be rationally ascribed to the abundant positive charge of these two biopolymers. Furthermore, C-P600 possesses both highly positive charge and strong hydrogen bonding capacity [239], which imparted it with the greatest mucoadhesion capacity.
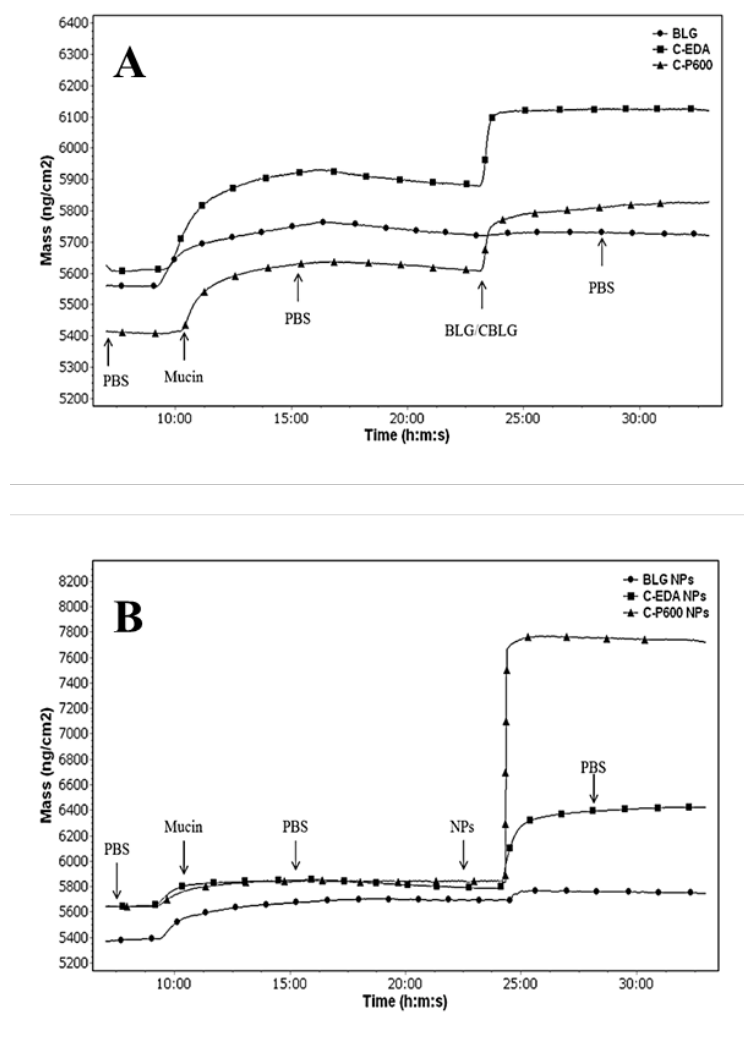


**Figure 8.4** Mucoadhesion of BLG/CBLG molecules (A) and nanoparticles (B)

Intriguingly, as shown in **Figure 8.4B**, the nanoparticles showed much higher mucoadhesion than their constituent molecules, in spite of the fact that the former exhibited less positive charges than the latter. The protein/mucin ratio of C-EDA and C-P600 nanoparticles increased phenomenally to 4.275 and 10.013, respectively, which were over 15 and 40 times higher than that of BLG nanoparticles (0.254). When protein molecules aggregated into nanoparticles, the total surface area was greatly reduced. As a result, the charged or hydrophilic groups might have been distributed densely on the newly formed surface of the nanoparticles in order to maximize their contact with water. This created a multivalent surface that could facilitate the interaction with the mucin layer [54, 240]. Another possible explanation was that nanoparticles as an assembly of biopolymers might have adhered to the mucin layer more cooperatively, although further studies are necessary to test this hypothesis.

### 8.4.4 Permeation across the small intestine epithelia

The transport of drugs across the small intestine epithelia could be promoted by two factors: disruption of the tight junctions between the epithelial cells [241] and enhanced endocytosis by these cells [34]. The former process is monitored by the progression of transepithelial electrical resistance (TEER) of Caco-2 monolayers. As shown in **Figure 8.5**, BLG molecule and nanoparticles did not show any significant ($P<0.10$) impact on the TEER values during the 2-hour period of treatment. On the other hand, C-EDA and C-P600 molecules were capable of

reducing the TEER by up to 27% and 88%, respectively, suggesting their ability of opening the tight junction between the Caco-2 cells to different extents. The fact that C-P600 reduced the TEER more profoundly than C-EDA might be ascribed to the multivalent property of P-600 as described before.
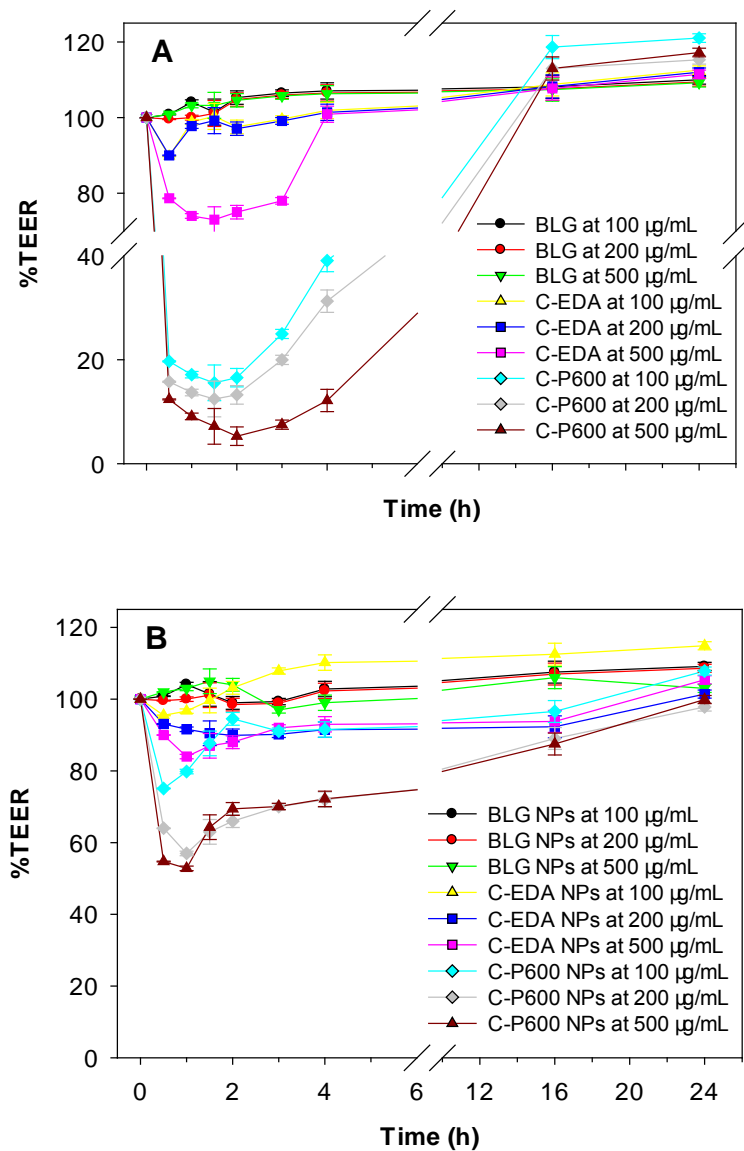


**Figure 8.5** Transepithelial electrical resistances (TEER) of Caco-2 monolayers in the presence of BLG/CBLG molecules (A) and nanoparticles (B)

Regardless of the type and concentration of samples, a satisfactory recovery in TEER was observed after the termination of treatment, with the TEER values reaching more than 95% of the original values after 22 h. This result was much better than that achieved using pure PEI as a tight junction opening reagent [242], which could alleviate the safety concern on the CBLG nanoparticles to some extent.

It was noteworthy that C-EDA and C-P600 nanoparticles exhibited lower capability of tight junction disruption than the protein molecules, causing a decrease of at most 17% and 32% respectively in the TEER. This phenomenon was consistent with the studies by Vllasaliu et al. [243] and Ma et al. [244] who reported higher TEER-lowering capacities for chitosan molecules compared to chitosan nanoparticles. Although the authors ascribed such difference to the consumption of positive charges during particle preparation, which led to weaker electrostatic attraction, we considered that the minor change might not be sufficient to cause this marked change in TEER. Instead, we postulated that the difference between the size of the protein molecules (several nanometers) and nanoparticles (approximately 100 nm) might have played an essential role. Ranaldi et al. [242] and Schipper et al. [241] found that polycations such as chitosan and PEI disrupted the tight junction by weakening the negative charge on the cell membrane, followed by the contact with cytoskeletal F-actin resulting in a conformational change, together with the dislocation of tight junction proteins

including ZO1 and occludin. Based on these findings, we hypothesized that protein molecules could diffuse to and interact with the cytoskeleton more rapidly than the nanoparticles because the former exhibits smaller size and higher surface area, although further studies are required to validate this assumption.
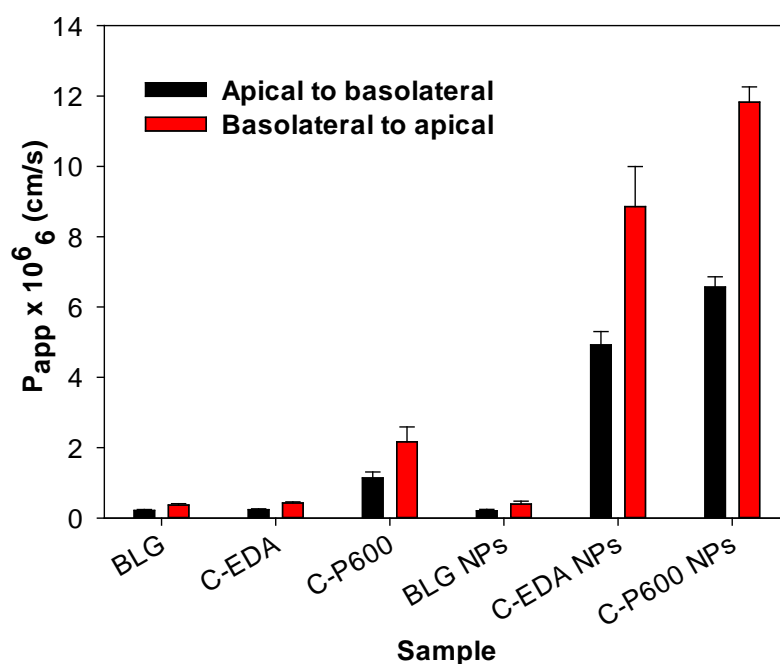


**Figure 8.6** Apparent permeabilities of different samples across the Caco-2 monolayer

The apparent permeabilities across the Caco-2 monolayer of different samples were compared in **Figure 8.6**. In the apical-basolateral permeation study, BLG molecules and nanoparticles exhibited the lowest $P_{app}$ value ($0.216 \times 10^{-6}$ and $0.208 \times 10^{-6}$ cm/s, respectively) among all samples, followed by C-EDA ($0.238 \times 10^{-6}$ cm/s) and C-P600 molecules ($1.140 \times 10^{-6}$ cm/s). Furthremore, the $P_{app}$ values for C-EDA and C-P600 nanoparticles were more than 20 and 30 times higher than that of native BLG molecules or nanoparticles, and they were comparable with a

number of polymers, such as chitosan [245] and PANAM dendrimers [240]. The basolateral-to-apical permeabilities were approximately 86% higher than those observed in the apical-to-basolateral analysis, but the ranking among different samples was not altered.

The permeability of both the protein molecules and nanoparticles decreased in the same order (C-P600>C-EDA>BLG) as for their tight junction disrupting capacities, which confirmed the advantage of cationic polymers in crossing the small intestine lining. However, it was unexpected that the nanoparticles demonstrated better permeability across the Caco-2 monolayer than the constituent molecules, although the latter demonstrated a more pronounced reduction in TEER. This result suggested that mechanisms other than tight junction opening might dominated the permeation process. Firstly, nanoparticles exhibited better mucoadhesion properties than the molecules as shown in this study; therefore, they were able to contact and permeate the mucin layer secreted by the Caco-2 cells more rapidly. Secondly, as will be demonstrated in the following section, nanoparticles were much more effectively internalized by the Caco-2 cells, which favored their transport via the transcellular approach. This effect was also reported in previous literature as a major mechanism causing the permeation of protein nanoparticles across the Caco-2 monolayer [34].

### 8.4.5 Cell viability

After the transport across the small intestine, the drug carriers reach the circulation system where a broad variety of serum proteins adsorb onto their surface [246]. Such process alters the surface properties of drug carriers, which influences their interaction with the cells as will be discussed in this section. The reason why we chose a cancer cell line (Caco-2) in this study was that particles with a diameter of 100-600 nm tend to pass through the loose blood vessels surrounding the tumor tissues, a phenomenon known as enhanced permeation and retention (EPR) or passive targeted delivery [247].

**Figure 8.7** compared the viability of Caco-2 cells exposed to different doses of samples. When dispersed in FBS-free DMEM (**Figure 8.7A**), C-P600 molecules exhibited significant cytotoxicity, reducing the viability of Caco-2 cells to 71% and 52% at the concentrations of 200 and 500 μg/mL, respectively. C-P600 nanoparticles, on the contrary, did not show any observable toxicity in this study. Cationic polymers and nanoparticles are known to be toxic to a broad range of cell lines [234], which has been frequently correlated to their ability to breach the negatively charged cell membranes through electrostatic attraction [234, 248]. Interestingly, Leroueil et al. found that the membrane breaching was induced by cationic nanoparticles in a size-independent manner [249]. However, this study did not point out whether successful membrane breaching could translate directly into potent cytotoxicity. On the other hand, Yen et al. [250] and Pan et al. [251]

found that the cytotoxicity of nanoparticles varied with the size and charge of the feed, with the smallest cationic (e.g., those smaller than 10 nm) particles being the most toxic. Bannunah et al. also reported that cationic polystyrene nanoparticles with an average size of 50 nm were slightly more toxic than those with an average size of 100 nm [252]. These results were similar to our study on C-P600 molecules and nanoparticles, suggesting that mechanisms other than cell membrane breaching might also be essential for the cytotoxicity of macromolecules or nanoparticles. Possible factors may include translocation of nanoparticles into the cytoplasm and the interaction with specific cellular components [253], although detailed pathways are yet to be established for each specific cell line.

On the other hand, dispersion in FBS-supplemented DMEM was shown to mitigate the cytotoxicity of C-P600 molecules significantly, increasing the cell viability to 92% and 88% at the concentrations of 200 and 500μg/mL, respectively. This could be explained with the study by Wang et al. [235], who claimed that the serum protein corona surrounding the cationic nanoparticles or biomacromolecules could be robustly retained until reaching the lysosome, thus protecting the cells from damage due to the positive surface charge. All other samples, regardless of the concentration, exhibited a cell viability of about 100% in FBS-free DMEM and higher than 105% in FBS-supplemented DMEM (**Figure 8.7B**).
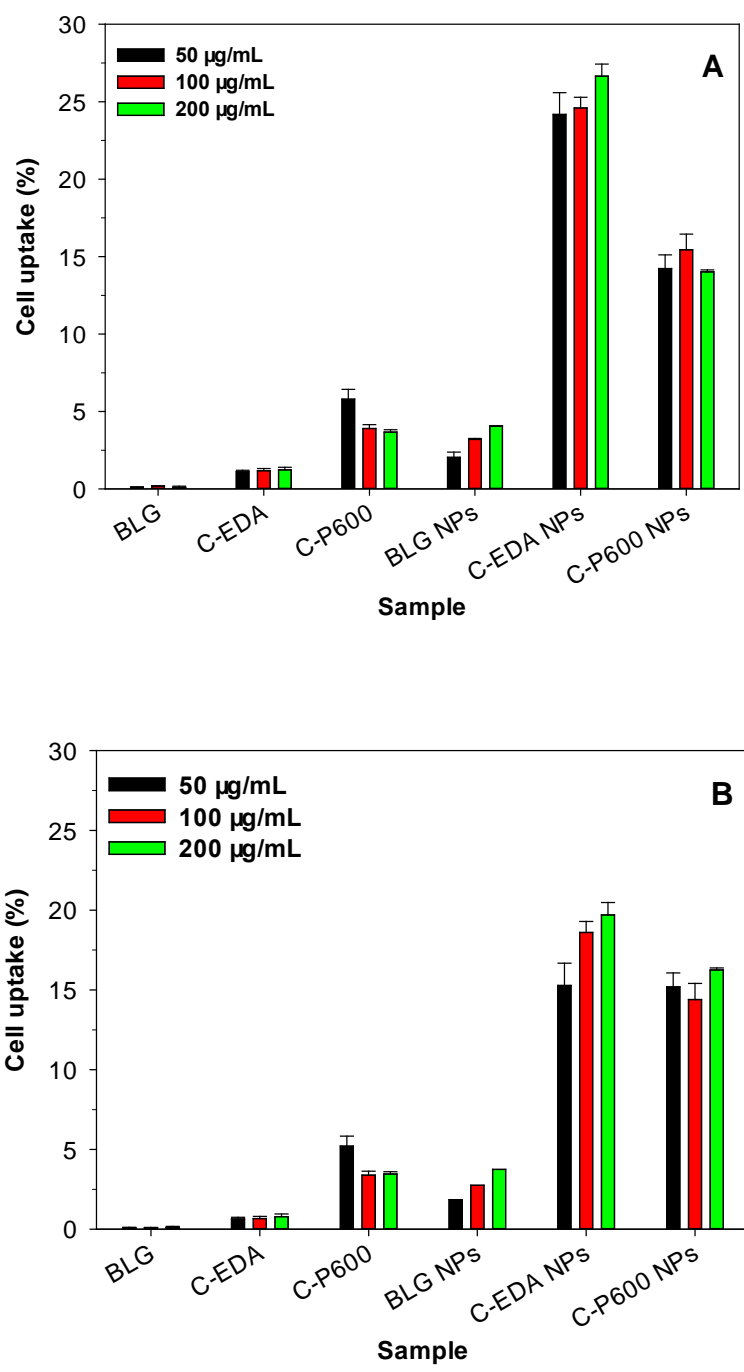
**Figure 8.7** Cytotoxicity of Caco-2 cells of samples dispersed in DMEM without (A) or with (B) FBS

### 8.4.6 Uptake by Caco-2 cells

As shown in Figure 8, nanoparticle samples showed significantly higher cellular uptake than their constituent molecules, a trend that was observed without regard for the type of protein and buffer as well as the concentration. For molecules, C-P600 demonstrated the highest cellular uptake (up to 5.74% in DMEM without FBS, **Figure 8.8A**, same hereinafter), followed by C-EDA (up to 1.86%) and BLG (up to 0.13%). On the other hand, the cellular uptake of nanoparticles followed the order of C-EDA (up to 26.5%)>C-P600 (up to 15.8%)>BLG (up to 6.82%). These results suggested the prominent influence of surface charge and hydrophobicity on the cellular uptake. CBLG molecules and nanoparticles exhibited significantly higher uptake compared to the BLG counterparts, which was likely attributed to their positive charge. C-EDA nanoparticles exhibited higher uptake than C-P600 nanoparticles possibly owing to its high hydrophobicity that facilitated the cell internalization via endocytosis [254]. For the molecules, they might have entered the cells mainly via direct translocation as their small sizes were unfavorable for endocytosis [255]. Therefore, C-P600 molecules bearing higher density charge may enter the cells more effectively than C-EDA.

The comparison between protein molecules and nanoparticles suggested a size-dependency of cellular uptake. This was similar with previous articles on gold nanoparticles [256, 257], which showed higher cellular uptake of nanoparticles with an average size of 25-75 nm compared with those with smaller (e.g., several

nanometers) or greater (e.g., above 100 nm) sizes. Lin et al. [258] suggested that cationic nanoparticles could be trafficked into cells following four steps: adhesion, direct translocation, endocytosis, and mixed entry. The direct translocation was caused by the disrupted electric field near the cell membrane, which is independent of particle size as discussed in the previous section [249]. However, as such process weakens the transmembrane potential gradually, it becomes no longer active at a certain point. Thereafter, endocytosis became the chief pathway for the entry of cationic nanoparticles. Since endocytosis is known to be closely related to the curvature of the incoming nanoparticles, which determines the effectiveness of cell membrane wrapping and endosome formation, the size and shape of the feed could play a major role in the cellular uptake at this stage [255]. As for anionic samples (BLG molecules and nanoparticles), they have been revealed to enter the cells mainly through endocytosis [34]. In addition, the endocytotic pathways for positively and negatively charged nanoparticles by Caco-2 cells are also different, as indicated by Bannunah et al [252]. Vesicular trans-monolayer transport was observed for both nanoparticles. In addition, calthrin-mediated endocytosis, and macropinocytosis played a major role in the internalization for positively charged nanoparticles, whereas lipid raft-associated pathway (caveolae-mediated endocytosis) was determined as the primary mechanism for the cellular uptake. Put together, the cellular uptake of

biomolecules or nanoparticles should be size- and charge-dependent, as confirmed

in our study.
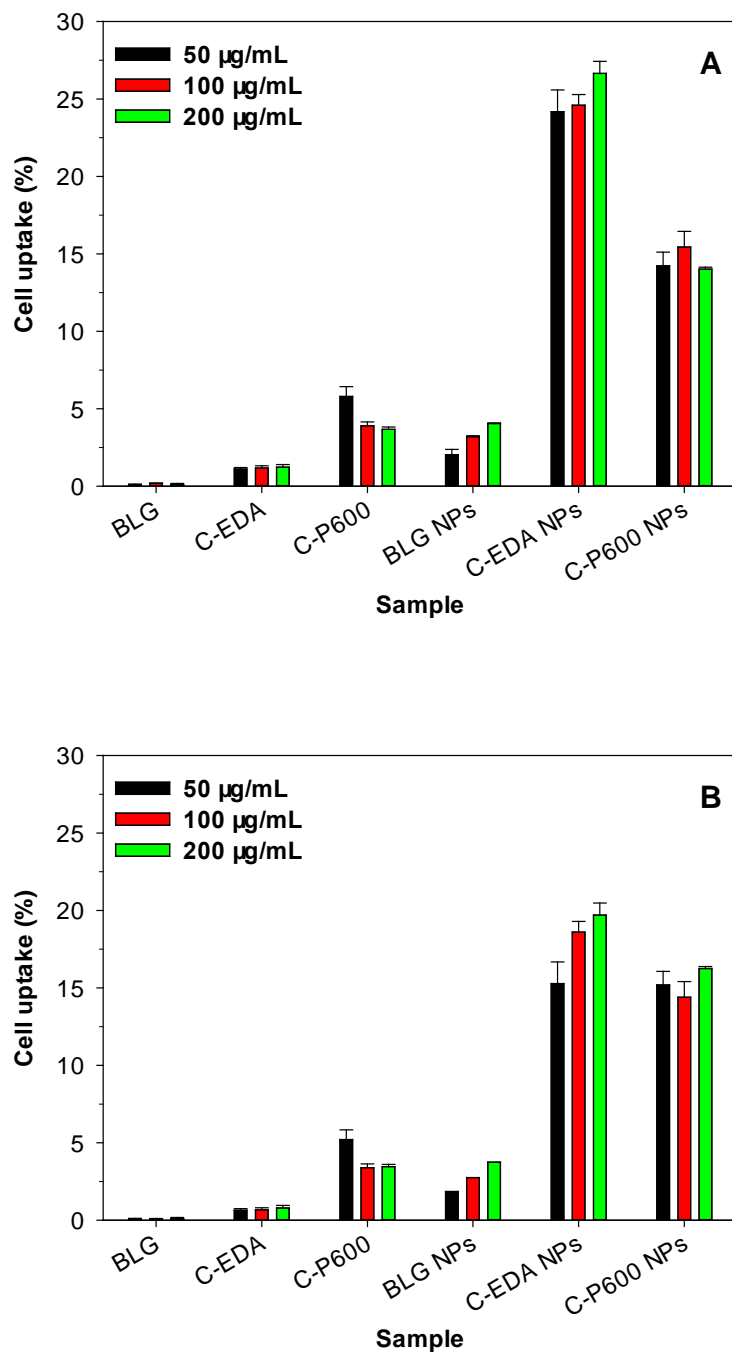


**Figure 8.8** Uptake by Caco-2 cells in DMEM without (A) or with FBS (B)

Lastly, although the supplementation of FBS in DMEM reduced the cellular uptake of C-EDA molecules and nanoparticles by at most 40%, it did not exhibit any significant (P<0.10) influence on the internalization of BLG and C-P600 molecules or nanoparticles. As a result, the uptake of C-EDA nanoparticles was merely 16% higher than that of C-P600 nanoparticles in the presence of FBS (**Figure 8.8B**). A recent study by Fischer et al. [191] revealed that the complex formed by cationic nanoparticles and serum proteins bound to the scavenger receptor on the surface of cell membrane, thus altering the cellular uptake of the nanoparticles. Furthermore, the effect of serum protein on the cellular uptake depended strongly on the particle size. This finding partly explained for the results obtained from our study, considering that the size of C-EDA particles was significantly higher than that of C-P600 particles.

## 8.5 Conclusion

In this study, we exploited CBLG molecules and nanoparticles to assess the impact of protein structure and physiological environment on the surface properties of the drug/nutraceutical carriers, and we related these characteristics to their performance in a series of processes that are relevant to drug/nutraceutical administration via oral route. The surface decoration by cationizers altered the surface properties (mainly the charge and hydrophobicity) of BLG molecules and nanoparticles, conferring them with satisfactory dispersion stability, particle integrity against digestive enzymes, sustained release in the GI tract, remarkable

mucoadhesion, desirable permeability across Caco-2 monolayer, and elevated cellular uptake. Furthermore, the form of samples (molecules or nanoparticles) also played a major role in these biochemical interactions. The processes studied in our study could be roughly divided into three categories. First, the processes that mainly involve the contact with a charged surface (e.g., mucoadhesion) may take place more effectively in the presence of larger nanoparticles, probably because of their appropriate curvatures, multivalency, and cooperative binding. Second, the procedures requiring rapid diffusion and interaction with certain biomacromolecules (e.g., tight junction opening and cytotoxicity) may proceed more effectively in the presence of smaller protein molecules, which possessed larger surface area and faster diffusion rate. Third, in the complex biological processes involving both of the abovementioned classes of procedures (e.g., cellular uptake and permeation across the Caco-2 monolayer), an optimal size that balances the performances in all these steps may exist. Finally, the surface properties and performances of all samples were significantly affected by the buffering system where they were situated. Binding of serum proteins in FBS mitigated the cytotoxicity of cationic polymers, but it also compromised the uptake of CBLG. Both changes could be attributed to the change in their surface properties. The principles extracted from our study may be utilized to explain the different performances of various drug/nutraceutical carriers both *in vitro* and *in vivo*. Moreover, our study provided some guidance for the design of

246

drug/nutraceutical carriers with well-defined surface properties, leading to controllable transport and delivery of the incorporated drugs/nutraceuticals. Follow-up studies on the performance of CBLG nanoparticles in various cell lines and their *in vivo* efficacy have been initiated.

# Chapter 9 Summary and perspectives

## 9.1    Summary

This project systematically investigated the preparation, characterization, and application of protein-based nanoparticles as effective transporting and delivering vehicles for poorly absorbed nutraceuticals or drugs. Extensive emphasis has been put on elucidating the structure-function relationship for natural and minimally modified polymers. The interplay among the matrix, the encapsulated compound, and the environment in which the delivery vehicles is situated was found to have a significant effect on the efficacy of nutraceutical (or drug) encapsulation and delivery. A series of encapsulating and delivery systems have been designed by far for two different bioactive compounds, vitamin $D_3$ and curcumin.

1.    Soy protein as one of the most commonly utilized plant proteins possesses desirable water solubility together with a considerable content of hydrophobic amino acids. The latter property indicates strong interaction between the protein and hydrophobic bioactives, which facilitates the encapsulation of these compounds. Nanoparticles were successfully synthesized with soy protein by the organic desolvation method. The formation of soy protein nanoparticles involves partial unfolding of protein molecules, limited aggregation in the presence of the antisolvent, crosslinking via chemical bonds, and refolding of the constituent monomers. Curcumin as a chemopreventive compound was successfully

incorporated into the soy protein nanoparticles. Satisfactory EE and time-dependent release profile were observed. The nanoparticles were further subjected to conjugation with folic acid, a cancer cell-targeting ligand. Compared to the native soy protein nanoparticles, folic acid-conjugated particles exhibited a 93% increase in the accumulation in tumor cells such as Caco-2, indicating that they may be a competitive candidate for the protection and target delivery for anti-cancer drugs. Other benefits resulting from folic acid conjugation included better particle forming capacity, higher EE, and more complete release *in vitro*. To overcome the rapid digestion of soy protein nanoparticles in the gastrointestinal tract, carboxymethyl chitosan was employed as a second coating layer by a simple ionic gelation method, using $Ca^{2+}$ as an ionic crosslinker. The SPI/CMCS complex inherited both the desirable particle forming capacity of SPI and the dispersion stability of CMCS. In addition, the formed particles exhibited satisfactory EE for vitamin $D_3$ and controlled releasing profile *in vitro*. These characteristics made SPI/CMCS complex nanoparticles an attractive candidate for delivering water insoluble micronutrients via oral administration.

2. Beta lactoglobulin (BLG) is the major component of whey protein, and it serves as a natural carrier for many lipophilic nutrients. This protein exhibits high water solubility and unique resistance against pepsin. A systematic study was conducted with the focus on improvement in the EE and LE, as well as reduced usage of toxic crosslinkers. Our study suggested that the interaction between BLG

and curcumin could be promoted by tuning the antisolvent content before evaporation. An LC and EE of up to 11% and 98% respectively could be achieved under the optimal condition. Additionally, curcumin served not only as a target compound but also as a partial crosslinker, which reduced the required dosage of glutaraldehyde by as much as 50%. Moreover, cationic beta lactoglobulin (CBLG) was developed as a multifunctional bioavailability enhancer for nutraceuticals. Nanoparticles with small average size (<100 nm) and narrow size distribution have been prepared by organic solvent desolvation method. These novel biopolymer nanoparticles inherited the merits from native BLG, exhibiting remarkable stability against precipitation and significant controlled-release properties. Besides, the positive charge on CBLG promoted the mucoadhesive capacity by over 40 times, and the cellular uptake was also significantly enhanced compared to native BLG. The nanoparticles remained intact in simulated gastric and intestinal fluids, with minimum leakage of curcumin in the GI tract. Surface properties, such as charge and hydrophobicity, together with the size, showed a pronounced impact on the protection, transport, and delivery of the entrapped compounds. These advantages made CBLG nanoparticles an attractive candidate as a bioavailability enhancer for poorly absorbed drugs or nutraceuticals.

## 9.2   Future studies

While protein-based nanoparticles demonstrated remarkable versatility and efficiency in the encapsulation and delivery of nutraceuticals or drug, further

studies are needed to overcome the weakness of current delivery systems or to confer them with novel features. Some possible areas of research pertaining to protein-based delivery systems are discussed below.

1.  As introduced in previous sections, various chemicals such as organic solvents, crosslinkers, catalysts, and co-surfactants are involved in the preparation of protein-based nutraceutical carriers. Many of these chemicals exhibit certain toxicity and elicit considerable public health concerns. For example, glutaraldehyde as a common crosslinking agent is toxic to the respiratory and reproductive system, and positive results on the genetic toxicity has also been documented [93]. Unlike the organic solvents or catalysts which can be removed by evaporation or dialysis, glutaraldehyde is integrated into the nutraceutical carrier by forming chemical bonds, and it may be released in human body when such bonds are cleaved by digestive enzymes. Such facts prompted the pursuit for natural crosslinkers such as genipin [94] and microbial transglutaminase (MTGase) [95]. In spite of the satisfactory performance of these compounds in crosslinking protein molecules and preparing hydrogels [95, 96], their application in systems such as nanoparticles has not been reported by far. The compact structure and the small intermolecular distance in the nanoparticles may be the major barrier for enzymes, preventing them from accessing and leaving the reactive sites. Combination of bulky enzymes with flexible substrates (e.g., short peptides or small organic molecules) may help overcoming this difficulty by producing small reactive

intermediates as an effective crosslinker. On the other hand, as introduced before, phenols such as EGCG show the ability to maintain the particle structure by non-covalent interaction, which may also be employed to synthesize "green" protein nanoparticles.

2. Systematic evaluation of the efficacy and toxicity associated with protein-based systems. Novel nutraceutical carriers, especially those with a nanoscaled size, have elicited considerable public concern. This is probably because of the lack of knowledge in whether the nanosized nutraceuticals (e.g., lipophilic vitamins that are entrapped in a nanoemulsion droplet) and carriers are metabolized via a similar or distinct pathway in human body compared with conventional microsized nutraceuticals (e.g., lipophilic vitamins that are micro-emulsified by the bile in the small intestine). *In vitro* and *in vivo* model studies are needed to understand the behaviors and fates of both the nutraceuticals and the carriers when administrated to a living body. The effects of the surface properties and particle/droplet size may be of special interest, since these characteristics govern a wide range of biological interactions.

3. The allergenicity associated with various proteins, including soy protein and BLG, leads to extensive concern on the safety of protein-based delivery systems. Although the particle forming process involves partial denaturation by organic solvent and sometimes thermal treatment, it remains unclear whether these

procedures can cause a conformational change sufficient to reduce or remove the allergenicity of the proteins. Conjugation with polymers such as polysaccharides has been shown to lower the allergenicity of soy proteins by a great extent; therefore, it is of interest to find out if other hybridization processes (such as cationization with PEI or ionic association with a polysaccharide) may exert a similar influence on the allergic properties of the protein-based delivery systems.

4. Sensory properties are another important factor affecting consumer acceptance on the protein-based nutraceutical carriers. It is of interest to find out whether proteins can mask the unpleasant flavor of certain nutraceuticals such as DHA or curcumin. The effect of processing (e.g., thermal treatment) on the flavor may also be assessed.

5. The application of protein-based carriers in the areas related to the food industry but different from nutraceutical delivery may also be pursued. For instance, proteins with suitable surface modification might serve as a potential carrier for pesticides or antimicrobial agents, providing satisfactory solubility, stability, and cell penetrating efficacy to the incorporated compounds.

6. From a more practical perspective, several issues must be addressed before a protocol for manufacturing protein-based nutraceutical carriers can be scaled up. Due to the delicate conformation of proteins, all of the systems described above are susceptible to environmental change. For example, the size and uniformity of

the nanoparticles is highly dependent on the organic solvent, pH, temperature, and ionic strength. A slight variation in the microenvironment may lead to either insufficient or excessive aggregation, which poses a daunting challenge to the consistency of product quality. Same challenges also apply to other encapsulation and delivery systems such as emulsions, gels, and molecular complex, which also require careful control over the synthesizing condition. Novel techniques such as microfluidic processing may provide more precisely controlled liquid diffusion and mixing, giving result to more predictable particle size, narrower size distribution, reduced reaction time, and possibly improved encapsulation efficiency.

# References

[1] M. Jahanshahi, Z. Babaei, Protein nanoparticle: A unique system as drug delivery vehicles, Afr J Biotechnol, 7 (2008) 4926-4934.

[2] Y. Kawashima, Nanoparticulate systems for improved drug delivery, Adv. Drug Delivery Rev., 47 (2001) 1-2.

[3] J.J. Marty, R.C. Oppenheim, P. Speiser, Nanoparticles - a new colloidal drug delivery system, Pharm. Acta Helv., 53 (1978) 17-23.

[4] R. Matsuno, S. Adachi, Lipid encapsulation technology-techniques and applications to food, Trends Food Sci. Technol., 4 (1993) 256-261.

[5] Zeta Potential of Colloids in Water and Waste Water, in:  ASTM Standard D, American Society for Testing and Materials, 1985, pp. 4187-4182.

[6] Y. Luo, Z. Teng, Q. Wang, Development of zein nanoparticles coated with carboxymethyl chitosn for encapsulation and controlled release of vitamin D3, J Agric Food Chem, 60 (2012) 836-843.

[7] Y. Luo, T. Wang, Z. Teng, P. Chen, J. Sun, Q. Wang, Encapsulation of indole-3-carbinol and 3, 3'-diindolylmethane in zein/carboxymethyl chitosan nanoparticles with controlled release property and improved stability, Food Chem., 139 (2013) 224-230.

[8] Y. Luo, B. Zhang, M. Whent, L. Yu, Q. Wang, Preparation and characterization of zein/chitosan complex for encapsulation of α-tocopherol, and its in vitro controlled release study, Colloids Surf., B, 85 (2011) 145-152.

[9] R. Bansil, B.S. Turner, Mucin structure, aggregation, physiological functions and biomedical applications, Curr. Opin. Colloid Interface Sci., 11 (2006) 164-170.

[10] J. Thongborisute, H. Takeuchi, Evaluation of mucoadhesiveness of polymers by BIACORE method and mucin-particle method, International Journal of Pharmaceutics, 354 (2008) 204-209.

[11] P.N. Wiecinski, K.M. Metz, A.N. Mangham, K.H. Jacobson, R.J. Hamers, J.A. Pedersen, Gastrointestinal biodurability of engineered nanoparticles: Development of an in vitro assay, Nanotoxicology, 3 (2009) 202-214.

[12] P.M. Claesson, B.W. Ninham, pH-Dependent Interactions between Adsorbed Chitosan Layers, Langmuir, 8 (1992) 1406-1412.

[13] S. Chayed, F.M. Winnik, In vitro evaluation of the mucoadhesive properties of polysaccharide-based nanoparticulate oral drug delivery systems, Eur J Pharm Biopharm, 65 (2007) 363-370.

[14] C. Delgado, G.E. Francis, D. Fisher, The Uses and Properties of Peg-Linked Proteins, Critical Reviews in Therapeutic Drug Carrier Systems, 9 (1992) 249-304.

[15] R.J. Kok, F. Grijpstra, K.H. Nederhoed, F. Moolenaar, Renal drug delivery with low-molecular-weight proteins: The effect of charge modifications on the body distribution of drug-lysozyme conjugates, Drug Delivery, 6 (1999) 1-8.

[16] S. Blau, T.T. Jubeh, S.M. Haupt, A. Rubinstein, Drug targeting by surface cationization, Critical Reviews in Therapeutic Drug Carrier Systems, 17 (2000) 425-465.

[17] Y.-b. Lim, E. Lee, M. Lee, Cell Penetrating Peptide-Coated Nanoribbons for Intracellular Nanocarriers, Angew. Chem., 119 (2007) 3545-3548.

[18] M. Lindgren, M. Hällbrink, A. Prochiantz, Ü. Langel, Cell-penetrating peptides, Trends in Pharmacological Sciences, 21 (2000) 99-103.

[19] J. Sudimack, R.J. Lee, Targeted drug delivery via the folate receptor, Adv Drug Delivery Rev, 41 (2000) 147-162.

[20] A. MaHam, Z.W. Tang, H. Wu, J. Wang, Y.H. Lin, Protein-Based Nanomedicine Platforms for Drug Delivery, Small, 5 (2009) 1706-1721.

[21] C. Bengoechea, I. Peinado, D.J. McClements, Formation of protein nanoparticles by controlled heat treatment of lactoferrin: Factors affecting particle characteristics, Food Hydrocolloids, 25 (2011) 1354-1360.

[22] L.Y. Chen, G.E. Remondetto, M. Subirade, Food protein-based materials as nutraceutical delivery systems, Trends Food Sci. Technol., 17 (2006) 272-283.

[23] C. Weber, C. Coester, J. Kreuter, K. Langer, Desolvation process and surface characterisation of protein nanoparticles, International Journal of Pharmaceutics, 194 (2000) 91-102.

[24] J. Lazko, Y. Popineau, J. Legrand, Soy glycinin microcapsules by simple coacervation method, Colloids and Surfaces B-Biointerfaces, 37 (2004) 1-8.

[25] J. Zhang, L. Liang, Z. Tian, L. Chen, M. Subirade, Preparation and in vitro evaluation of calcium-induced soy protein isolate nanoparticles and their formation mechanism study, Food Chem, 133 (2012) 390-399.

[26] X.H. Li, Y. Li, Y.F. Hua, A.Y. Qiu, C. Yang, S. Cui, Effect of concentration, ionic strength and freeze-drying on the heat-induced aggregation of soy proteins, Food Chemistry, 104 (2007) 1410-1417.

[27] M. Riche, T.N. Williams, Apparent digestible protein, energy and amino acid availability of three plant proteins in Florida pompano, Trachinotus carolinus L. in seawater and low-salinity water, Aquac Nutr, 16 (2010) 223-230.

[28] E. Gianazza, V. Viglienghi, P.G. Righetti, F. Salamini, C. Soave, Amino acid composition of zein molecular components, Phytochemistry, 16 (1977) 315-317.

[29] Q. Zhong, M. Jin, Nanoscalar structures of spray-dried zein microcapsules and in vitro release kinetics of the encapsulated lysozyme as affected by formulations, J Agric Food Chem, 57 (2009) 3886-3894.

[30] Q.X. Zhong, M.F. Jin, Zein nanoparticles produced by liquid-liquid dispersion, Food Hydrocolloids, 23 (2009) 2380-2387.

[31] N. Parris, P.H. Cooke, K.B. Hicks, Encapsulation of essential oils in zein nanospherical particles, J Agric Food Chem, 53 (2005) 4788-4792.

[32] A. Patel, Y.C. Hu, J.K. Tiwari, K.P. Velikov, Synthesis and characterisation of zein-curcumin colloidal particles, Soft Matter, 6 (2010) 6192-6199.

[33] A.R. Patel, E.C.M. Bouwens, K.P. Velikov, Sodium caseinate stabilized zein colloidal particles, J Agric Food Chem, 58 (2010) 12497-12503.

[34] Y. Luo, Z. Teng, T.T.Y. Wang, Q. Wang, The cellular uptake and transport of zein nanoparticles: Effects of sodium caseinate, Journal of Agricultural and Food Chemistry, 61 (2013) 7621-7629.

[35] L.H. Chuah, N. Billa, C.J. Roberts, J.C. Burley, S. Manickam, Curcumin-containing chitosan nanoparticles as a potential mucoadhesive delivery system to the colon, Pharmaceutical Development and Technology, 18 (2013) 591-599.

[36] J. Modi, G. Joshi, K. Sawant, Chitosan based mucoadhesive nanoparticles of ketoconazole for bioavailability enhancement: formulation, optimization, in vitro and ex vivo evaluation, Drug Development and Industrial Pharmacy, 39 (2013) 540-547.

[37] B. Hu, C.L. Pan, Y. Sun, Z.Y. Hou, H. Ye, B. Hu, X.X. Zeng, Optimization of fabrication parameters to produce chitosan-tripolyphosphate nanoparticles for delivery of tea catechins, J Agric Food Chem, 56 (2008) 7451-7458.

[38] X. Shi, Y. Du, J. Yang, B. Zhang, L. Sun, Effect of degree of substitution and molecular weight of carboxymethyl chitosan nanoparticles on doxorubicin delivery, Journal of Applied Polymer Science, 100 (2006) 4689-4696.

[39] S.A. Agnihotri, N.N. Mallikarjuna, T.M. Aminabhavi, Recent advances on chitosan-based micro- and nanoparticles in drug delivery, J Control Release, 100 (2004) 5-28.

[40] A.K. Anal, A. Tobiassen, J. Flanagan, H. Singh, Preparation and characterization of nanoparticles formed by chitosan-caseinate interactions, Colloids Surf., B, 64 (2008) 104-110.

[41] S.A. Papadimitriou, D.S. Achilias, D.N. Bikiaris, Chitosan-g-PEG nanoparticles ionically crosslinked with poly(glutamic acid) and tripolyphosphate as protein delivery systems, Int. J. Pharm., 430 (2012) 318-327.

[42] J. Futami, M. Kitazoe, H. Murata, H. Yamada, Exploiting protein cationization techniques in future drug development, (2007).

[43] R.J. Lee, P.S. Low, G.E. Francis, C. Delgado, Folate as a Targeting Device for Proteins Utilizing Folate Receptor-Mediated Endocytosis Drug Targeting, in: J.M. Walker (Ed.), Humana Press, 2000, pp. 69-76.

[44] S. Ko, S. Gunasekaran, Preparation of sub-100-nm beta-lactoglobulin (BLG) nanoparticles, J. Microencapsul., 23 (2006) 887-898.

[45] J. Adler-Nissen, Enzymic hydrolysis of food proteins, Elsevier Applied Science Publishers, 1986.

[46] L. Chen, M. Subirade, Chitosan/β-lactoglobulin core-shell nanoparticles as nutraceutical carriers, Biomaterials, 26 (2005) 6041-6053.

[47] G. Kontopidis, C. Holt, L. Sawyer, Invited Review: β-Lactoglobulin: Binding Properties, Structure, and Function, J Dairy Sci, 87 (2004) 785-796.

[48] W. Lin, M.C. Garnett, E. Schacht, S.S. Davis, L. Illum, Preparation and in vitro characterization of HSA-mPEG nanoparticles, Int. J. Pharm., 189 (1999) 161-170.

[49] R. Caillard, G.E. Remondetto, M. Subirade, Physicochemical properties and microstructure of soy protein hydrogels co-induced by Maillard type cross-linking and salts, Food Res Int, 42 (2009) 98-106.

[50] C. Bengoechea, O.G. Jones, A. Guerrero, D.J. McClements, Formation and characterization of lactoferrin/pectin electrostatic complexes: Impact of composition, pH and thermal treatment, Food Hydrocolloids, 25 (2011) 1227-1232.

[51] Y. Luo, Z. Teng, Q. Wang, Development of zein nanoparticles coated with carboxymethyl chitosan for encapsulation and controlled release of vitamin $D_3$, J Agric Food Chem, (2012) 836-843.

[52] J.L. Doublier, C. Garnier, D. Renard, C. Sanchez, Protein-polysaccharide interactions, Curr. Opin. Colloid Interface Sci., 5 (2000) 202-214.

[53] X.B. Zhao, H. Li, R.J. Lee, Targeted drug delivery via folate receptors, Expert Opin. Drug Deliv., 5 (2008) 309-319.

[54] S. Franzen, A comparison of peptide and folate receptor targeting of cancer cells: from single agent to nanoparticle, Expert Opin. Drug Deliv., 8 (2011) 281-298.

[55] S.J. Yang, F.H. Lin, K.C. Tsai, M.F. Wei, H.M. Tsai, J.M. Wong, M.J. Shieh, Folic Acid-Conjugated Chitosan Nanoparticles Enhanced Protoporphyrin IX Accumulation in Colorectal Cancer Cells, Bioconjug Chem, 21 (2010) 679-689.

[56] L.K. Zhang, S.X. Hou, S.J. Mao, D.P. Wei, X.R. Song, Y. Lu, Uptake of folate-conjugated albumin nanoparticles to the SKOV3 cells, Int. J. Pharm., 287 (2004) 155-162.

[57] S.-J. Yang, F.-H. Lin, K.-C. Tsai, M.-F. Wei, H.-M. Tsai, J.-M. Wong, M.-J. Shieh, Folic acid-conjugated chitosan nanoparticles enhanced protoporphyrin IX accumulation in colorectal cancer cells, Bioconjugate Chemistry, 21 (2010) 679-689.

[58] Y.G. Zu, Y. Zhang, X.H. Zhao, Q. Zhang, Y. Liu, R. Jiang, Optimization of the preparation process of vinblastine sulfate (VBLS)-loaded folate-conjugated bovine serum albumin (BSA) nanoparticles for tumor-targeted drug delivery using response surface methodology (RSM), Int. J. Nanomedicine, 4 (2009) 321-333.

[59] K.A. Mislick, J.D. Baldeschwieler, J.F. Kayyem, T.J. Meade, Transfection of Folate-Polylysine DNA Complexes - Evidence for Lysosomal Delivery, Bioconjug Chem, 6 (1995) 512-515.

[60] I.A. Sogias, A.C. Williams, V.V. Khutoryanskiy, Why is chitosan mucoadhesive?, Biomacromolecules, 9 (2008) 1837-1842.

[61] J. Futami, M. Kitazoe, H. Murata, H. Yamada, Exploiting protein cationization techniques in future drug development, Expert Opinion on Drug Discovery, 2 (2007) 261-269.

[62] W. Lu, Y. Zhang, Y.Z. Tan, K.L. Hu, X.G. Jiang, S.K. Fu, Cationic albumin-conjugated pegylated nanoparticles as novel drug carrier for brain delivery, J Control Release, 107 (2005) 428-448.

[63] H. Lv, S. Zhang, B. Wang, S. Cui, J. Yan, Toxicity of cationic lipids and cationic polymers in gene delivery, Journal of Controlled Release, 114 (2006) 100-109.

[64] L. Jong, S.C. Peterson, Effects of soy protein nanoparticle aggregate size on the viscoelastic properties of styrene-butadiene composites, Composites Part A: Applied Science and Manufacturing, 39 (2008) 1768-1777.

[65] C.H. Wang, S. Damodaran, Thermal Gelation of Globular-Proteins - Influence of Protein Conformation on Gel Strength, J Agric Food Chem, 39 (1991) 433-438.

[66] Z. Teng, C. Liu, X.Q. Yang, L. Li, C.H. Tang, Y.M. Jiang, Fractionation of Soybean Globulins Using Ca(2+) and Mg(2+): A Comparative Analysis, J. Am. Oil Chem. Soc., 86 (2009) 409-417.

[67] D.G. Liu, H.F. Tian, J. Zeng, P.R. Chang, Core-shell nanoblends from soy protein/polystyrene by emulsion polymerization, Macromol. Mater. Eng., 293 (2008) 714-721.

[68] A. Malhotra, J.N. Coupland, The effect of surfactants on the solubility, zeta potential, and viscosity of soy protein isolates, Food Hydrocolloids, 18 (2004) 101-108.

[69] M.A. Tomren, M. Masson, T. Loftsson, H.H. Tønnesen, Studies on curcumin and curcuminoids: XXXI. Symmetric and asymmetric curcuminoids: stability, activity and complexation with cyclodextrin, International Journal of Pharmaceutics, 338 (2007) 27-34.

[70] A. Goel, B.B. Aggarwal, Curcumin, the golden spice from Indian saffron, is a chemosensitizer and radiosensitizer for tumors and chemoprotector and radioprotector for normal organs, Nutrition and Cancer, 62 (2010) 919-930.

[71] B.B. Patel, A.P.N. Majumdar, Synergistic role of curcumin with current therapeutics in colorectal cancer: minireview, Nutrition and Cancer, 61 (2009) 842-846.

[72] F. Akhtar, M. Rizvi, S.K. Kar, Oral delivery of curcumin bound to chitosan nanoparticles cured *Plasmodium yoelii* infected mice, Biotechnology Advances, 30 (2011) 310-320.

[73] Y.-J. Wang, M.-H. Pan, A.-L. Cheng, L.-I. Lin, Y.-S. Ho, C.-Y. Hsieh, J.-K. Lin, Stability of curcumin in buffer solutions and characterization of its degradation products, Journal of Pharmaceutical and Biomedical Analysis, 15 (1997) 1867-1876.

[74] I. Stankovic, Curcumin: Chemical and Technical Assessment (CTA), JECFA, Rome, (2004) 8.

[75] A. Sahu, N. Kasoju, P. Goswami, U. Bora, Encapsulation of Curcumin in Pluronic Block Copolymer Micelles for Drug Delivery Applications, J. Biomater. Appl., 25 (2011) 619-639.

[76] L.A.G. Armas, B.W. Hollis, R.P. Heaney, Vitamin D2 is much less effective than vitamin D3 in humans, Journal of Clinical Endocrinology and Metabolism, 89 (2004) 5387-5391.

[77] R. Bouillon, W.H. Okamura, A.W. Norman, Structure-function relationships in the vitamin D endocrine system, Endocrine Reviews, 16 (1995) 200-257.

[78] M.F. Holick, Vitamin D deficiency, New England Journal of Medicine, 357 (2007) 266-281.

[79] A. Moshfegh, J. Goldman, J. Ahuja, D. Rhodes, R. Lacomb, What we eat in America, NHANES 2005-2006: usual nutrient intakes from food and water compared to 1997 dietary reference intakes for vitamin D, calcium, phosphorus, and magnesium, US Department of Agriculture, Agricultural Research Service, (2009).

[80] R. Vieth, Vitamin D supplementation, 25-hydroxyvitamin D concentrations, and safety, The American journal of clinical nutrition, 69 (1999) 842-856.

[81] A.S. Narang, D. Delmarre, D. Gao, Stable drug encapsulation in micelles and microemulsions, International Journal of Pharmaceutics, 345 (2007) 9-25.

[82] X.-Y. Shi, T.-W. Tan, Preparation of chitosan/ethylcellulose complex microcapsule and its application in controlled release of Vitamin $D_2$, Biomaterials, 23 (2002) 4469-4473.

[83] A.O. Elzoghby, W.S. Abo El-Fotoh, N.A. Elgindy, Casein-based formulations as promising controlled release drug delivery systems, Journal of Controlled Release, 153 (2010) 206-216.

[84] J.J. Marty, R.C. Oppenheim, P. Speiser, Nanoparticles - New Colloidal Drug Delivery System, Pharmaceutica Acta Helvetiae, 53 (1978) 17-23.

[85] M.P. Desai, V. Labhasetwar, E. Walter, R.J. Levy, G.L. Amidon, The mechanism of uptake of biodegradable microparticles in Caco-2 cells is size dependent, Pharm. Res., 14 (1997) 1568-1573.

[86] I. Ezpeleta, J.M. Irache, S. Stainmesse, C. Chabenat, J. Gueguen, Y. Popineau, A.M. Orecchioni, Gliadin nanoparticles for the controlled release of all-trans-retinoic acid, International Journal of Pharmaceutics, 131 (1996) 191-200.

[87] A. Jithan, K. Madhavi, K. Prabhakar, M. Madhavi, Preparation and characterization of albumin nanoparticles encapsulating curcumin intended for the treatment of breast cancer.

[88] Y. Luo, B. Zhang, M. Whent, L. Yu, Q. Wang, Preparation and characterization of zein/chitosan complex for encapsulation of a-tocopherol, and its in vitro controlled release study, Colloids and Surfaces B: Biointerfaces, 85    145-152.

[89] L.W. Yu, D.Y. Yan, G. Sun, L.X. Gu, Preparation and characterization of pH-sensitive hydrogel fibers based on hydrolyzed-polyacrylonitrile/soy protein, Journal of Applied Polymer Science, 108 (2008) 1100-1108.

[90] S. Utsumi, J.E. Kinsella, Structure-function relationships in food proteins: subunit interactions in heat-induced gelation of 7S, 11S, and soy isolate proteins, J. Agric. Food. Chem., 33 (1985) 297-303.

[91] S. Petruccelli, M.C. Anon, Thermal aggregation of soy protein isolates, Journal of Agricultural and Food Chemistry, 43 (1995) 3035-3041.

[92] A. Phianmongkhol, J. Varley, $\zeta$-potential measurement for air bubbles in protein solutions, J. Colloid Interface Sci., 260 (2003) 332-338.

[93] D. Fukushima, Denaturation of soybean proteins by organic solvents, Cereal Chem., 46 (1969) 156-163.

[94] G.M. Kavanagh, A.H. Clark, S.B. Ross-Murphy, Heat-induced gelation of globular proteins: part 3. Molecular studies on low pH beta-lactoglobulin gels, Int J Biol Macromol, 28 (2000) 41-50.

[95] L.H. Dao, H.M. Nguyen, H.H. Mai, A fiber optic turbidity system for in-situ monitoring protein aggregation, nucleation and crystallisation, Acta Astronautica, 47 (2000) 399-409.

[96] C.E. LaClair, M.R. Etzel, Turbidity and Protein Aggregation in Whey Protein Beverages, J Food Sci, 74 (2009) C526-C535.

[97] T. Mirshahi, J.M. Irache, J. Gueguen, A.M. Orecchioni, Development of drug delivery systems from vegetal proteins: Legumin nanoparticles, Drug Dev. Ind. Pharm., 22 (1996) 841-846.

[98] Y.Y. Liu, X.A. Zeng, Z. Deng, S.J. Yu, S. Yamasaki, Effect of pulsed electric field on the secondary structure and thermal properties of soy protein isolate, Eur. Food Res. Technol., 233   841-850.

[99] A.H. Zaibunnisa, R. Siti Rashima, A.H. Nur Ain, Stabilisation of Curcumin With g-Cyclodextrin: Phase Solubility Study and its Characterisation, in:   2nd International Conference on Biotechnology and Food Science, IACSIT Press, Singapore, 2011, pp. 9-13.

[100] E.I. Paramera, S.J. Konteles, V.T. Karathanos, Microencapsulation of curcumin in cells of Saccharomyces cerevisiae, Food Chem, 125   892-902.

[101] J. Shaikh, D.D. Ankola, V. Beniwal, D. Singh, M.N.V.R. Kumar, Nanoparticle encapsulation improves oral bioavailability of curcumin by at least 9-fold when compared to curcumin administered with piperine as absorption enhancer, Eur J Pharm Sci, 37 (2009) 223-230.

[102] D. McClements, E. Decker, Y. Park, J. Weiss, Designing Food Structure to Control Stability, Digestion, Release and Absorption of Lipophilic Food Components, Food Biophysics, 3 (2008) 219-228.

[103] K. Patel, V. Patel, M. Patel, P. Patel, A. Ajmera, K. Rathod, Preparation and characterization of Tramadol Hydrochloride microspheres, Int. J. Drug Dev. Res., 2   605-611.

[104] F.M. Netto, M.A.M. Galeazzi, Production and Characterization of Enzymatic Hydrolysate from Soy Protein Isolate, LWT - Food Science and Technology, 31 (1998) 624-631.

[105] Z. Teng, Y.C. Luo, Q. Wang, Nanoparticles Synthesized from Soy Protein: Preparation, Characterization, and Application for Nutraceutical Encapsulation, J. Agric. Food. Chem., 60 (2012) 2712-2720.

[106] S.D. Weitman, R.H. Lark, L.R. Coney, D.W. Fort, V. Frasca, V.R. Zurawski, B.A. Kamen, Distribution of the Folate Receptor GP38 in Normal and Malignant Cell Lines and Tissues, Cancer Res, 52 (1992) 3396-3401.

[107] Q. Li, C. Liu, X. Zhao, Y. Zu, Y. Wang, B. Zhang, D. Zhao, Q. Zhao, L. Su, Y. Gao, B. Sun, Preparation, characterization and targeting of micronized 10-hydroxycamptothecin-loaded folate-conjugated human serum albumin nanoparticles to cancer cells, Int. J. Nanomedicine, 6   397-405.

[108] D. Zhao, X. Zhao, Y. Zu, J. Li, Y. Zhang, R. Jiang, Z. Zhang, Preparation, characterization, and in vitro targeted delivery of folate-decorated paclitaxel-loaded bovine serum albumin nanoparticles, Int. J. Nanomedicine, 5 (2010) 669-677.

[109] R. Kuttan, P. Bhanumathy, K. Nirmala, M.C. George, Potential anticancer activity of turmeric (Curcuma longa), Cancer Lett, 29 (1985) 197-202.

[110] D.-W. Tang, S.-H. Yu, Y.-C. Ho, B.-Q. Huang, G.-J. Tsai, H.-Y. Hsieh, H.-W. Sung, F.-L. Mi, Characterization of tea catechins-loaded nanoparticles prepared from chitosan and an edible polypeptide, Food Hydrocolloids, 30 (2012) 33-41.

[111] A.E. Robinson, Isolation and identification of drugs in pharmaceuticals, body fluids and postmortem material. Edited by E. G. C. Clarke assisted by Judith Berle, J Pharm Pharmacol, 21 (1969) 559-560.

[112] S.L. Jordan, M.R. Russo, R.L. Blessing, A.B. Theis, Inactivation of glutaraldehyde by reaction with sodium bisulfite, J. Toxicol. Environ. Health, 47 (1996) 299-309.

[113] D. Prajakta, J. Ratnesh, K. Chandan, S. Suresh, S. Grace, V. Meera, P. Vandana, Curcumin Loaded pH-Sensitive Nanoparticles for the Treatment of Colon Cancer, J. Biomed. Nanotechnol., 5 (2009) 445-455.

[114] M. Das, S.K. Sahoo, Folate Decorated Dual Drug Loaded Nanoparticle: Role of Curcumin in Enhancing Therapeutic Potential of Nutlin-3a by Reversing Multidrug Resistance, PLoS One, 7    18.

[115] N.S. Rejinold, M. Muthunarayanan, K.P. Chennazhi, S.V. Nair, R. Jayakumar, Curcumin Loaded Fibrinogen Nanoparticles for Cancer Drug Delivery, J. Biomed. Nanotechnol., 7    521-534.

[116] A.J. Ditto, K.N. Shah, N.K. Robishaw, M.J. Panzner, W.J. Youngs, Y.H. Yun, The Interactions between L-tyrosine based nanoparticles decorated with folic acid and cervical cancer cells under physiological flow, Mol Pharm, 9 (2012) 3089-3098.

[117] S. Madrigal-Carballo, S. Lim, G. Rodriguez, A.O. Vila, C.G. Krueger, S. Gunasekaran, J.D. Reed, Biopolymer coating of soybean lecithin liposomes via layer-by-layer self-assembly as novel delivery system for ellagic acid, Journal of Functional Foods, 2 (2010) 99-106.

[118] R. Rajam, P. Karthik, S. Parthasarathi, G.S. Joseph, C. Anandharamakrishnan, Effect of whey protein-alginate wall systems on survival of microencapsulated Lactobacillus plantarum in simulated gastrointestinal conditions, Journal of Functional Foods, 4 (2012) 891-898.

[119] C.J. Barrow, C. Nolan, B.J. Holub, Bioequivalence of encapsulated and microencapsulated fish-oil supplementation, Journal of Functional Foods, 1 (2009) 38-43.

[120] S.E. Molina Ortiz, J.R. Wagner, Hydrolysates of native and modified soy protein isolates: structural characteristics, solubility and foaming properties, Food Res Int, 35 (2002) 511-518.

[121] D. Guzey, D.J. McClements, Formation, stability and properties of multilayer emulsions for application in the food industry, Adv. Colloid Interface Sci., 128-130 (2006) 227-248.

266

[122] A. Madene, M. Jacquot, J. Scher, S. Desobry, Flavour encapsulation and controlled release – a review, Int J Food Sci Technol, 41 (2006) 1-21.

[123] Y.C. Luo, B.C. Zhang, W.H. Cheng, Q. Wang, Preparation, characterization and evaluation of selenite-loaded chitosan/TPP nanoparticles with or without zein coating, Carbohydr Polym, 82 (2010) 942-951.

[124] K.S. Snima, R. Jayakumar, A.G. Unnikrishnan, S.V. Nair, V.K. Lakshmanan, O-Carboxymethyl chitosan nanoparticles for metformin delivery to pancreatic cancer cells, Carbohydr Polym, 89 (2012) 1003-1007.

[125] X.-G. Chen, H.-J. Park, Chemical characteristics of O-carboxymethyl chitosans related to the preparation conditions, Carbohydr Polym, 53 (2003) 355-359.

[126] S.S. Vaghani, M.M. Patel, C.S. Satish, Synthesis and characterization of pH-sensitive hydrogel composed of carboxymethyl chitosan for colon targeted delivery of ornidazole, Carbohydr Res, 347 (2012) 76-82.

[127] Y. Luo, Z. Teng, X. Wang, Q. Wang, Development of carboxymethyl chitosan hydrogel beads in alcohol-aqueous binary solvent for nutrient delivery applications, Food Hydrocolloids, 31 (2013) 332-339.

[128] S.C. Chen, Y.C. Wu, F.L. Mi, Y.H. Lin, L.C. Yu, H.W. Sung, A novel pH-sensitive hydrogel composed of N,O-carboxymethyl chitosan and alginate cross-linked by genipin for protein drug delivery, Journal of Control Release, 96 (2004) 285-300.

[129] C. Schmitt, C. Sanchez, S. Desobry-Banon, J. Hardy, Structure and Technofunctional Properties of Protein-Polysaccharide Complexes: A Review, Crit Rev Food Sci Nutr, 38 (1998) 689-753.

[130] K. Ogawa, T. Yui, K. Okuyama, Three D structures of chitosan, Int J Biol Macromol, 34 (2004) 1-8.

[131] M.M. Coleman, D.J. Skrovanek, J. Hu, P.C. Painter, Hydrogen bonding in polymer blends. 1. FTIR studies of urethane-ether blends, Macromolecules, 21 (1988) 59-65.

[132] C. Liu, Z. Teng, Q.Y. Lu, R.Y. Zhao, X.Q. Yang, C.H. Tang, J.M. Liao, Aggregation kinetics and ζ-potential of soy protein during fractionation, Food Res Int, 44 (2011) 1392-1400.

[133] Z. Teng, Y. Luo, T. Wang, B. Zhang, Q. Wang, Development and Application of Nanoparticles Synthesized with Folic Acid Conjugated Soy Protein, J Agric Food Chem, 61 (2013) 2556-2564.

[134] S.-Y.-R. Paik, H.H. Nguyen, J. Ryu, J.-H. Che, T.S. Kang, J.K. Lee, C.W. Song, S. Ko, Robust size control of bovine serum albumin (BSA) nanoparticles by intermittent addition of a desolvating agent and the particle formation mechanism, Food Chem, 141 (2013) 695-701.

[135] Q. Zhong, M. Jin, Zein nanoparticles produced by liquid-liquid dispersion, Food Hydrocolloids, 23 (2009) 2380-2387.

[136] Y. Zhang, Y. Niu, Y. Luo, M. Ge, T. Yang, L.L. Yu, Q. Wang, Fabrication, characterization and antimicrobial activities of thymol-loaded zein nanoparticles stabilized by sodium caseinate-chitosan hydrochloride double layers, Food Chem, 142 (2014) 269-275.

[137] Z. Teng, Y. Luo, Q. Wang, Carboxymethyl Chitosan-Soy Protein Complex Nanoparticles for the Encapsulation and Controlled Release of Vitamin D3, Food Chem, 141 (2013) 524-532.

[138] A. Kumari, S.K. Yadav, S.C. Yadav, Biodegradable polymeric nanoparticles based drug delivery systems, Colloids Surf., B, 75 (2010) 1-18.

[139] L. Wang, J. Dong, J. Chen, J. Eastoe, X. Li, Design and optimization of a new self-nanoemulsifying drug delivery system, J. Colloid Interface Sci., 330 (2009) 443-448.

[140] D. Hu, C. Lin, L. Liu, S. Li, Y. Zhao, Preparation, characterization, and in vitro release investigation of lutein/zein nanoparticles via solution enhanced dispersion by supercritical fluids, J Food Eng, 109 (2012) 545-552.

[141] J. Chen, J. Zheng, D.J. McClements, H. Xiao, Tangeretin-loaded protein nanoparticles fabricated from zein/b-lactoglobulin: Preparation, characterization, and functional performance, Food Chem, 158 (2014) 466-472.

[142] A. Maghsoudi, S.A. Shojaosadati, E.V. Farahani, 5-Fluorouracil-loaded BSA nanoparticles: formulation optimization and in vitro release study, Aaps Pharmscitech, 9 (2008) 1092-1096.

[143] A.V. Jithan, K. Madhavi, M. Madhavi, K. Prabhakar, Preparation and characterization of albumin nanoparticles encapsulating curcumin intended for the treatment of breast cancer, Int. J. Pharm. Invest., 1 (2011) 119.

[144] J. Shaikh, D.D. Ankola, V. Beniwal, D. Singh, M.N.V. Kumar, Nanoparticle encapsulation improves oral bioavailability of curcumin by at least 9-fold when compared to curcumin administered with piperine as absorption enhancer, Eur J Pharm Sci, 37 (2009) 223-230.

[145] H. Zhou, X. Sun, L. Zhang, P. Zhang, J. Li, Y.-N. Liu, Fabrication of Biopolymeric Complex Coacervation Core Micelles for Efficient Tea Polyphenol Delivery via a Green Process, Langmuir, 28 (2012) 14553-14561.

[146] A. Shpigelman, Y. Cohen, Y.D. Livney, Thermally-induced beta-lactoglobulin-EGCG nanovehicles: Loading, stability, sensory and digestive-release study, Food Hydrocolloids, 29 (2012) 57-67.

[147] J.P. Van Buren, W.B. Robinson, Formation of complexes between protein and tannic acid, J Agric Food Chem, 17 (1969) 772-777.

[148] D.M. Kirchmajer, C.A. Watson, M. Ranson, M.i.h. Panhuis, Gelapin, a degradable genipin cross-linked gelatin hydrogel, RSC Advances, 3 (2013) 1073-1081.

[149] P.C. Lorenzen, E. Schlimme, N. Roos, Crosslinking of sodium caseinate by a microbial transglutaminase, Food/Nahrung, 42 (1998) 151-154.

[150] A.O. Elzoghby, M.W. Helmy, W.M. Samy, N.A. Elgindy, Novel ionically crosslinked casein nanoparticles for flutamide delivery: formulation, characterization, and in vivo pharmacokinetics, Int. J. Nanomedicine, 8 (2013) 1721.

[151] Z. Teng, Y. Li, Y. Luo, B. Zhang, Q. Wang, Cationic β-Lactoglobulin Nanoparticles as a Bioavailability Enhancer: Protein Characterization and Particle Formation, Biomacromolecules, 14 (2013) 2848-2856.

[152] O.P. Sharma, Antioxidant activity of curcumin and related compounds, Biochem Pharmacol, 25 (1976) 1811-1812.

[153] A.H. Sneharani, J.V. Karakkat, S.A. Singh, A.G.A. Rao, Interaction of Curcumin with b-Lactoglobulin-Stability, Spectroscopic Analysis, and Molecular Modeling of the Complex, J Agric Food Chem, 58 (2010) 11130-11139.

[154] S. Podaralla, R. Averineni, M. Alqahtani, O. Perumal, Synthesis of Novel Biodegradable Methoxy Poly(ethylene glycol)-Zein Micelles for Effective Delivery of Curcumin, Mol Pharm, 9 (2012) 2778-2786.

[155] J. Otte, M. Zakora, K.B. Qvist, C.E. Olsen, V. Barkholt, Hydrolysis of bovine β-lactoglobulin by various proteases and identification of selected peptides, Int. Dairy J., 7 (1997) 835-848.

[156] N. Fotaki, M. Vertzoni, Biorelevant Dissolution Methods and Their Applications in In Vitro-In Vivo Correlations for Oral Formulations, Open Drug Delivery J., 4 (2010) 2-13.

[157] E. Dufour, T. Haertl, Alcohol-induced changes of b-lactoglobulin-retinol-binding stoichiometry, Protein Eng, 4 (1990) 185-190.

[158] E. Dufour, C. Genot, T. Haertlé, b-lactoglobulin binding properties during its folding changes studied by fluorescence spectroscopy, Biochim. Biophys. Acta, Protein Struct. Mol. Enzymol., 1205 (1994) 105-112.

[159] A.H. Sneharani, J.V. Karakkat, S.A. Singh, A.G.A. Rao, Interaction of Curcumin with β-Lactoglobulin: Stability, Spectroscopic Analysis, and Molecular Modeling of the Complex, J Agric Food Chem, 58 (2010) 11130-11139.

[160] K.J. Siebert, N.V. Troukhanova, P.Y. Lynn, Nature of Polyphenol-Protein Interactions, J Agric Food Chem, 44 (1996) 80-85.

[161] H.H. Tonnesen, J. Karlsen, Studies on curcumin and curcuminoids. VI. Kinetics of curcumin degradation in aqueous solution, Z. Lebensm. Unters. Forsch., 180 (1985) 402-404.

[162] S. Dash, P.N. Murthy, L. Nath, P. Chowdhury, Kinetic modeling on drug release from controlled drug delivery systems, Acta Pol. Pharm., 67 (2010) 217-223.

[163] Z. Teng, Y. Li, Y. Niu, Y. Xu, L. Yu, Q. Wang, Cationic b-lactoglobulin nanoparticles as a bioavailability enhancer: Comparison between ethylenediamine and polyethyleneimine as cationizers, Food Chem, 159 (2014) 333-342.

[164] S. Ko, S. Gunasekaran, Preparation of sub-100-nm beta-lactoglobulin (BLG) nanoparticles, J Microencapsul, 23 (2006) 887-898.

[165] G.P. Andrews, D.S. Jones, Rheological characterization of bioadhesive binary polymeric systems designed as platforms for drug delivery implants, Biomacromolecules, 7 (2006) 899-906.

[166] L. Chen, G.E. Remondetto, M. Subirade, Food protein-based materials as nutraceutical delivery systems, Trends Food Sci. Technol., 17 (2006) 272-283.

[167] X.F. Liu, X.N. Zhi, Y.F. Liu, B. Wu, Z. Sun, J. Shen, Effect of Chitosan, O-Carboxymethyl Chitosan, and N-[(2-Hydroxy-3-N,N-dimethylhexadecyl ammonium)propyl] Chitosan Chloride on Overweight and Insulin Resistance in a Murine Diet-Induced Obesity, J. Agric. Food. Chem., 60 (2012) 3471-3476.

[168] H.Y. Tang, L.C. Yin, H. Lu, J.J. Cheng, Water-Soluble Poly(L-serine)s with Elongated and Charged Side-Chains: Synthesis, Conformations, and Cell-Penetrating Properties, Biomacromolecules, 13 (2012) 2609-2615.

[169] W.-C. Shen, H. Ryser, Conjugation of poly-L-lysine to albumin and horseradish peroxidase: a novel method of enhancing the cellular uptake of proteins, Proc. Natl. Acad. Sci., 75 (1978) 1872-1876.

[170] S.H. Kim, J.H. Jeong, K.W. Chun, T.G. Park, Target-specific cellular uptake of PLGA nanoparticles coated with poly (L-lysine)-poly (ethylene glycol)-folate conjugate, Langmuir, 21 (2005) 8852-8857.

[171] C.L. Watkins, P. Brennan, C. Fegan, K. Takayama, I. Nakase, S. Futaki, A.T. Jones, Cellular uptake, distribution and cytotoxicity of the hydrophobic cell penetrating peptide sequence PFVYLI linked to the proapoptotic domain peptide PAD, J Control Release, 140 (2009) 237-244.

[172] S. Deshayes, M. Morris, G. Divita, F. Heitz, Cell-penetrating peptides: tools for intracellular delivery of therapeutics, Cell. Mol. Life Sci., 62 (2005) 1839-1849.

[173] B. Hu, S.S. Wang, J. Li, X.X. Zeng, Q.R. Huang, Assembly of Bioactive Peptide-Chitosan Nanocomplexes, J. Phys. Chem. B, 115 (2011) 7515-7523.

[174] L.F. Qi, L.X. Wu, S. Zheng, Y.L. Wang, H.L. Fu, D.X. Cui, Cell-Penetrating Magnetic Nanoparticles for Highly Efficient Delivery and Intracellular Imaging of siRNA, Biomacromolecules, 13 (2012) 2723-2730.

[175] C.B. Furlund, A.B. Kristoffersen, T.G. Devold, G.E. Vegarud, C.M. Jonassen, Bovine lactoferrin digested with human gastrointestinal enzymes inhibits replication of human echovirus 5 in cell culture, Nutr. Res., 32 (2012) 503-513.

[176] O.G. Jones, S. Handschin, J. Adamcik, L. Harnau, S. Bolisetty, R. Mezzenga, Complexation of beta-Lactoglobulin Fibrils and Sulfated Polysaccharides, Biomacromolecules, 12 (2011) 3056-3065.

[177] M. Papiz, L. Sawyer, E. Eliopoulos, A. North, J. Findlay, R. Sivaprasadarao, T. Jones, M. Newcomer, P. Kraulis, The structure of β-lactoglobulin and its similarity to plasma retinol-binding protein, Nature, 324 (1986) 383-385.

[178] I.M. Reddy, N.K.D. Kella, J.E. Kinsella, Structural and conformational basis of the resistance of β-lactoglobulin to peptic and chymotryptic digestion, J. Agric. Food. Chem., 36 (1988) 737-741.

[179] A. Dong, J. Matsuura, S.D. Allison, E. Chrisman, M.C. Manning, J.F. Carpenter, Infrared and circular dichroism spectroscopic characterization of structural differences between beta-lactoglobulin A and B, Biochemistry, 35 (1996) 1450-1457.

[180] P.S. Given Jr, Encapsulation of flavors in emulsions for beverages, Curr. Opin. Colloid Interface Sci., 14 (2009) 43-47.

[181] W. Zhang, Q. Zhong, Microemulsions as nanoreactors to produce whey protein nanoparticles with enhanced heat stability by thermal pretreatment, Food Chem., 119 (2010) 1318-1325.

[182] P. Zimet, Y.D. Livney, Beta-lactoglobulin and its nanocomplexes with pectin as vehicles for ω-3 polyunsaturated fatty acids, Food Hydrocolloids, 23 (2009) 1120-1126.

[183] N.L. Mattarella, T. Richardson, Physicochemical and functional properties of positively charged derivatives of bovine .beta.-lactoglobulin, J. Agric. Food. Chem., 31 (1983) 972-978.

[184] D.G. Hoare, D.E. Koshland, A Method for Quantitative Modification and Estimation of Carboxylic Acid Groups in Proteins, J. Biol. Chem., 242 (1967) 2447-&.

[185] L. Castaneda, J. Valle, N. Yang, S. Pluskat, K. Slowinska, Collagen Cross-Linking with Au Nanoparticles, Biomacromolecules, 9 (2008) 3383-3388.

[186] A. Laligant, E. Dumay, C.C. Valencia, J.L. Cuq, J.C. Cheftel, Surface Hydrophobicity and Aggregation of Beta-Lactoglobulin Heated near Neutral Ph, J. Agric. Food. Chem., 39 (1991) 2147-2155.

[187] C. Bhattacharjee, S. Saha, A. Biswas, M. Kundu, L. Ghosh, K.P. Das, Structural changes of beta-lactoglobulin during thermal unfolding and refolding-an FT-IR and circular dichroism study, Protein J, 24 (2005) 27-35.

[188] W.H. Stein, Amino acid composition of beta-lactoglobulin and bovine serum albumin, J. Biol. Chem., 178 (1949) 79-91.

[189] N.A. Stasko, C.B. Johnson, M.H. Schoenfisch, T.A. Johnson, E.L. Holmuhamedov, Cytotoxicity of polypropylenimine dendrimer conjugates on cultured endothelial cells, Biomacromolecules, 8 (2007) 3853-3859.

[190] B. Hu, Y. Ting, X. Zeng, Q. Huang, Cellular uptake and cytotoxicity of chitosan-caseinophosphopeptides nanocomplexes loaded with epigallocatechin gallate, Carbohydr. Polym., 89 (2012) 362-370.

[191] D. Fischer, Y. Li, B. Ahlemeyer, J. Krieglstein, T. Kissel, In vitro cytotoxicity testing of polycations: influence of polymer structure on cell viability and hemolysis, Biomaterials, 24 (2003) 1121-1131.

[192] A. Laligant, E. Dumay, C. Casas Valencia, J.L. Cuq, J.C. Cheftel, Surface hydrophobicity and aggregation of β-lactoglobulin heated near neutral pH, J. Agric. Food. Chem., 39 (1991) 2147-2155.

[193] M. Cardamone, N.K. Puri, Spectrofluorimetric assessment of the surface hydrophobicity of proteins, Biochem J, 282 ( Pt 2) (1992) 589-593.

[194] O.K. Gasymov, B.J. Glasgow, ANS fluorescence: Potential to augment the identification of the external binding sites of proteins, Biochim. Biophys. Acta: Proteins Proteomics, 1774 (2007) 403-411.

[195] G.R. Penzer, 1-Anilinonaphthalene-8-sulphonate, Eur. J. Biochem., 25 (1972) 218-228.

[196] S. Tcholakova, N.D. Denkov, D. Sidzhakova, I.B. Ivanov, B. Campbell, Effects of electrolyte concentration and pH on the coalescence stability of beta-lactoglobulin emulsions: Experiment and interpretation, Langmuir, 21 (2005) 4842-4855.

[197] J. Kong, S. Yu, Fourier transform infrared spectroscopic analysis of protein secondary structures, Acta Biochim. Biophys. Sin., 39 (2007) 549-559.

[198] M. Carbonaro, A. Nucara, Secondary structure of food proteins by Fourier transform spectroscopy in the mid-infrared region, Amino Acids, 38 (2010) 679-690.

[199] W.K. Surewicz, H.H. Mantsch, D. Chapman, Determination of protein secondary structure by Fourier transform infrared spectroscopy: A critical assessment, Biochemistry, 32 (1993) 389-394.

[200] D.M. Byler, H. Susi, Examination of the Secondary Structure of Proteins by Deconvolved Ftir Spectra, Biopolymers, 25 (1986) 469-487.

[201] A. Dong, P. Huang, W.S. Caughey, Protein secondary structures in water from second-derivative amide I infrared spectra, Biochemistry, 29 (1990) 3303-3308.

[202] L.J. Alexander, G. Hayes, M.J. Pearse, C.W. Beattie, A.F. Stewart, I.M. Willis, A.G. Mackinlay, Complete sequence of the bovine beta-lactoglobulin cDNA, Nucleic Acids Res, 17 (1989) 6739.

[203] L. Hedstrom, Serine protease mechanism and specificity, Chem. Rev., 102 (2002) 4501-4524.

[204] Y.L. Khmelnitsky, V.V. Mozhaev, A.B. Belova, M.V. Sergeeva, K. Martinek, Denaturation capacity: a new quantitative criterion for selection of organic solvents as reaction media in biocatalysis, Eur J Biochem, 198 (1991) 31-41.

[205] N.L. Mattarella, T. Richardson, Physicochemical and functional properties of positively charged derivatives of bovine β-lactoglobulin, J Agric Food Chem, 31 (1983) 972-978.

[206] Z. Teng, Q. Wang, Extraction, identification and characterization of the water-insoluble proteins from tobacco biomass, J Sci Food Agric, (2011).

[207] M.A. Augustin, Y. Hemar, Nano-and micro-structured assemblies for encapsulation of food ingredients, Chem Soc Rev, 38 (2009) 902-912.

[208] Y. Luo, Q. Wang, Recent Advances of Chitosan and Its Derivatives for Novel Applications in Food Science, J Food Processing & Beverages, 1 (2013) 1-13.

[209] Y. Luo, Z. Teng, T.T.Y. Wang, Q. Wang, Cellular Uptake and Transport of Zein Nanoparticles: Effects of Sodium Caseinate, J. Agric. Food Chem., 61 (2013) 7621-7629.

[210] F. Wang, L. Yu, M.P. Monopoli, P. Sandin, E. Mahon, A. Salvati, K.A. Dawson, The biomolecular corona is retained during nanoparticle uptake and protects the cells from the damage induced by cationic nanoparticles until degraded in the lysosomes, Nanomedicine, 9 (2013) 1159-1168.

[211] M. Lundqvist, Nanoparticles: Tracking protein corona over time, Nat. Nanotechnol., 8 (2013) 701-702.

[212] C. Wiegand, M. Bauer, U.-C. Hipler, D. Fischer, Poly(ethyleneimines) in dermal applications: Biocompatibility and antimicrobial effects, Int. J. Pharm., 456 (2013) 165-174.

[213] R.V. Benjaminsen, M.A. Mattebjerg, J.R. Henriksen, S.M. Moghimi, T.L. Andresen, The possible 'proton sponge' effect of polyethylenimine (PEI) does not include change in lysosomal pH, Mol. Ther., 21 (2012) 149-157.

[214] W.T. Carpenter, Secondary Direct Food Additives Permitted in Food for Human Consumption; Periodic Acid and Polyethylenimine, Fed. Regist., 61 (1996) 4871-4874.

[215] J. Futami, M. Kitazoe, T. Maeda, E. Nukui, M. Sakaguchi, J. Kosaka, M. Miyazaki, M. Kosaka, H. Tada, M. Seno, Intracellular delivery of proteins into mammalian living cells by polyethylenimine-cationization, J Biosci Bioeng, 99 (2005) 95-103.

[216] Y.Q. Dai, R.M. Whittal, L. Li, Two-layer sample preparation: A method for MALDI-MS analysis of complex peptide and protein mixtures, Anal Chem, 71 (1999) 1087-1091.

[217] S. Chelulei Cheison, J. Brand, E. Leeb, U. Kulozik, Analysis of the Effect of Temperature Changes Combined with Different Alkaline pH on the β-Lactoglobulin Trypsin Hydrolysis Pattern Using MALDI-TOF-MS/MS, J Agric Food Chem, 59 (2011) 1572-1581.

[218] S. Lakard, G. Herlem, B. Lakard, B. Fahys, Theoretical study of the vibrational spectra of polyethylenimine and polypropylenimine, Journal of Molecular Structure: THEOCHEM, 685 (2004) 83-87.

[219] N. Khanam, C. Mikoryak, R.K. Draper, K.J. Balkus Jr, Electrospun linear polyethyleneimine scaffolds for cell growth, Acta Biomater., 3 (2007) 1050-1059.

[220] H.L. Monaco, G. Zanotti, Three-dimensional structure and active site of three hydrophobic molecule-binding proteins with significant amino acid sequence similarity, Biopolymers, 32 (1992) 457-465.

[221] J. Godovac-Zimmermann, I. Krause, J. Buchberger, G. Weiss, H. Klostermeyer, Genetic variants of bovine beta-lactoglobulin. A novel wild-type beta-lactoglobulin W and its primary sequence, Bio. Chem. Hoppe-Seyler, 371 (1990) 255-260.

[222] A. Ludwig, The use of mucoadhesive polymers in ocular drug delivery, Adv Drug Delivery Rev, 57 (2005) 1595-1639.

[223] L. Brannon-Peppas, J.O. Blanchette, Nanoparticle and targeted systems for cancer therapy, Adv Drug Delivery Rev, 64 (2012) 206-212.

[224] K.S. Soppimath, T.M. Aminabhavi, A.R. Kulkarni, W.E. Rudzinski, Biodegradable polymeric nanoparticles as drug delivery devices, J Control Release, 70 (2001) 1-20.

[225] J. Panyam, V. Labhasetwar, Biodegradable nanoparticles for drug and gene delivery to cells and tissue, Adv Drug Delivery Rev, 55 (2003) 329-347.

[226] M.J. Hawkins, P. Soon-Shiong, N. Desai, Protein nanoparticles as drug carriers in clinical medicine, Adv Drug Delivery Rev, 60 (2008) 876-885.

[227] Z. Teng, Y. Li, Q. Wang, Insight into Curcumin-Loaded β-Lactoglobulin Nanoparticles: Incorporation, Particle Disintegration, and Releasing Profiles, J Agric Food Chem, 62 (2014) 8837-8847.

[228] I. Bravo-Osuna, C. Vauthier, A. Farabollini, G.F. Palmieri, G. Ponchel, Mucoadhesion mechanism of chitosan and thiolated chitosan-poly(isobutyl cyanoacrylate) core-shell nanoparticles, Biomaterials, 28 (2007) 2233-2243.

[229] Y. Yonamine, K. Yoshimatsu, S.-H. Lee, Y. Hoshino, Y. Okahata, K.J. Shea, Polymer Nanoparticle-Protein Interface. Evaluation of the Contribution of Positively Charged Functional Groups to Protein Affinity, ACS applied materials & interfaces, 5 374-379.

[230] C.C. Fleischer, C.K. Payne, Nanoparticle surface charge mediates the cellular receptors used by protein-nanoparticle complexes, The Journal of Physical Chemistry B, 116 (2012) 8901-8907.

[231] C.-C. Lin, H.-Y. Lin, H.-C. Chen, M.-W. Yu, M.-H. Lee, Stability and characterisation of phospholipid-based curcumin-encapsulated microemulsions, Food Chem, 116 (2009) 923-928.

[232] O. Rolland, C.-O. Turrin, A.-M. Caminade, J.-P. Majoral, Dendrimers and nanomedicine: multivalency in action, New J. Chem., 33 (2009) 1809-1824.

[233] S. Hong, P.R. Leroueil, I.J. Majoros, B.G. Orr, J.R. Baker Jr, M.M. Banaszak Holl, The Binding Avidity of a Nanoparticle-Based Multivalent Targeted Drug Delivery Platform, Chem. Biol., 14 (2007) 107-115.

[234] M. Merhi, C.Y. Dombu, A. Brient, J. Chang, A. Platel, F. Le Curieux, D. Marzin, F. Nesslany, D. Betbeder, Study of serum interaction with a cationic nanoparticle: Implications for *in vitro* endocytosis, cytotoxicity and genotoxicity, Int. J. Pharm., 423 (2012) 37-44.

[235] F. Wang, L. Yu, M.P. Monopoli, P. Sandin, E. Mahon, A. Salvati, K.A. Dawson, The biomolecular corona is retained during nanoparticle uptake and protects the cells from the damage induced by cationic nanoparticles until degraded in the lysosomes, Nanomedicine: Nanotechnology, Biology and Medicine, 9 (2013) 1159-1168.

[236] M.-H. Dufresne, M.A. Gauthier, J.-C. Leroux, Thiol-Functionalized Polymeric Micelles: From Molecular Recognition to Improved Mucoadhesion, Bioconjug Chem, 16 (2005) 1027-1033.

[237] J.D. Smart, The basics and underlying mechanisms of mucoadhesion, Adv Drug Delivery Rev, 57 (2005) 1556-1568.

[238] J.D. Smart, I.W. Kellaway, H.E.C. Worthington, An *in vitro* investigation of mucosa-adhesive materials for use in controlled drug delivery, J Pharm Pharmacol, 36 (1984) 295-299.

[239] S. Kim, J.S. Choi, H.S. Jang, H. Suh, J. Park, Hydrophobic modification of polyethyleneimine for gene transfectants, BULLETIN-KOREAN CHEMICAL SOCIETY, 22 (2001) 1069-1075.

[240] M. El-Sayed, M. Ginski, C. Rhodes, H. Ghandehari, Transepithelial transport of poly (amidoamine) dendrimers across Caco-2 cell monolayers, J Control Release, 81 (2002) 355-365.

[241] N.G.M. Schipper, S. Olsson, J.A. Hoogstraate, A.G. deBoer, K.M. Varum, P. Artursson, Chitosans as absorption enhancers for poorly absorbable drugs .2. Mechanism of absorption enhancement, Pharm. Res., 14 (1997) 923-929.

[242] G. Ranaldi, I. Marigliano, I. Vespignani, G. Perozzi, Y. Sambuy, The effect of chitosan and other polycations on tight junction permeability in the human intestinal Caco-2 cell line, The Journal of nutritional biochemistry, 13 (2002) 157-167.

[243] D. Vllasaliu, R. Exposito-Harris, A. Heras, L. Casettari, M. Garnett, L. Illum, S. Stolnik, Tight junction modulation by chitosan nanoparticles: comparison with chitosan solution, Int. J. Pharm., 400 (2010) 183-193.

[244] Z. Ma, L.-Y. Lim, Uptake of chitosan and associated insulin in Caco-2 cell monolayers: a comparison between chitosan molecules and chitosan nanoparticles, Pharm. Res., 20 (2003) 1812-1819.

[245] P. Artursson, T. Lindmark, S.S. Davis, L. Illum, Effect of chitosan on the permeability of monolayers of intestinal epithelial cells (Caco-2), Pharm. Res., 11 (1994) 1358-1361.

[246] F.D. Sahneh, C. Scoglio, J. Riviere, Dynamics of nanoparticle-protein corona complex formation: analytical results from population balance equations, PLoS One, 8 (2013) e64690.

[247] H. Maeda, J. Wu, T. Sawa, Y. Matsumura, K. Hori, Tumor vascular permeability and the EPR effect in macromolecular therapeutics: a review, J Control Release, 65 (2000) 271-284.

[248] J. Chen, J.A. Hessler, K. Putchakayala, B.K. Panama, D.P. Khan, S. Hong, D.G. Mullen, S.C. DiMaggio, A. Som, G.N. Tew, Cationic nanoparticles induce nanoscale disruption in living cell plasma membranes, The Journal of Physical Chemistry B, 113 (2009) 11179-11185.

[249] P.R. Leroueil, S.A. Berry, K. Duthie, G. Han, V.M. Rotello, D.Q. McNerny, J.R. Baker, B.G. Orr, M.M. Banaszak Holl, Wide varieties of cationic nanoparticles induce defects in supported lipid bilayers, Nano Lett., 8 (2008) 420-424.

[250] H. Yen, S. Hsu, C. Tsai, Cytotoxicity and immunological response of gold and silver nanoparticles of different sizes, Small, 5 (2009) 1553-1561.

[251] Y. Pan, S. Neuss, A. Leifert, M. Fischler, F. Wen, U. Simon, G. Schmid, W. Brandau, W. Jahnen-Dechent, Size-Dependent Cytotoxicity of Gold Nanoparticles, Small, 3 (2007) 1941-1949.

[252] A.M. Bannunah, D. Vllasaliu, J. Lord, S. Stolnik, Mechanisms of Nanoparticle Internalization and Transport Across an Intestinal Epithelial Cell Model: Effect of Size and Surface Charge, Molecular pharmaceutics, 11 (2014) 4363-4373.

[253] C.T. Thach, J.N. Finkelstein, Cationic nanoparticles disrupt cellular signaling in a cholesterol dependent manner, Toxicol In Vitro, 27 (2013) 1277-1286.

[254] A. Gupta, D. Mandal, Y. Ahmadibeni, K. Parang, G. Bothun, Hydrophobicity drives the cellular uptake of short cationic peptide ligands, Eur Biophys J, 40 (2011) 727-736.

[255] B.D. Chithrani, A.A. Ghazani, W.C.W. Chan, Determining the size and shape dependence of gold nanoparticle uptake into mammalian cells, Nano Lett., 6 (2006) 662-668.

[256] A.C. Sabuncu, J. Grubbs, S. Qian, T.M. Abdel-Fattah, M.W. Stacey, A. Beskok, Probing nanoparticle interactions in cell culture media, Colloids Surf., B, 95 (2012) 96-102.

[257] A.M. Alkilany, C.J. Murphy, Toxicity and cellular uptake of gold nanoparticles: what we have learned so far?, J Nanopart Res, 12 (2010) 2313-2333.

[258] J. Lin, A. Alexander-Katz, Cell Membranes Open 'Doors' for Cationic Nanoparticles/Biomolecules: Insights into Uptake Kinetics, ACS Nano, 7 (2013) 10799-10808.